# REPORT DOCUMENTATION PAGE

**AD-A247 293**

| | |
|---|---|
| 1b. RESTRICTIVE MARKINGS | |
| 2b. DECLASSIFICATION/DOWNGRADING SCHEDULE | 3. DISTRIBUTION/AVAILABILITY OF REPORT<br>Distribution Unlimited |
| 4. PERFORMING ORGANIZATION REPORT NUMBER(S) | 5. MONITORING ORGANIZATION REPORT NUMBER(S)<br>AFOSR-TR- 92 0114 |

ELECTE MAR 0 6 1992 D

| 6a. NAME OF PERFORMING ORGANIZATION<br>University of Illinois | 6b. OFFICE SYMBOL *(If applicable)* | 7a. NAME OF MONITORING ORGANIZATION<br>*Same as 8a* |
|---|---|---|
| 6c. ADDRESS *(City, State, and ZIP Code)*<br>Department of Electrical and Computer Engineering<br>1406 W. Green St.<br>Urbana, IL 61801 | | 7b. ADDRESS *(City, State, and ZIP Code)*<br>*Same as 8c* |
| 8a. NAME OF FUNDING/SPONSORING ORGANIZATION<br>AFOSR/NE | 8b. OFFICE SYMBOL *(If applicable)*<br>NE | 9. PROCUREMENT INSTRUMENT IDENTIFICATION NUMBER<br>Purchase Request No. F08671-9000284<br>AFOSR-89-0038 |

| 8c. ADDRESS *(City, State, and ZIP Code)*<br>Building 410<br>Bolling AFB, DC 20332-6448 | 10. SOURCE OF FUNDING NUMBERS | | | |
|---|---|---|---|---|
| | PROGRAM ELEMENT NO.<br>61103F | PROJECT NO.<br>2301 | TASK NO.<br>A1 | WORK UNIT ACCESSION NO. |

**11. TITLE** *(Include Security Classification)*

VUV AND UV SOURCES AND SPECTROSCOPIC APPLICATIONS

12. PERSONAL AUTHOR(S)
J. G. Eden

| 13a. TYPE OF REPORT<br>Final Technical | 13b. TIME COVERED<br>FROM 11-1-89 TO 10-31-91 | 14. DATE OF REPORT *(Year, Month, Day)*<br>December 1991 | 15. PAGE COUNT<br>149 |
|---|---|---|---|

16. SUPPLEMENTARY NOTATION

| 17. | COSATI CODES | | 18. SUBJECT TERMS *(Continue on reverse if necessary and identify by block number)* |
|---|---|---|---|
| FIELD | GROUP | SUB-GROUP | laser, shortwavelength, energy storage, compound semiconductors, photochemical deposition |

19. ABSTRACT *(Continue on reverse if necessary and identify by block number)*

Extensive experimental studies of small molecules as potential "hosts" for short wavelength ( $\lambda < 200$ nm) energy-storage lasers have been conducted. Laser spectroscopy of the rare gas dimers and Group IIB dimers have yielded structural constants for a significant number of previously unobserved states. Also, Fano "windows" have been observed in $Ne_2$ in the energy region lying between $v^+ = 0$ and $v^+ = 3$ of the $Ne_2^+$ ground state ($X^2\Sigma$). Bound $\rightarrow$ free emission studies of $Cd_2$ and $Zn_2$ have been carried out and the structural constants for the $^1\Sigma$ upper states have been determined.

The growth of GaAs and GaN by photo-assisted MOCVD has also been demonstrated. Gallium arsenide has been grown epitaxially at temperatures as low as 450°C by illuminating the surface with ArF (193 nm) radiation. Also, polycrystalline GaN (preferentially oriented (100)) has been grown on GaAs and sapphire at temperatures as low as 700°C and at growth rates exceeding 2 μm/hour.

| 20. DISTRIBUTION/AVAILABILITY OF ABSTRACT<br>☒ UNCLASSIFIED/UNLIMITED ☐ SAME AS RPT. ☐ DTIC USERS | 21. ABSTRACT SECURITY CLASSIFICATION<br>Unclassified |
|---|---|
| 22a. NAME OF RESPONSIBLE INDIVIDUAL<br>J. G. Eden | 22b. TELEPHONE *(Include Area Code)*<br>203-767-4906 | 22c. OFFICE SYMBOL<br>NE |

DD FORM 1473, 84 MAR

83 APR edition may be used until exhausted.
All other editions are obsolete.

# FINAL TECHNICAL REPORT FOR

## AFOSR GRANT 89-0038:

## "VUV AND UV SOURCES AND SPECTROSCOPIC APPLICATIONS"

DTIC
COPY
INSPECTED
6

| Accesion For | |
|---|---|
| NTIS CRA&I | ☑ |
| DTIC TAB | ☐ |
| Unannounced | ☐ |
| Justification | |
| By | |
| Distribution / | |
| Availability Codes | |
| Dist | Avail and/or Special |
| A-1 | |

Prepared for

Dr. Howard R. Schlossberg
Physics Directorate
AFOSR
Bolling Air Force Base
Washington, DC

by

J. G. Eden
Department of Electrical and Computer Engineering
Everitt Laboratory
University of Illinois
Urbana, IL 61801

December 1991

92-05467

92 3 03 199

# I. INTRODUCTION

This AFOSR-supported program has been directed over the past $2\frac{1}{2}$ years primarily towards identifying new sources of coherent radiation with emphasis on the vacuum UV, UV and low end of the visible ($\lambda < 500$ nm). The motivation for this effort is provided by the tantalizing applications in materials processing, (such as *in situ* photochemical processing), holography and surface analysis that require short wavelength lasers that do not exist. A good example is the VUV spectral region where tunable, high peak power sources are simply not available.

The work carried out under this grant has been multi-faceted and the following accomplishments realized in the past $1\frac{1}{2}$ years alone:

1. Photoexcitation experiments of the $^1\Sigma_u^+$ states of $Zn_2$ and $Cd_2$ have been completed and the resulting bound→free emission spectra have been analyzed. Those molecules were identified in joint theoretical studies with a Soviet physicist, Dr. V. Kochelap, as good candidates for an anti-Stokes Raman laser operating in the deep UV or VUV. The results have been published in the Journal of Chemical Physics.

2. The gerade Rydberg states of $Ne_2$ have been observed by laser excitation spectroscopy and the results have yielded precise structural constants for the molecule. More importantly, we have observed Fano windows in $Ne_2$ which arise from a Rydberg series of super-excited $^3\Pi_g$ states approaching the $v^+ = 1, 2$ and $3$ states of $Ne_2^+$. This is an exciting result because we have learned a great deal about coupling of the continuum to these embedded states.

3. Experiments in which an AlGaAs diode laser has been pulse-amplified in a system of four dye amplifiers have been nearly completed. After frequency doubling the near IR output beam, ~100 $\mu$J of narrow linewidth radiation is obtained at 390 nm. We are presently testing this source by optogalvanic spectroscopy on Fe. The results are described in the attached thesis that was prepared by Ann Farkas for her Master's degree.

4. The photochemical vapor deposition of GaN at 700°C has been accomplished. Although the films are presently polycrystalline, they are preferentially-oriented (100) and grow at rates exceeding 2 μm/hour.

In addition to these results, a book chapter on photochemical vapor deposition has been published as a portion of Werner Kern and John Vossen's book entitled Thin Film Processes II (Academic Press, 1991). This chapter has recently been expanded upon and will be published as a monograph under the title Photochemical Vapor Deposition. It will be published by John Wiley in 1992. Also, the U. S. Patent Office awarded a patent to the Air Force this year for work done under this grant. A copy of that patent is attached. The next section describes several of these results in more detail.

## II. RESULTS

A major component of this research program has been the investigation of the excited state structure of the rare gas dimers and, more recently, the Column IIB metal dimers. The rationale for this effort stems basically from the fact that the well-known energy storage capability of the rare gas dimers has never been fully exploited. All of the excited states of the rare gas dimers are Rydberg and lie more than halfway from ground to the first ionization limit. The lowest excited states of these homonuclear molecules are essentially metastable. For the lighter species ($He_2$ and $Ne_2$), Hund's case (b) provides a good description of the excited states and the lowest one is denoted $^3\Sigma_u^+$ which is, of course, not optically connected to ground ($^1\Sigma_u^+$) by dipole transitions. As the mass of the dimers increases, however, spin-orbit coupling gradually reduces the lifetime of this state as Hund's case (c) notation of the state—$1_u$, $0_u^-$—becomes appropriate.

In any event, the ability of these metastable molecules to store energy makes them attractive candidates as amplifiers or anti-Stokes Raman media. Also, since $T_e$ for these states lie at >8 eV, one can immediately envision their potential utility for the VUV and, perhaps, XUV as well.

The motivation, then, for this program was to develop a data base for these molecules that would allow one to subsequently design the types of devices cited above. The paucity of data

available regarding the Rydberg states of all the rare gas dimers (except $He_2$) prompted us to conduct the experiments discussed in the next few sections.

**Laser Excitation of Spectroscopy of $Ne_2$ and $Ar_2$**

The long radiative lifetimes (> 1 $\mu$sec) of their $ns^3\Sigma_u^+$ metastable levels (n = 2–4 for $He_2$, $Ne_2$ and $Ar_2$, respectively), and the high energies ($\geq$ 9 eV) and large rotational constants ($\geq 0.15$ cm$^{-1}$) for their Rydberg states make $Ar_2$ and $Ne_2$, in particular, excellent possibilities for the applications mentioned earlier. In contrast to $He_2$, unfortunately, little was known of the $Ar_2$ or $Ne_2$ states lying above the lowest levels (correlated with $ns[3/2]_2 + {}^1S_0$) because virtually all of their Rydberg states are strongly predissociated. To circumvent this difficulty, we developed a simple spectroscopic approach that is actually <u>dependent</u> upon the predissociation of the higher Rydberg.

Figure 1 shows the dramatic improvement in resolution that is afforded by this experimental approach as opposed to conventional absorption methods. The upper spectrum is one that was acquired in the present experiments whereas the lower profile was that obtained by absorption in an electron-beam-pumped plasma in 7600 Torr of Ar. Spectra such as that in Figure 1 have made it possible to extract a tremendous amount of information concerning the structure and kinetics of the excited states of $Ar_2$ and $Ne_2$. The details of the analysis of the $Ar_2$ excitation spectra will not be described here but Table I, which summarizes the characteristics of a number of $Ne_2$ Rydberg states, conveys some idea of the wealth of information to which one has access. The attached reprints describe some of our results obtained to date. The significance of this is that, for the first time, one can design (rather than speculate about) a non-linear optical scheme for extracting energy from the lowest $ns^3\Sigma_u^+$ metastable states of the rare gas dimers.

Also, in $Ne_2$, vibrational autoionization of $np^3\Pi_g$ Rydberg states (n $\geq$ 15) that converge to $v^+ = 1$ of the $Ne_2^+$ ground state has been observed. As indicated in Figure 2, these states are observed as "windows" in a predissociative continuum lying above the $Ne_2^+$ ($v^+ = 0$) limit. Similar series converging to the $Ne_2^+$ $v^+ = 2$ and 3 limits are also observed. The intriguing aspect of this spectrum is the sharpness of the autoionizing resonances which implies that the vibrational
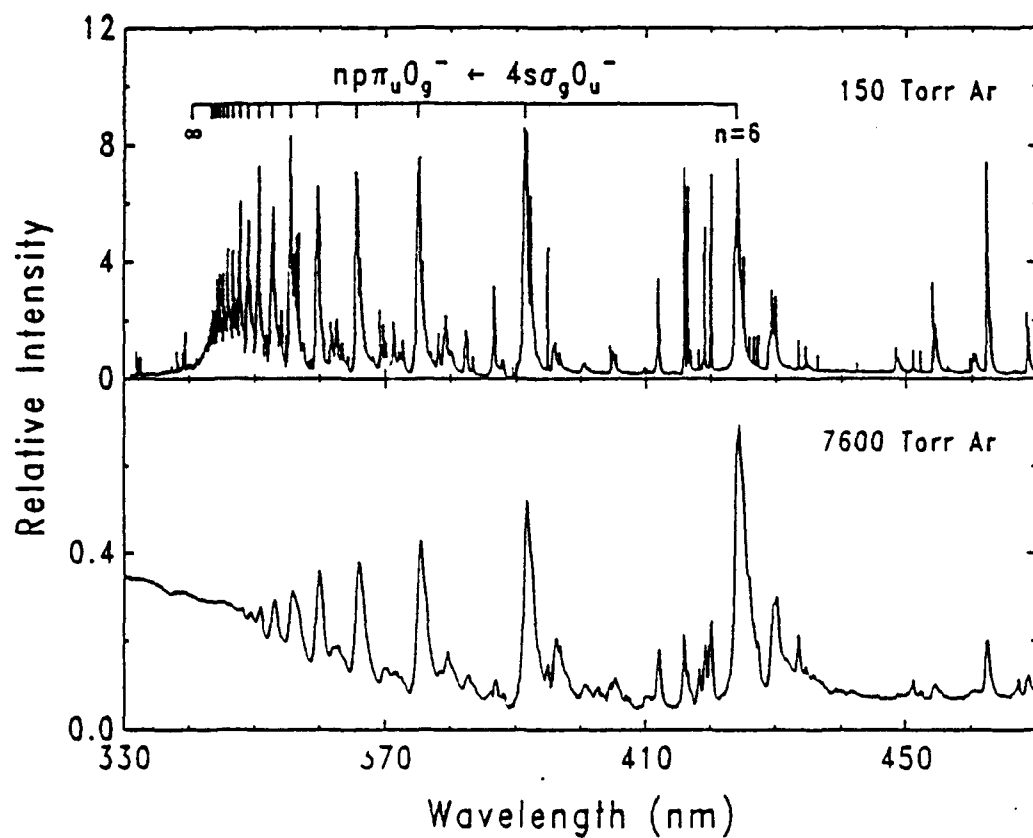
Fig. 1 Comparison of $Ar_2$ spectrum obtained by the LIF method with that recorded by Killeen using a classical absorption method: (a) the $Ar_2^*$ excitation spectrum determined in this work by an LIF method; (b) a low resolution version obtained by Killeen et al. (*J. Chem. Phys.* **84**, 6048 (1986)) in absorption.

TABLE I. Effective molecular parameters (cm$^{-1}$) and quantum numbers for the experimentally characterized np$\lambda$ $^3\Lambda_g^+$ ($v = 0$) states of $^{20}$Ne$_2$.

| State | E(N=0) | $n^*$ | $B_0 \times 10$ | $D_0 \times 10^5$ | $H_0 \times 10^8$ |
|---|---|---|---|---|---|
| 6p$\sigma$ $^3\Sigma_g^+$ | 23510[b] | 3.175 | | | |
| 4p$\pi$ $^3\Pi_g^+$ | 23972.80±0.08[c] | 3.2442 | 5.743±0.008[c] | 0.9±0.5[c] | 1.2±0.8[c] |
| 7p$\sigma$ $^3\Sigma_g^+$ | 28080[b] | 4.167 | | | |
| 5p$\pi$ $^3\Pi_g^+$ | 28324.5±0.1[c] | 4.250 | 5.758±0.010[c] | 0.5±0.4[c] | 0.1±0.2[c] |
| 8p$\sigma$ $^3\Sigma_g^+$ | 30294[b] | 5.162 | | | |
| 6p$\pi$ $^3\Pi_g^+$ | 30424.6±0.2[c] | 5.255 | 5.82±0.02[c] | 0.9±0.5[c] | 0.5±0.3[c] |
| 9p$\sigma$ $^3\Sigma_g^+$ | 31526[b] | 6.180 | | | |
| 7p$\pi$ $^3\Pi_g^+$ | 31603.3±0.2[c] | 6.256 | 5.89±0.02[c] | 0.9±0.5[c] | 0.2±0.2[c] |
| 10p$\sigma$ $^3\Sigma_g^+$ | 32277.8±0.2[d] | 7.193[d] | 5.40±0.02[d] | -2.3±2.0[d] | 4.0±4.5[d] |
| 8p$\pi$ $^3\Pi_g^+$ | 32320.2±0.2[c] | 7.266 | 5.98±0.02[c] | 2.2±0.7[c] | 1.1±0.5[c] |
| 11p$\sigma$ $^3\Sigma_g^+$ | 32747±1[e] | 8.15[e] | 5.0±.2[e] | N.D. | N.D. |
| 9p$\pi$ $^3\Pi_g^+$ | 32796.1±0.2[c] | 8.274 | 5.77±0.02[c] | 5.2±0.02[c] | 0.1±0.2[c] |
| 12p$\sigma$ $^3\Sigma_g^+$ | 33101.0±0.2 | 9.195 | 4.90±0.08 | -15.±12. | -18.±17. |
| 10p$\pi$ $^3\Pi_g^+$ | 33125.7±0.2 | 9.283 | 6.10±0.02 | 5.7±0.7 | 2.0±1.5 |
| 13p$\sigma$ $^3\Sigma_g^+$ | 33350.8±0.3 | 10.232 | 4.85±0.10 | -16±13 | -15.0±15.0 |
| 11p$\pi$ $^3\Pi_g^+$ | 33363.9±0.3 | 10.296 | 6.32±0.10 | 7.6±2.0 | 3.3±3.0 |
| 14p$\sigma$ $^3\Sigma_g^+$ | 33520.0±0.3 | 11.173 | 5.30±0.10 | -2.0±2.5 | -0.5±1.0 |
| 12p$\pi$ $^3\Pi_g^+$ | f | f | f | f | f |
| 15p$\sigma$ $^3\Sigma_g^+$ | 33667.7±0.4 | 12.250 | 4.90±0.10 | -4.0±4.5 | -6.0±5.0 |
| 13p$\pi$ $^3\Pi_g^+$ | 33677.8±0.4 | 12.335 | 6.30±0.15 | 8.0±3.0 | N.D. |
| 16p$\sigma$ $^3\Sigma_g^+$ | 33772.8±0.4 | 13.238 | 4.90±0.15 | -16.0±14.0 | -16.±8.0 |
| 14p$\pi$ $^3\Pi_g^+$ | 33785.0±0.3 | 13.369 | 6.35±0.15 | 6.8±4.0 | N.D. |
| 17p$\sigma$ $^3\Sigma_g^+$ | 33853.3±0.4 | 14.181 | 4.80±0.20 | -23.0±22.0 | -30.±20.0 |
| 15p$\pi$ $^3\Pi_g^+$ | 33867.2±0.3[g] | 14.365[g] | 6.37±0.10[g] | 13.0±10.0[g] | N.D. |
| 18p$\sigma$ $^3\Sigma_g^+$ | h | h | h | h | h |
| 16p$\pi$ $^3\Pi_g^+$ | 33938.4±0.3 | 15.435 | 6.30±0.15 | N.D. | N.D. |
| 19p$\sigma$ $^3\Sigma_g^+$ | 33987.0±0.3 | 16.320 | 4.50±0.20 | -25.0±20.0 | -20.0±15.0 |
| 17p$\pi$ $^3\Pi_g^+$ | 33993.4±0.2 | 16.448 | 6.60±0.20 | 20.0±20 | N.D. |
| 20p$\sigma$ $^3\Sigma_g^+$ | 34030.9±0.2 | 17.266 | 4.50±0.30 | N.D. | N.D. |
| 21p$\sigma$ $^3\Sigma_g^+$ | 34075.0±0.4 | 18.404 | 4.20±.60 | N.D. | N.D. |
| 22p$\sigma$ $^3\Sigma_g^+$ | 34099.0±0.3 | 19.125 | 4.50±0.30 | N.D. | N.D. |
| 23p$\sigma$ $^3\Sigma_g^+$ | 34133.1±0.3 | 20.315 | 4.60±0.30 | N.D. | N.D. |

Fig. 2    Absorption spectra for the lowest excited (and metastable) states of $^{20}Ne_2$ and $^{22}Ne_2$ showing "windows" in the region above the first ionization limit ($Ne_2^+$ $X^2\Sigma$, $v^+ = 0$). These spectra clearly show evidence for the competition between vibrational autoionization and predissociation.
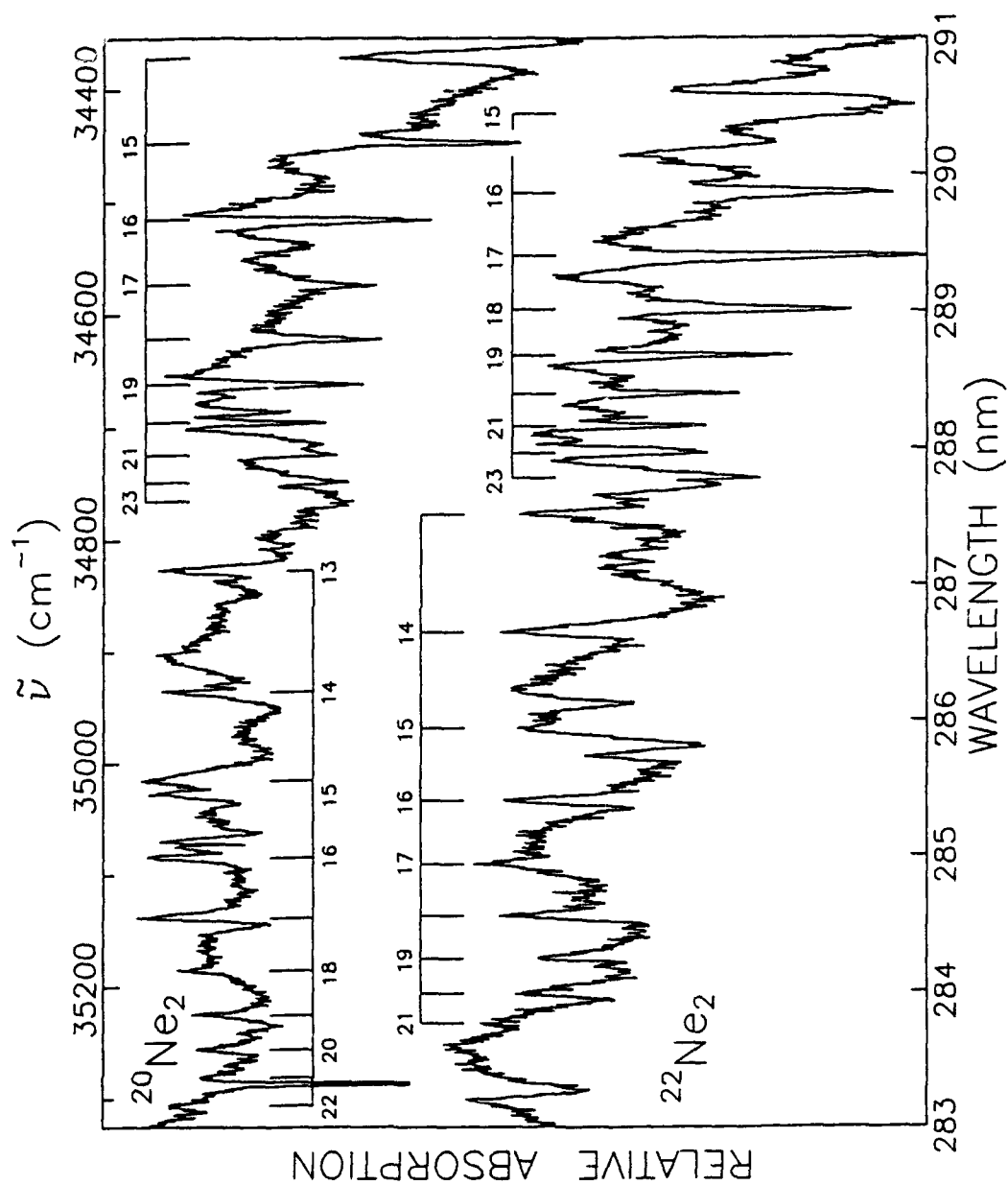


FIG. 3    Kim et al.

autoionization lifetimes of these states exceeds several picoseconds, a property which may be useful in a nonlinear mixing or wavelength conversion scheme. A paper describing these results will be published in <u>Physical Review Letters</u> in early 1992.

## Bound → Free Emission in Cd$_2$ and Zn$_2$

Another set of diatomic molecules that are potential energy storage systems are the Group IIB dimers Cd$_2$, Zn$_2$ and Hg$_2$. Although the use of, for example, Hg$_2$ as a laser is certainly not new, the almost complete absence of information concerning all but the lowest-lying excited states of the molecule has thus far prevented the design of the type of energy extraction scheme described earlier for the rare gas dimers. In an effort to explore the structure of the Group IIB dimers in more detail, a number of emission spectra from the B$^1\Sigma_u^+$ state of the dimers have been acquired by photoassociating pairs of ground state atoms at various wavelengths in the ultraviolet. The attached reprint, which was published in a recent issue of the <u>Journal of Chemical Physics</u>, describes the accuracy with which excited state potentials can be constructed in this way.

## Photochemical Growth of Wide Bandgap III-V Semiconductor Films

During this three year grant period we have also been pursuing the photo-CVD growth of III-V films and the attached reprints describe the first results obtained on GaAs through a collaborative program with Professor J. Coleman. In the past year, we have concentrated on GaN and have successfully grown thin films at rates exceeding 2 μm/hour at 700°C. These films were grown on GaAs (100) substrates and are polycrystalline but are preferentially oriented (100). The primary impurity in the film is oxygen which appears to be originating from the Ga precursor (TMG). The ease with which these films can be grown is encouraging and our plans for the immediate future center on obtaining epitaxial films on sapphire and then studying the control on the electrical properties of GaN that photo-CVD offers by substitutional doping.

# APPENDIX:
# RECENT REPRINTS PUBLISHED UNDER
# AFOSR GRANT 89-0038

# III-3

# Photochemical Vapor Deposition

*J. G. EDEN*

University of Illinois
Everitt Laboratory
Department of Electrical and Computer Engineering
Urbana, Illinois

443

## I. INTRODUCTION

Although the deposition of films by gas phase photochemical reactions was first reported in the scientific literature more than 50 years ago [1, 2], only since the late 1970s has the application of laser and lamp radiation to the growth of high-quality elemental and compound films been pursued vigorously. The expansion of the variety of materials that can be deposited by photochemical processes is truly remarkable; to date, photo-assisted chemical vapor deposition (photo-CVD) encompasses 24 elements of the periodic chart, in addition to at least 20 insulator and semiconductor compound films.

Interest in photo-CVD partially stems from the ability of optical radiation to induce specific chemical reactions in the gas phase or at a surface. The selective, optical production of atoms, molecular radicals, or even excited species in the vicinity of a surface, and the ability to do so independently of the substrate temperature, effectively decouples temperature from the number density of the species of interest. Said another way, the introduction of photons into a thin film deposition reactor allows one to drive the chemical environment far from equilibrium by selectively producing species that are not normally present in significant concentrations in conventional CVD, MBE, or MOCVD reactors. This flexibility inherent with the photodeposition of films often permits operation at lower temperatures, where impurity redistribution and thermally induced mechanical stress are minimized. Other attractive aspects of photo-CVD include the capability for selective area deposition and, in general, the absence of ion damage to the film. In short, the spatial resolution, chemical specificity, and reduced temperature capability of photodeposition are among the factors driving the current efforts in this field.

Several excellent reviews of photo-assisted deposition of semiconductor, metal, and insulator films have appeared in the literature. Early work in this field was summarized by Osgood [3] and, over the past five years, a half-dozen journal articles [4–8] and several chapters or entire books [9–13] devoted to reviewing the fundamental chemical and physical aspects of laser microchemical processing have been published.

It is the goal of this chapter to provide a broad overview of the photodeposition methods and materials that have been reported to date. Emphasis is placed on the practical aspects of both laser and ultraviolet (UV) lamp photodeposition techniques for films of interest to microelectronics; for more detailed discussions of reactor photochemistry, precursor chemical structure, or the metallurgical quality of the films, the reader is referred to selected references or to one of the reviews mentioned above. Because of their similarity to conventional CVD techniques, those photodeposition processes that are primarily thermal in nature are not treated in

this chapter. Such *photothermal* processes rely on the spatial properties of laser radiation to locally heat a substrate, and the reaction zone is laterally confined by the substrate's thermal conductivity and the nonlinear dependencies of reaction rates on temperature. Deposition processes involving the multiphoton absorption of infrared radiation to thermally dissociate polyatomic molecules are also not discussed here. Rather, the application of visible or shorter-wavelength radiation to the deposition of films from the gas phase is stressed.

Photo-CVD is only one member of an ever-growing class of processes, including those fundamentally photochemical *or* thermal in nature, that are now accessible with optical radiation. Laser-assisted doping, for example, is only briefly discussed here in conjunction with specific epitaxial semiconductor films and the rapidly expanding and fertile field of laser-induced etching of films is reviewed in detail in Chapter V.3 by Carol Ashby. Another closely allied processing subfield is that of selective area processing. Frequently combining photochemical and thermal mechanisms, and often drawing upon physical processes identical to those underlying broad-area deposition techniques, this area of film processing is described by Thomas Mayer and Susan Allen in Chapter IV.3.

## II. FUNDAMENTAL ASPECTS OF PHOTOCHEMICAL VAPOR DEPOSITION

### A. Photothermal and Photochemical Processes

Photo-assisted film deposition methods and laser-assisted deposition techniques, in particular, may be broadly subdivided into one of several categories, depending upon which of the three media (or combination thereof) present in a reactor absorbs strongly at the laser wavelength. As illustrated in Fig. 1, the substrate is normally immersed in a gas that gives rise to the formation of an adlayer at the surface of the substrate [14]. At the core of all photo-assisted deposition processes is the gas, vapor, or mixture of gases from which we wish to extract the element(s) of interest. Known as the precursor or "parent," the gas is generally molecular and is chosen for its combination of thermochemical and spectral properties. All photodeposition methods, then, can be qualitatively distinguished from one another according to the manner in which the precursor is decomposed to yield the desired film.

Depending upon the wavelength and intensity of the optical source, either the gas, adlayer, or substrate will be the predominant absorber that has a critical bearing on the physical characteristics and growth rate of the resulting film. The first question to be considered when attempting to categorize photo-assisted deposition processes is: How is the absorbed
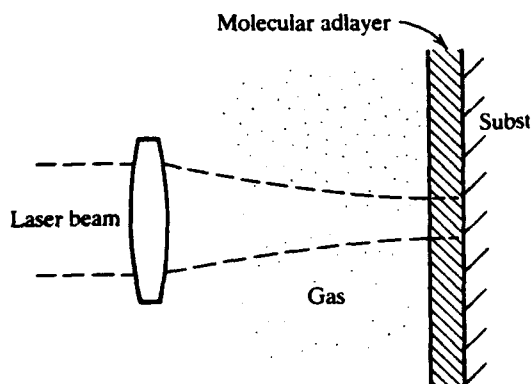
**Fig. 1.** Diagram illustrating the three media—gas, adlayer, and substrate—that are generally present in a photodeposition reactor. The optical and chemical properties of these three play a key role in determining the nature of the reactions that culminate in film growth and in the metallurgical and electrical properties of the deposit. Although the laser is shown irradiating the substrate, films are often grown with the optical beam directed parallel to the surface (adapted from Ref. 14).

energy disposed of? If the optical source energy is immediately converted primarily into heat, then the film growth process is said to be photothermal. Often referred to as laser chemical vapor deposition (LCVD), this approach is based on the laser providing a spatially localized source of heat at the substrate that decomposes (pyrolyzes) the precursor molecules once the surface temperature exceeds a critical value that varies from molecule to molecule. In this case, the gas in the reactor is often transparent at the laser wavelength and, except for the heat source, LCVD is otherwise similar to conventional chemical vapor deposition (CVD). As is discussed in more detail in Chapter III.1, LCVD places few constraints on the wavelength of the laser, and the lateral extent of film growth in the plane of the substrate's surface is determined not only by the cross-sectional geometry of the laser beam itself, but also by the thermal conductivity of the substrate and the nonlinear variation of the pyrolytic reaction rate constant with surface temperature. A second variation of LCVD depends on the gas of interest absorbing the laser radiation in such a way that the precursor molecules are not dissociated optically but are heated and eventually fragmented by thermal processes. Whether the substrate or gas (or both) is heated by the optical source, the results are similar and are categorized as photothermal.

*Photochemical* vapor deposition, on the other hand, owes its existence to the fact that UV and visible photon energies ( ~ 2–6 eV) are often

Laser evaporation

Laser chemical vapor deposition
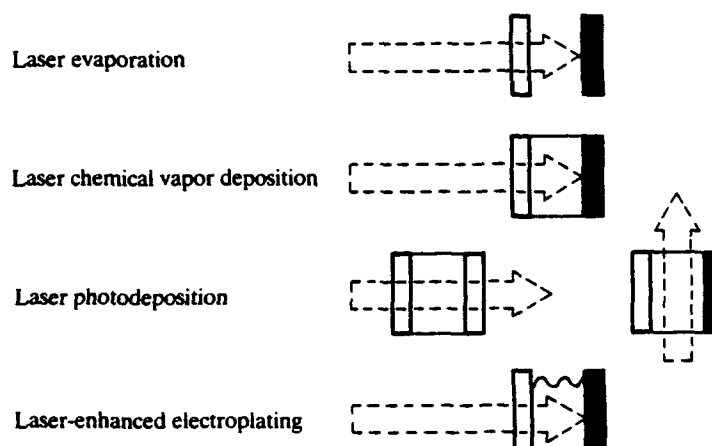
Laser photodeposition

Laser-enhanced electroplating

*Fig. 2.* Schematic representations of the various methods available for the laser-assisted deposition of films. The darkened rectangles represent substrates that absorb strongly at the laser wavelength, whereas the open rectangles are transparent materials. Note that laser-enhanced electroplating occurs in the presence of a liquid. This chapter is directed towards the third area, laser (or lamp) photodeposition of thin films (adapted from Ref. 15).

sufficiently large that chemical bonds in polyatomic molecules can be ruptured by the absorption of one or perhaps two photons. A wide range of photo-assisted deposition techniques have been demonstrated, and, bearing the above principles in mind, most are readily classified as shown schematically in Fig. 2. In this diagram, substrates that absorb strongly at the laser wavelength are denoted by solid rectangles, while optically transparent materials are represented by open rectangles. Laser evaporation consists of rapidly heating a target with a pulsed laser, which results in the ablation of surface molecules and their subsequent deposition onto a nearby substrate. In this case, the gas (if present) is nonreactive, and frequently the process is carried out in vacuum. A reactive ambient gas is essential for laser CVD or photochemical deposition, however, and the processes that culminate in film growth can occur either at the substrate surface or in the gas phase. The remainder of this chapter concentrates on film growth processes based predominantly on *photochemical* interactions with molecules in the gas phase or in the adlayer.

The reactor configurations generally used in photo-CVD can, as depicted in Fig. 2, involve an absorbing or optically transparent substrate, and it is not necessary for the optical beam to actually irradiate the surface. Both the so-called perpendicular (or normal incidence) and parallel
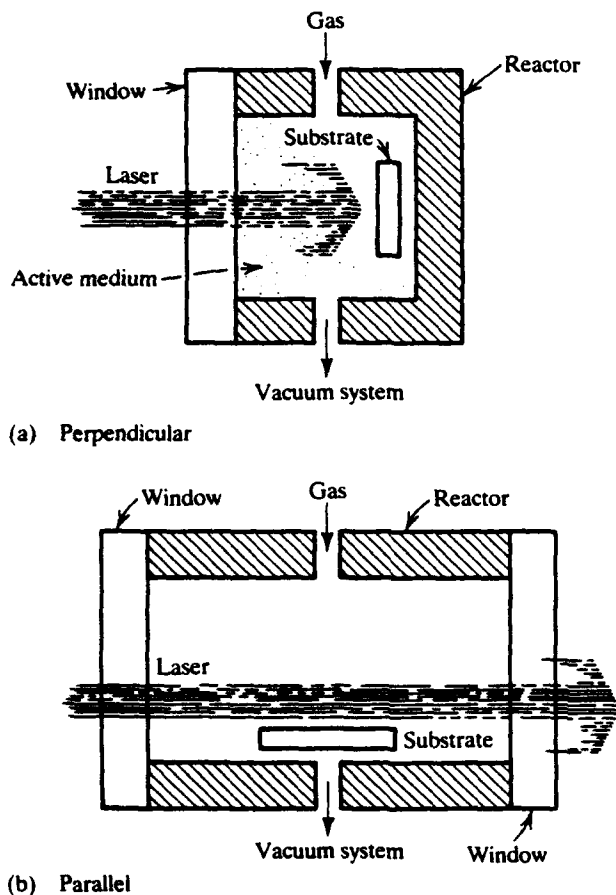
Fig. 3. (a) Perpendicular (or normal incidence) and (b) parallel geometry configurations typically used in laser photodeposition. Because of their lower intensities, ultraviolet lamps can irradiate the substrate (configuration (a)) without inducing a significant rise in surface temperature.

geometries common to photochemical vapor deposition are illustrated in more detail in Fig. 3. As its name implies, perpendicular geometry involves irradiating the substrate directly, and the critical photochemical mechanisms in this configuration generally occur in the adlayer. While Fig. 3 illustrates a laser as the optical source, a large fraction of photodeposition processes yield excellent results with ultraviolet or vacuum ultraviolet (VUV) lamps, and because of their lower instantaneous output

powers, one is able to directly irradiate the substrate as in Fig. 3a without concern for significantly heating the surface by the optical source. In parallel geometry, the optical beam does not impinge on the substrate, but rather produces atomic or molecular species that migrate to the substrate and react with the surface and adlayer, resulting in the desired film. In both cases (perpendicular or parallel geometry), the "active" medium of Fig. 3 is, in fact, initially inactive in the sense that no film is grown until the optical radiation photochemically alters the molecules (in the adlayer or gas phase) into a more chemically reactive form. One of the attractive features of photochemical deposition, then, is the control that it offers— spatial and temporal—since, in the absence of the external radiation provided by the lamp or laser, the film growth rate is negligible or zero.

## B. Overview of Photochemical Processes

Photochemistry in the gas and liquid phases is a well-established science, and considerable effort has been devoted over the last half-century to determining the products formed when small molecules absorb a visible, ultraviolet or vacuum ultraviolet photon (photon energy, $h\nu =$ 2–10 eV; bond-breaking with radiation of longer wavelengths [infrared] typically requires the absorption of more than one photon). Most of this information has been obtained from gas phase experiments, and considerably less is known of the interactions of optical radiation with molecular adlayers.

The absorption of optical radiation by a column of gas of number density $N$ (expressed in $cm^{-3}$) and path length $L$ is, at low intensities, governed by the relation known as the Beer–Lambert law:

$$I_t = I_i e^{-N\sigma L}, \tag{2.1}$$

where $I_i$ and $I_t$ are the optical intensities ($W\text{-}cm^{-2}$) incident upon and transmitted by the gaseous medium, respectively, and $\sigma$ is the absorption cross-section (generally expressed in $cm^2$) for the gas in question. Equation (2.1) is valid only when the precursor molecule absorbs a single photon from the optical source beam; multiphoton absorption rates, which vary nonlinearly with the source intensity $I$ and are usually significant only for $I \gtrsim 10^5–10^6\ W\text{-}cm^{-2}$, will be discussed later. Consequently, the fraction of the laser or lamp beam energy absorbed by the gas hinges upon the value of $\sigma$ at the source wavelength. For example, given a precursor partial pressure of 1 torr and an absorption cross-section of $10^{-18}\ cm^2$, 3% of the optical source energy will be absorbed over a 1-cm path length. If $\sigma = 10^{-17}\ cm^2$ at the source wavelength, the absorbed power rises to 27%. Since the absorption cross-section is a function of the source wavelength,
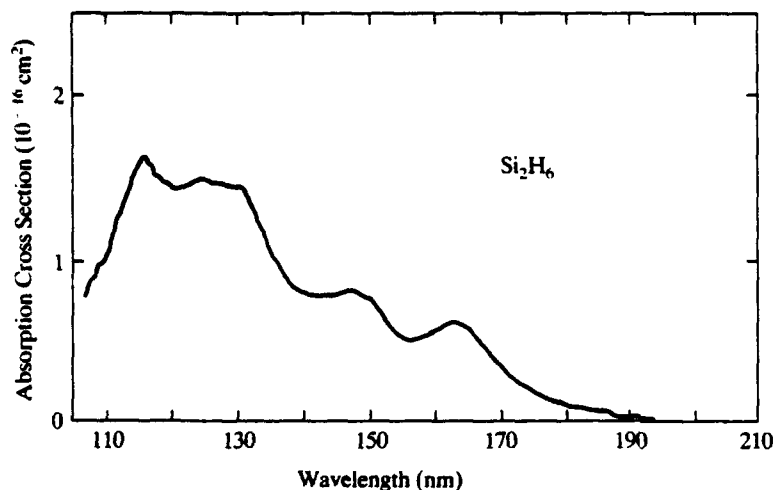
**Fig. 4.** Disilane ($Si_2H_6$) absorption spectrum in the VUV ($110 \leq \lambda \leq 210$ nm) (adapted from Ref. 16).

significant effort has been directed over the past decade, in particular, toward measuring the visible UV and VUV absorption spectra for volatile precursors containing metal or semiconductor atoms.

Essential properties for any molecule to be a viable precursor for photo-CVD are that: (1) it must be volatile (i.e., vapor pressure exceeding tens of millitorr at temperatures <100°C) in order to transport the desired species to the deposition chamber; and (2) the resulting polyatomic molecule must absorb optical radiation in a portion of the spectrum where efficient optical sources (lamps or lasers) exist. While most of the work to date in photo-CVD has involved precursors that were previously developed for thermal (chemical vapor) deposition techniques (MOCVD, CBE, etc.), future efforts will undoubtedly focus increasingly on the synthesis and engineering of new precursors.

Figure 4 shows the absorption spectrum of disilane ($Si_2H_6$), one of the most widely used precursors for the photodeposition of silicon. Note that absorption peaks in the vacuum ultraviolet (wavelengths below 200 nm or photon energies >6.2 eV), which presents difficult decisions when choosing an optical source from the lamps and lasers that are commercially available (cf. Section III.C). For the acetylacetonates (known as acacs) of platinum and iridium, however, absorption maxima (cf. Fig. 5) lie in the deep UV, which are conveniently accessible with both lamps and laser sources. Absorption coefficients at specific wavelengths, as well as entire
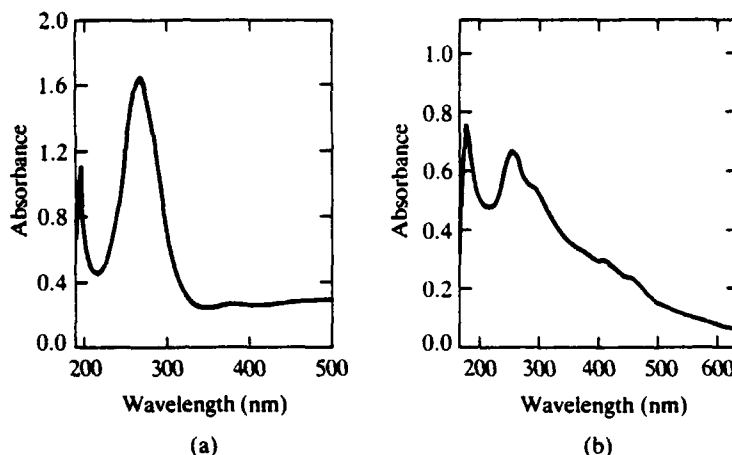
*Fig. 5.* Vapor phase absorption spectra of the acetylacetonates (acacs) of (a) platinum and (b) iridium in the UV and visible (reprinted from Ref. 17, by permission).

absorption spectra for several other molecular precursors of interest to photochemical vapor deposition, can be found in Refs. 18 and 19.

Although $\sigma$ describes the degree to which power is absorbed by a given gas, it says nothing of the manner in which the energy is disposed. One of the factors contributing most to the complexity (and breadth!) of photo-CVD is that the atomic and molecular fragments from a particular precursor are not only dependent upon the choice of parent molecule itself, but are also a function of the wavelength of the source. Furthermore, although absorption cross-sections are generally straightforward to measure, the products and their relative yields are difficult to obtain, and for many of the photo-assisted deposition processes reported to date, are not known. The remainder of this section briefly discusses the most common photochemical processes underlying photo-assisted deposition—photodissociation, photoionization, optically driven secondary (collisional) reactions, and multiphoton processes.

## 1. Photodissociation

Far and away the most common photochemical process invoked in photodeposition is photodissociation, which involves the absorption of one or more photons by a molecule, which ultimately results in the scission of a chemical bond. Photodissociation of a polyatomic molecule ABC can be

expressed as

$$ABC + nh\nu \rightarrow A + BC, \tag{2.2}$$

where A is the desired atom or molecular radical, BC represents the remaining molecular ligands, and $n$ is an integer (generally, $n = 1$). As mentioned earlier, the identity of the photofragments and the distribution of energy (internal and translational) among the products is a function of wavelength. Also, photodissociation often results in the rupture of the weakest bond in the molecule, which may yield, for example,

$$ABC + h\nu \rightarrow AB + C \tag{2.3}$$

rather than the desired products of reaction (2.2). Similarly, the fraction of the total absorbed photon energy that appears as translational energy (heat) of the fragments depends on the strength of the bond(s) broken, the number of bonds involved, and the laser wavelength.

While a wide variety of precursors have been explored for photo-assisted deposition, the most common are carbonyls, alkyls or hydrides, which are not only (of necessity) volatile but also widely available. These parent molecules are of the form $AB_m$, where $m$ is also an integer and $B = CO$, $CH_3$ (or $C_2H_5$), or H. Halides have also been investigated, but to a lesser degree. Early photo-CVD experiments were largely empirical in the sense that little was known of the photoproducts that one could expect at a given wavelength. Consequently, only the most generally features of the photochemistry could be inferred either from the known chemical and optical characteristics of analogue molecules (such as $CH_4$ for $SiH_4$) or from the chemical composition of deposited films. Such a situation is not conducive to exploiting to the maximum the capabilities of gas phase photochemistry for film deposition and its ability to produce specific products, in particular. Recently, however, several studies have been reported that have investigated in detail the products of photodissociation for several precursors of interest to photo-CVD. A few of these are reviewed here.

### a. Column IIIA Alkyls

Not only are the Column IIIA alkyls such as trimethylaluminum, $Al(CH)_3$:TMA, or triethylgallium, $Ga(C_2H_5)_3$:TEG, widely used in the epitaxial growth of III–V semiconductor films (such as AlGaAs) by metal-organic CVD (MOCVD), but they were also among the first precursors investigated for use in photo-CVD processes. Since the photochemistry of TMA has been most thoroughly studied and is representative of that for other members of the Column IIIA alkyl family, trimethylgallium and
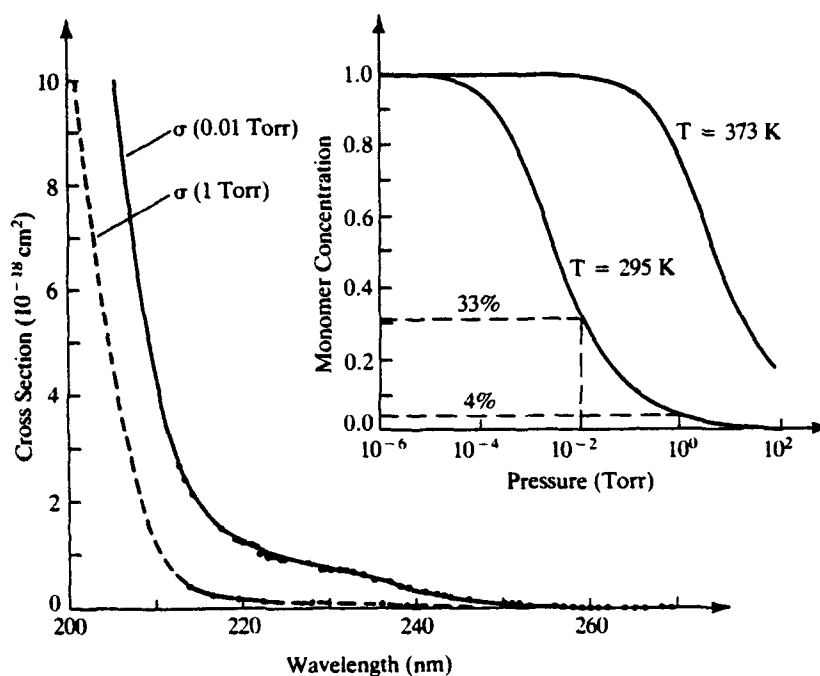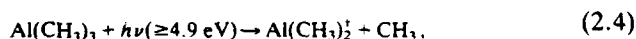
***Fig. 6.*** Expanded view of the TMA absorption spectrum between 200 and 260 nm. As shown by the inset, the cross-section is dependent upon pressure because of the rising concentration of the TMA dimer $(Al_2(CH_3)_6)$ at higher pressures. At room temperature, the TMA monomer $(Al(CH_3)_3)$ relative number density falls from 33% at a pressure of $10^{-2}$ torr to 4% at 1 torr of total pressure. For wavelengths longer than ~220 nm, only the monomer absorbs significantly. (Reprinted with permission from Springer-Verlag, Th. Beuermann and M. Stuke, *Appl. Phys. B* **49**, 145 (1989).

trimethylindium (TMI), the discussion will be limited to its properties. In the 190–255 nm spectral region, TMA is photodissociated by the absorption of a single photon, giving rise to the absorption spectrum of Fig. 6, which shows the 200–260 nm region in detail. The primary products are free Al atoms and $AlCH_3$ radicals and, as illustrated in Figs. 7 and 8, the relative yields are strongly dependent upon laser wavelength [20]. For wavelengths below 255 nm, Al atoms are produced by the two-step process [20, 21].
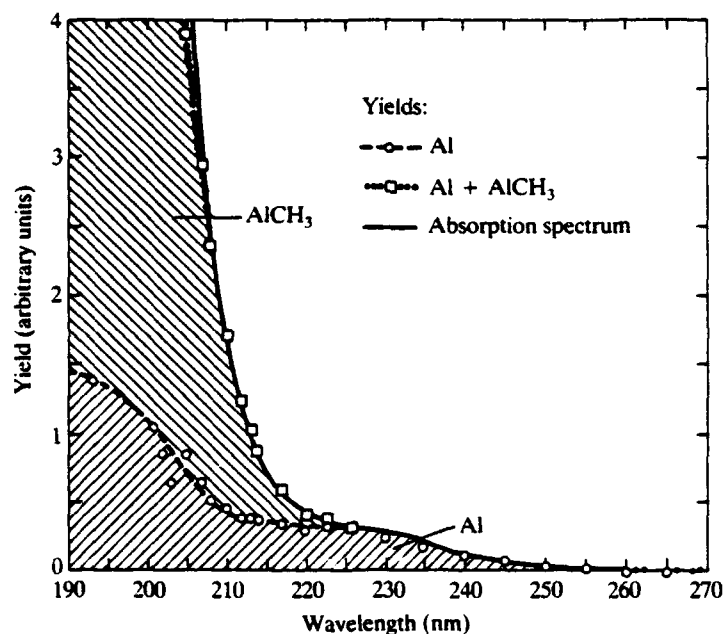
$$Al(CH_3)_3 + h\nu(\geq 4.9 \text{ eV}) \rightarrow Al(CH_3)_2^{\ddagger} + CH_3, \qquad (2.4)$$

$$Al(CH_3)_2^{\ddagger} \rightarrow Al + C_2H_6. \qquad (2.5)$$

*Fig. 7.* Relative yields of Al and AlCH₃ resulting from the photodissociation of TMA in the 190–270 nm spectral region. The absorption spectrum for TMA is represented by the solid curve. Note that for wavelengths greater than ~220 nm, Al is the predominant product. (Reprinted with permission from Springer-Verlag, Th. Beuermann and M. Stuke, *Appl. Phys. B* **49**, 145 (1989).

The threshold for AlCH₃ production was observed by Beuermann and Stuke [20] to be approximately 230 nm. For this fragment, the production process appears to be

$$Al(CH_3)_3 + h\nu(\geq 5.4\ eV) \rightarrow AlCH_3 + 2CH_3. \tag{2.6}$$

The key point to be made here is that to produce free aluminum atoms requires an optical source wavelength between ~230 and 255 nm. For $\lambda > 220$ nm, it was also found that only the TMA monomer, $Al(CH_3)_3$, absorbs, and the dimer, $Al_2(CH_3)_6$, contribution rises rapidly at shorter wavelengths. TMA, TMG, and TMI apparently are all photodissociated in the same manner [20]. The results of Refs. 20, 22, and 23 explain the presence of objectionable levels of carbon in Al films deposited by photodissociating TMA at 193 nm and suggest that the best future course would be to use a source in the $\lambda \geq 220$–230 nm region—perhaps the KrCl laser at 222 nm. As will be discussed in Section IVB, experiments in which TMA was
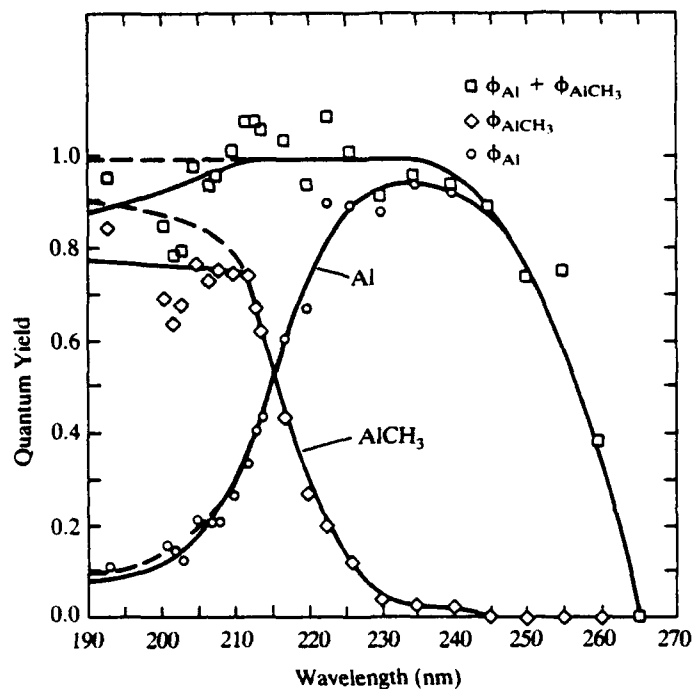
**Fig. 8.** Absolute quantum yields for Al and AlCH₃ in the photodissociation of TMA (Reprinted with permission from Springer-Verlag, Th. Beuermann and M. Stuke. *Appl. Phys. B* **49**, 145, 1989). (□) $\phi_{Al}$ + $\phi_{AlCH_3}$; (◇) $\phi_{AlCH_3}$; (○) $\phi_{Al}$. The dominance of atomic aluminum as a product at longer wavelengths is again clearly evident.

photodissociated at 248 nm (KrF laser) to deposit Al films having lower carbon impurity concentrations support the conclusions of Beuermann *et al.* [20, 22, 23].

## b. Column V Hydrides

The Column V hydrides NH₃ (ammonia), PH₃ (phosphine), AsH₃ (arsine), and SbH₃ (stibine) are also frequently employed in the MOCVD and chemical beam epitaxy (CBE) growth of III–V compound films. All absorb strongly in the VUV, with absorption maxima occurring in the 180–200 nm region [18], [19]. Also, except for ammonia, the absorption spectra for all of the Column V hydrides are continua. The NH₃ spectrum is oscillatory in the 180–200 nm region, and the 193 nm cross-section is $(1.5 \pm 0.3) \times 10^{-17}$ cm². Photodissociation of the hydrides at these photon

energies results in the removal of a single hydrogen atom. For phosphine, for example [19],

$$PH_3 + h\nu \rightarrow \begin{cases} PH_2(\tilde{A}(^2A_1)) + H \\ PH_2(\tilde{X}(^2B_1)) + H \end{cases} \cdot \qquad (2.7)$$
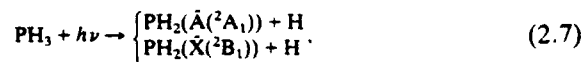
where only ~1% of the $PH_2$ radicals are produced in the excited ($\tilde{A}$) state—most are formed directly into the ground state. Similar statements could be made for the other hydrides—for $NH_3$, the yield into the $NH_2$ ($\tilde{A}$) state is 2.5%, with the remainder produced once again in the $\tilde{X}$ ground state.

### c. Metal Carbonyls

The carbonyls of Cr, W, Fe, Mo, Mn, and Ni absorb strongly below 300 nm, and in most instances the dissociation of these polyatomics proceeds by the sequential elimination of carbonyl ligands [19]. Although the energy required to remove one or two CO ligands is 1.6 and 3.3 eV, respectively, the photodissociation of chromium hexacarbonyl, for example, in the 351–355 nm region proceeds predominantly by the process:

$$Cr(CO)_6 + h\nu(\approx 3.5 \text{ eV}) \rightarrow Cr(CO)_5 + CO. \qquad (2.8)$$

At 248 nm, while two photons have sufficient energy (10 eV) to remove all of the carbonyl ligands, a single 5 eV photon leads to the removal of two carbonyls by the two-step sequence

$$Cr(CO)_6 + h\nu(5 \text{ eV}) \rightarrow [Cr(CO)_5]^* + CO \rightarrow Cr(CO)_4 + 2CO. \qquad (2.9)$$
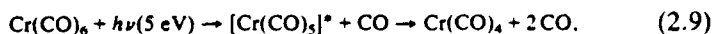
where the asterisk indicates that the pentacarbonyl species is unstable. At laser intensities exceeding several hundred kilowatts per square centimeter, electronically excited metal atoms are produced as a result of two photon absorption at 248 nm by the parent molecule.

### 2. Photoionization

Although the photodeposition processes developed to date almost universally involve electrically neutral products, *selective* photoionization of reactants presents several advantages for photo-CVD, insofar as process control and impurity rejection and chemical specificity, in particular, are concerned.

Upon absorbing a single photon of sufficiently high energy, the entire molecule AB can be photoionized,

$$AB + h\nu \rightarrow (AB)^+ + e^-. \qquad (2.10)$$
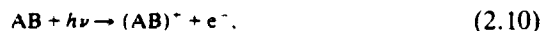
or the molecule may be dissociated in the process, yielding a single, positively charged ion and an electron,

$$AB + h\nu \rightarrow A^+ + B + e^-,$$  (2.11)

or only a pair of ions,

$$AB + h\nu \rightarrow A^+ + B^-.$$  (2.12)

The first of these processes (reaction (2.10)) is generally not useful in photochemical vapor deposition, since the precursor ligands are usually required *only* as a vehicle for raising the vapor pressure of the parent. Once the precursor is present at the substrate, the ligands are no longer necessary (and are often a nuisance since they frequently contain undesirable atoms such as carbon), and the molecule must be dismantled so as to gain access to the desired atom. Occasionally, however, photoionization of the entire precursor molecule at short (i.e., VUV) wavelengths is an attractive deposition process, particularly for hydrogenated films. Calloway *et al.* [24], for example, have shown that thin Al films can be deposited by photoionizing TMA with rare-gas lamp resonance radiation. At these short wavelengths, the entire molecule is apparently positively charged, leading to incorporation of carbon (and H) into the film.
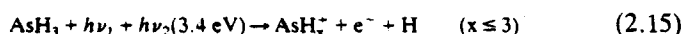
An excellent example of the latter reaction (Eq. (2.12)), however, is the *dissociative* photoionization of selected metal halides. In 1932, Terenin and Popov [25] found that certain metal-halide molecules, when irradiated with photons lying within a narrow energy range, undergo dissociative photoionization, resulting in the production of only charged fragments— a metal cation and a halogen anion. For the diatomic metal halide thallium iodide, for example,

$$TlI + h\nu \rightarrow Tl^+ + I^-.$$  (2.13)

Ion pair production processes analogous to reaction (2.13) occur in other metal halides such as InI. ArF laser photons ($h\nu = 6.4$ eV) have sufficient energy to directly produce $In^+ - I^-$ ion pairs, and this process competes with the formation of electronically excited, neutral In atoms and a ground-state I atom. One of the attractive features of dissociative photoionization of metal halides insofar as photochemical vapor deposition is concerned is that, by the careful choice of the precursor and laser wavelength, only one positively charged ion is produced (that of the metal atom), and the undesired species (halogen atom) is oppositely charged— consequently, with the aid of an electric field, one can minimize the incorporation of contaminants into the resulting film.

## a. Column V Hydrides

Although little is known of the details of the photochemistry of arsine and the other Column V hydrides, Koplitz *et al.* [26] have demonstrated that the photoproducts for $AsH_3$ can be readily switched from predominantly neutral to ionic species with a "two-color" laser approach. As noted earlier, the absorption of a single 193-nm photon by $AsH_3$ predominantly produces $AsH_2$ radicals in the $\tilde{X}$ (ground) of $\tilde{A}$ (excited) electronic states. Upon adding $\lambda \simeq 365$ nm (3.4 eV) photons concurrently with the ArF radiation, however, strong ionization of the molecule and the formation of $AsH^+$, specifically, is observed. Consequently, the $AsH_3$ fragments can be readily manipulated with the aid of UV radiation, which acts in concert with 6.4 eV photons to photoionize $AsH_3$ ($\tilde{A}$) molecules. This scheme can be expressed as

$$AsH_3 + h\nu_1(6.4\ eV) \rightarrow AsH_2(\tilde{X}, \tilde{A}) + H \qquad (2.14)$$

$$AsH_3 + h\nu_1 + h\nu_2(3.4\ eV) \rightarrow AsH_x^+ + e^- + H \qquad (x \leq 3) \qquad (2.15)$$

and is shown schematically in Fig. 9. Similar approaches are almost certainly available for other precursors of interest to photochemical vapor deposition, but further fundamental studies of the photochemistry of these molecules will be necessary to assess the full scope of the chemical pathways and subsequent process engineering that is possible.

## 3. Optically Driven Secondary Reactions

## a. Sensitizers

Often, a mismatch exists between the wavelengths available from existing (and efficient) UV and VUV lasers (and lamps) and the spectral regions in which volatile, high-purity precursors absorb. A more subtle difficulty arises if, as discussed previously, the photodecomposition of a given precursor at a particular optical source wavelength does occur rapidly but yields undesirable products. In such situations, intermediate species, known as *photosensitizers*, may occasionally be employed to act as a bridge between the optical source and the precursor molecule in the sense that the photosensitizer species must absorb strongly at the optical source wavelength and efficiently transfer its internal energy to the polyatomic precursor molecule.

Atomic mercury is the oldest and most thoroughly studied photosensitizer, as the decomposition of silane by Hg photosensitization was reported more than a half-century ago [2]. Mercury is an effective photosensitizer for the Column IV hydrides in that it couples Hg resonance lamps emitting at 253.7 nm (and 184.9 nm) with precursors such as $SiH_4$ and $Si_2H_6$, which are virtually transparent for wavelengths beyond 160 and 200 nm, respec-
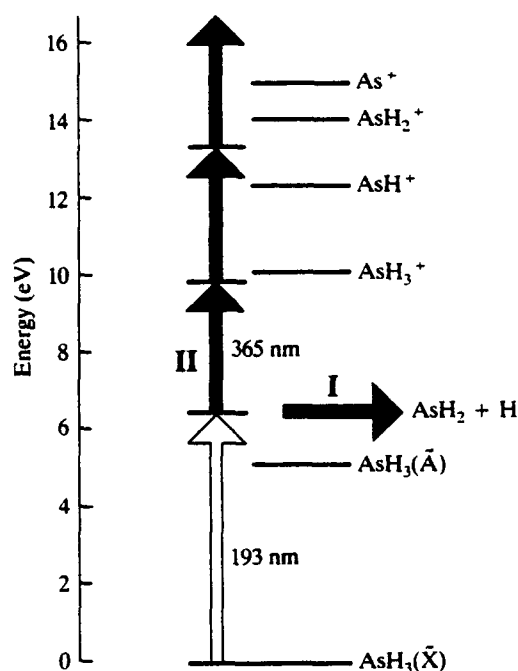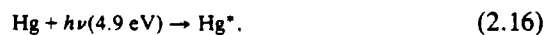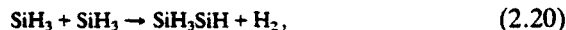
*Fig. 9.* Generalized energy level diagram for AsH$_3$ showing the switch between photodissociation (denoted pathway I) and dissociative photoionization that is induced by simultaneously irradiating the molecule with 6.4 and ~3.4 eV photons (from Ref. 26).

tively. Consequently, in the absence of a photosensitizer, decomposing precursors such as SiH$_4$ by single photon processes precludes the use of the most efficient, commercially available sources (such as the ArF and KrF excimer lasers). Central to Hg photosensitization is the $6p^3P_1$ electronic excited state of the atom, which lies ~4.9 eV above the ground state. Mercury $^3P_1$ atoms, produced by 254 nm radiation from a low-pressure resonance lamp, are well suited for collisionally exciting (and dissociating) various polyatomic molecules. A complete discussion of the photochemistry of the Hg($6p^3P_1$) species can be found in Okabe [18].

The collisional processes that are critical to the photochemical growth of amorphous hydrogenated Si films from the photosensitized decomposition of SiH$_4$ are [27]

$$Hg + h\nu(4.9 \text{ eV}) \rightarrow Hg^*. \tag{2.16}$$

$$Hg^* + SiH_4 \rightarrow Hg + SiH_3 + H. \tag{2.17}$$

$$H + SiH_4 \rightarrow H_2 + SiH_3, \qquad\qquad (2.18)$$

$$SiH_3 + SiH_3 \rightarrow SiH_2 + SiH_4, \qquad\qquad (2.19)$$

$$SiH_3 + SiH_3 \rightarrow SiH_3SiH + H_2, \qquad\qquad (2.20)$$

where the asterisk denotes the $6p^3P_1$ excited state of mercury. Although the actual production of a-Si:H films appears to occur when $SiH_2SiH_3$ or $SiH_3 SiH$ radicals impinge on the substrate, efforts to unravel the complicated gas phase chemistry of this photochemical system are continuing. Nevertheless, the chemical versatility of Hg photosensitization, combined with the economy and simplicity of Hg resonance lamps, makes this an attractive approach to the deposition of the Column IV elemental films, in particular.

### b. Bimolecular Collisional Formation of Compounds

Compound film growth by photochemical vapor deposition is, at present, a class of complex and poorly understood processes. The deposition of the compound material $A_xB_y$ (where $x$ and $y$ are often not integers) usually requires molecular precursors for both elements A and B and is similar to photosensitized deposition in that generally only one of the two precursors absorbs strongly at the optical source wavelength. Upon absorbing a photon, this precursor is either excited to a relatively stable excited state or dissociated. In either case, *the products formed by irradiating the molecule are more chemically reactive than the ground state species*, and the ensuing collisions of these photofragments with the remaining precursor eventually culminate in the production of the desired film.

An example of this process is the photochemical sequence responsible for the deposition of the insulator films $Si_3N_4$ and $SiO_2$. In both cases, the silicon precursor is a silane ($SiH_4$, $Si_2H_6$, or $Si_3H_8$), all of which, as noted earlier, are essentially transparent (nonabsorbing) in the UV. Interaction of the optical source occurs primarily with the N or O precursor, whose dissociation fragments chemically react with the silane to form the desired film. In the photodeposition of $SiO_2$, the oxygen precursor is frequently $N_2O$, which, when photodissociated at 193 nm, yields

$$N_2O + h\nu \ (\sim 6.5 \ eV) \rightarrow N_2 + O^*(^1P). \qquad\qquad (2.21)$$
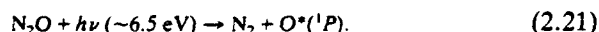
Following relaxation of the excited $O(^1P)$ species to the ground $(^3P)$ state, compound formation apparently proceeds by the reaction:

$$SiH_4 + 4O(^3P) \rightarrow SiO_2 + 2H_2O. \qquad\qquad (2.22)$$
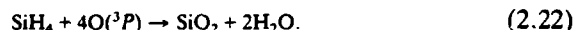
The photochemistry of $Si_3N_4$ deposition is considerably more complicated, since it entails the photodissociation of $SiH_4$ (or $Si_2H_6$)/$NH_3$ mixtures in the VUV and generally at 193 nm. Two of the early steps in the reaction

chain are expected to be

$$NH_3 + h\nu \rightarrow NH_2(\tilde{X}, \tilde{A}) + H, \tag{2.23}$$

$$H + SiH_4 \rightarrow H_2 + SiH_3, \tag{2.18}$$
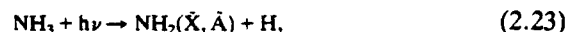
with the final deposit-producing reactions involving the interaction of laser-generated radicals (such as amidogen, $NH_2$) with $SiH_4$.

### 4. Multiphoton Processes

The photoreactions discussed to this point have generally assumed the absorption of a single photon per precursor molecule as a necessary condition for triggering the photodeposition process of interest. As we have seen, however, several parent molecules of interest (such as $SiH_4$) are "transparent" in spectral regions where efficient optical sources presently exist. While transparency is a notion that is a result of a small single photon absorption cross-section, $\sigma$, multiphoton processes often become important at higher optical intensities and can alter the situation entirely. Recalling, for example, the generalized photodissociation process, Eq. 2.2,

$$ABC + nh\nu \xrightarrow{\sigma^{(n)}} \text{products,}$$
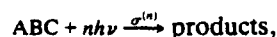
where $n$ is again an integer, we denote the $n$th-order photoabsorption cross-section as $\sigma^{(n)}$, and the rate $R$ at which ABC molecules are photodissociated is given by perturbation theory as

$$R = \sigma^{(n)}\left(\frac{I}{h\nu}\right)^n, \tag{2.24}$$

where $I$ is the optical intensity (expressed in W-cm$^{-2}$) and $\sigma^{(n)}$ is expressed in units of cm$^{2n}$-(s)$^{n-1}$ [i.e., cm$^2$ for $n = 1$, cm$^4$-s for $n = 2$, cm$^6$-s$^2$ for $n = 3 \ldots$]. Note the strong nonlinearity of the process for $n > 1$ (i.e., the absorption of more than one photon by the precursor), which favors large laser intensities.

As an example, silane is essentially transparent at 193 nm ($h\nu \approx 6.4$ eV) owing to a single photon absorption cross-section at that wavelength of $\sigma^{(1)} = 1.1 \times 10^{-21}$ cm$^2$. However, the two-photon cross-section, $\sigma^{(2)}$, at the same wavelength is $(6 \pm 2) \times 10^{-44}$ cm$^4$-s [28], and since the ratio of the single photon absorption rate to that for two photons is $(\sigma^{(1)}/\sigma^{(2)})h\nu/I$, then the rates for these two processes are equal for laser intensities of only $\sim$19 kW-cm$^{-2}$ (or 0.2 mJ-cm$^{-2}$ for 10 ns laser pulses). This intensity is easily exceeded with commercially available excimer lasers, which generally produce unfocused intensities >4 MW-cm$^2$ per pulse. Consequently, two (or more) photon processes can dominate single photon dissociation of a molecule and, in such cases, conventional absorption spectra are of little

value. Because of the large optical intensities required, multiphoton processes are usually accessible only with pulsed laser sources.

In summary, whether the pivotal photochemical process is photodissociation, photoionization, or photosensitization, the role of the optical source in photochemical vapor deposition is to transform the chemical environment in the vicinity of the substrate from a quiescent to a reactive one, but to do so in a manner that discriminates against undesired products.

## C. Adlayer Characteristics

Photochemical interactions in adlayers of molecules at a surface underlie many photochemical deposition processes and are particularly useful in those applications for which spatial resolution is an important consideration. In the gas phase, the lateral diffusion of photoproducts imposes a limit on the smallest features sizes obtainable by photo-assisted film deposition, and while this can be suppressed to some extent by controlling the identity and pressure of the background gas, the restricted mobility of atomic and molecular species in an adlayer is much more conducive to depositing patterned films. Because of the proximity of a surface, the optical and chemical properties of adsorbed layers of polyatomic molecules can differ considerably from those in the gas phase. Qualitatively, adlayers can be categorized as chemisorbed or physisorbed. For the former, the interaction of the adlayer with the surface is comparable to the precursor's intramolecular bond strengths. Physisorbed adlayers, in contrast, interact weakly with the surface, and their absorption spectra are generally similar to those for the gas phase species.

The characteristics of adsorbed layers of a variety of molecules have been studied extensively and, for a broad review of the subject, the reader is referred to the excellent discussion by Rothschild [19]. Considerably less is known regarding adlayers of the polyatomic molecules that are suitable precursors for photochemical vapor deposition. Of the few precursors that have been studied, the Column IIIB alkyls are the most thoroughly characterized and are briefly discussed here. Measurements made by Sasaki et al. [29] of the gas phase and adlayer absorption spectra of trimethylgallium show that the chemisorbed spectrum is broader than its gas phase counterpart, and that the physisorbed spectrum, relative to the gas phase profile, peaks at a shorter wavelength. Their results were also in accord with previous studies that revealed an elongation of the chemisorbed layer's absorption spectrum towards the red. One other aspect of chemisorbed layers that has a direct bearing on photochemical deposition is that the absorption cross-section for the adlayer is generally larger than that for the vapor.

Not only does the adlayer–surface interaction manifest itself in a broadened absorption spectrum and increased absorption strengths, but it also alters the photochemistry of the precursor relative to that for the gas phase. Zhang and Stuke [30] investigated the photochemistry of metal alkyl adlayers by laser time-of-flight mass spectroscopy and showed that photodissociation of chemisorbed adlayers of TMA (on Si or quartz) at 248 nm yields much higher abundances of $AlCH_3$ radicals than are measured for the gas phase process. Furthermore, photodissociation of adsorbed aluminum-bearing alkyls at 308 nm occurs quite readily, in contrast with the gas phase species, which is transparent at wavelength [30].

One practical ramification of adlayer photolysis is *prenucleation* [31] or *photonucleation* [32], a process in which laser photodeposition from a chemisorbed adlayer controls the nucleation of metal films. That is, surfaces that have small sticking coefficients for gas phase metal atoms, for example, can be "seeded" by photolyzing metal–alkyl adlayers with a focused UV laser beam. The resulting metal atoms on the surface act as nucleation sites on which further deposition can occur. This process, which overcomes nucleation barriers that often exist at surfaces, has been exploited to deposit patterned metal films with excellent spatial resolution ($<4\mu$m feature widths).

## III. REACTORS, OPTICAL SOURCES, AND ASSOCIATED EQUIPMENT

All photochemical vapor deposition systems include these elements:

(1)  Gas flow equipment for delivering the desired precursor(s) to the substrate at a specified pressure and mass flow rate;

(2)  A substrate and, in most cases, heated susceptor;

(3)  An optical source (lamp or laser) and beam delivery scheme; and

(4)  An exhaust system.

Aside from item (3), photochemical vapor deposition reactors are quite similar to conventional MOCVD or CBE systems. Consequently, the remainder of this section concentrates on the characteristics of commercially available optical sources and the trade-offs associated with different approaches for delivering the optical beam to the gas or adlayer immediately adjacent to the substrate surface.

### A. Reactor Characteristics

Even though all reactors have several common components, Figs. 10, 12, and 13 illustrate the wealth of experimental configurations that have
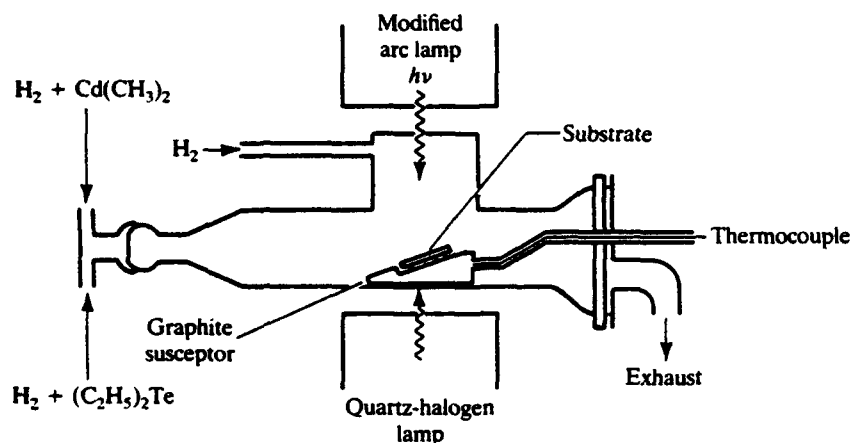
**Fig. 10.** Schematic diagram of a photochemical vapor deposition reactor for the growth of CdTe and HgTe epitaxial films. In this arrangement, the optical source is a 1,000 W Hg-Xe arc lamp whose spectrum is modified by reflecting the lamp radiation off a dichroic mirror that is highly reflecting in the 200–250 nm region (from Ref. 33).

been employed thus far for photo-assisted CVD. A simplified schematic diagram of a reactor for the photo-CVD growth of CdTe [33] is given in Fig. 10. The precursors (diethyl tellurium (DET) and dimethyl cadmium (DMC), in this case) are entrained in hydrogen and introduced upstream of the deposition region. The substrate is mounted on a graphite susceptor heated by a quartz halogen lamp, and the unreacted gases (and gaseous byproducts of the deposition process) are exhausted at the rear of the reactor. A 1,000 W Hg–Xe arc lamp provides the necessary UV radiation for photodissociating the alkyl precursors, but Ahlgren et al. [33] have introduced a clever modification to the system. By reflecting the arc lamp beam off of a dichroic mirror, radiation outside the 200–250 nm region is rejected and only photons in the ~5–6.2 eV range reach the surface.

In order to introduce the UV or VUV radiation from the source into the reactor, an entrance window must be provided, and the material required is dependent upon the wavelengths involved. Since the reactor of Fig. 10 utilizes wavelengths in the 200–250 nm region, the optical beam can be propagated efficiently through air, and quartz is an acceptable window material. For wavelengths below ~180–190 nm, air absorbs strongly (owing to the Schumann–Runge bands of $O_2$), and different crystalline materials are required for reactor windows. The optical transmission curves for
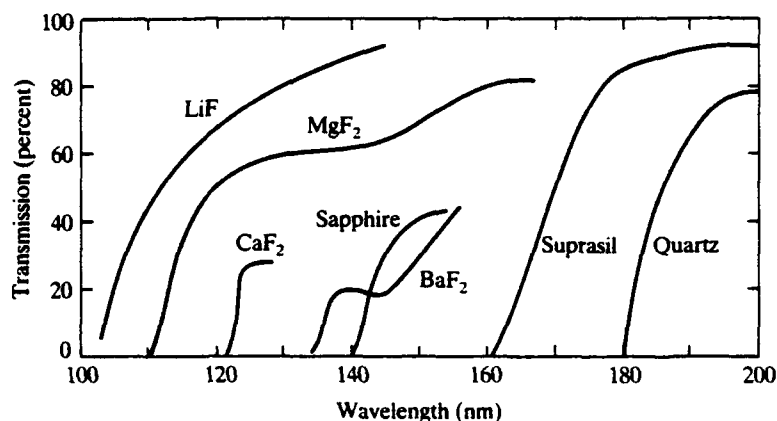
**Fig. 11.** Transmission of readily available window materials in the VUV: LiF—1.95 mm thick; MgF₂—1 mm thick; CaF₂—0.25 mm thick; sapphire—0.32 mm thick; BaF₂— 1.95 mm thick; Suprasil (enhanced UV transmission quartz)—10 mm thick; and quartz— 2 mm thick. Copyright 1965 by The American Institute of Physics.

readily available window materials in the VUV are shown in Fig. 11. Most are fluoride crystals, and the material offering maximum transmission at the shortest wavelengths, lithium fluoride, "cuts off" below ~100 nm (50% transmission at ~112 nm). One of the materials in Fig. 11 is generally more than adequate for most photochemical deposition processes. Note that not only are new materials required in this spectral range for transmitting and focusing the incoming radiation, but it is necessary that the entire optical path be evacuated or purged with $N_2$ gas. The latter is only effective for wavelengths down to 150–160 nm. Below ~105 nm, no windows are available, and it is necessary to resort to a windowless configuration [34]. Although this allows one to utilize short-wavelength optical sources, the disadvantage of the windowless approach is that the plasma generating the VUV radiation is not physically isolated from the thin film precursor.

A detailed diagram of a commercially available, low-pressure photo-CVD reactor (Tystar PVD 1000) designed for the deposition of $SiO_2$, $Si_3N_4$, and silicon oxynitride ($SiO_xN_y$) dielectric films is given in Fig. 12 [35]. Based on the decomposition of mixtures of $SiH_4$ and $N_2O$ or $NH_3$ by Hg photosensitization, this reactor includes two growth chambers that are capable of independently processing nine 75-mm diameter wafers or five 100-mm diameter wafers. The optical source is an array of low-pressure Hg lamps or a single grid lamp, and the substrate is heated by four quartz
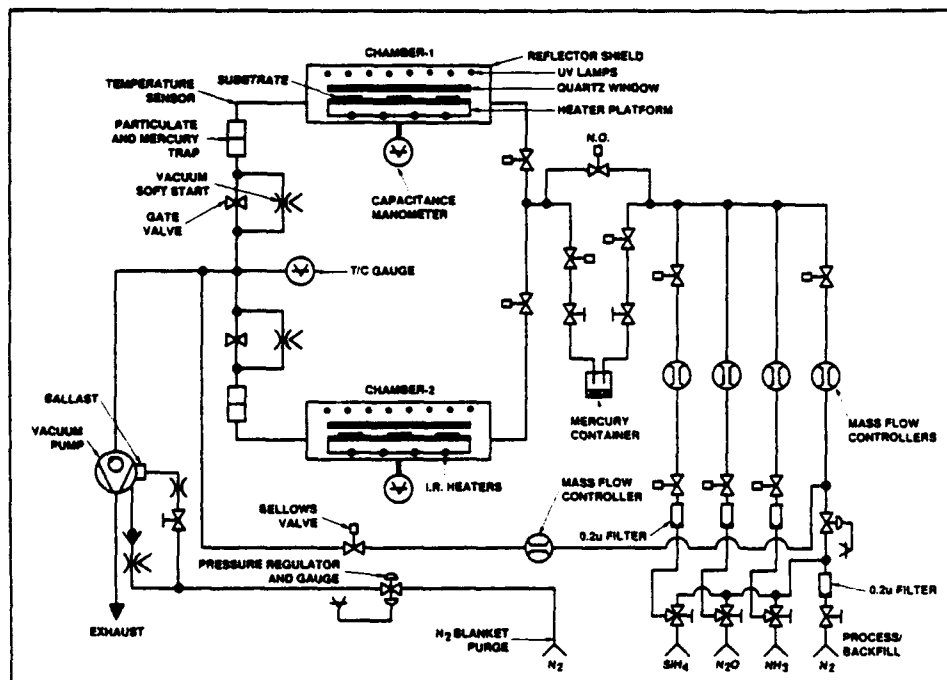
**Fig. 12.** Layout of a commercial photo-CVD reactor designed for the deposition of silicon dioxide and silicon nitride dielectric films by Hg photosensitization (reprinted by permission of Tystar Corp., licensee of Hughes Aircraft Co.—1989).

lamps. Depending on the grade of fused quartz chosen for the window, transmission at 254 nm (resonance line of Hg) ranges from ~50 to 90%. Tables I and II give details of the reactor's operating characteristics and film growth process parameters for both $SiO_2$ and $Si_3N_4$ films. Although Hg is incorporated into the resulting films, concentrations are in the parts-per-billion range.

Broad-area deposition of dielectric films with a laser is generally accomplished with a parallel configuration such as that illustrated in Fig. 13. Avoiding direct irradiation of the substrate eliminates transient heating of the growing film by the laser. Because of the ~1 $cm^2$ cross-sectional area and large divergence angle of most commercially available excimer laser beams, it is generally necessary to compress the rectangular beam in one dimension and collimate it with a simple optical telescope prior to directing the radiation into the reactor [36]. Note also in Fig. 13 that provision is

TABLE I

GENERAL CHARACTERISTICS OF A COMMERCIALLY AVAILABLE PHOTO-CVD
REACTOR (TYSTAR PVD 1000) BASED ON HG PHOTOSENSITIZATION
(AFTER REF. 35)

| | | |
|---|---|---|
| 1. Recommended gas flow rates | | |
| $SiO_2$: | Silane ($SiH_4$): | 2 sccm |
| | Nitrous oxide: | 60 sccm |
| | Nitrogen (pump injection): | 42 sccm |
| | Total gas flow rate: | 104 sccm |
| | Reactor chamber pressure: | 1 torr |
| | Substrate temperature: | 150°C |
| $Si_3N_4$: | Silane: | 2 sccm |
| | Ammonia ($NH_3$): | 50 sccm |
| | Nitrogen (pump injection): | 42 sccm |
| | Total gas flow rate: | 94 sccm |
| | Reactor chamber pressure: | 1 torr |
| | Substrate temperature: | 150°C |
| 2. Mercury: | Triple distilled, reagent grade: | 500 g |
| 3. Substrate heater: | Infrared quartz lamps, $4 \times 375$ W = 1500 W total Heat-up time to 150°C: 10 min | |

TABLE II

TYPICAL PROCESS PARAMETERS FOR THE DEPOSITION OF $SiO_2$ AND
$Si_3N_4$ FILMS BY HG PHOTOSENSITIZATION IN A COMMERCIAL REACTOR
(AFTER REF. 35)

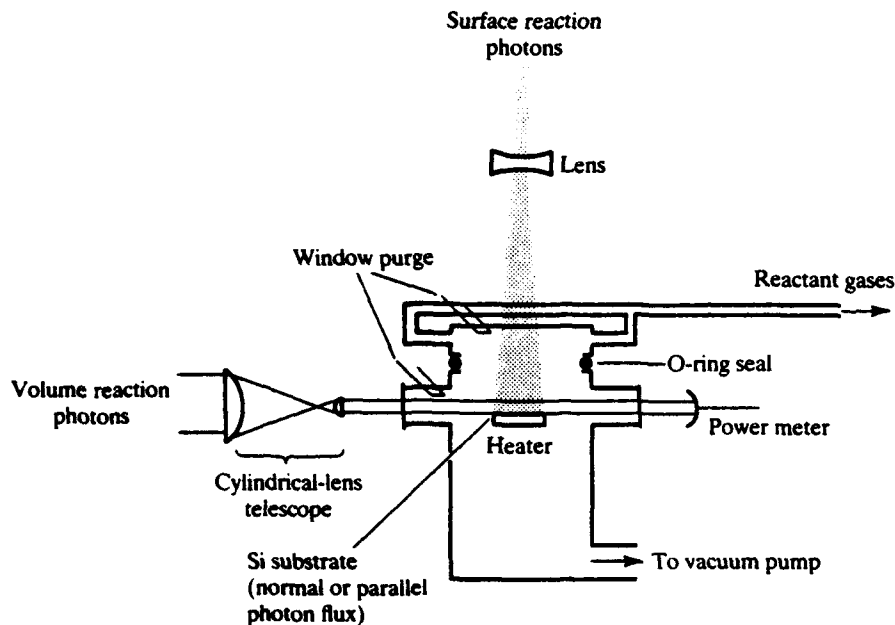| | Film | |
|---|---|---|
| Parameter | Silicon dioxide | Silicon nitride |
| Thickness uniformity: | | |
| within wafer | ±3% | ±10% |
| across heater substrate | ±10% | ±15% |
| repeatability | ≤±3% | ≤±5% |
| Deposition temperature | 50 to 200°C | 100 to 200°C |
| Deposition pressure | 0.3–1.0 torr (40–133 Pa) | 0.3–1.0 torr (40–133 Pa) |
| Cycle time (150 nm) | 45 min | 55 min |
| Maximum deposition rate | 15 nm·min$^{-1}$ | 6.5 nm·min$^{-1}$ |

**Fig. 13.** Parallel geometry reactor for the laser photochemical deposition of ZnO films (from Ref. 36).

made for a low-intensity beam, directed onto the substrate, to stimulate surface reactions.

As discussed in Section II.B.2, greater selectivity in the photodeposition process is available by photoionizing only the atom or molecular radical of interest. Such an approach was reported by Geohegan and Eden [37] to deposit thin films of aluminum, thallium, or indium by dissociatively photoionizing metal halide precursors to generate metal–halogen ion pairs (i.e., $M^+-X^-$, where M and X represent metal and halogen atoms, respectively). In their apparatus (cf. Fig. 14), the substrates were arranged on a negatively biased plate, and the metal cations produced in the gas phase above the substrate were drawn to the substrates under the influence of the electric field.

Regardless of the specifics of reactor design, one problem to be dealt with in all photo-CVD processes is the tendency for films to grow on the optical window in addition to the substrate. A flow of "purge" gas (typically $H_2$) across the interior surface of the window will minimize or eliminate this problem–cf.Figs. 10 and 13. An oil coating on the window or *in situ* etching of the window during photodeposition with $XeF_2$ or discharge-generated F atoms has also been demonstrated successfully.
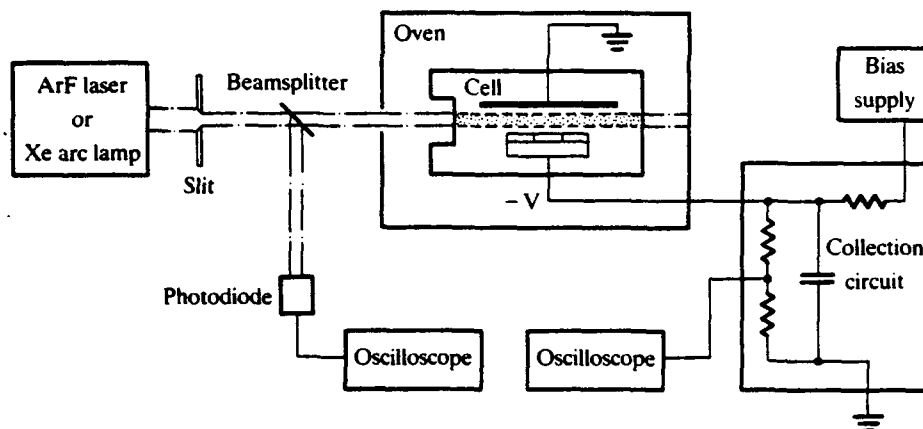
*Fig. 14.* Schematic diagram of apparatus employed in Ref. 37 to deposit thin thallium, aluminum, or indium films by the photoproduction of metal (M) and halogen (X) ion pairs $(M^+-X^-)$.

## B. Optical Beam Delivery

The optimal manner for delivering the optical beam to the reactor is dependent upon the desired application. Figure 15 qualitatively illustrates the four most common beam delivery configurations [15]. The first two parts of Fig. 15 (shown as parts (a) and (b)) are intended for situations requiring spatially selective deposition. The simplest approach, the spot focus, more commonly known as the direct write configuration, entails scanning a focused laser beam across the substrate. Deposition processes based on this approach generally involve photochemical interactions within the adlayer. Assuming the laser beam to be gaussian and in the fundamental mode $(TEM_{oo})$, then the diffraction-limited spot size is approximately given by

$$W \simeq \frac{2\lambda}{\pi} \frac{f}{d} \approx 0.64\lambda \frac{f}{d},$$   (3.1)

where $\lambda$ is the laser wavelength, and $f$ and $d$ are the focal length and diameter of the focusing lens, respectively. Given a high-quality UV laser beam such as the second harmonic of the $Ar^+$ laser 514-nm line (257 nm), for example, feature sizes below 1 $\mu$m can readily be deposited. The major drawback of direct writing is its low scanning speed (typically $\ll 100$ $\mu$m-s$^{-1}$). Patterned deposition (illustrated in Fig. 15b) can be obtained by projection, an approach in which a mask is optically imaged onto the substrate.
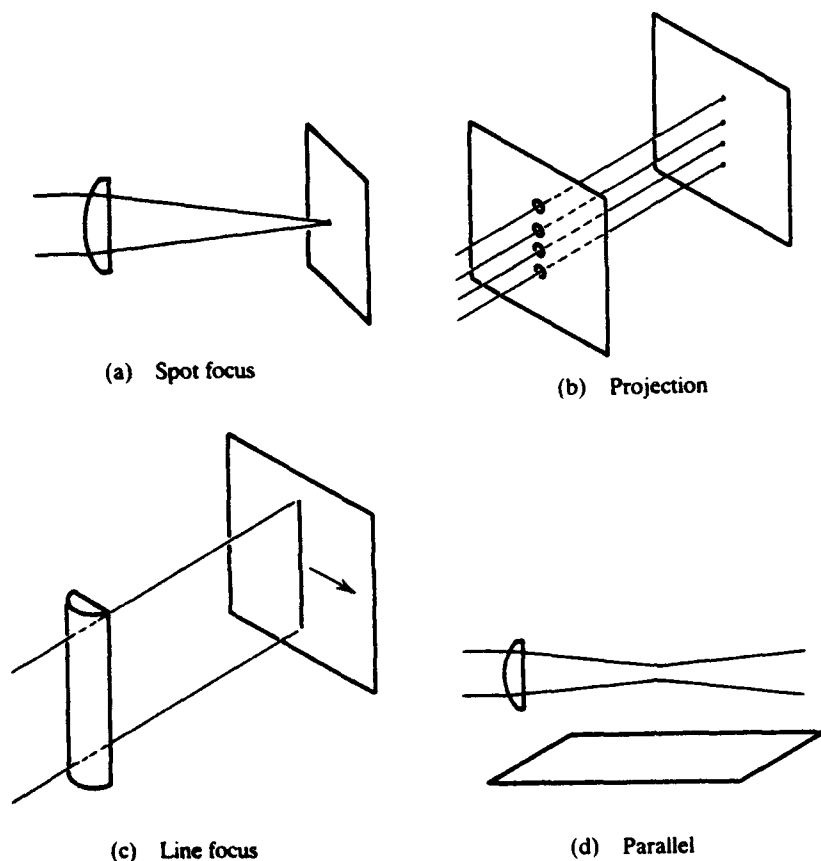
Fig. 15. Four most common modes for optical beam delivery in photochemical vapor deposition: (a) spot focus, (b) projection, (c) line focus, and (d) parallel. The first two are designed for the deposition of small features, whereas (c) and (d) are intended for large-area deposition techniques (adapted from Ref. 15).

Techniques (c) and (d) in Fig. 15, the line focus and parallel geometries, are designed for large-area deposition. For the line focus, the optical beam (or substrate) is scanned, but for the parallel configuration, the optical beam does not irradiate the surface. The primary advantage of the latter is that the laser intensity can be increased at will without the possibility of thermally damaging the substrate. Of course, diffusion of the gaseous photoproducts makes this approach less attractive for spatially delineated applications.

## C. Optical Sources

A variety of continuous (cw) and pulsed lamps and lasers is available for photochemical vapor deposition. Several of the most widely used sources—and their output wavelengths and power capabilities—are discussed.

### 1. Lamps

The relatively low cost, high duty cycle, and reliability of discharge lamps have already made them attractive for commercial applications. Low intensity is the only major drawback of lamps for broad area deposition, which relegates them to driving single-photon absorption processes. Since the poor beam quality of lamps is also an issue for applications involving spatially delineated deposition, this area has thus far been the sole domain of lasers. One of the first lamps to be used in photochemical vapor deposition is the low-pressure mercury discharge lamp. Its UV spectrum is dominated by two lines, the most intense lying at 253.7 nm and the other in the VUV at 184.9 nm. As discussed earlier, the 253.7 nm radiation is effective in triggering the deposition of elemental or compound films by photosensitization processes. Because of their utility in commercial applications other than photo-CVD (such as curing and sterilization), these lamps are commercially available in both linear and grid configurations with output powers (at 254 nm) as high as 8 W.

Several other commercially available UV lamps, such as xenon and high-pressure Hg lamps, produce broad continua that extend from the infrared to below 250 nm. The quartz halogen lamp also generates a blackbody spectrum, but its low color temperature results in weak output below 350 nm, the region where the majority of precursors of interest to photo-CVD absorb.

Shorter-wavelength (VUV) lamps include deuterium ($D_2$), hydrogen, and the rare gases. Deuterium lamps produce negligible radiation in the visible but generate continua that peak near $\lambda = 180$ nm. Also, $D_2$ lamps having average powers up to 60 W are readily available. Hydrogen emits a highly structured spectrum consisting of two bands (Lyman and Werner) peaking near 120 and 160 nm. In contrast, microwave discharges in the rare gases Ar, Kr, and Xe at high pressure ($\sim 200$ torr) emit continua in the VUV that arise from electronic transitions of the transient molecules $Ar_2$, $Kr_2$, and $Xe_2$. The spectral width of each of the continua exceeds 200 nm.

A recent and important entry into VUV lamp family is the microwave-excited rare gas–halide lamp. Kumagai and Obara [38] have generated 29 W of average power at 193 nm from ArF molecules produced in 2% $F_2$, 2%

Ar, 48% He, and 48% Ne mixture discharges. The average deposited microwave power was 655 W for an intrinsic efficiency exceeding 4%. Because of their efficiency and potential for operating at several discrete wavelengths in the UV and VUV, these newly developed lamps will undoubtedly play an increasing role in future photo-assisted deposition processes. To summarize, owing to their low intensities, UV and VUV lamps are most useful for those processes in which reliability, duty cycle, and low cost, rather than peak power, are the driving considerations.

## 2. Lasers

Despite the fact that the energies required for the rupture of chemical bonds within a polyatomic molecule ($\sim$3–6 eV) generally dictate the need for UV photons, prior to 1975 few efficient lasers existed in this spectral region. However, the discovery and commercial development of the rare gas–halide lasers has dramatically transformed that situation by making available photons ranging in energy from 3.5 to 6.4 eV ($193 \leq \lambda \leq 351$ nm) in beams having peak intensities (unfocused) exceeding 10 MW-cm$^{-2}$. In fact, much of the early work in photo-CVD was driven by the availability of these laser sources. It is not surprising, then, that a large fraction of the photochemical processes to be discussed in Sections IV–VI rely on an excimer laser as the optical source.

Over the last five years, the major improvements that have been made in excimer laser performance, such as gas fill lifetime and laser pulse repetition frequency, have permitted the introduction of these lasers into the industrial environment. At the present time, commercial excimer lasers are capable of producing in excess of 100 W of average power at 248 nm (>30 W at 193 nm) at pulse repetition frequencies > 100 Hz for more than $10^8$ pulses (roughly 12 days of continuous operation at 100 Hz).

Another workhorse of photo-assisted deposition has been the argon ion (Ar$^+$) laser. Although generally operated on the visible lines lying between 454.5 and 528.7 nm (with the strongest line at 514.5 nm), this laser also produces significant output power on several discrete lines in the ultraviolet (275–364 nm). Recent advances in the materials used in contact with the high-current discharge have permitted the power deposited into the plasma to be increased, with a resulting improvement in output power. At present, commercial models are available that will generate 1.5 and 7.0 W of cw power on two separate groups of lines in the 275.4–305.5 nm and 333.6–363.8 nm regions, respectively. In addition, a number of photochemical vapor deposition experiments and direct write studies, in particular, have employed the second harmonic of the 514.5 nm line (intracavity doubled) at 257 nm.

These UV lasers are well suited for those photodeposition applications in which the source intensity and beam quality are key considerations. Despite their relatively high cost and (for pulsed lasers) low duty cycle operation, these characteristics, as well as the capability to quickly change the output wavelength, make them attractive in photo-assisted processes for which lamps are not suitable.

### 3. Other Sources

Although conventional lamps and pulsed lasers are most widely used for photo-CVD, several new optical sources have been reported. Window-less lamps, based on high-current, low-voltage ($\sim 0.5$ A, 200-600 V) dc discharges in gases such as He and $N_2$, have been shown to efficiently generate VUV and deep UV radiation (He: 121.5 nm, $N_2$: 120-400 nm) [34]. Also, the increasing availability of synchrotrons, coupled with their ability to produce tunable UV and VUV radiation, has prompted several reports of synchrotron radiation–assisted deposition of elemental and compound films.

### IV. METAL FILMS

Because of their varied applications to microelectronics, metal films have been the focus of much of the effort in photochemical vapor deposition. This chapter reviews the elements that have been deposited to date, with emphasis given to the growth conditions. For a detailed discussion of the composition and structure of the films, the reader is referred to the reviews of Houle [6], Haigh and Aylett [7], Bäuerle [9], and Jackson et al. [39].

### A. Column IIB Metals (Cd, Zn)

Photodeposition of the Column IIB metals cadmium and zinc from their respective alkyls has been the subject of intense scrutiny (mercury will be discussed in Chap. V, Sect. B in conjunction with the II–VI compound semiconductors). In 1966, Jones et al. [40] demonstrated that thin Cd films ($<100$ Å thick) could be patterned on $SiO_2$ substrates by photodissociating dimethylcadmium (DMC) with 254 nm radiation from an Hg resonance lamp. Subsequent work has centered on the photodissociation of DMC in the gas phase or in an adlayer with excimer or $Ar^+$ (257 nm: second harmonic of 514.5 nm) radiation. In a series of papers, Deutsch, Ehrlich and Osgood [14], [31], [41] reported the broadarea deposition of Cd films, as well as the writing of lines with widths as small as

0.7 $\mu$m. DMC pressures of 1–4 torr in the reactor allowed deposition rates of 7–13 Å-sec$^{-1}$ to be obtained by photodissociating chemisorbed and physisorbed alkyl molecules on glass and quartz substrates. At higher intensities, deposition rates up to 1,000 Å-sec$^{-1}$ have been achieved, and an Hg arc lamp (200 W), ArF laser (30–300 mJ-cm$^{-2}$) or cw argon or krypton ion lasers have successfully served as optical sources.

Similar studies have been carried out for zinc where dimethylzinc, $Zn(CH_3)_2$, or diethylzinc, $Zn(C_2H_5)_2$, acted as the gas phase precursor. Several square centimeters of Zn films have been deposited on quartz or sapphire substrates by illuminating $Zn(CH_3)_2$/Ar gas mixtures with deep UV radiation from a mercury–xenon arc lamp. The threshold wavelength for dissociating the zinc alkyl is ~245 nm, and film thicknesses up to 0.6 $\mu$m have been obtained [42]. Also, Zn lines with widths as small as 2 $\mu$m and larger area films (400 $\mu$m$^2$) have been deposited with an ArF or KrF laser operated in an unstable resonator so as to minimize diffraction of the beam.

## B. Column IIIA Metals (Al, Ga, In, Tl)

The Column IIIA metals aluminum, gallium, and indium have also found widespread use in microelectronic and optoelectronic devices as interconnects and as elements in III–V semiconductor compounds. Of the three, aluminum has received the most attention in photodeposition studies because of its excellent bulk conductivity. Both direct writing of Al lines and broad-area deposition of metal films have been demonstrated. With dimethylaluminum hydride (DMAH) as the precursor and 60–100 mW of 257 nm laser power, for example, Al lines of ~2–3 $\mu$m in width have been written on a variety of substrates at speeds of 1 $\mu$m-sec$^{-1}$ [43]. At this scanning speed and a laser intensity of ~115 kW-cm$^{-2}$, deposition rates of 0.09 $\mu$m-sec$^{-1}$ were obtained. Broad-area deposition on polysilicon was demonstrated by Solanki et al. [44] by photodissociating TMA in parallel geometry with a KrF laser. Deposition rates up to 1,000 Å-min$^{-1}$ and film thicknesses > 0.5 $\mu$m were recorded.

Aluminum films having resistivities as low as 6.2 $\mu\Omega$-cm(2.3 times the bulk value) were deposited from TMA with a deuterium lamp by Hanabusa et al. [45]. Deposition rates up to 200 Å-min$^{-1}$ were realized at 200°C, and, in contrast to the photochemically deposited films, Al films deposited by pyrolysis at 260°C were highly resistive (140 $\mu\Omega$-cm). With essentially the same experimental arrangement but studying DMAH as the Al precursor, Hanabusa et al. [46] compared the results obtained with a D$_2$ lamp and the ArF laser. At 200°C, deposition rates of 190 Å-min$^{-1}$ and 380 Å-min$^{-1}$ were obtained with lamp (140 mW-cm$^{-2}$) and laser (230 mW-cm$^{-2}$) radia-

tion, respectively. Not only did the presence of VUV illumination at the substrate permit Al film deposition to occur at considerably lower temperatures than those accessible by pyrolysis, but the VUV once again dramatically improved the film conductivity. Because of the low concentrations of carbon in the photolytically deposited films (<6%), DMAH is a particularly attractive new precursor for optical source wavelengths below 200 nm.

Considerably less is known of the photodeposition of Ga and In. Gallium films have been deposited from $Ga(CH_3)_3$ with both arc lamps [47] and a frequency-doubled $Ar^+$ laser [48]. Deposition rates up to 70 $\text{Å-s}^{-1}$ have been achieved with the latter, while the large-area studies [47] yielded gallium metal droplets. Aylett and Haigh [47] carried out similar experiments with various indium precursors (indium trimethyl and cyclopentadienyl indium) and GaAs and Pyrex substrates. They once again observed the formation of droplets on glass but obtained films with smoother morphology on GaAs. Thin In films have also been deposited by dissociatively photoionizing InI at 193 nm to yield $In^+-I^-$ pairs [37]. For an InI number density of $10^{15}$ $cm^{-3}$, deposition rates were ~400 $\text{Å-h}^{-1}$. Similar results were obtained for thallium films deposited on silver by dissociatively photoionizing TlI with a Xe arc lamp [37].

## C. Column IVA, VIA and VIIA Transition Metals (Cr, Mo, W, Tl, Mn)

Because of their applications as interconnects and in gate metallization, the transition metals are of interest for photodeposition, and specifically in those situations where processing temperature is a critical factor (such as in III–V device fabrication). Extensive studies of the photo-CVD of Cr, Mo, and W have been carried out, with most prior work involving the photodissociation of their respective hexacarbonyls with an excimer laser. Large-area (>6 $cm^2$) Cr films have been deposited with XeCl (308 nm), KrF (248 nm), and ArF (193 nm) lasers in perpendicular and parallel geometries [49], but most efforts have concentrated on the perpendicular configuration because of the poor adhesion of deposited films if the substrate is not irradiated. The highest deposition rates, 2,000 $\text{Å-min}^{-1}$, are observed at 248 nm, but the films contain only ~50% Cr, with the remainder consisting of C and O because of the fact that all CO ligands are not removed when adsorbed carbonyls are photodissociated. Direct writing of lines (and dots) has also been demonstrated [50] at 257 nm.

Similar results have been reported for tungsten. Lines (<3 $\mu$m width) and ohmic contacts have been deposited from the carbonyl precursor, and broad-area deposition rates up to 1,700 $\text{Å-min}^{-1}$ obtained at 248 nm [49]. If one resorts to $WF_6$ (in the presence of $H_2$) as the precursor, deposition rates in excess of 1,000 $\text{Å-min}^{-1}$ are obtained in *parallel* geometry at

TABLE III

SUMMARY OF THE PHYSICAL PROPERTIES OF Mo, W, AND Cr FILMS PHOTODEPOSITED WITH
A KrF LASER (248 nm) FROM METAL HEXACARBONYL PRECURSORS (AFTER REF. 49)

| | Deposition rate ($\text{Å}$/min) | Resistivity ($\Omega/\square$) | Percent carbon in film | Adherence (PSI) | Tensile stress (dyn-cm$^{-2}$) |
|---|---|---|---|---|---|
| Mo | 2,500 | 0.9 | 0.9 | >8,000 | $<3 \times 10^9$ |
| W | 1,700 | 4.5 | 0.7 | >9,400 | $<2 \times 10^9$ |
| Cr | 2,000 | 6 | 0.8 | >7,800 | $<7 \times 10^9$ |

193 nm, with film resistivities within a factor of two of the bulk value [51].
Less work has been reported for the photodeposition of molybdenum, but
the results are comparable to those obtained for Cr and W. Gilgen *et al.* [52]
have deposited molybdenum and tungsten lines on glass, GaAs, and sap-
phire substrates by scanning the focused UV lines (350–360 nm) from an
$Ar^+$ laser. For $Mo(CO)_6$ and $W(CO)_6$ pressures of 0.17 and 0.035 torr,
respectively, and a writing speed of $1 \ \mu\text{m-s}^{-1}$, deposition rates up to
$2,700 \ \text{Å-s}^{-1}$ for Mo lines and W film thicknesses up to $1,100 \ \text{Å}$ were
observed. Several properties of Cr, W, and Mo films photodeposited in
parallel geometry from their respective hexacarbonyls with a KrF laser
(248 nm) are summarized in Table III.

Two other transition metals that have been deposited photochemically
are titanium and manganese. Direct writing of 4-$\mu$m-width Ti lines on
$LiNbO_3$ has been exploited to fabricate single mode waveguides [53] with
only 5 mW of power on the second harmonic of the $Ar^+$ laser (257.2 nm).
Manganese films have also been photodeposited from a methylcyclopenta-
dienyl precursor with a 2.5 kW Hg–Xe lamp [54].

## D. Column IVB Metals (Sn, Pb)

Although tin and lead films have been photodeposited from alkyl
precursors, characterization of the gas and surface processes and resulting
films has been limited. In both cases, adlayer photolysis appears to trigger
film deposition and thin ($<100 \ \text{Å}$ thick) films have been deposited on
GaAs, glass, and sapphire substrates. Chiu *et al.* [55] have deposited Pb
films from tetraethyl lead with frequency-doubled $Ar^+$ laser radiation and
obtained deposition rates up to $30 \ \text{Å-s}^{-1}$ for a precursor pressure of 0.7
torr. Mingxin *et al.* [56] deposited tin films on both quartz and carbon sub-
strates by photodissociating $Sn(CH_3)_4$ with the second harmonic of the
$Ar^+$ 514 nm laser line or an Hg resonance lamp. Depending on the source
intensity, both amorphous and polycrystalline films resulted. With Hg

resonance lamp (3 mW, 254 nm) dissociation of the metal alkyl, deposition rates were much smaller than those obtained with the laser—typically, 0.06 Å-min$^{-1}$. Interference structures appearing in the photodeposited films indicate that patterned tin films with features as small as 0.2 $\mu$m can be deposited by this approach.

### E. Column VIII Transition Metals (Fe, Pt, Ir)

Conducting films of iron were deposited onto various substrates by George and Beauchamp [54] by photodissociating the pentacarbonyl with an Hg-Xe arc lamp. Carried out at Fe(CO)$_5$ partial pressures of $10^{-2}$ torr, these studies yielded ~300 Å thick films after an exposure period of $10^4$ s. The authors attributed deposition to photoelectrons (ejected from the substrate by the optical source) that decomposed the carbonyl precursor. Thin iron films have also been deposited under UHV conditions by photo-lyzing Fe(CO)$_5$ adsorbed onto GaAs or Si substrates. Both excimer lasers and arc lamps have been used in perpendicular geometry, and the films studied to date contain significant concentrations (>10 at %) of carbon and oxygen. Iron has also been deposited onto Pyrex, quartz, and GaAs at rates up to 30 Å-s$^{-1}$ with 257 nm radiation from a frequency-doubled Ar$^+$ laser [50].

Recently, Armstrong et al. [57] deposited Fe/Ni composite films by photodissociating mixtures of ferrocene and nickelocene vapor at room temperature. The ferrocene absorption spectrum peaks near 190 nm, while that for nickelocene reaches its maximum value at ~285 nm. When the ferrocene/nickelocene mixture was irradiated at 193 nm (ArF laser), the deposit was found to consist of 92% Fe and 8% Ni. Similar measurements made at 337 nm with a pulsed N$_2$ laser ($\lambda$ = 337 nm) yielded 65% Fe–35% Ni deposits. Film deposition rates at 193 and 337 nm were determined to be 20 Å-s$^{-1}$ and >200 Å-s$^{-1}$, respectively.

Platinum films have been deposited from a variety of precursors onto quartz, graphite, glass, sapphire, and GaAs substrates. Utilizing both pulsed and cw ultraviolet sources, Koplitz et al. [58] demonstrated that ~1,000 Å thick Pt films can be deposited from CpPt(CH$_3$)$_3$ where Cp = $\eta^5$—C$_5$H$_5$. For 26 mW of average power at 308 nm (10 Hz), films were observed to grow at a rate of ~100 Å-min$^{-1}$ over an area of ~3 mm$^2$. Similar results were obtained for Pt films photodeposited with a cw Ar$^+$ ion laser operating simultaneously on the 351 and 364 nm lines. Platinum films have also been deposited on quartz and graphite with KrF excimer radiation and the frequency-doubled 514 nm line of Ar$^+$ [56]. Gilgen et al. [52] deposited thin Pt lines (from Pt(Hfacac)$_2$) on glass and GaAs at a scan speed of 0.4$\mu$m-s$^{-1}$ with the 350–360 nm UV lines of an Ar$^+$ laser. For

glass substrates, the film resistivities were ~2 to 10 times the bulk value. Both Pt and Ir films have also been deposited from their respective acetyl-acetonates by photoionizing the precursors with frequency-quadrupled radiation (266 nm) from an Nd:YAG laser [17]. The beam was passed 0.5 cm from the Si(111) substrate, resulting in the deposition of ~330 $\mu$m wide metal stripes consisting of >95 at % Pt.

## F. Group IB (Cu, Au)

Despite the importance of the Column IB metals copper, silver, and gold to an array of fundamental microelectronics processes (doping, metal-lization line and mask repair, etc.), photodeposition of these metals from the vapor phase is complicated by the scarcity of precursors. Simple alkyl molecules (i.e., of the form $MX_n$ where $M = Cu$, Ag, or Au; $X = CH_3$, $C_2H_5$, $C_4H_9 \ldots$, and $n$ is an integer) are not volatile and the carbonyls $[M(CO)_n]$ are unavailable or do not exist. It was not until 1985 that Jones *et al.* [59] demonstrated the viability of volatile coordination complexes as precursors by depositing Cu films upon photodissociating a fluorinated acetylacetonate complex, bis(1,1,1, 5,5,5-hexafluoropentanedionate) cop-per (II)-(Cu(Hfac)$_2$), with both pulsed and cw UV optical sources. A frequency-doubled $Ar^+$ ion laser (257 nm), ArF and KrF excimer lasers, and a low pressure Hg lamp were all investigated.

With the frequency-doubled $Ar^+$ ion laser, deposition was observed with laser intensities of $0.2-2 \times 10^4$ W-cm$^{-2}$ at a Si substrate. Films ~1 $\mu$m in thickness were deposited at rates between 1 and 200 Å-min$^{-1}$. ArF or KrF laser irradiation of quartz substrates at peak intensities $\geq 1$ MW-cm$^{-2}$ yielded thin Cu films (thicknesses $\leq 500$ Å), and the threshold intensity for film deposition was found to be ~1 MW-cm$^{-2}$. Regardless of the optical source, the resulting Cu films also contained 10-90% C depending on whether ethanol was added to the Cu(Hfac)$_2$ vapor.

Similar comments could be made for the photodeposition of gold from the vapor phase. Baum, *et al.* [60] demonstrated that Au can be pat-terned onto quartz substrates with a simple optical projection system to produce metal line widths as small as 2 $\mu$m. In their experiments, di-methylgold (III) acetylacetonate, Me$_2$Au(acac), was photodissociated by pulsed excimer radiation at 193 nm (ArF), 248 nm(KrF) or 308 nm(XeCl) or by an Hg resonance lamp. Films, 2,000-3,000 Å thick were produced, and the highest Au content was achieved in films deposited with KrF laser radiation. No deposition was observed if $\lambda = 351$ nm, which demonstrated that the film growth processes are photochemical in nature. Deposition was also observed with a Hg resonance lamp. Aylett and Haigh [61] also photo-

deposited gold films by photodissociating trimethylgold(III)-trimethyl-phosphine [(CH$_3$)$_3$ Au-P(CH$_3$)$_3$] at 248 nm. Both broad-area and patterned deposition were demonstrated, the latter by projecting a mask onto the substrate. Considerably more work has been reported in which Cu or Au films were deposited from *liquids*, and, for details, the reader is referred to the excellent review by Haigh and Aylett [62].

## V. SEMICONDUCTORS

The potential economic impact of photochemically deposited semiconductor films has driven the tremendous activity in the growth of both elemental and compound materials that this field has witnessed over the past decade. While efforts to deposit amorphous and epitaxial films of Si have accounted for most of the work in this area, considerable success has also been realized in the deposition of II–VI and III–V compound films.

### A. Elemental Films

#### 1. Carbon

The deposition of amorphous carbon films has been accomplished by photodissociating halomethanes or vinylchloride (CCl$_4$, C$_2$H$_3$Cl) [63] or acetylene with an ArF excimer laser. For C$_2$H$_3$Cl as a precursor, film deposition rates up to 150 Å-min$^{-1}$ were measured, and the films contained up to ~1 at % Cl. Graphite films can also be deposited by the photodissociation of C$_2$H$_2$ in parallel geometry or when the substrate is irradiated at a glancing angle. Recently, Ohashi *et al.* [64] deposited amorphous hydrogenated carbon films by irradiating *n*-butane vapor with unfiltered radiation from a 750 MeV synchrotron. Films having thicknesses >0.4 μm were deposited with *n*-butane pressures under 1 torr, and the film deposition rate was found to increase linearly with negative bias on the substrate. Accordingly, the production of positive ions by the synchrotron radiation was identified as the dominant contributor to film deposition.

#### 2. Silicon

All of the techniques that have been developed thus far for photodepositing Si may be classified into one of three categories: (1) Hg-photosensitized deposition; (2) direct decomposition of higher silanes; and (3) laser photodeposition, where the first two approaches rely on lamps as the optical source.

Since the pioneering work of Emeléus and Stewart [2] and Niki and Mains [65] exploring the Hg photosensitized decomposition of monosilane

(SiH$_4$) and germane (GeH$_4$), both amorphous hydrogenated and micro-crystalline Si films have been deposited by a number of groups [66,67]. These studies showed photo-CVD deposited a-Si films to be of comparable quality to plasma CVD deposited films, with the added benefit that ion-induced damage is not present in photochemical processing. Early work reported film deposition rates of 20–35 Å-min$^{-1}$, which was subsequently increased to 600 Å-min$^{-1}$ by improvements in reactor and Hg lamp design. In addition, Mizukawa *et al.* [68] deposited *p*-type amorphous Si films by adding small concentrations of diborane (B$_2$H$_6$) to the silane vapor in the reactor (200–250°C substrate temperatures).

Studies of the Hg photosensitization kinetics chain have identified the production of the higher silanes (Si$_2$H$_6$, Si$_3$H$_8$) from the collisional dissociation of SiH$_4$ as a critical step. Consequently, in an effort to bypass the unnecessary *in situ* conversion of SiH$_4$ to Si$_2$H$_6$, most recent Si photodeposition by Hg sensitization has utilized Si$_2$H$_6$ directly. Inoue *et al.* [69] reported the deposition of amorphous Si films having thicknesses up to ~1 $\mu$m by irradiating a Si$_2$H$_6$/Hg mixture for 10 min. Without the presence of Hg in the reactor, the film deposition rate was observed to fall by one to two orders of magnitude. Both *n*- and *p*-type amorphous hydrogenated and microcrystalline Si films have also been deposited [70] by adding phosphine (PH$_3$) or B$_2$H$_6$, respectively, to the reactor. The ratio of PH$_3$ or B$_2$H$_6$ to Si$_2$H$_6$ was 6,000 or 10,000 ppm, respectively, and the total gas pressure in the reactor was 2 torr. Solar cells (SiC/Si *p–i–n* structures) have also been fabricated [71] from photodeposited amorphous films and have yielded efficiencies at AM1.5 of up to 8.5% [72].

A major development in the application of Hg photosensitization to film deposition was the report of Nishida *et al.* [72] in 1986 that epitaxial Si films could be grown at substrate temperatures as low as 200°C by this process. The addition of SiH$_2$F$_2$ to the gas stream was found to be critical, not only in the early stages of film growth but throughout the deposition process. It was concluded that halogen-bearing radicals or free F atoms may be responsible for removing the native oxide. Mass flow rates for the SiH$_2$F$_2$ exceeding ~20 sccm at a total reactor pressure of 2 torr were necessary to grow epitaxial films, and deposition rates up to 0.7 Å-sec$^{-1}$ were observed.

The underlying motivation behind Hg photosensitized deposition of Si from monosilane is the weak absorption of the precursor in the UV and at the 185 and 254 nm lines of the Hg resonance lamp, in particular. Because of the increasing absorption at longer wavelengths that is associated with resorting to progressively higher silanes (i.e., SiH$_4 \rightarrow$ Si$_2$H$_6 \rightarrow$ Si$_3$H$_8$), however, one can avoid the presence of Hg in the reactor entirely by photodissociating disilane (or trisilane, Si$_3$H$_8$) directly. Early attempts at
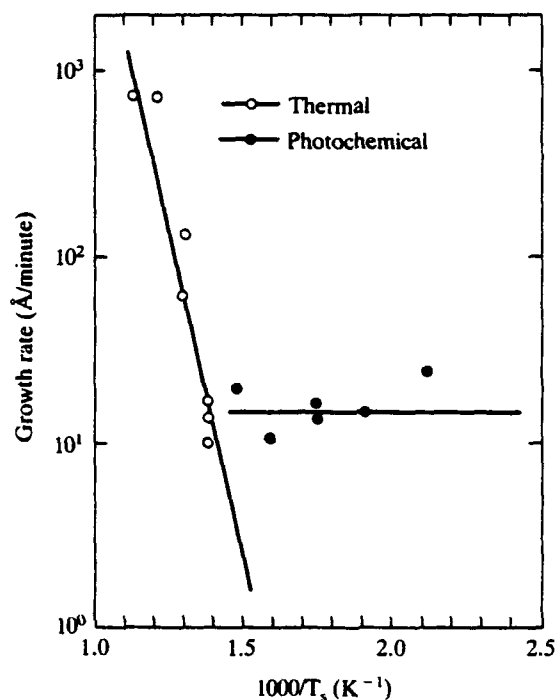
**Fig. 16.** Growth rate as a function of temperature for amorphous Si films deposited by photo-CVD or pyrolysis of $Si_2H_6$. The data show a characteristic of photo-CVD: its low inherent activation energy. (Adapted with permission from the *Japanese Journal of Applied Physics*, **22**, L46, Y. Mishima. M. Hirose, Y. Osaka, K. Nagamine, Y. Ashida, N. Kitagawa, and K. Isogaya, 1983).

photodissociating $Si_2H_6$ with Hg lamp radiation resulted in deposition rates that were low compared to those obtained by Hg photosensitization. Mishima et al.[73] observed deposition rates for amorphous Si films as high as 15 Å-min$^{-1}$ when $Si_2H_6$ was directly photodissociated with the 185 and 254 nm lines from an Hg lamp. The lamp intensity was ~80 mW-cm$^{-2}$, the quartz or Si substrate temperature was varied between 200 and 400°C, the gas feedstock mixture consisted of 1% $Si_2H_6$ in He, and $N_2$ acted as the carrier gas. As shown in Fig. 16, the photochemical film growth rate is independent of substrate temperature in the 200–400°C range, which is consistent with the low activation energy ($E_a$) also reported in Ref. 72 (0.18 eV).

Increased deposition rates and the growth of epitaxial films were reported by Gonohe et al.[74], who illuminated a $Si_2H_6/N_2$ gas mixture and

Si(100) substrates with the VUV radiation from a $D_2$ lamp. Epitaxial films were obtained at 650°C, and at that substrate temperature, the deposition rate was measured to be ~900 Å-min$^{-1}$. Over the 550–650°C temperature range, the activation energy for the deposition process is 23 kcal/mol ≈ 1 eV, which is roughly 66% of the value for thermal deposition (conventional CVD). Consequently, at the low end of the temperature region studied (550°C), the photo-CVD deposition rate was found to be more than double the thermal rate. The assistance of the incident VUV photons in cleaning the Si surface was also clearly demonstrated.

Fuyuki et al. [75] also explored the use of a $D_2$ lamp in depositing Si films but focused on a-Si:H films deposited in the 200–300°C temperature range. No dependence of the 15 Å-min$^{-1}$ deposition rate in this temperature interval was observed, but substituting a microwave-excited Xe lamp for the $D_2$ source dramatically improved the rate. For ~120 and 50 W of input power to the lamp, the a-Si:H film deposition rate was observed to be 75 Å-min$^{-1}$ and 10 Å-min$^{-1}$, respectively. By changing the optical window on the reactor from $CaF_2$ or $MgF_2$ to quartz, it was shown that film growth requires radiation wavelengths below 180 nm. After photolyzing $Si_2H_6$ and $Si_3H_8$ with an Hg lamp producing 3.5 mW-cm$^{-2}$ at 185 nm, Kumata et al. [76] found that the deposition rate for a-Si:H films grown from $Si_3H_8$ was five times that for $Si_2H_6$ as a precursor. The conductivity of films deposited from $Si_3H_8$ at 300°C ($10^{-5}(\Omega\text{-cm})^{-1}$) makes them well-suited for incorporation into solar cells. Recently, Kim et al. [77] prepared p–i–n a-Si:H solar cells from films photodeposited from $Si_2H_6$ and measured efficiencies >11%.

Amorphous, polycrystalline, and epitaxial Si films have been deposited with lasers from several different precursors and in both parallel and perpendicular configurations. Andreatta et al. [78] deposited polycrystalline Si films on quartz substrates at rates up to 9.8 Å-sec$^{-1}$ with a weakly focused KrF laser and peak intensities of ~20 MW-cm$^{-2}$. The high intensities required are a consequence of the dominance of two-photon dissociation of silane at 193 nm. Film thicknesses up to ~2,000 Å were obtained with ≥400 s exposure times and 10% $SiH_4$ in $N_2$ gas (total pressure of several hundred torr). Several films were also deposited with $Si(CH_3)_4$ as the precursor.

Several groups [79, 80] have reported the deposition of hydrogenated amorphous films from the photodissociation of $Si_2H_6$ and $Si_3H_8$ with an ArF excimer laser. Deposition rates typically range from 100 to 300 Å-min$^{-1}$, and the film properties are comparable to those for films deposited by plasma processes.

Epitaxial Si films were deposited by excimer laser-assisted CVD by Yamada et al. [81] in the 600–650°C temperature range. Not only did the

presence of UV photons at the substrate triple the film growth rate, but crystallinity and hole mobilities were both markedly improved with the UV laser beam, particularly at the lowest substrate temperature studied (600°C). At lower $Si_2H_6$ pressures (0.01–0.1 torr), thin Si films have also been deposited on quartz or sapphire substrates. Frieser [82] found that the deposition of epitaxial Si films from the pyrolysis of $Si_2Cl_6/H_2$ gas mixtures was accelerated when the substrate was irradiated by an Hg arc lamp. Since the lamp's 5 eV ($\lambda \sim 254$ nm) photons are not sufficiently energetic to rupture the $Cl_3Si$–$SiCl_3$ bond, the observed enhancement was attributed to surface interactions. Similar results were obtained by Ishitani et al. [83], who measured significant increases in the deposition rate of epitaxial Si (by CVD from $SiH_2Cl_2$, dichlorosilane) when Hg–Xe UV radiation was directed onto the substrate. Specifically, the growth rate at 900°C rose from 1.8 to 2.8 $\mu$m-min$^{-1}$, which was attributed to the photodissociation of the $SiCl_2$ radical at the substrate surface.

## 3. Germanium

Fewer studies have been concerned with the photodeposition of elemental germanium. Polycrystalline films up to 1,500 Å in thickness were deposited by Andreatta et al. [78] by photodissociating germane ($GeH_4$) with 193 or 248 nm excimer radiation. The perpendicular geometry yielded deposition rates of 4–5 Å-sec$^{-1}$ for ArF laser intensities of 2 MW-cm$^{-2}$. Higher 248 nm intensities ($\sim$8 MW-cm$^{-2}$) were required to reach the maximum film deposition rate (5–6 Å-sec$^{-1}$) for that source wavelength. No film growth was observed when the laser wavelength was 308 nm (XeCl laser), which demonstrates the wavelength threshold and, therefore, the photochemical nature of the process.

Epitaxial Ge films were later grown by Eden et al. [84] on NaCl (100) substrates at substrate temperatures as low as 120°C. Polycrystalline films were deposited on quartz substrates ($T_S \leq 250$°C) with grain sizes ranging from 0.3 to 0.7 $\mu$m. In parallel geometry, thin epitaxial films have been deposited on GaAs (100) substrates at temperatures as low as 285°C by photodissociating $GeH_4$ with an ArF laser [85]. The position of the laser beam was maintained at $\geq$2 mm above the substrate, and the dominant role played by the laser appears to be the conversion of $GeH_4$ to $Ge_2H_6$, which migrates more than 10 mean free paths to the substrate, where it subsequently pyrolyzes. Etching the substrate in situ by flowing 5% HCl (in He) through the reactor for 5 min was found to be necessary for obtaining epitaxial films. After $\sim$400–700 Å of epitaxial growth, the growing film switches abruptly to amorphous material, which is apparently caused by the buildup of carbon (from the vacuum system) at the solid/vapor

interface. More than an order of magnitude increase in the Ge film growth rate is observed if small amounts of ammonia are added to the $GeH_4$/He gas flow stream. Kiely *et al.* [86] demonstrated that, despite the acceleration in the deposition rate, the Ge films are nevertheless epitaxial. Upon absorbing a 193-nm photon, $NH_3$ produces an H atom, which subsequently decomposes $GeH_4$ by hydrogen abstraction. Furthermore, the absorption cross-section of $NH_3$ at 193 nm is almost three orders of magnitude larger than that for $GeH_4$ at the same wavelength ($\sigma_{NH_3}$: $\sim 10^{-17}$ cm$^2$; $\sigma_{GeH_4}$: $2\text{--}3 \times 10^{-20}$ cm$^2$).

Structures consisting of alternating layers of amorphous Ge and Si were deposited entirely by photochemical processes by Lowndes *et al.* [87]. Film deposition was carried out in parallel geometry (laser beam-to-substrate distance $\geq 1$ mm) by photodissociating $Si_2H_6$ or $GeH_4$ in the reactor. Ge and Si layer thicknesses of $5.4 \pm 0.2$ and $10.7 \pm 0.4$ nm, respectively, were deposited in fabricating a nine-layer structure. Germanium/silicon alloy films have also been photodeposited from $GeH_4$/$Si_2H_6$ mixtures, using an ArF laser [88]. For substrate temperatures below 350°C, deposition occurred entirely by photochemical processes, and deposition rates ranged from 150 to 300 Å-min$^{-1}$. The ratio of Si to Ge concentrations in the films was found to be a factor of three higher than the $Si_2H_6$:$GeH_4$ partial pressure ratio, which suggests the importance of cross-reactions between Ge and Si-containing species in the film deposition process. Alternative precursors for the photo-CVD of Ge were explored by Stanley *et al.* [89], who deposited polycrystalline Ge films from ethylgermane and diethylgermanium. Although an infrared ($CO_2$), rather than UV, laser was used, the photochemical nature of the deposition process was demonstrated by the need for the laser to be tuned to an IR absorption band of the precursor.

## B. II–VI Binary and Ternary Compounds

Photo-assisted CVD is a particularly attractive deposition technique for those materials and devices that are sensitive to processing temperature. As Irvine [90] has pointed out, interdiffusion in the II–VI ternary compound $Cd_xHg_{1-x}Te$, for example, is typically $\geq 100$ $\mu$m at a growth temperature of 600°C but is $<1$ $\mu$m for temperatures at or below 400°C. Efforts to fabricate multilayer structures with abrupt interfaces in the II–VI compounds, therefore, hinge on an ability to deposit high-quality films at reduced temperatures. While the temperatures at which the binary II–VI semiconductors ZnSe, ZnS, CdS, CdSe, CdTe, and HgTe are deposited by MOCVD can be reduced to below 250°C by resorting to less thermally stable precursors, photo-CVD of these compounds at temperatures as low as 150–200°C has yielded epitaxial films of high quality.

## 1. Zinc Compounds

The earliest work in II–VI compound photodeposition centered on the zinc-containing binary compounds ZnSe and ZnO. Johnson and Schlie [42] were the first to demonstrate the deposition of zinc selenide films by irradiating mixtures of $Zn(CH_3)_2$ and $Se(CH_3)_2$ vapor with an Hg arc lamp. Although the films were not stoichiometric, film thicknesses up to ~0.6 $\mu$m over more than 3 $cm^2$ of surface were obtained. Exposure periods of 1–2 h were necessary to deposit these films due to the low fluence of the Hg lamp for wavelengths below ~245 nm, which was found to be the wavelength threshold for the photodissociation process. Polycrystalline zinc monoxide films were subsequently reported by Solanki and Collins [36], who employed an ArF or KrF excimer laser to photodissociate $Zn(CH_3)_2$ and $NO_2$ (or $N_2O$). Both parallel and perpendicular geometries were explored, but the highest optical quality (defined with regard to film transmission) and lowest resistivity films were obtained by irradiating the Si substrate. Deposition rates up to 18 $\mu$m-h$^{-1}$ were measured, and the uniformity in film thickness over 10 $cm^2$ of surface area was ±5%.

In 1985, Ando et al. [91] photodeposited ZnSe epitaxial films at temperatures as low as 200°C. Diethylzinc and dimethylselenide were the alkyl precursors and the UV radiation was provided by a low-pressure Hg lamp. At 400°C, the presence of the UV improved the film deposition rate by a factor of two. Epitaxial ZnS and ZnSe films have also been deposited on GaAs with excimer laser radiation (193 and 248 nm) by Fujita et al. [92] and Shinn et al. [93], respectively. In both cases, the UV laser beam passed parallel to the substrate and epitaxial films were obtained in the 100–150°C range for ZnS and at temperatures as low as 200°C for ZnSe. Although single pulse laser energies were varied from 7.5 to 50 mJ, deposition rates did not exceed 1 $\mu$m-h$^{-1}$.

## 2. Cadmium and Mercury Binary and Ternary Compounds

Considerably more effort has been devoted to the Cd and Hg-based II–VI films. Virtually all of the photodeposition studies reported to date have relied upon the alkyls as sources for one or both of the Column IIB and VIA atoms. The first photodeposited epitaxial II–VI film, HgTe, was grown by Irvine and co-workers [94] from Te $(C_2H_5)_2$ and mercury vapor by Hg photosensitization. Films ~1 $\mu$m thick were deposited at rates up to ~2 $\mu$m-h$^{-1}$ in the 240–310°C interval, and epitaxial films could be grown at temperatures as low as ~180°C. In the 180–250°C range, no film deposition occurs in the absence of UV radiation. Increasing the precursor partial pressures and/or Hg lamp intensity will offset the decline in film growth rate at low temperatures, and it has been estimated that a deposition rate of 1 $\mu$m-h$^{-1}$ could be obtained at 180°C for UV intensities at the

substrate of 100 W-cm$^{-2}$. Utilizing the radiation from an Hg/Xe arc lamp. Ahlgren et al. [33, 95] also photochemically deposited HgTe films at temperatures as low as 182°C and successfully fabricated HgTe–CdTe superlattices (>50 periods) by alternately introducing Te (C$_2$H$_5$)$_2$ and Cd(CH$_3$)$_2$ into the reactor (in the presence of Hg vapor). HgTe film deposition rates were <0.1 $\mu$m-h$^{-1}$ at 182°C when diethyltellurium was the Te precursor but, at 240°C, growth rates rose to roughly 1 $\mu$m-h$^{-1}$ when using the diisopropyl as the precursor. Laser photochemical vapor deposition of HgTe was recently reported by Fujita et al. [92]. With KrF or ArF lasers and a parallel configuration, epitaxial films were grown on CdTe (111) substrates at deposition rates up to ~1 $\mu$m-h$^{-1}$.

Kisker and Feldman [96, 97] grew epitaxial CdTe films on GaAs (100) at substrate temperatures down to 250°C with a low-pressure Hg lamp. For dimethylcadmium and diethyltellurium as the precursors, obtaining epitaxial films required that the Cd(CH$_3$)$_2$:Te(C$_2$H$_5$)$_2$ partial pressure ratio be 1.5:1. Long-term film growth rates up to 2 $\mu$m-h$^{-1}$ were recorded at 350°C. Cody et al. [98, 99] have also grown epitaxial CdTe films on GaAs with an Hg lamp. For only 100 mW-cm$^{-2}$ of radiation incident on the surface (200 $\le \lambda \le$ 250 nm), maximum deposition rates were found to be as high as 13 and 9 $\mu$m-h$^{-1}$ for CdTe and GaAs (100) substrates, respectively [98]. For (CH$_3$)$_2$Cd and (C$_2$H$_5$)$_2$Te partial pressures of 5.4 × 10$^{-4}$ and 1.6 × 10$^{-3}$ atm, respectively, photodeposition rates were typically 6 $\mu$m-h$^{-1}$ at 250°C [99].

Excimer laser-assisted photoepitaxy of CdTe was demonstrated by Zinck et al. [100, 101]. Growth rates as high as 2 $\mu$m-h$^{-1}$ were recorded at a deposition temperature of 165°C. The precursors for these studies were also Cd(CH$_3$)$_2$ and Te(C$_2$H$_5$)$_2$, but partial pressures for both reactants were low: 10$^{-3}$–10$^{-2}$ torr. Also, while both 193- and 248-nm radiation were investigated, most of the effort focused on the KrF laser.

The ternary alloy, Cd$_x$Hg$_{1-x}$Te, was deposited by Irvine et al. [102, 103], who grew thin epitaxial films by Hg photosensitization. With diethyltelluride, dimethylcadmium, and Hg vapor as the precursors and a 3 kW Hg arc lamp, epitaxial films 1.3 $\mu$m thick were grown at temperatures down to 250°C. The use of He rather than H$_2$ as the carrier gas was found to be necessary for the growth of epitaxial films. Morris [104] subsequently grew epitaxial Cd$_{0.8}$Hg$_{0.2}$Te films with an ArF laser in parallel geometry and, rather than Hg vapor, employed Hg(CH$_3$)$_2$, dimethylmercury, as the Hg donor molecule. With CdTe substrates, growth rates of ~4 $\mu$m-h$^{-1}$ and >2 $\mu$m film thicknesses were obtained at a temperature of 150°C. Since the laser did not irradiate the substrate, transient heating of the growing film by the optical source was avoided. Recently, Cody et al. [99] obtained similar growth rates (4 $\mu$m-h$^{-1}$) for 20% CdTe/80% HgTe

alloy films that were deposited at 250°C with the aid of a 2 kW Hg lamp. The best film quality resulted from using methylallyltelluride as the Te precursor, and the variation in film composition, $x$ (i.e., $Cd_xHg_{1-x}Te$), was only 4% over 1 $cm^2$ of surface area.

## C. III–V Compound Films

Although the first efforts to photodeposit III–V films were reported early in the last decade, the application of photo-CVD to this family of materials initially developed more slowly than metal or II–VI film deposition, but progress has recently accelerated significantly. The presence of an optical beam at the substrate during the growth of III–V films has been demonstrated to yield several beneficial results, such as improvements in surface morphology, modification of carrier concentrations, and, in several cases, increases in deposition rates. This section will provide an overview of the work reported to date in this area with emphasis on the photo-assisted deposition of GaAs.

### 1. Gallium Arsenide

Most of the effort in photodepositing III–V films has concentrated on the binary compound GaAs. Pütz et al. [105] examined the growth of GaAs in the 510–650°C range and found that the presence of UV photons from an Hg lamp improved the maximum (saturated) growth rate from 5 to 8 $\mu$m-h$^{-1}$ at 510°C. Also, they observed that "... in all epitaxial runs improved surfaces were obtained upon illumination ..." [105] and that mirrorlike surfaces were produced, even at temperatures as low as 510°C. Similar results were obtained subsequently by Balk et al. [106], who employed ArF and XeF excimer lasers in addition to the Hg lamp. While the film growth rate was observed to double for 193 nm illumination of the substrate, no effect was detected for $\lambda = 351$ nm, which points to the photochemical nature of the effect.

Nishizawa et al. [107] explored the impact of excimer laser radiation at the substrate on the growth of GaAs by chloride-transport vapor phase epitaxy (VPE) and MOCVD. Not only were film growth rates enhanced, but the Hall mobilities of films grown in the presence of UV photons were improved over those deposited without substrate illumination. At a substrate temperature of 600°C, for example, the growth of epitaxial GaAs from $AsCl_3$ and $GaCl_3$ by VPE was roughly quadrupled (from ~1.2 to 4.5 $\mu$m-h$^{-1}$) by irradiating the GaAs(100) substrate with 2.7 W of average laser power at 248 nm (KrF laser). Similar improvements were observed over the 480–700°C range. Also, epitaxial films were grown at temperatures as low as 350°C.

Chu *et al.* [108] grew epitaxial GaAs films on *n*-type GaAs(100) substrates at temperatures in the 425–500°C range by irradiating the substrate during film growth with an ArF laser fluence of 19–38 mJ-cm$^{-2}$. In the absence of the UV irradiation, no deposition was observed at temperatures up to 600°C under conditions that were otherwise identical. Deposition rates ranging from 0.02 $\mu$m-min$^{-1}$ at 425°C to 0.1 $\mu$m-min$^{-1}$ at 500°C were measured and the electrical and chemical characteristics of the films were determined to be similar to those for films grown by conventional MOCVD. Hole mobilities, for example, for films grown in the 425–500°C interval varied from 150 to 200 cm$^2$/V-sec, with carrier concentrations ranging from $5 \times 10^{16}$ to $\sim 3 \times 10^{17}$ cm$^{-3}$. The carbon number density was measured by SIMS to be $4 \times 10^{17}$–$2 \times 10^{18}$ cm$^{-3}$ for films deposited at 500°C. York *et al.* [109] carried out similar experiments but with lower laser fluences (<13 mJ-cm$^{-2}$) and at wavelengths of 248 and 351 nm rather than 193 nm. They observed growth rate enhancements of 5–15% at 450°C when KrF photons were present, but no measurable effect was observed at 351 nm, which supports the photochemical nature of the enhancement. The effect was attributed to photolysis of adsorbed Ga(CH$_3$)$_3$ molecules; KrF was chosen rather than ArF to intentionally avoid photodissociation of AsH$_3$.

Several groups have also successfully revisited the growth of GaAs films with UV lamps. In a clever series of experiments, Kachi *et al.* [110] combined a cw CO$_2$ laser with a high-pressure Hg lamp to grow epitaxial GaAs films at temperatures down to 500°C. The role played by the CO$_2$ laser was to vibrationally excite AsH$_3$ at the surface, while the Hg lamp served to improve layer quality and surface morphology. Confirmation of the CO$_2$ laser's involvement in the growth process was demonstrated by tuning the laser to the 10.531 $\mu$m absorption line of AsH$_3$, whereupon the growth rate was enhanced by more than a factor of two at 500°C. Tuning the CO$_2$ laser wavelength to a region where AsH$_3$ does *not* absorb ($\lambda = 9.260$ $\mu$m), or directing 10.531 $\mu$m radiation *parallel* to the substrate, yielded no effect.

Norton and Ajmera [111, 112] deposited polycrystalline GaAs on quartz by photodissociating Ga(C$_2$H$_5$)$_3$ in the presence of AsH$_3$ with an Hg–Xe arc lamp or by Hg photosensitization with a 500-W low-pressure Hg resonance grid lamp. All of the films were deposited at 240°C, a temperature at which growth will not normally occur without lamp radiation.

## 2. Al-containing Compounds

Recently, Tokumitsu *et al.* [113] combined an ArF laser and a metalorganic MBE (MOMBE) reactor to grow epitaxial AlAs and polycrystalline GaAlAs films at 350°C. Crystalline AlAs films up to 1.25 $\mu$m in

thickness were grown by irradiating the substrate, whereas, in the absence of UV photons, films only ~500 Å thick were obtained. Similarly, 0.2-$\mu$m-thick polycrystalline GaAlAs films were deposited with surface illumination. Without the UV laser beam, film thicknesses were limited to 200–300 Å. For these studies, the gallium precursor was triethylgallium $(Ga(C_2H_5)_3)$, and heating of elemental arsenic provided a beam of $As_4$ at the substrate. AlAs, GaAs, and [Al, Ga] As were deposited by Zinck et al. [114] from Lewis acid–base adducts such as $(CH_3)_3Al:As(CH_3)_3$. The vapor pressure of this adduct at 25°C is ~0.5 torr, and both the Ga–As and Al–As adducts investigated in Ref. 114 absorb strongly at 193 nm but only weakly at 248 nm. Best film morphology was obtained when the excimer laser beam was directed parallel to the Ge substrate, but the maximum growth rates were observed to be 0.03 Å per pulse. For the GaAs films, the As/Ga ratio was found to increase for KrF laser fluences above 140 mJ-cm$^{-2}$ and, for AlAs and [Al, Ga] As films as well, the film stoichiometry was observed to be a function of the laser fluence. The Ga/Al ratio in [Al, Ga] As films, for example, was determined to be 20 for $\lambda$ = 193 nm, a laser fluence of 320 mJ-cm$^{-2}$ and a Ga/Al ratio in the gas phase of 17. At 248 nm, however, a Ga/Al ratio (gas phase) of 14, and 100 mJ-cm$^{-2}$ of fluence, the Ga/Al ratio in the deposit fell to 0.2.

### 3. Gallium Phosphide

Epitaxial films of the wider-bandgap binary GaP have been deposited by Sudarsan et al. [115, 116] onto GaP (100) at 500°C by photodissociating a mixture of trimethylgallium and tertiarybutylphosphine (TBP) with an ArF laser. In the absence of the excimer laser radiation, a thermal film growth rate of 60 Å-min$^{-1}$ is observed, and the material is polycrystalline. With 110 mJ-cm$^{-2}$ of 193 nm laser fluence at the substrate, however, epitaxial films are grown at a deposition rate six times larger (i.e., ~360 Å-min$^{-1}$) than that of the thermal background. Although pulsed heating of the substrate undoubtedly plays a role in film growth for this fluence, identical experiments carried out at 248 nm yielded only polycrystalline films. Since both TMG and TBP absorb less strongly at 248 nm than at 193 nm, it is apparent that photodissociation of the precursors also plays a role in determining the structure of the film. Epitaxial films were obtained only in a narrow range of laser fluences. Below 100 mJ-cm$^{-2}$, the films were polycrystalline, but above 120 mJ-cm$^{-2}$, surface ablation dominated.

### 4. Indium Phosphide and Indium Antimonide

Indium phosphide (along with HgTe) was one of the first semiconductor compounds to be deposited by photochemical processes in the gas

phase. Donnelly *et al.* [117–119] deposited amorphous, polycrystalline, and epitaxial InP films on quartz, GaAs or InP substrates by photodissociating mixtures of $(CH_3)_3InP(CH_3)_3$ and $P(CH_3)_3$ with an ArF laser beam at normal incidence to the surface. Film thicknesses typically were $<1,000$ Å, and deposition rates were measured to be ~0.2 Å per pulse. Epitaxial films were obtained only for laser fluences exceeding $~100$ mJ-cm$^{-2}$, which suggests the contribution of thermal effects to the deposition process. This was confirmed by the fact that film growth also occurred for an excimer laser wavelength of 351 nm (XeF), in a spectral region where both precursors are transparent. However, at 351 nm, the film growth rates were roughly a factor of four smaller than those at 248 and 193 nm, which indicates that film growth is controlled by both pyrolytic and photochemical mechanisms. The highest-quality epitaxial films were grown at 320°C.

Zuhoski *et al.* [120] have recently reported the photodeposition of polycrystalline InSb films on GaAs (100) at room temperature. The precursors, $In(CH_3)_3$ and $Sb(CH_3)_3$, both absorb strongly at 193 nm, but the absorption cross-section falls by an order of magnitude in going to 248 nm. Nevertheless, $\sigma$ at 248 nm for $In(CH_3)_3$ and $Sb(CH_3)_3$ is $1.2 \times 10^{-18}$ and $1.7 \times 10^{-18}$ cm$^2$, respectively [120], and it was found that the highest-quality InSb films were deposited with KrF radiation (50 mJ-cm$^{-2}$) and for an $Sb(CH_3)_3/In(CH_3)_3$ partial pressure ratio of 17 : 1.

## VI. DIELECTRICS

Among the materials that have been photodeposited, the dielectrics were the earliest to have significant commercial impact. Photo-CVD $SiO_2$, for example, has been introduced into the processing of 4-megabit devices [121, 122], and reactors are now commercially available for the broad-area deposition of both the oxides and nitrides of Si by Hg photosensitization [35] and ArF laser photodissociation. The primary factors driving the introduction of photodeposited dielectrics into commercial processing are its associated step coverage and low defect density. Aside from $SiO_2$ and $Si_3N_4$, a variety of other dielectric films, such as the oxides of aluminum, tin, and zinc, have been deposited by photochemical processes.

### A. Aluminum Oxide

Solanki *et al.* [44] demonstrated in 1983 that stoichiometric $Al_2O_3$ films can be deposited uniformly over 75-mm diameter wafers at 200°C by photodissociating mixtures of trimethylaluminum and $N_2O$ with an ArF or KrF laser beam. At a source wavelength of 248 nm and an average laser power of 10 W, film deposition rates up to 2,000 Å-min$^{-1}$ were measured

at the substrate temperature of 350°C. While higher deposition rates were measured at 193 nm, it was necessary to reduce the TMA partial pressure from 80–120 mtorr to 30 mtorr to obtain films of uniform thickness. The carbon content was <1 at %, and the pinhole defect density was <0.2-$cm^{-2}$. All experiments were carried out in parallel geometry, and Deutsch et al. [123] subsequently demonstrated that irradiating the growing $Al_2O_3$ film with 193 or 248 nm fluences as low as 1 mJ-$cm^{-2}$ measurably increased the film's refractive index. An increase in the index from ~1.6 to 1.7, for example, was observed when the surface was illuminated with 1.6 mJ-$cm^{-2}$ of 193-nm radiation.

Hudson et al. [124] synthesized several novel precursors from the aluminum $\beta$-diketonate family specifically for $Al_2O_3$ photodeposition. Containing both the necessary Al and oxygen atoms, these molecules absorb strongly over a broad spectral region in the UV, making them suitable for photodissociation by a lamp. One of the diisopropoxy aluminum diketonates, $Al(OPr^i)_2Acac(OMe)$, which contains $CH_3$ and $OCH_3$ ligands, was studied as a precursor. Although its vapor pressure at 120°C is only ~0.03 torr, stoichiometric $Al_2O_3$ films having a carbon content of <1 at % were deposited with a growth rate of 0.25 $\mu$m-$h^{-1}$.

## B. Silicon Dioxide

Silicon dioxide is the most widely deposited and thoroughly characterized of the photo-CVD dielectrics, owing to its fundamental importance in VLSI technology. The low processing temperatures (<200°C), reduced defect densities, and absence of heavy ion damage characteristic of photo-deposited $SiO_2$, combined with good step coverage and capacity for broad-area deposition, make this dielectric of increasing interest for incorporation into commercial semiconductor processing.

The deposition of $SiO_2$ by Hg photosensitization was demonstrated in the early 1980s [35, 125]. Irradiating mixtures of $SiH_4$, $N_2O$, and Hg vapor yielded deposition rates up to 150 Å-$min^{-1}$ at a total pressure of 0.3 to 1.0 torr and substrate temperatures as low as 50°C. Tables II and IV summarize the reactor conditions and electrical and structural characteristics of the deposited dielectric films [35]. More recent studies by Padmanabhan et al. [126] with a commercially available reactor examined silicon oxide deposition at 100 and 200°C. Deposition rates in excess of 150 Å-$min^{-1}$ were again observed, but pinhole densities ranging from ~200-$cm^{-2}$ to 600-$cm^{-2}$ and refractive indices between ~1.5 and 2.0 were measured for 0.3-$\mu$m-thick films grown at 200°C. Depending on the growth conditions, intermediate oxide phases such as $Si_2O_3$, SiO, and $Si_2O$ were also present.

TABLE IV

CHARACTERISTICS OF SILICON OXIDE AND SILICON NITRIDE FILMS DEPOSITED BY
PHOTO-CVD IN A COMMERCIAL REACTOR (AFTER REF. 35)

| Characteristic | Film | |
|---|---|---|
| | Silicon dioxide | Silicon nitride |
| Density | 2.10 g/cm$^3$ | 1.8 to 2.4 g/cm$^{3a}$ |
| Index of refraction | 1.45–1.49$^a$ | 1.8–2.4$^a$ |
| Dielectric constant | 3.9 | 5.5$^a$ |
| Dielectric strength | 4.0–6.0 × 10$^6$ V/cm | 4 × 10$^6$ V/cm$^a$ |
| Defect density | <10/cm$^2$ | <10/cm$^2$ |
| Film adhesion (tensile) | >5.2 × 10$^5$ torr (10$^4$ lb/in$^2$) | 3.1–5.2 × 10$^4$ torr (0.6 to 1 × 10$^3$ lb/in$^2$) |
| Etch rate | 9 nm-s$^{-1b}$ | 6 to 10 nm-s$^{-1c}$ |
| Film composition | SiO$_2$ | Si$_x$O$_y$N$_z^a$ |

$^a$ Film composition characteristics can be varied by reactant gas ratio.
$^b$ Buffered oxide etch, film densified (15 min at 450°C in N$_2$).
$^c$ 1:10 HF, as deposited.

Mishima et al. [127] reported the direct photodeposition of SiO$_2$ from mixtures of SiH$_4$ and O$_2$ with a low-pressure Hg lamp. For each temperature studied in the 150–350°C range, photo-CVD growth rates exceeded those obtained by pyrolysis. At 300°C, the photochemical and thermal deposition rates were >500 and ~350 Å-min$^{-1}$, respectively. Also, since the activation energy for the photo-CVD process in the 150 to ~280°C range (0.53 eV) is roughly half that for thermal deposition (0.96 eV), the difference between the photo and thermal deposition rates becomes more pronounced at lower substrate temperatures. At 150°C, the rates differ by more than an order of magnitude. Inushima et al. [122] used a low-pressure Hg lamp to obtain a deposition rate of 200 Å-min$^{-1}$ from SiH$_4$ and N$_2$O at a total pressure of 30 torr.

Scoles et al. [128] carried out similar experiments with SiH$_4$ and O$_2$ with an Hg–Xe arc lamp acting as the optical source. For substrate temperatures between 150 and 350°C, deposition rates ranging from 230 to 1140 Å-min$^{-1}$ were recorded, and the electrical and structural properties of the films (such as the dielectric constant, breakdown voltage and capacitance) were found to be comparable to those for thermally deposited films.

Several groups have also explored the D$_2$ lamp as an excitation source. Silicon dioxide films were deposited by Okuyama et al. [129] from Si$_3$H$_8$/O$_2$ mixtures at a rate of 150 Å-min$^{-1}$ at 25°C. The deposition rate declined with increasing temperature, which was attributed to desorption of an adlayer of lamp-produced radical species. Nonaka et al. [130] have reported significant increases (i.e., factors of 2–4) in the deposition rate of amorphous SiO$_2$ films when Si$_2$F$_6$ is added to the feedstock gas stream. At

200°C and an $Si_2H_6$ mass flow rate of 2.4 sccm, for example, the $SiO_2$ deposition rate rose linearly from ~140 Å-min$^{-1}$ to almost 600 Å-min$^{-1}$ when ~3.5 sccm of $Si_2F_6$ was introduced to the gas stream. Similar improvements in deposition rate (factors of two to three) were also observed at other disilane mass flow rates, and the presence of $Si_2F_6$ dramatically reduced the number of Si–OH and Si–H defects in the dielectric film.

Efforts to deposit $SiO_2$ with shorter-wavelength optical sources include the work of Baker et al. [131] with a windowless $N_2$ lamp. At 275°C, the deposition rate was 180 Å-min$^{-1}$ and the refractive index of the films was 1.46. Although the deposition process is initiated by lamp radiation, atomic nitrogen produced in the lamp also appears to play a significant role. Thin film MOS field effect transistors fabricated from such photo-CVD, amorphous $SiO_2$ films yielded a gate leakage current of 1 pA. $SiO_2$ films have also been deposited with VUV resonance radiation at 106.6 nm from a microwave-excited Ar lamp. Marks and Robertson [132] photodissociated mixtures of $NO_2$ and $SiH_4$ at 100°C (and up to 250°C) with the lamp to obtain deposition rates of 100 Å-min$^{-1}$ on Si; the resulting films exhibited refractive indices between 1.45 and 1.47.

While most $SiO_2$ deposition studies have relied on lamps as the optical source, Boyer et al. [133, 134] resorted to an ArF (193 nm) laser in parallel geometry to deposit films at rates up to 3,000 Å-min$^{-1}$. The deposition rate was insensitive to substrate temperature in the 20–600°C temperature interval but was linear in gas pressure and laser intensity. Transparent, scratch-resistant films were obtained at temperatures above 200°C, and the refractive indices ranged from 1.476 (250°C) down to 1.457 (350°C).

Oxynitrides of Si have been deposited by adding ammonia to a disilane and nitrogen dioxide ($NO_2$) gas stream. Watanabe and Hanabusa [135] showed that the $SiO_xN_y$ composition is quite sensitive to the $NO_2$ mass flow rate, which is the smallest of those for the three precursors. Deposition rates up to 120 Å-min$^{-1}$ were reported.

## C. Silicon Nitride

Although photodeposited $Si_3N_4$ has not been as thoroughly characterized as its oxide counterpart, the growth conditions for the two dielectrics are similar. Several groups [35, 136] recognized that Hg photosensitization of $SiH_4$ in the presence of $NH_3$ would yield silicon nitride films. Utilizing a process developed by Hughes Aircraft, Schuegraf [35] obtained deposition rates up to 65 Å-min$^{-1}$ in the 100–200°C temperature range with Hg impurity concentrations in the resulting films of several parts per billion. Also, the film index of refraction is adjustable between 1.8 and 2.4 by varying the gas mixture ratio. Further details regarding the deposition process parameters and film characteristics can be found in Tables II and IV.

Inushima *et al.* [122] photodeposited SiN$_x$ films by photodissociating NH$_3$ and Si$_2$H$_6$ (in the absence of Hg vapor) with the 185 nm line from an Hg resonance lamp. For substrate temperatures between 300 and 350°C, the deposition rate was 40 Å-min$^{-1}$, the hydrogen content was 20 at %, and the refraction index for the films was 2.0. Also, the deposition rate was independent of substrate temperature, and the film thickness was uniform to ±5%.

Early demonstrations of the ability of excimer laser radiation to deposit silicon nitride were carried out by Boyer *et al.* [137]. With the ArF laser beam parallel to the substrate, they obtained deposition rates up to 700 Å-min$^{-1}$, and the physical properties of the photodeposited films were found to be comparable to those of plasma CVD films, but of higher quality (particularly insofar as pinhole densities are concerned) than those of films deposited by Hg photosensitization. Weak illumination of the substrate with 254 or 193 nm photons ("surface photons") reduced the etch rate of the laser-deposited nitride films by more than a factor of five.

Obtaining stoichiometric silicon nitride (Si$_3$N$_4$) is hindered by the presence of oxygen in most of the films reported to date. Sugii *et al.* [138] have explored this by photodissociating mixtures of Si$_2$H$_6$ and NH$_3$ with an ArF laser in *perpendicular* geometry. Below 400°C, film growth is primarily photochemical, and the deposition rate is roughly constant at 50 Å-min$^{-1}$. Thermal effects become dominant at higher temperatures, and at 550°C, the deposition rate has risen to ~200 Å-min$^{-1}$. Auger electron spectroscopy reveals the composition of the photodeposited films to be Si$_3$O$_x$N$_y$, where the nitrogen content gradually declines for substrate temperatures above 200°C, with $y$ falling from ~4 at 200°C to ~3.5 at 400°C. Recently, Urisu *et al.* [139] have deposited hydrogenated silicon nitride films at 190°C with radiation from a synchrotron. Since VUV and extreme ultraviolet (XUV, $\lambda \leq 100$ nm) photons are available with this device, precursors having stronger chemical bonds (i.e., more stable) are accessible, and N$_2$, rather than ammonia, can be used as the nitrogen precursor. With a mixture composed of 0.02 torr SiH$_4$ and 0.1 torr N$_2$, deposition rates of 4 Å-min$^{-1}$ were obtained for a ring current of 100 mA.

## D. Other Oxides and Nitrides

Several other oxides have been deposited by photo-CVD. Matsui and co-workers [140] successfully deposited TaO$_x$ films from mixtures of TaCl$_5$ and O$_2$. At 500°C, the growth rate was >30 Å-min$^{-1}$ for a total reactor pressure of 1 torr. Also, TaO$_x$ deposition rates are inversely proportional to growth temperature but, without the external UV radiation, the deposition rate falls to 2 Å-min$^{-1}$ at 400°C. At 350°C, Yamagishi and Tarui

[141] deposited amorphous $TaO_x$ ($x \approx 0.2$) films at a rate of 120 Å-min$^{-1}$ by photodissociating pentamethoxy tantalum, $Ta(OCH_3)_5$, in the presence of $O_2$. X-ray analysis revealed that the nonstoichiometric films were composed of $TaO_2$ and $Ta_2O_5$.

Tin dioxide films 1,000 Å thick have been deposited from mixtures of $SnCl_4$ vapor and $N_2O$. Kunz et al. [142] irradiated fused silica substrates at room temperature and normal incidence in the presence of such a mixture, and for laser energy fluences of 10–20 mJ-cm$^{-2}$, highly conductive $SnO_2$ films resulted. Resistivities as low as $4 \times 10^{-2}$ Ω-cm were measured. At lower fluences, $SnOCl_2$ is formed and the film resistivity rises rapidly. For fluences beyond 70 mJ-cm$^{-2}$, in contrast, ablation becomes dominant and the net deposition rate vanishes. Lines of 10 μm width were also deposited by proximity printing through a mask.

Reduction of the growth temperature of TiN films and 35–300% increases in the film deposition rate were realized by Motojima and Mizutani [143] by irradiating $TiCl_4$, $NH_3$ (or $N_2$) and $H_2$ gas mixtures with a deuterium lamp. In the absence of the UV radiation, and using $N_2$ as the nitrogen donor, substrate temperatures above 800°C were required in order to observe film growth. With the lamp, however, film deposition occurred at 700°C and, at 900°C, the deposition rate, 2.1 μm-h$^{-1}$, was a factor of three larger than that observed without the UV source. Substituting $NH_3$ for $N_2$ as the N precursor enables film deposition to occur at temperatures as low as 450°C, and at 800°C, the TiN deposition rate (55 μm-h$^{-1}$) is ~35% higher than that measured without the lamp radiation. Consequently, the addition of the $D_2$ lamp to the TiN reactor permitted deposition temperatures to be reduced 50–100°C below those normally required.

## VII. CONCLUSIONS

Although photochemical vapor deposition is still in its infancy, the quality of the metal, semiconductor, and dielectric films obtainable by this technique has progressed rapidly. This is especially true of silicon dioxide, which has already been incorporated into the processing of VLSI devices. As increasing effort is invested in synthesizing new precursors that are tailored for the deposition of specific elements or compounds, it can be expected that the broad-area deposition of other dielectrics and several metals will be the next to become economically attractive. Further engineering development of new, high duty cycle lasers and lamps operating in the deep UV and near VUV, such as the new rare gas ion laser transitions and the microwave-excited rare gas halide lamp discussed in Section III.C, will undoubtedly accelerate this trend.

## ACKNOWLEDGMENTS

## REFERENCES

1. H. Romeyn, Jr., and W. A. Noyes, Jr., *J. Am. Chem. Soc.* **54**, 4143 (1932).
2. H. J. Emeléus and K. Stewart, *Trans. Faraday Soc.* **32**, 1577 (1936).
3. R. M. Osgood, Jr., *Ann. Rev. Phys. Chem.* **34**, 77 (1983).
4. R. M. Osgood, Jr., and T. F. Deutsch, *Science* **227**, 709 (1985).
5. Y. Rytz-Froidevaux, R. P. Salathé, and H. H. Gilgen, *Appl. Phys. A* **37**, 121 (1985).
6. F. A. Houle, *Appl. Phys. A* **41**, 315 (1986).
7. J. Haigh and M. R. Aylett, *Prog. Quant. Electr.* **12**, 1 (1988).
8. I. P. Herman, *Chem. Rev.* **89**, 1323 (1989).
9. D. Bäuerle, "Chemical Processing With Lasers," Vol. 1 of Springer Series in Materials Science Springer-Verlag, Berlin, 1986.
10. I. W. Boyd, "Laser Processing of Thin Films and Microstructures," Vol. 3 in Springer Series in Materials Science, Springer-Verlag, Berlin, 1987.
11. "Laser Microfabrication: Thin Film Processes and Lithography," D. J. Ehrlich and J. Y. Tsao, eds. Academic Press, New York, 1989.
12. "Laser Chemical Processing for Microelectronics," K. G. Ibbs and R. M. Osgood, Jr., eds., Cambridge, 1989.
13. V. R. McCrary and V. M. Donnelly, in "Chemical Vapor Deposition," K. F. Jensen, ed., Academic Press, New York, in press.
14. D. J. Ehrlich, R. M. Osgood, Jr., and T. F. Deutsch, *J. Vac. Sci. Technol.* **21**, 23 (1982).
15. F. A. Houle and S. D. Allen, "Laser Deposition and Etching," American Vacuum Society Education Committee—course notes.
16. U. Itoh, Y. Toyoshima, H. Onuki, N. Washida, and T. Ibuki, *J. Chem. Phys.* **85**, 4867 (1986).
17. J. Heidberg, R. Daghighi-Ruhi, H. von Weyssenhoff, and A. Habekost, *Mat. Res. Soc. Symp. Proc.* **101**, 221 (1988).
18. H. Okabe, "Photochemistry of Small Molecules," John Wiley and Sons, New York, 1978.
19. M. Rothschild in Ref. 11, pp. 163–230, and refs. cited therein.
20. Th. Beuermann and M. Stuke, *Appl. Phys. B* **49**, 145 (1989).
21. G. S. Higashi and M. L. Steigerwald, *Appl. Phys. Lett.* **54**, 81 (1989).
22. Y. Zhang and M. Stuke, *Jpn. J. Appl. Phys.* **27**, L1349 (1988).
23. Y. Zhang, Th. Beuermann, and M. Stuke, *Appl. Phys. B* **48**, 97 (1989).
24. A. R. Calloway, T. A. Galantowicz, and W. R. Fenner, *J. Vac. Sci. Technol. A* **1**, 534 (1983); A. R. Calloway and W. R. Fenner, *Aerospace Corp. Report No. ATR-84(8503)-1* (1984).
25. A. Terenin and B. Popov, *Phys. Z. Sowjetunion* **2**, 299 (1932).
26. B. Koplitz, Z. Xu, and C. Wittig, *Appl. Phys. Lett.* **52**, 860 (1988).
27. K. Kamisako, T. Imai, and Y. Tarui, *Jpn. J. Appl. Phys.* **27**, 1092 (1988).
28. C. Fuchs, E. Boch, E. Fogarassy, B. Aka, and P. Siffert, *Mat. Res. Soc. Symp. Proc.* **101**, 361 (1988).

29. M. Sasaki, Y. Kawakyu, and M. Mashita, *Jpn. J. Appl. Phys.* **28**, L131 (1989).
30. Y. Zhang and M. Stuke, *J. Cryst. Growth* **93**, 143 (1988).
31. D. J. Ehrlich, R. M. Osgood, Jr., and T. F. Deutsch, *Appl. Phys. Lett.* **38**, 946 (1981).
32. J. Y. Tsao and D. J. Ehrlich, *Appl. Phys. Lett.* **45**, 617 (1984).
33. W. L. Ahlgren, E. J. Smith, J. B. James, T. W. James, R. P. Ruth, and E. A. Patten, *J. Cryst. Growth* **86**, 198 (1988).
34. H. Zarnani, Z. Q. Yu, G. J. Collins, E. Bhattacharya, and J. I. Pankove, *Appl. Phys. Lett.* **53**, 1314 (1988).
35. K. K. Schnegraf, in "Microelectronic Manufacturing and Testing," pp. 1–4. Lake, Libertyville, March 1983.
36. R. Solanki and G. J. Collins, *Appl. Phys. Lett.* **42**, 662 (1983).
37. D. B. Geohegan and J. G. Eden, *Appl. Phys. Lett.* **45**, 1146 (1984).
38. H. Kumagai and M. Obara, *Appl. Phys. Lett.* **55**, 1583 (1989).
39. R. L. Jackson, T. H. Baum, T. T. Kodas, D. J. Ehrlich, G. W. Tyndall, and P. B. Comita, in Ref. 11.
40. M. W. Jones, L. J. Rigby, and D. Ryan, *Nature* **212**, 177 (1966).
41. T. F. Deutsch, D. J. Ehrlich, and R. M. Osgood, Jr., *Appl. Phys. Lett.* **35**, 175 (1979).
42. W. E. Johnson and L. A. Schlie, *Appl. Phys. Lett.* **40**, 798 (1982).
43. T. Cacouris, G. Scelsi, P. Shaw, R. Scarmozzino, R. M. Osgood, and R. R. Krchnavek, *Appl. Phys. Lett.* **52**, 1865 (1988).
44. R. Solanki, W. H. Ritchie, and G. J. Collins, *Appl. Phys. Lett.* **43**, 454 (1983).
45. M. Hanabusa, K. Hayakawa, A. Oikawa, and K. Maeda, *Jpn. J. Appl. Phys.* **27**, L1392 (1988).
46. M. Hanabusa, A. Oikawa, and P. Y. Cai, *J. Appl. Phys.* **66**, 3268 (1989).
47. M. R. Aylett and J. Haigh, in "Laser Diagnostics and Photochemical Processing for Semiconductor Devices," R. M. Osgood, Jr., S. R. J. Brueck, and H. R. Schlossberg, eds., *Mat. Res. Soc. Symp. Proc.*, **17**, p. 177. Elsevier, 1983.
48. Y. Rytz-Froidevaux, R. P. Salathé, and H. H. Gilgen, *Mat. Res. Soc. Symp. Proc.* **17**, 29 (1983).
49. R. Solanki, P. K. Boyer, and G. J. Collins, *Appl. Phys. Lett.* **41**, 1048 (1982) and refs. cited therein.
50. D. J. Ehrlich, R. M. Osgood, Jr., and T. F. Deutsch, *J. Electrochem. Soc.* **128**, 2039 (1981).
51. T. F. Deutsch and D. D. Rathman, *Appl. Phys. Lett.* **45**, 623 (1984).
52. H. H. Gilgen, T. Cacouris, P. S. Shaw, R. R. Krchnavek, and R. M. Osgood, Jr., *Appl. Phys. B* **42**, 55 (1987).
53. J. Y. Tsao, R. A. Becker, D. J. Ehrlich, and F. J. Leonberger, *Appl. Phys. Lett.* **42**, 559 (1983).
54. P. M. George and J .L. Beauchamp, *Thin Solid Films* **67**, L25 (1980).
55. M. S. Chiu, K. P. Shen, and Y. K. Ku, *Appl. Phys. B* **37**, 63 (1985).
56. Q. Mingxin, R. Monot, and H. van den Bergh, *Scientia Sinica* **A27**, 531 (1984).
57. J. V. Armstrong, A. A. Burk, Jr., J. M. D. Coey, and K. Moorjani, *Appl. Phys. Lett.* **50**, 1231 (1987).
58. L. V. Koplitz, D. K. Shuh, Y. -J. Chen, R. S. Williams, and J. I. Zink, *Appl. Phys. Lett.* **53**, 1705 (1988).
59. C. R. Jones, F. A. Houle, C. A. Kovac, and T. H. Baum, *Appl. Phys. Lett.* **46**, 97 (1985).
60. T. H. Baum, E. E. Marinero, and C. R. Jones, *Appl. Phys. Lett.* **49**, 1213 (1986).
61. M. R. Aylett and J. Haigh, *Extended Abstracts of Mat. Res. Soc. Symp.*, Boston, Massachusetts, 1985.

62. J. Haigh and M. R. Aylett, in Ref. 11.
63. H. Tachibana, A. Nakaue, and Y. Kawate. *Mat. Res. Soc. Symp. Proc.* **101**, 367 (1988).
64. H. Ohashi, K. Inoue, Y. Saito, A. Yoshida, H. Ogawa, and K. Shobatake. *Appl. Phys. Lett.* **55**, 1644 (1989).
65. H. Niki and G. J. Mains. *J. Phys. Chem.* **68**, 304 (1964).
66. T. Saitoh, T. Shimada, M. Migitaka, and Y. Tarui. *J. Non-Cryst. Solids* **59**, 715 (1983).
67. Y. Tarui, K. Sorimachi, K. Fujii, K. Aota, and T. Saito, *J. Non-Cryst. Solids* **59/60**, 711 (1983).
68. S. Mizukawa, K. Sato, K. Yasuhiro, M. Isawa, K. Kuroiwa, and Y. Tarui. *Jpn. J. Appl. Phys.* **28**, 961 (1989).
69. T. Inoue, M. Konagai, and K. Takahashi, *Appl. Phys. Lett.* **43**, 774 (1983).
70. S. Nishida, H. Tasaki, M. Konagai, and K. Takahashi, *J. Appl. Phys.* **58**, 1427 (1985).
71. T. Tatsuya, W. Y. Kim, M. Konagai, and K. Takahashi, *Appl. Phys. Lett.* **45**, 865 (1984).
72. S. Nishida, T. Shiimoto, A. Yamada, S. Karasawa, M. Konagai, and K. Takahashi. *Appl. Phys. Lett.* **49**, 79 (1986).
73. Y. Mishima, M. Hirose, Y. Osaka, K. Nagamine, Y. Ashida, N. Kitagawa, and K. Isogaya. *Jpn. J. Appl. Phys.* **22**, L46 (1983).
74. N. Gonohe, S. Shimizu, K. Tamagawa, T. Hayashi, and H. Yamakawa. *Jpn. J. Appl. Phys.* **26**, L1189 (1987).
75. T. Fuyuki, K. -Y. Du, S. Okamoto, S. Yasuda, T. Kimoto, M. Yoshimoto, and H. Matsunami, *J. Appl. Phys.* **64**, 2380 (1988).
76. K. Kumata, U. Itoh, Y. Toyoshima, N. Tanaka, H. Anzai, and A. Matsuda, *Appl. Phys. Lett.* **48**, 1380 (1986).
77. W. -Y. Kim, A. Shibata, Y. Kazama, M. Konagai, and K. Takahashi. *Jpn. J. Appl. Phys.* **28**, 311 (1989).
78. R. W. Andreatta, C. C. Abele, J. F. Osmundsen, J. G. Eden, D. Lubben, and J. E. Greene, *Appl. Phys. Lett.* **40**, 183 (1982).
79. A. Yoshikawa and S. Yamaga, *Jpn. J. Appl. Phys.* **24**, 1585 (1985).
80. H. Zarnani, H. Demiryont, and G. J. Collins, *J. Appl. Phys.* **60**, 2523 (1986).
81. A. Yamada, A. Satoh, M. Konagai, and K. Takahashi, *J. Appl. Phys.* **65**, 4268 (1989).
82. R. G. Frieser, *J. Electrochem. Soc.* **115**, 401 (1968).
83. A. Ishitani, Y. Oshita, K. Tanigaki, and K. Takada, *J. Appl. Phys.* **61**, 2224 (1987).
84. J. G. Eden, J. E. Greene, J. F. Osmundsen, D. Lubben, C. C. Abele, S. Gorbatkin, and H. D. Desai, *Mat. Res. Soc. Symp. Proc.* **17**, 185 (1983).
85. C. J. Kiely, V. Tavitian, and J. G. Eden, *J. Appl. Phys.* **65**, 3883 (1989).
86. C. J. Kiely, V. Tavitian, C. Jones, and J. G. Eden, *Appl. Phys. Lett.* **55**, 65 (1989).
87. D. H. Lowndes, D. B. Geohegan, D. Eres, S. J. Pennycook, D. N. Mashburn, and G. E. Jellison, Jr., *Appl. Phys. Lett.* **52**, 1868 (1988).
88. H. H. Burke, I. P. Herman, V. Tavitian, and J. G. Eden, *Appl. Phys. Lett.* **55**, 253 (1989).
89. A. E. Stanley, R. A. Johnson, J. B. Turner, and A. H. Roberts, *Appl. Spectroscopy* **40**, 374 (1986).
90. S. J. C. Irvine, in Ref. 11, pp. 503–538.
91. H. Ando, H. Inuzuka, M. Konagai, and K. Takahashi, *J. Appl. Phys.* **58**, 802 (1985).
92. Y. Fujita, S. Fujii, and T. Iuchi, *J. Vac. Sci. Technol. A* **7**, 276 (1989).
93. G. B. Shinn, P. M. Gillespie, W. L. Wilson, Jr., and W. M. Duncan, *Appl. Phys. Lett.* **54**, 2440 (1989).
94. S. J. C. Irvine, J. B. Mullin, and J. Tunnicliffe, *J. Cryst. Growth* **68**, 188 (1984).
95. W. I. Ahlgren, J. B. James, R. P. Ruth, E. A. Patten, and J. L. Staudenmann, *Mat. Res. Soc. Symp. Proc.* **90**, 405 (1987).

96. D. W. Kisker and R. D. Feldman, *Mat. Lett.* **3**, 485 (1985).
97. D. W. Kisker and R. D. Feldman, *J. Cryst. Growth* **72**, 102 (1985).
98. N. W. Cody, U. Sudarsan, and R. Solanki. *J. Mater. Res.* **3**, 1144 (1988).
99. N. W. Cody, U. Sudarsan, and R. Solanki. *J. Appl. Phys.* **66**, 449 (1989).
100. J. J. Zinck, P. D. Brewer, J. E. Jensen, G. L. Olson, and L. W. Tutt, *Appl. Phys. Lett.* **52**, 1434 (1988).
101. J. J. Zinck, P. D. Brewer, J. E. Jensen, G. L. Olson, and L. W. Tutt, *Mat. Res. Soc. Symp. Proc.* **101**, 319 (1988).
102. S. J. C. Irvine, J. B. Mullin, G. W. Blackmore, and O.D. Dosser, *J. Vac. Sci. Technol. B* **3**, 1450 (1985).
103. S. J. C. Irvine, J. B. Mullin, H. Hill, G. T. Brown, and S. J. Barnett, *J. Cryst. Growth* **86**, 188 (1988).
104. B. J. Morris. *Appl. Phys. Lett.* **48**, 867 (1986).
105. N. Pütz, H. Heinecke, E. Veuhoff, G. Arens, M. Heyen, H. Lüth. and P. Balk, *J. Cryst. Growth* **68**, 194 (1984).
106. P. Balk, M. Fischer, D. Grundmann, R. Lückerath, H. Lüth, and W. Richter, *J. Vac. Sci. Technol. B* **5**, 1453 (1987).
107. J. Nishizawa, H. Shimawaki, and Y. Sakuma, *J. Electrochem. Soc.* **133**, 2567 (1986), and refs. cited therein.
108. S. S. Chu, T. L. Chu, C. L. Chang, and H. Firouzi, *Appl. Phys. Lett.* **52**, 1243 (1988).
109. P. K. York, J. G. Eden, J. J. Coleman, G. E. Fernández, and K. J. Beernink, *Appl. Phys. Lett.* **54**, 1866 (1989).
110. T. Kachi, H. Ito, and S. Terada, *Jpn. J. Appl. Phys.* **27**, L1556 (1988).
111. D. P. Norton and P. K. Ajmera, *Appl. Phys. Lett.* **53**, 595 (1988).
112. D. P. Norton and P. K. Ajmera, *J. Electrochem. Soc.* **136**, 2371 (1989).
113. E. Tokumitsu, T. Yamada, M. Konagai, and K. Takahashi, *J. Vac. Sci. Technol. A* **7**, 706 (1989); *Mat. Res. Soc. Symp. Proc.* **101**, 307 (1988).
114. J. J. Zinck, P. D. Brewer, J. E. Jensen, G. L. Olson, and L. W. Tutt, *Mat. Res. Soc. Symp. Proc.* **75**, 233 (1987).
115. U. Sudarsan, N. W. Cody, T. Dosluoglu, and R. Solanki, *Appl. Phys. Lett.* **55**, 738 (1989).
116. U. Sudarsan, N. W. Cody, T. Dosluoglu, and R. Solanki, *Appl. Phys. A*, in press.
117. V. M. Donnelly, M. Geva, J. Long, and R. F. Karlicek, *Appl. Phys. Lett.* **44**, 951 (1984).
118. V. M. Donnelly, D. Brasen, A. Appelbaum, and M. Geva, *J. Appl. Phys.* **58**, 2022 (1985).
119. V. M. Donnelly, D. Brasen, A. Appelbaum, and M. Geva, *J. Vac. Sci. Technol. A* **4**, 716 (1986).
120. S. P. Zuhoski, K. P. Killeen, and R. M. Biefeld, *Mat. Res. Soc. Symp. Proc.* **101**, 313 (1988).
121. K. Yano, S. Tanimura, T. Ueda, and T. Fujita. 1987 Symposium on VLSI Technology, Business Center for Academic Society of Japan, Karuizawa, Japan (1987), p. 71.
122. T. Inushima, N. Hirose, K. Urata, K. Ito, and S. Yamazaki. *Appl. Phys. A* **47**, 229 (1988).
123. T. F. Deutsch, D. J. Silversmith, and R. W. Mountain. *Mat. Res. Soc. Symp. Proc.* **29**, 67 (1984).
124. M. D. Hudson, C. Trundle, and C. J. Brierley, *J. Mater. Res.* **3**, 1151 (1988).
125. R. F. Sarkozy, in *"Technical Digest of 1981 Symposium on VLSI Technology,"* p. 68. Japan Society of Applied Physics, Hawaii, 1981.
126. R. Padmanabhan, B. J. Miller, and N. C. Saha. *Mat. Res. Soc. Symp. Proc.* **101**, 385 (1988).

127. Y. Mishima, M. Hirose, Y. Osaka, and Y. Ashida, *J. Appl. Phys.* **55**, 1234 (1984).
128. K. J. Scoles, A. H. Kim, M. -H. Jiang, and B. C. Lee, *J. Vac. Sci. Technol. B* **6**, 470 (1988).
129. M. Okuyama, N. Fujiki, K. Inoue, and Y. Hamakawa, *Jpn. J. Appl. Phys.* **26**, L908 (1987).
130. H. Nonaka, K. Arai, Y. Fujino, and S. Ichimura, *J. Appl. Phys.* **64**, 4168 (1988).
131. S. D. Baker, W. I. Milne, and P. A. Robertson, *Appl. Phys. A* **46**, 243 (1988).
132. J. Marks and R. E. Robertson, *Appl. Phys. Lett.* **52**, 810 (1988).
133. P. K. Boyer, G. A. Roche, W. H. Ritchie, and G. J. Collins, *Appl. Phys. Lett.* **40**, 716 (1982).
134. P. K. Boyer, K. A. Emery, H. Zarnani, and G. J. Collins, *Appl. Phys. Lett.* **45**, 979 (1984).
135. J. Watanabe and M. Hanabusa, *J. Mater. Res.* **4**, 882 (1989).
136. J. W. Peters, in "*Technical Digest of the International Electron Devices Meeting 1981,*" p. 240, Institute of Electrical and Electronics Engineers, New York, 1981.
137. P. K. Boyer, C. A. Moore, R. Solanki, W. K. Ritchie, G. A. Roche, and G. J. Collins, *Mat. Res. Soc. Symp. Proc.* **17**, 119 (1983).
138. T. Sugii, T. Ito, and H. Ishikawa, *Appl. Phys. A* **46**, 249 (1988).
139. T. Urisu, H. Kyuragi, Y. Utsumi, J. Takahashi, and M. Kitamura, *Rev. Sci. Instrum.* **60**, 2157 (1989).
140. M. Matsui, S. Oka, K. Yamagishi, K. Kuroiwa, and Y. Tarui, *Jpn. J. Appl. Phys.* **27**, 506 (1988).
141. K. Yamagishi and Y. Tarui, *Jpn. J. Appl. Phys.* **25**, L306 (1986).
142. R. R. Kunz, M. Rothschild, and D. J. Ehrlich, *Appl. Phys. Lett.* **54**, 1631 (1989).
143. S. Motojima and H. Mizutani, *Appl. Phys. Lett.* **54**, 1104 (1989).

[54] MINIATURE, OPTICALLY PUMPED NARROW LINE SOLID STATE LASER

[75] Inventors: James G. Eden, Mahomet; Mark J. Kushner, Urbana, both of Ill.

[73] Assignee: The United States of America as represented by the Secretary of the Air Force, Washington, D.C.

[56]                    References Cited

### U.S. PATENT DOCUMENTS

| | | | |
|---|---|---|---|
| 3,573,653 | 4/1971 | Smiley | 372/7 |
| 3,573,654 | 4/1971 | Smiley | 372/7 |
| 3,579,130 | 5/1971 | Smiley | 372/7 |
| 3,579,142 | 5/1971 | Smiley | 372/7 |
| 3,747,021 | 7/1973 | Smiley | 372/7 |
| 3,967,213 | 6/197? | Yariv | 331/94.5 C |
| 4,002,998 | 1/1977 | Conwell et al. | 372/7 |
| 4,087,764 | 5/1978 | Young | 372/7 |
| 4,395,769 | 7/1983 | Damen et al. | 372/7 |
| 4,827,479 | 5/1989 | Campbell et al. | 372/5 |

Primary Examiner—Léon Scott, Jr.
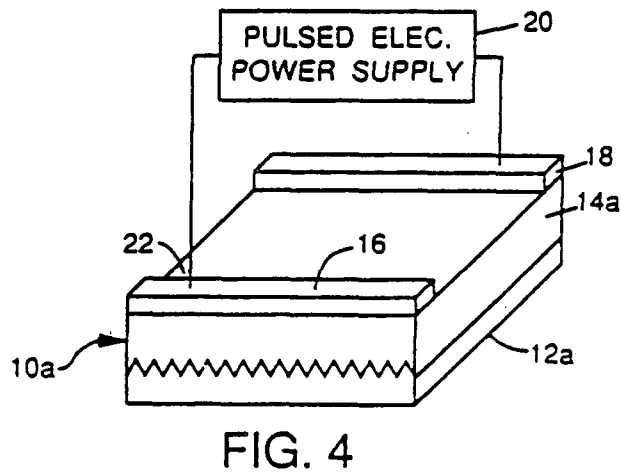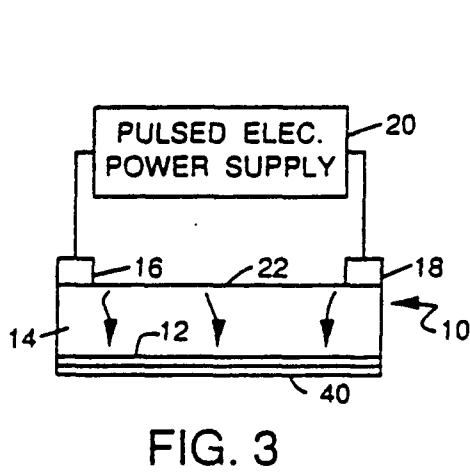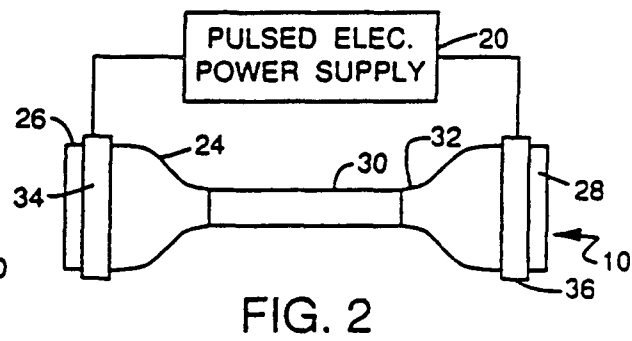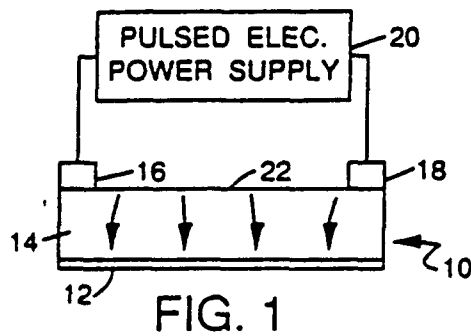
Attorney, Agent, or Firm—Irwin P. Garfinkle; Donald J. Singer

[57]                    ABSTRACT

A miniature solid state laser is optically pumped by ultraviolet radiation produced by a surface or corona discharge. The device is monolithic in that both the optical pump and the active medium are contiguous to a base material which is optically transparent in the ultraviolet range. The disclosed device consists of a substrate, a thin metal halide or crystalline or amorphous film deposited on the bottom of the substrate and a pair of spaced electrodes on the top of the substrate. When a high voltage pulse is applied across the spaced electrodes, discharge occurs between the electrodes and produces strong ultraviolet emissions which propagate through the substrate and dissociates the metal halide molecules in the film. This causes laser emission to occur on an atomic transition of the metal atom. The active laser medium may also be a crystalline platelet or amorphous thin film containing an impurity atom or molecule (an example would be YAG doped with Nd or LiYF₄(YLF) doped with cerium). In this case, the active medium may provide its own mechanical support, provides a surface on which the discharge may occur and thus eliminates the need for a separate optical substrate.

27 Claims, 1 Drawing Sheet

PULSED ELEC.
POWER SUPPLY —20

16    22         18
14        ↓ ↓ ↓ ↓      ←10
12    FIG. 1

PULSED ELEC.
POWER SUPPLY —20

26        24        32
34                30        28
                            ←10
                        36
FIG. 2

PULSED ELEC.
POWER SUPPLY —20

16    22         18
14    ↓ 12 ↓ ↓      ←10
        40
FIG. 3

PULSED ELEC.
POWER SUPPLY —20

                    18
                    14a
22        16
10a        WWWWWW        12a
FIG. 4

50
54        56
        58
52
FIG. 5

54    52    56
        58
FIG. 6

1
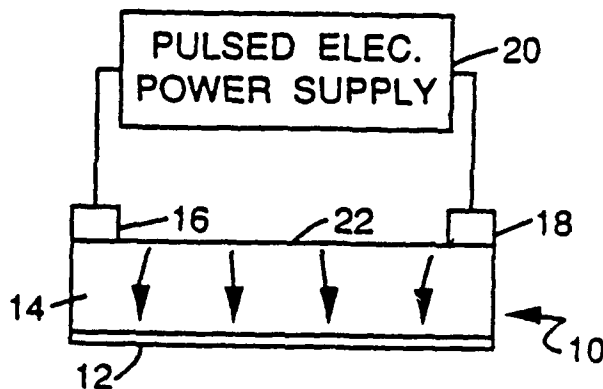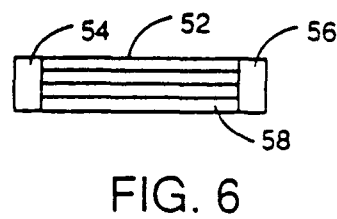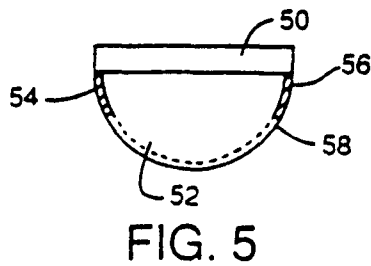
# MINIATURE, OPTICALLY PUMPED NARROW LINE SOLID STATE LASER

## STATEMENT OF GOVERNMENT INTEREST

The invention described herein may be manufactured and used by or for the Government for governmental purposes without the payment of any royalty thereon.

This invention relates to miniature solid state lasers that are optically pumped by the ultraviolet (UV) radiation emitted by a surface or corona discharge. The laser is monolithic in that both the optical pump and the active laser medium are contiguous to a "base" or substrate material that is optically transparent in the visible, ultraviolet (UV) and in some cases, at least, a portion of the vacuum ultraviolet (VUV) region.

## BACKGROUND OF THE INVENTION

The most relevant known background art is described in a paper by Schmiele, Luthy, Henchoz and Weber, entitled Miniaturization of a Thallium Iodide Photodissociation Laser, published in Applied Physics, Volume 29, pp. 201-3 in 1982. Schmiele et al. describe a miniature Thallium Iodide photodissociation gas laser in which the active medium was in the form of a thin layer on a quartz wall. An ArF excimer laser was used to pump the active medium in the vapor phase. The Schmiele et al. laser differs from the present invention in that it was pumped by another laser, (an ArF laser), and it used an active medium in the vapor phase.

A search of the patented background art revealed U.S. Pat. No. 3,573,653 issued to Smiley, U.S. Pat. No. 3,967,213 issued to Yariv, and U.S. Pat. No. 4,827,479 issued to Campbell et al.

Smiley discloses a tunable thin film laser consisting of laser material that is excited by a source which is described as comprising "an appropriate noncoherent light source such as a gas discharge device or alternatively a source of coherent excitation energy such as another laser." Conductive means are positioned on either side of the laser material and insulated therefrom, and a variable electric field is generated between the electrodes to provide tuning for the laser output. Yariv discloses an X-ray laser comprising a single crystal in the form of a thin film with an oriented set of prominent atomic planes so that when the crystal is excited by an appropriate pumping source, such as electrons, X-rays, or intense laser radiation, X-ray photons, which are emitted from the crystal, experience internal feedback from the atomic planes, thereby eliminating the need for external feedback. In addition, the crystal functions as a thin planar waveguide confining the X-ray waves therein, thereby reducing the necessary pumping power and increasing overall efficiency. Campbell et al. disclose an operational X-ray laser comprising a free thin foil which is optically pumped by a high power laser.

## SUMMARY OF THE INVENTION

The invention claimed herein is for a miniature solid state laser comprising a thin film of a metal monohalide, such as indium monoiodide or thallium monoiodide, which is deposited onto a substrate. The device is optically pumped by the optical emission from an electrical discharge sustained between two electrodes in contact with the substrate. When a pulsed voltage is applied to the electrodes, a corona discharge results which tracks along the surface and produces strong emission in the UV and VUV. The short wavelength radiation passes

2

through the substrate and photodisssociates the metal halide molecules on the film which causes laser emission to occur on a metal transition of the metal atom. For thallium, for example, this occurs at a wavelength of 535 nm (green) and in atomic indium at a wavelength of 451 nm (blue). The active laser medium may also be a crystalline platelet or film of a material, such as YAG doped with Nd, which is directly pumped by the optical emission from the discharge. In the case of a platelet, the substrate may no longer be necessary since the laser medium (platelet) now provides its own mechanical support.

## OBJECTS OF THE INVENTION

It is an object of this invention to provide a solid state miniature laser that is optically pumped by the ultraviolet radiation emitted by a surface or corona discharge.

Another object of this invention is to provide a laser in which the optical pump and the active medium are both contiguous to a base material that is optically transparent.

Still another object of this invention is to provide a monolithic, miniature laser comprising a metal halide laser material deposited as a film on one side of a transparent base material, and a pair of electrodes on the other side for producing radiation that passes through the base material to photodissociate the molecules of the laser material to produce lasing. The active laser medium may also be a thin film or platelet of solid state laser material.

## BRIEF DESCRIPTION OF THE DRAWINGS

For a more complete understanding of the objects, nature and advantages of this invention, reference should now be made to the accompanying drawings, in which:

FIG. 1 is a diagrammatic representation of one embodiment of this invention.

FIG. 2 is a diagrammatic representation of a second modification of this invention;

FIG. 3 is a diagrammatic representation of another modification of this invention;

FIG. 4 is a diagrammatic representation of yet another modification of this invention; and

FIGS. 5 and 6 are diagrammatic representations of another modification of this invention in which the substrate is formed as a lens.

## DESCRIPTION OF THE PREFERRED EMBODIMENTS

Referring to FIG. 1, a miniaturized laser 10 comprises, a thin film 12 of a metal monohalide, such as indium monoiodide or thallium moniodide or a solid state laser material such as Nd:YAG, deposited onto a substrate 14. The substrate 14 is transparent in the visible and UV regions, down to below 200 nm. On the other side of the substrate 14 are mounted two electrodes 16 and 18 across which is connected a pulsed electrical power supply 20.

When a pulsed voltage is applied to the electrodes 16 and 18, a discharge occurs through the air or prepared gas adjacent to the substrate in the space between the electrodes. This discharge tracks along the surface 22 of the substrate 14 and produces strong emission in the UV and VUV ranges. The short wavelength radiation passes through the substrate and photodissociates the metal halide molecules in the film. This causes laser

3

emission to occur on an atomic transition of the metal atom or in the solid state laser material. For thallium this occurs at a wavelength of 535 nm, and in atomic indium, at a wavelength of 451 nm.

In the embodiment of FIG. 2, a laser 10 having a circular cross-section comprises a substrate 24 which is flared at its ends 26 and 28. A monohalide film material 30 is deposited on the inner surface of a central capillary portion 32, and band electrodes 34 and 36 are mounted on the exterior of the flared ends. A source 20 of voltage pulses is connected across the electrodes. With this embodiment, the surface current flux can be small at the electrode but large at the center where the active laser medium is located. It would appear that it may also be advantageous for the active medium to be in a crystalline state, such as Nd:YAG or Ti-doped sapphire which would be optically pumped in the same fashion as the metal-halides described here.

In the FIG. 3 embodiment of the invention, the apparatus is similar to that shown in FIG. 1, and the same reference characters are used to denote the same components. The difference is that the embodiment of FIG. 3 adds a fluorescent converter 40 either between the substrate and the active laser material 12 or mounted on the exterior surface of the laser material, as shown in the FIG. 3. This fluorescent converter 40 improves laser efficiency by absorbing pump light that is not efficiently absorbed by the film 12, but converts the pump radiation wavelengths to a spectral region at which the laser medium does strongly absorb passes through it. That is, the absorbed energy in the converter 40 is re-emitted at wavelengths that are absorbed by the active layer.

The embodiment of FIG. 4 is also similar to the embodiment of FIG. 1, except that the lower surface of the substrate 14a is corrugated prior to applying the very thin layer of active material 12a. It is pointed out that because the layer of active material is very thin, the devices are compatible with integrated optics techniques. For example, with the surface of the substrate corrugated as in this embodiment, the laser can be operated in a distributed feedback mode without the need for mirrors. Therefore, it can be coupled to optical fibers or planar waveguides.

Although not illustrated in the embodiment of FIGS. 1-4, the surface on the discharge side of the substrate can be grooved to improve the reproducibility of the discharge and, hence, the operation of the device.

The embodiment illustrated in FIGS. 5 and 6 shows a modification of the basic idea, but in which the laser medium 50 is deposited on a substrate 52 formed as a lens. A pair of band electrodes 54 and 56 is attached to the substrate 52 and a pulsed electrical power supply (not shown in FIGS. 5 and 6) is connected across the bands. The curved surface of the substrate 52 is provided with a plurality of parallel grooves 58 to allow the discharge to be reproducible. The light produced by the various discharge grooves or "channels" is focused by the curved substrate to a line inside or at the surface of the active medium. This concentrated pump radiation will allow laser oscillations to be realized with less power delivered to the corona discharge.

The disclosed embodiments of this laser have a number of advantages. For one, the laser is in the solid state. It uses a metal halide in a solid form. Any amorphous crystalline or polycrystalline laser material is also acceptable. The disclosed laser system is compact and, except for the power supply, is self contained. The entire system can be constructed on a substrate only

4

approximately 1 mm in length, and thus, pulsed voltages as low as 1 to 3 KV applied across the electrodes will yield electric field strengths of 10 to 30 KV per cM. These field strengths are more than enough to generate the necessary corona or surface discharge. These voltages may be generated from compact, low voltage batteries using step up coils.

It is pointed out that the layer of active material is very thin, and therefore, the devices are compatible with integrated optics techniques. For example, the surface of the substrate can be corrugated prior to applying the metal-halide or other crystalline film, and thus, this laser can be operated in a distributed feedback mode without the need for mirrors. Also, this system can be coupled to optical fibers or planar waveguides.

Another advantage is that waveguiding can be obtained in the active region, thereby reducing threshold pumping requirements.

The wavelengths obtainable using these lasers are much shorter than those realizable with III-IV semiconductor lasers. Through the proper choice of a metal halide, obtaining laser wavelengths in the UV range are quite possible. The green and violet wavelengths mentioned earlier are considerably smaller than the current state of the art in semiconductors lasers (yellow-red). Moreover, the radiation emitted by this laser is narrow in linewidth and locked to a wavelength determined by the metal atom (or impurity ion in the crystal such as Nd in YAG or Ce in YLF). This feature is extremely valuable for communications system Which require a reproducible frequency standard as a master oscillator.

Because this invention is subject to numerous variations, adaptations and improvements, it is intended that the scope of the invention be limited only by the following claims as interpreted in the light of the prior art.

What is claimed is:

1. A miniature, optically pumped, narrow line width solid state laser comprising:
   an optically transparent substrate;
   an active laser medium comprising a film of lasing material on said substrate, said laser material comprising a thin film of a metal monohalide;
   a pair of spaced electrodes on said substrate;
   a source of short duration high voltage pulses connected across said electrodes, said pulses arcing between said electrodes and producing short wavelength light energy, said light energy passing through said transparent substrate to photodissociate molecules in said film, thereby causing laser emission to occur on a transition of the metal atom, thereby producing a narrow line width laser.

2. The invention as defined in claim 1 wherein said substrate is transparent in the vacuum ultraviolet range.

3. The invention as defined in claim 1 wherein said metal monohalide is indium monoiodide.

4. The invention as defined in claim 1 wherein said metal monohalide is thallium moniodide.

5. The invention as defined in claim 1 wherein said substrate is rectangular in cross section and wherein said active medium is on one side of said substrate and said electrodes are on the opposite side of said substrate.

6. The invention as defined in claim 5 wherein said substrate is transparent in the vacuum ultraviolet range.

7. The invention as defined in claim 4 wherein said active material is indium monoiodide.

8. The invention as defined in claim 6 wherein said active material is thallium monoiodide.

9. The invention as defined in claim 1 wherein said substrate is a capillary having flared ends and a central capillary section. and wherein said active material is deposited inside the central section. and said spaced electrodes are mounted on said flared ends.

10. The invention as defined in claim 9 wherein said substrate is transparent in the ultraviolet range.

11. The invention as defined in claim 9 wherein said substrate is transparent in the vacuum ultraviolet range.

12. The invention as defined in claim 11 wherein said active material is indium monoiodide.

13. The invention as defined in claim 11 wherein said active material is thallium monoiodide.

14. A miniature solid state laser comprising:

an optically transparent substrate;

an active medium comprising a film of lasing material on said substrate;

an optical pump for driving said lasing material, said active material being a thin film of a metal monohalide. said pump comprising a pair of spaced electrodes on said substrate and a source of short duration high voltage pulses connected across said electrodes. said pulses arcing between said electrodes, the resulting arc producing short wavelength light energy. said short wavelength light energy passing through said transparent substrate to photodissociate molecules in said film thereby causing laser emission to occur on a transition of the metal atom, thereby producing a narrow line width laser.

15. The invention as defined in claim 14 wherein said substrate is transparent in the vacuum ultraviolet range.

16. The invention as defined in claim 15 wherein said active material is indium moniodide.

17. The invention as defined in claim 15 wherein said active material is thallium moniodide.

18. The invention as defined in claim 14 wherein said substrate is rectangular in cross section and wherein said active medium is on one side of said substrate and said electrodes are on the opposite side of said substrate.

19. The invention as defined in claim 14 wherein said substrate is a capillary having flared ends and a central capillary section. and wherein said active material is deposited inside the central section. and said spaced electrodes are mounted on said flared ends.

20. The invention as defined in claim 19 wherein said substrate is transparent in the vacuum ultraviolet range.

21. The invention as defined in claim 20 wherein said active material is indium moniodide.

22. The invention as defined in claim 20 wherein said active material is thallium moniodide.

23. The invention as defined in claim 14 wherein the said substrate is corrugated on said one side. and wherein said film is deposited onto such corrugations.

24. The invention as defined in claim 14 wherein said substrate is shaped as a lens for focusing light onto said active laser medium.

25. The invention as defined in claim 24 wherein said active material is indium moniodide.

26. The invention as defined in claim 24 wherein said active material is thallium moniodide.

27. The invention as defined in claim 24 wherein the surface of said lens shaped substrate is grooved.

* * * * *

35

40

45

50

55

60

65

# THE JOURNAL

## OF

# CHEMICAL PHYSICS

## 1 JANUARY 1991

**Spectroscopic characterizations of the $^3\Sigma_g^+$ and $^3\Pi_g$ components of *nf* complexes of Ne$_2$ with *n* = 4–6**

S. B. Kim, D. J. Kane,   and J. G. Eden
*Everitt Laboratory, University of Illinois, Urbana, Illinois 61801*

Marshall L. Ginter
*Institute for Physical Science and Technology, University of Maryland, College Park, Maryland 20742*

*Published by the*

# Spectroscopic characterizations of the $^3\Sigma_g^+$ and $^3\Pi_g$ components of *nf* complexes of Ne$_2$ with *n*=4–6

S. B. Kim, D. J. Kane,[a] and J. G. Eden
*Everitt Laboratory, University of Illinois, Urbana, Illinois 61801*

Marshall L. Ginter
*Institute for Physical Science and Technology, University of Maryland, College Park, Maryland 20742*

Rotationally resolved, laser-induced fluorescence spectra for the transitions $nf$ ($^1\Sigma_g^-$, $^3\Pi_g$) $\leftarrow a\ ^3\Sigma_u^-$ ($n = 4$–6) in Ne$_2$ are presented and analyzed. The rotational structures of the upper states are found to be strongly *l*-uncoupled. Effective rotational constants for the $a\ ^3\Sigma_u^-$, $nf\sigma\ ^3\Sigma_u^-$, and $nf\pi\ ^3\Pi_g$ states with $n = 4$–6 are reported and the structures of the *nf* complexes discussed.

## I. INTRODUCTION

Until recently,[1–3] relatively little has been published concerning the spectroscopy of the excited electronic states of the Ne$_2$ molecule. Presumably, earlier experimental efforts to directly observe spectra attributable to transitions involving more than the lowest few excited states of Ne$_2$ were unsuccessful because of the difficulties encountered in detecting bound states which are coupled to open channels. In the energy region below the $X\ ^2\Sigma_u^+$ ground state of Ne$_2^+$, the intrinsically bound excited electronic states of Ne$_2$ are Rydberg states[4] while the open channels lead to dissociation.[5]

Well developed vibronic spectra involving electronic transitions between a number of Rydberg levels in Ne$_2$ have been reported previously.[1–10] However, the only published rotational analysis[3] for Ne$_2$ is for the transition tentatively assigned as $4p\pi\ ^3\Pi_g - 3s\sigma\ ^3\Sigma_u^+$ (0–0), which was observed in both the $^{20}$Ne$_2$ and $^{22}$Ne$_2$ molecules. These observations[3] confirmed the identity of the molecular carrier of an extensive body of spectra,[1,2,6] the vibrational numbering of the observed bands, and the $\Delta\Lambda$ character of the transition. Comparison of these results with theoretical calculations[7–9] and with the expected properties of similar Rydberg states in other molecules[4] implied the specific electronic state assignments indicated.

The present work deals with the analysis of rotationally resolved spectra for several bands associated with transitions from the lowest stable $^3\Sigma_u^-$ state of Ne$_2$, denoted here as the $a\ ^3\Sigma_u^-$ state, to the *l*-uncoupled[10–12] $^3\Sigma_g^-$ and $^3\Pi_g$ components of the 4*f*, 5*f*, and 6*f* complexes. Such *f* complexes are the collection of interacting electronic states of a single multiplicity from the set of four Rydberg united atom molecular orbitals $nf\sigma$, $nf\pi$, $nf\delta$, and $nf\phi$ for a specific $nl$ with $l = 3$. Besides the Ne$_2$ spectra described below, rotationally resolved spectra involving *f* complexes have been reported for He$_2$,[12] H$_2$,[13] N$_2$,[14] and NO.[15]

## II. EXPERIMENTAL TECHNIQUE AND DATA ACQUISITION

The experimental approach invoked here is similar to that of Ediger and Eden[16] in that production of electronically excited rare gas dimers in their lowest metastable state, $a\ ^3\Sigma_u^-$, is followed by dye laser excitation of the molecule. Subsequent predissociation of the highly excited Rydberg diatomic state results in $np \to 3s(n > 3)$ atomic fluorescence which is a convenient measure of the relative excimer population in the dissociating state. Consequently, high-lying rare gas dimer Rydberg states, which, because of predissociation, are inaccessible for study by conventional discharge emission spectroscopy, can now be examined by an optical pumping technique in which the spectral resolution is determined by the gas pressure, dye laser linewidth, and lifetime broadening of the upper molecular state.

Because of the energies of the Ne and Ne$_2$ excited states, however, the present experiments differ from those of Ref. 16 primarily in that Ne$_2$ metastable molecules are more conveniently formed in the afterglow of a pulsed corona or capacitive discharge as opposed to optical excitation. While adequate Kr($6p$) and, ultimately, Kr$_2$ number densities are readily produced by the two photon excitation of Kr($^1S_0$) with an untuned excimer laser, similar experiments with Ne$_2$ are hampered by the lack of intense, tunable coherent sources in the VUV.

### A. Discharge cell design and operation

A diagram of the corona discharge cell developed for these experiments is given in Fig. 1. To minimize the introduction of impurities into the discharge, the metal cathode (either a section of wire or a threaded rod) was encased in a glass tube which protruded into the gas. A stainless steel screen held in contact with the glass-sheathed cathode aided in the production of a uniform, corona-like discharge by suppressing streamer formation. The anode-to-cathode separation was set at 6 mm and all electrical feedthroughs employed standard glass-to-metal seals. Also, the anode was

---

[a] Present address: CLS-4 Division, Los Alamos National Laboratory, Los Alamos, NM 87545
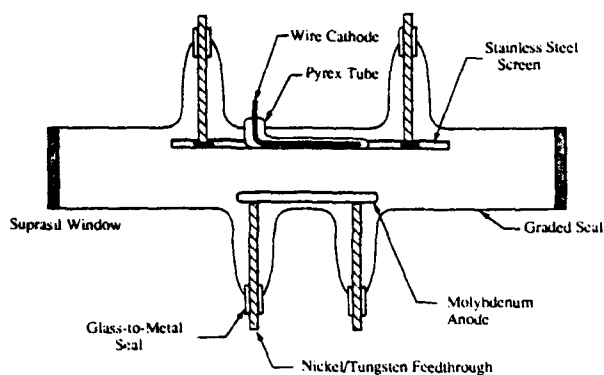
FIG. 1. Diagram of the corona discharge tube adopted in these experiments. The purpose of the stainless steel screen was to reduce charging of the surface of the glass tube enveloping the cathode and suppress streamer formation.
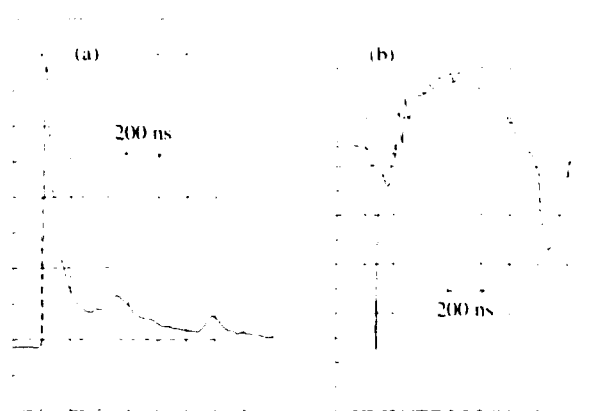


FIG. 2. Waveforms representative of those observed for: (a) the atomic Ne sidelight from the discharge cell (horizontal scale: 200 ns/div) and (b) the discharge voltage (horizontal scale: 200 ns/div and vertical sensitivity: ~5 kV/div). Note in (a) the two weak fluorescence pulses which arise from restriking of the discharge. The rise time of the dominant sidelight pulse is ~2 ns. Also, the ringing arising from the impedance mismatch between the power generator and the discharge itself is evident in (b). All waveforms were photographed for a Ne pressure of 200 Torr.

machined from molybdenum. Suprasil quartz windows were attached to each end of the discharge cell via quartz-to-Pyrex graded seals. After being evacuated to $< 5 \times 10^{-7}$ Torr with a turbomolecular vacuum system and baked at 200 °C for 3 to 4 days, each discharge cell was backfilled with isotopically enriched (99.5%, Isotec) $^{20}$Ne or $^{22}$Ne. Most of the data were acquired with 200 Torr $^{20}$Ne discharges but experiments to date have been carried out at pressures as low as 120 Torr.

The Ne discharge was driven by a grounded-grid thyratron pulser having an internal capacitance of 5 nF and operated at a charging voltage between 7 and 15 kV. For the experiments described here, the cathode was pulsed negative with respect to the grounded anode for ~150 ns (full width at half maximum, FWHM). Because little effort was expended in matching the driver impedance to that for the discharge, a small fraction ( ~5% ) of the power reflected by the low impedance discharge reignited the plasma ~1.1 μs after the initial power pulse. Both the side-light fluorescence and discharge voltage waveforms [presented in Figs. 2(a) and 2(b), respectively] show this clearly. For a charging voltage of 15 kV, the peak voltage and discharge current for the first pulse were ~15 kV and 10 A, respectively; for the second, time-delayed pulse, the peak voltage was 5 kV and the maximum current 1.5 A. Therefore, the total energy deposited in the gas was ~5 mJ, which corresponds to an increase in the instantaneous temperature in the discharge region of ~30 K.

were obtained for time delays ranging from 40 to >100 μs. $\Delta t$ was fixed at 60 μs for most of the spectra reported here.

Dye laser pulse energies, typically chosen to be between 1 and 2 mJ, were measured by a Gen-Tec pyroelectric detector and maintained to within ±10% of a specified value throughout a scan by varying the time delay for the Nd:YAG laser's Q switch. After doubling the red fundamental in a potassium dihydrogen phosphate crystal, the harmonics were separated from the fundamental by a sequence of four Pellin–Brocca prisms. Survey spectra were recorded with a dye laser linewidth of ~0.2 cm$^{-1}$ whereas the installation of an intracavity etalon (FSR = 1 cm$^{-1}$) in the dye laser reduced the linewidth to ~0.04 cm$^{-1}$ for higher resolution scans. The linewidth of the laser radiation was monitored on a continuous basis with a solid etalon and a Si pin photodiode. Wavelength calibration of the excitation spectra was accomplished by optogalvanic spectroscopy using U/He or Ne hollow cathode lamps. Line positions were determined to within ±0.1 cm$^{-1}$ for the data presented below.
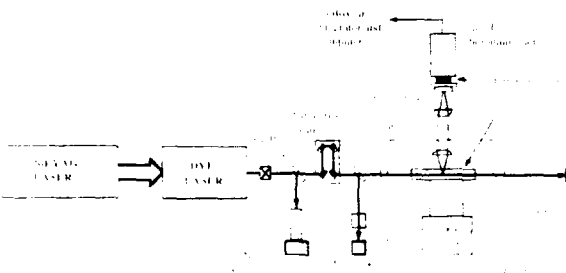
## B. Apparatus and data acquisition

A schematic diagram of the experimental arrangement is given in Fig. 3. At an adjustable delay time ( $\Delta t$ ) following the production of Ne metastable molecules in the pulsed discharge, the beam from a frequency-doubled, Nd:YAG-pumped dye laser ( Lambda Physik FL2002 ) was propagated along the axis of the discharge cell. For convenience, $\Delta t = 0$ is defined as the time at which peak current occurs in the second pulse through the discharge cell. Although data



FIG. 3. Partial schematic diagram of the experimental apparatus ( optical train for obtaining laser excitation spectra of Ne ).
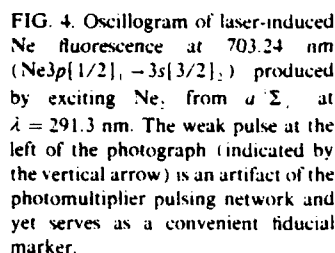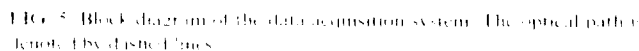
FIG. 4. Oscillogram of laser-induced Ne fluorescence at 703.24 nm ($Ne3p[1/2]_1 - 3s[3/2]_2$) produced by exciting Ne₂ from $a^3\Sigma$ at $\lambda = 291.3$ nm. The weak pulse at the left of the photograph (indicated by the vertical arrow) is an artifact of the photomultiplier pulsing network and yet serves as a convenient fiducial marker.

Dye laser-induced Ne atomic fluorescence was collected at 90° to the discharge tube axis with three plano-convex lenses and detected by a cooled photomultiplier. Spatial filtering further defined the region of the discharge under observation and a dielectric interference filter selected a particular $3p$ or $4p \to 3s$ transition for study. Most of the experiments to date have monitored the $3p[1/2]_1 \to 3s[3/2]_2$ transition at 703.24 nm. In order to avoid saturating the photomultiplier with the intense visible fluorescence produced by the active discharge, the photomultiplier bias was kept at a low value during the two discharge pulses and pulsed "on" $\sim 7\,\mu s$ prior to the arrival of the dye laser beam. Ten microseconds later, the bias voltage was returned to its lower ("off") value. A representative laser-induced fluorescence waveform for Ne₂, obtained for $\lambda_{ex} = 291.3$ nm, is shown in Fig. 4.

Data acquisition essentially consisted of sampling the photomultiplier signal immediately prior to and during the dye laser pulse with two boxcar integrators having gate widths of 20 ns (cf. Fig. 5). The difference in signal amplitude was stored by a DEC LSI 11/73 computer which also controlled the frequency doubling crystal, the scanning etalon, and the dye laser grating. A minimum of ten pulses were accumulated at each dye laser wavelength. For higher resolution studies, the laser wavelength was stepped in $8 \cdot 10^{-3}$ cm⁻¹ increments (i.e., 20% of the dye laser's linewidth) while survey spectra were recorded in steps 4 times larger. Software written for these experiments controlled all phases of the data acquisition process. Fluorescence data obtained with probe (dye) laser energies lying more than $\pm 10\%$ from a preset value, for example, were automatically rejected. Also, the relative intensity data were averaged and checked for consistency by comparing each datum to 3.5 times the standard deviation of the 10 point set acquired at each dye laser wavelength. Points falling more than $3.5\sigma$ from the average value were deemed to be unacceptable and the process was repeated until the criterion was satisfied for each datum at each dye laser wavelength. Further details regarding the experimental techniques and data analysis procedures can be found in Ref. 6.

## III. RESULTS

A low resolution ($\Delta\bar{\nu} \simeq 2$ cm⁻¹) scan of the 352–369 nm region of the Ne₂ excitation spectrum, acquired in 200 Torr of ²⁰Ne, is presented in Fig. 6. Although the entire spectrum of the molecule from $\sim 282$ to 450 nm will be discussed in detail elsewhere, it should be noted that the dominant bandhead in Fig. 6 ($\lambda \sim 356$ nm) appears to be associated[1,6] with transitions to the ¹Π component of the third member of the $np\pi$ Rydberg series.[1,6] The second member of this series, which lies at $\sim 425$ nm, was reported previously.[1] Efforts to rotationally resolve the peaks near 356 nm have thus far proven unsuccessful, presumably due to lifetime broadening. However, several other weaker bands in Fig. 6 clearly exhibit resolved rotational structure.

The spectroscopic data reported in this section were obtained by analyzing rotationally resolved bands for transitions from vibrational levels $v''$ in the $a^3\Sigma_u^+$ state to vibrational levels $v'$ in excited electronic states believed (see below) to be the $^3\Sigma_g^+$ and $^3\Pi_g$ components of the manifolds of states associated with $nf$ Rydberg orbitals. The (0–0) and (1–0) bands [where $(v' - v'')$] of the $4f$ member of this series appear in Fig. 6. Figures 7 and 8 provide expanded and higher resolution ($\sim 0.1$ cm⁻¹) views of the 27 260–27 520 cm⁻¹ region which contains the $4f(^3\Sigma_g^+, ^3\Pi_g) \leftarrow a^3\Sigma_u^+$ (0–0) bands.

To date, triplet splitting has not been resolved in Ne₂ spectra, a situation similar to electronic spectra observed in He₂ where such splittings were observed[12,17,18] to be negligible in most cases. Because the nuclear spins are zero in ²⁰Ne₂, only alternate branch lines can occur in $\Sigma_g^+ - \Sigma_u^+$ and $\Pi_g - \Sigma_u^+$ type transitions. Thus, each band of Ne₂ associated with transitions of $^3\Sigma_g^+ - ^3\Sigma_u^+$ type will consist of one $R(N)$ and one $P(N)$ branch only with odd $N$ values, $N$ being the quantum number for total angular momentum excluding spin. Transitions of $^3\Pi_g - ^3\Sigma_u^+$ type will have three branches which can be divided into two groups: one $R(N)$ and one $P(N)$ branch with $N$ odd for $^3\Pi_g - ^3\Sigma_u^+$ and one $Q(N)$ branch with $N$ odd for $^3\Pi_g - ^3\Sigma_u^+$. The $^3\Pi_g^-$ and $^3\Pi_g^+$ states are reflection symmetry eigenstates which are called $\Lambda$ doublets when their energy splittings are small. When $\Lambda$ doubling becomes large, the same phenomenon is referred to as $l$ uncoupling.[1]



FIG. 5. Block diagram of the data acquisition system. The optical path lengths (by dashed lines).
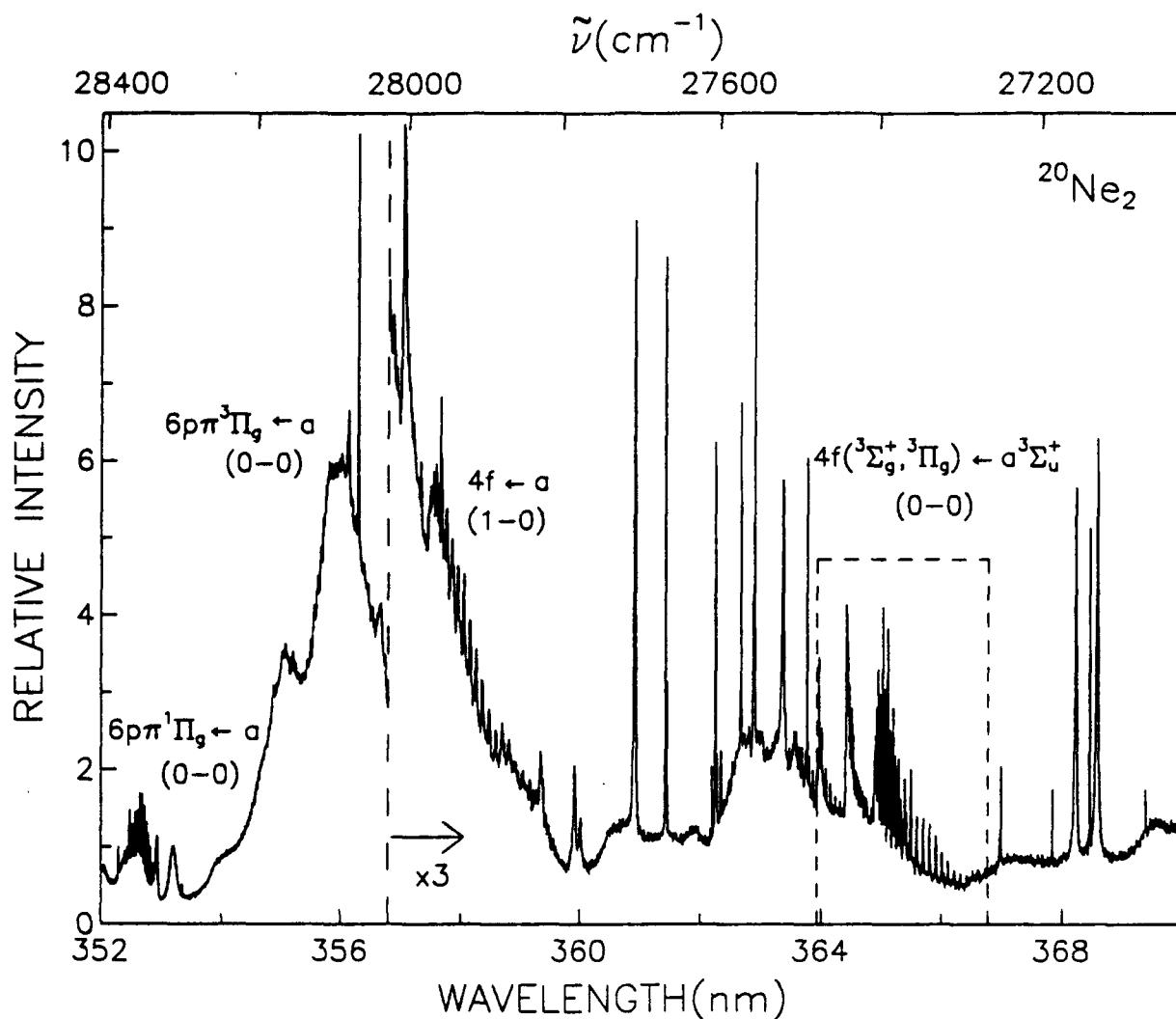
$\tilde{\nu}(\mathrm{cm}^{-1})$



FIG. 6. Portion of the Ne$_2$ $a\,{}^3\Sigma_u^+$ laser excitation spectrum observed for 352 ≤ λ ≤ 369 nm. In acquiring these data, the laser linewidth was 0.2 cm$^{-1}$, $p_{Ne}$ = 200 Torr (300 K), and $\Delta t$ = 60 μs. The spectral region enclosed by the dashed rectangle, which contains the 4f ← a(0–0) transitions, is illustrated in greater detail in Figs. 7 and 8. Note that the λ ≤ 357 nm region has been magnified by a factor of 3 for convenience.
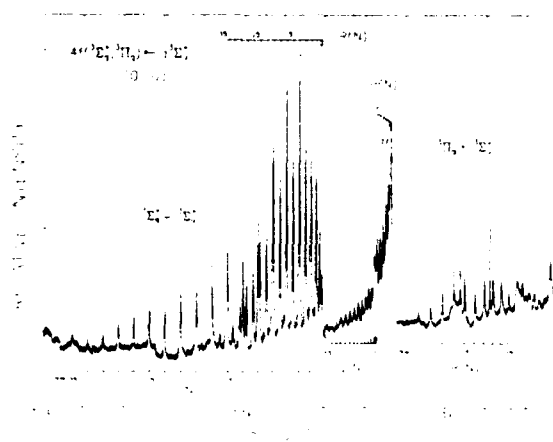


FIG. 7. Laser excitation spectrum for Ne$_2$ $a\,{}^3\Sigma_u^+$ in the 27 260–27 520 cm$^{-1}$ region obtained with a laser linewidth of 0.3 cm$^{-1}$ and $p_{Ne}$ = 200 Torr. Branch assignments for the 4f $\Sigma_g^+$, $\Pi_g$ ← a$\,{}^3\Sigma_u^+$ (0–0) bands are included.
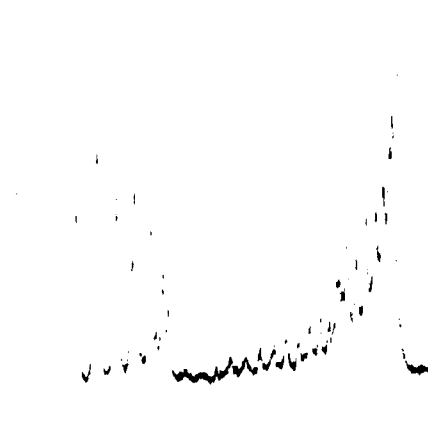
FIG. 8. Expanded view of the 27 350 to 27 440 cm$^{-1}$ interval showing details of the 4f $\Pi_g$ ← a$\,{}^3\Sigma_u^+$ (0–0) transitions as well as a portion of the 4f $\Sigma_g^+$ ← a$\,{}^3\Sigma_u^+$ (0–0) band.

Line positions. in cm⁻¹ vacuum. of the (0–0) bands of the $nf(^1\Sigma_g^+, ^1\Pi_g) - a\,^3\Sigma_u^+$ transitions for $n = 4$–6 appear in Tables I–III. respectively. while typical high resolution spectra of these bands appear in Figs. 7 through 10. Also included in Table I are the line positions of the $4f(^1\Sigma_g^+, ^1\Pi_g) - a\,^3\Sigma_u^+$ (1–0) bands. Portions of (1–0) bands associated with the 5f and 6f–a transitions and the (0–0) bands associated with the 7f–a transitions also were observed. but the current data on these bands were considered too fragmentary for inclusion here.

Band origins and *effective* rotational constants (i.e.. rotational constants not corrected for *l* uncoupling or other perturbations) were determined from the data in Tables I–III using least-squares-fitting procedures and the power series relations:[19]

**TABLE I.** Line positions (in cm⁻¹ vac) of the $4f(^1\Sigma_g^+, ^1\Pi_g) - a\,^3\Sigma_u^+$ ($v' - v''$) transitions in ²⁰Ne₂.

| | $4f\sigma\,^1\Sigma_g^+ - a\,^3\Sigma_u^+$ (0–0) | | $4f\pi\,^1\Pi_g - a\,^3\Sigma_u^+$ (0–0) | | |
|---|---|---|---|---|---|
| *N* | *R(N)* | *P(N)* | *R(N)* | *Q(N)*[a] | *P(N)* |
| 1 | 27 398.73 | 27 396.85 | | | |
| 3 | 27 397.85 | 27 393.07 | | | |
| 5 | 27 396.02 | (27 387.74) | | (27 426.01) | |
| 7 | 27 393.53 | 27 381.35 | 27 446.66 | 27 425.37 | (27 426.01) |
| 9 | 27 390.71 | 27 374.43 | 27 452.54 | 27 424.49 | 27 427.43 |
| 11 | (27 387.74) | 27 367.10 | 27 458.53 | 27 423.41 | 27 428.92 |
| 13 | 27 384.56 | 27 359.62 | 27 464.18 | 27 422.05 | 27 430.31 |
| 15 | 27 381.35 | (27 352.00) | 27 469.54 | 27 420.49 | (27 431.49) |
| 17 | 27 378.09 | 27 344.26 | 27 474.54 | 27 418.78 | (27 432.51) |
| 19 | 27 374.65* | 27 336.45 | 27 479.24 | 27 416.82 | (27 432.86) |
| 21 | 27 371.44 | 27 328.69 | 27 483.64 | 27 414.91 | (27 432.86) |
| 23 | 27 368.11 | 27 320.88 | 27 487.56 | 27 412.82 | (27 432.86) |
| 25 | 27 364.76 | 27 313.18 | 27 491.35 | 27 410.54 | (27 432.51) |
| 27 | 27 361.41 | 27 305.30 | | 27 408.30 | (27 431.49) |
| 29 | 27 358.19 | 27 297.58 | | 27 406.18 | |
| 31 | 27 354.87 | 27 289.97 | | 27 403.86 | |
| 33 | (27 352.00) | 27 282.23 | | 27 401.1 | |
| 35 | 27 348.38 | 27 274.45 | | | |

| | $4f\sigma\,^1\Sigma_g^+ - a\,^3\Sigma_u^+$ (1–0) | | $4f\pi\,^1\Pi_g - a\,^3\Sigma_u^+$ (1–0) | | |
|---|---|---|---|---|---|
| *N* | *R(N)* | *P(N)* | *R(N)* | *Q(N)*[a] | *P(N)* |
| 1 | | | | | |
| 3 | | | 28 006.9 | broad | |
| 5 | | (27 956.62) | 28 012.9 | peak | (27 997.1) |
| 7 | (27 962.29) | 27 950.84 | 28 018.1 | 27 999.3 | (27 998.1) |
| 9 | 27 959.70 | 27 942.96 | 28 023.7 | | (27 999.3) |
| 11 | (27 956.62) | 27 936.07 | 28 028.0 | | (27 999.3) |
| 13 | 27 952.80 | 27 928.07 | 28 034.0 | | (27 999.3) |
| 15 | 27 949.36 | 27 919.96 | 28 040.4 | | (27 999.3) |
| 17 | 27 945.80 | 27 912.10 | 28 046.1 | | |
| 19 | 27 942.10 | 27 904.49 | 28 051.2 | | |
| 21 | 27 937.91 | 27 896.15 | | | |
| 23 | 27 933.80 | 27 887.57 | | | |
| 25 | 27 929.67 | 27 878.89 | | | |
| 27 | 27 925.12 | 27 870.17 | | | |
| 29 | 27 919.96 | 27 860.99 | | | |

Parentheses and an asterisk denote a blended line and a shoulder feature. respectively
The *N* numbering of this branch has been chosen to make its origin match the origin observed for the Π component
Weak transition poorly resolved near heads.
This *Q(N)* branch is blended with a broad peak which includes lines from the collapsed *P(N)* head.

**TABLE II.** Line positions (in cm⁻¹ vac) of the $5f(^1\Sigma_g^+, ^1\Pi_g) - a\,^3\Sigma_u^+$ (0–0) transitions in ²⁰Ne₂.

| | $5f\sigma\,^1\Sigma_g^+ - a\,^3\Sigma_u^+$ | | $5f\pi\,^1\Pi_g - a\,^3\Sigma_u^+$ | | |
|---|---|---|---|---|---|
| *N* | *R(N)* | *P(N)* | *R(N)* | *Q(N)*[a] | *P(N)* |
| 1 | 29 937.58 | (29 935.13) | | | |
| 3 | (29 935.13) | (29 932.21) | 29 963.76 | (29 955.67) | |
| 5 | (29 932.21) | (29 925.53) | 29 969.45 | (29 954.73) | (29 953.41) |
| 7 | 29 929.02 | 29 917.60 | 29 974.83 | (29 953.41) | (29 955.02) |
| 9 | (29 925.53) | 29 910.20* | 29 979.55 | (29 952.57) | (29 955.67) |
| 11 | 29 922.05 | 29 902.02 | 29 983.71 | (29 950.58) | (29 955.67) |
| 13 | (29 918.38) | (29 893.85) | 29 987.01 | (29 948.32) | (29 955.67) |
| 15 | 29 914.80 | (29 885.78) | 29 989.76 | (29 945.68) | (29 954.73) |
| 17 | 29 911.14 | 29 877.80 | 29 992.30 | 29 942.76 | (29 952.57) |
| 19 | 29 907.47 | 29 869.54 | 29 993.92 | 29 939.94 | (29 950.58) |
| 21 | 29 903.80 | 29 861.29 | 29 996.18 | 29 937.11* | (29 948.32) |
| 23 | 29 900.43 | 29 853.24 | 29 998.46 | | (29 945.68) |
| 25 | 29 896.57 | 29 845.10 | | | |
| 27 | (29 893.85) | 29 837.05 | | | |
| 29 | 29 889.53 | 29 829.20 | | | |
| 31 | (29 885.78) | 29 821.05 | | | |
| 33 | 29 883.05 | 29 813.58 | | | |
| 35 | 29 879.77 | 29 805.74 | | | |

Parentheses and an asterisk denote a blended line and a shoulder feature. respectively
The *N* numbering of this branch has been chosen to make its origin match the origin observed for the Π component.

$$\Delta_v F(N) = \sum_i a_i (N + 1/2)^{2i-1}, \tag{1}$$

$$Q(N) = \sum_i b_i [N(N+1)]^i, \tag{2}$$

and

$$R(N) + P(N) = \sum_i c_i [N(N+1)]^i. \tag{3}$$

**TABLE III.** Line positions (in cm⁻¹ vac) of the $6f(^1\Sigma_g^+, ^1\Pi_g) - a\,^3\Sigma_u^+$ (0–0) transitions in ²⁰Ne₂.

| | $6f\sigma\,^1\Sigma_g^+ - a\,^3\Sigma_u^+$ | | $6f\pi\,^1\Pi_g - a\,^3\Sigma_u^+$ | | |
|---|---|---|---|---|---|
| *N* | *R(N)* | *P(N)* | *R(N)* | *Q(N)*[a] | *P(N)* |
| 1 | 31 311.92 | | 31 328.25 | 31 324.67 | |
| 3 | 31 308.94 | 31 306.36 | 31 333.53 | 31 324.25 | (31 322.18) |
| 5 | 31 305.51 | 31 298.78 | 31 338.01 | (31 323.47) | (31 323.47) |
| 7 | 31 301.63 | 31 290.93 | 31 341.62 | (31 322.18) | (31 323.47) |
| 9 | 31 297.88 | (31 282.46) | 31 343.84 | (31 319.87) | (31 322.18) |
| 11 | 31 294.01 | 31 274.39 | 31 345.91 | (31 317.33) | (31 319.87) |
| 13 | 31 290.00 | 31 265.86 | | (31 314.30) | (31 317.33) |
| 15 | 31 286.05 | 31 257.34 | | 31 311.16 | |
| 17 | (31 282.46) | 31 249.03 | | 31 307.80 | |
| 19 | 31 278.70 | 31 240.70 | | 31 304.70* | |
| 21 | 31 274.68 | 31 232.70 | | | |
| 23 | 31 271.00 | 31 223.96 | | | |
| 25 | 31 267.09 | 31 215.68 | | | |
| 27 | 31 263.80 | 31 207.75 | | | |
| 29 | 31 260.72 | 31 199.61 | | | |
| 31 | 31 256.9 | 31 192.2 | | | |

Parentheses and an asterisk denote a blended line and a shoulder feature. respectively
The *N* numbering of this branch has been chosen to make its origin match the origin observed for the Π component
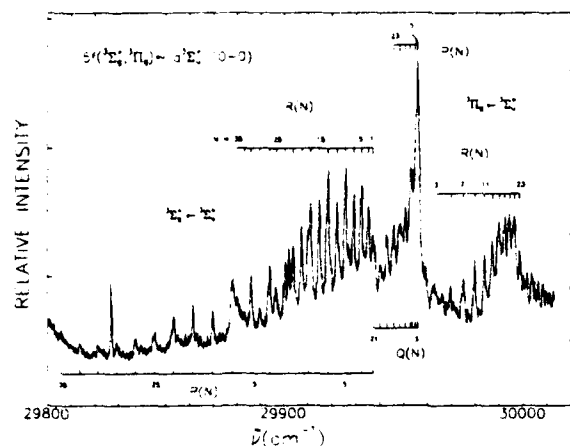
FIG. 9. Laser-induced fluorescence spectrum in the near ultraviolet illustrating the rotational branches of the $5f(^1\Sigma_g, ^1\Pi_g) - a\,^3\Sigma_u^+$ (0–0) transitions in $^{20}$Ne.
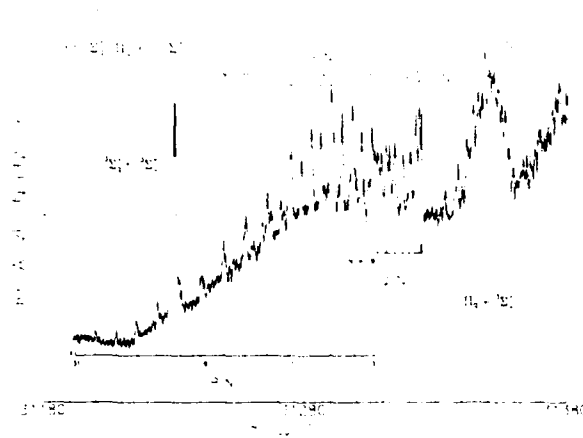
FIG. 10. Spectral region between 31 180 and 31 380 cm$^{-1}$ showing branch assignments for $6f(^1\Sigma_g, ^1\Pi_g) - a\,^3\Sigma_u^+$ (0–0) transitions of $^{20}$Ne. Experimental conditions are the same as those for Figs. 7–9.

The coefficients of $f(N)$ in Eqs. (1)–(3) contain the effective rotational constants, and several orders (several values of $i$) were equally satisfactory in reproducing the data being fitted. Through $i = 2$ one has:[19] $a_0 = 4B - 6D + ...$, $a_1 = -8D + 34H + \cdots$, $a_2 = 12H + \cdots$, $b_0 = v(v' - v'')$, $b_1 = B' - B'' - 6D + \cdots$, $b_2 = D' - D''$, $c_0 = 2(v_0 + B' - 2D' + \cdots)$, $c_1 = 2(B' - B'' - 6D + \cdots)$, and $c_2 = 2(D' - D'' + \cdots)$, with higher-order constants available[19] when needed. $\Delta_2 F'(N) = R(N) - P(N)$ values are used in (1) to obtain the upper state constants $B'$, $D'$, etc., while $\Delta_2 F''(N) = R(N-1) - P(N+1)$ values are used to determine the lower state (double primed) constants. The $v(v' - v'')$ value in Eqs. (2) and (3) is the band origin, which is the energy difference between the $N' = 0, v'$ and $N'' = 0, v''$ levels. For the $^1\Pi_g$ and $a\,^3\Sigma_u$ states, the $N = 0$ level does not exist and the $v(v' - v'')$ values are extrapolations.

The rotational energies for the $v = 0$ level of the $a\,^3\Sigma_u$ state were calculated from a best set of $\Delta_2 F''$ values determined by averaging data from Refs. 3 and 6 and Tables I–III. These energy levels were combined with the branch data in the Tables to calculate upper state energies for each spectral transition. These spectrally determined values were averaged to produce best sets of energy levels for the $nf(^1\Sigma_g, ^1\Pi_g)$ states with $n = 4$–6. For each state, the resulting energy levels, $F_i(N)$, were fitted to the expression[19]

$$F_i(N) = \sum_{i_0} C_{i_0} [N(N+1)]^i, \tag{4}$$

where $C_0$ represents the energy of the $N = 0$ level (real or hypothetical) above the zero chosen for the $F$ energies (the $N = 0, v = 0$ level of $a\,^3\Sigma_u$ in the present case). $C_1 = B_i$, $C_2 = -D_i$, and $C_3 = H_i$.

The results obtained from Eqs. (1)–(4) were averaged (see below) to produce the effective molecular parameters reported in Table IV. Energy levels (term energies) for the $a\,^3\Sigma_u$, $4f(^1\Sigma_g, ^1\Pi_g)$, $5f(^1\Sigma_g, ^1\Pi_g)$, and $6f(^1\Sigma_g, ^1\Pi_g)$ states are summarized in Table V.

TABLE IV. Effective molecular constants in cm$^{-1}$.

| State | $v$ level | $B$ | $D \cdot 10^6$ | $H \cdot 10^{10}$ | $F_i(0)$ |
|---|---|---|---|---|---|
| $a\,^3\Sigma$ | 0 | 0.5626 ± 0.0006 | 0.892 ± 0.06 | 0.34 ± 0.2 | 0.00 |
| $4f\,^1\Sigma$ | 0 | 0.405 ± 0.030 | 147 ± 130 | 65 ± 50 | 27 397.2 ± 0.8 |
| $4f\,^1\Sigma$ | 1 | 0.379 ± 0.030 | 280 ± 200 | 300 ± 230 | 27 965.6 ± 0.5 |
| $4f\,^1\Pi$ | 0 | 0.710 ± 0.030 | 296 ± 140 | 250 ± 200 | 27 428.0 ± 1.0 |
| $4f\,^1\Pi$ | 1 | 0.680 ± 0.080 | 180 ± 140 | 130 ± 120 | 28 000.0 ± 1.2 |
| $4f\,^1\Pi$ | 0 | 0.535 ± 0.004 | 2.6 ± 1.5 | | 27 426.8 ± 0.5 |
| $5f\,^1\Sigma$ | 0 | 0.370 ± 0.030 | 250 ± 100 | 250 ± 100 | 29 935.0 ± 1.0 |
| $5f\,^1\Pi$ | 0 | 0.713 ± 0.040 | 490 ± 300 | 510 ± 400 | 29 956.3 ± 0.8 |
| $5f\,^1\Pi$ | 0 | 0.519 ± 0.005 | 7.7 ± 2.5 | | 29 956.2 ± 0.8 |
| $6f\,^1\Sigma$ | 0 | 0.311 ± 0.050 | 500 ± 500 | 580 ± 400 | 31 309.5 ± 1.0 |
| $6f\,^1\Pi$ | 0 | 0.803 ± 0.100 | 700 ± 250 | 3000 ± 7500 | 31 324.8 ± 1.0 |
| $6f\,^1\Pi$ | 0 | 0.503 ± 0.008 | 7.0 ± 3.0 | | 31 325.0 ± 0.5 |

The uncertainties estimated are maximum deviations from the average values of the constants obtained from various fitting procedures, and are large for $\pi$-uncoupled states because of slow convergence of the usual power series relations (see text).

Energy of the $N = 0$ level (real or hypothetical) for the state (see text).

TABLE V. Level energies (cm⁻¹) of the $a\,^3\Sigma$ and $n/\lambda(\,^1\Sigma,\,^1\Pi\,)$ states with $n = 4, 5,$ and 6.[a]

| $N$ | $a\,^3\Sigma$ $(v=0)$ | $4/\pi\,^1\Pi$ $(v=0)$ | $5/\pi\,^1\Pi$ $(v=0)$ | $6/\pi\,^1\Pi$ $(v=0)$ |
|---|---|---|---|---|
| 1 | 1.12 | | | 31 325.79 |
| 3 | 6.74 | | 29 962.41 | 31 330.99 |
| 5 | 16.85 | 27 442.86 | 29 971.58 | 31 340.32 |
| 7 | 31.49 | 27 456.86 | 29 984.90 | 31 353.67 |
| 9 | 50.63 | 27 475.12 | 30 003.20 | 31 370.50 |
| 11 | 74.23 | 27 497.64 | 30 024.81 | 31 391.56 |
| 13 | 102.38 | 27 524.43 | 30 050.70 | 31 416.68 |
| 15 | 135.01 | 27 555.50 | 30 080.69 | 31 446.17 |
| 17 | 172.07 | 27 590.85 | 30 114.83 | 31 479.87 |
| 19 | 213.69 | 27 630.51 | 30 153.63 | 31 518.39 |
| 21 | 259.78 | 27 674.69 | 30 196.39 | |
| 23 | 310.36 | 27 723.18 | | |
| 25 | 365.36 | 27 775.90 | | |
| 27 | 424.80 | 27 833.10 | | |
| 29 | 488.63 | 27 894.81 | | |
| 31 | 556.85 | 27 960.71 | | |
| 33 | 629.49 | 28 030.59 | | |

| $N$ | $4/\sigma\,^1\Sigma$ $(v=0)$ | $4/\pi\,^1\Pi$ $(v=0)$ | $5/\sigma\,^1\Sigma$ $(v=0)$ | $5/\pi\,^1\Pi$ $(v=0)$ |
|---|---|---|---|---|
| 0 | 27 397.97 | | 29 936.25 | |
| 2 | 27 399.83 | | 29 938.70 | |
| 4 | 27 404.59 | | 29 942.07 | 29 970.50 |
| 6 | 27 412.86 | 27 457.50 | 29 949.07 | 29 986.30 |
| 8 | 27 425.04 | 27 478.11 | 29 960.20 | 30 006.32 |
| 10 | 27 441.34 | 27 503.16 | 29 976.20 | 30 030.18 |
| 12 | 27 462.00 | 27 532.73 | 29 996.28 | 30 057.94 |
| 14 | 27 486.94 | 27 566.56 | 30 020.77 | 30 089.39 |
| 16 | 27 516.34 | 27 604.55 | 30 049.84 | 30 124.77 |
| 18 | 27 550.15 | 27 646.61 | 30 083.22 | 30 164.37 |
| 20 | 27 588.47 | 27 692.93 | 30 121.11 | 30 207.61 |
| 22 | 27 631.23 | 27 743.42 | 30 163.58 | 30 255.96 |
| 24 | 27 678.50 | 27 797.92 | 30 210.62 | 30 308.82 |
| 26 | 27 730.11 | 27 856.71 | 30 261.89 | |
| 28 | 27 786.21 | | 30 317.83 | |
| 30 | 27 846.82 | | 30 378.02 | |
| 32 | 27 911.72 | | 30 443.07 | |
| 34 | 27 981.25 | | 30 512.54 | |
| 36 | 28 055.18 | | 30 586.57 | |

| $N$ | $6/\sigma\,^1\Sigma$ $(v=0)$ | $6/\pi\,^1\Pi$ $(v=0)$ | $4/\sigma\,^1\Sigma$ $(v=1)$ | $4/\pi\,^1\Pi$ $(v=1)$ |
|---|---|---|---|---|
| 0 | | | | |
| 2 | 31 313.07 | 31 329.37 | | |
| 4 | 31 315.65 | 31 340.27 | 27 973.47 | 28 013.6 |
| 6 | 31 322.39 | 31 354.86 | 27 982.33 | 28 029.7 |
| 8 | 31 333.12 | 31 373.11 | 27 993.59 | 28 049.6 |
| 10 | 31 348.56 | 31 394.47 | 28 010.32 | 28 074.3 |
| 12 | 31 368.24 | 31 420.14 | 28 030.45 | 28 102.2 |
| 14 | 31 392.37 | | 28 055.07 | 28 136.4 |
| 16 | 31 421.08 | | 28 084.27 | 28 175.4 |
| 18 | 31 454.39 | | 28 118.03 | 28 218.2 |
| 20 | 31 492.44 | | 28 155.86 | 28 264.2 |
| 22 | 31 534.50 | | 28 197.81 | |
| 24 | 31 581.20 | | 28 244.21 | |
| 26 | 31 632.50 | | 28 295.00 | |
| 28 | 31 688.42 | | 28 349.77 | |
| 30 | 31 748.64 | | 28 408.59 | |
| 32 | 31 813.7 | | | |

[a] Based on $N$' = 0 for $a\,^3\Sigma$.

The large uncertainties listed for the parameters in Table IV represent the range of values obtained for these parameters from fitting the data to within experimental uncertainties using the different polynomial expressions presented above. When applying the method of least squares to polynomials such as Eqs. (1)–(4), one finds that the values of the molecular "constants" depend on: (a) the total number of data points used in their determination (i.e., the number of $N$ values included), (b) the order of the polynomial employed, and (c) the specific equation used to obtain the molecular constant. In most cases, the number of data points was varied by ~10–25 % from the maximum possible number, all polynomial orders between 2 and 4 were considered, and the data were fitted to all of the equations (1)–(4) to which they could be applied. The spread in the set of values for a constant obtained from the *range* of procedures summarized in the preceding sentence is usually larger than predicted from the standard deviation analyses for individual fittings. This spread will increase markedly in the presence of strong channel mixings (*l* uncoupling accompanied by configuration interactions).

The ranges of empirically determined molecular constants reproducing energy level data for electronic states which are approximately case (a) or case (b) states are relatively small, because the case (a) and case (b) energy relations[4] are functionally consistent with Eqs. (1)–(4). The constants and "uncertainties" (range of possible parametric values) for the $a\,^3\Sigma_u$ state in Table IV provide a typical example. However, states which $l$ uncouple approach case (d)[4] or its multichannel equivalent and are poorly represented by Eqs. (1)–(4), which only slowly converge with increasing order. This slow convergence leads to strong dependences of the parameter sets on the specific procedure employed and, collaterally, to values of the effective constants which, although not interpretable in the same way as the constants obtained for states not affected by $l$ uncoupling, are characteristic of multichannel coupled states.

## IV. DISCUSSION AND CONCLUSIONS

The assignments of the transitions in Tables I–III to upper states associated with $n/\sigma\,^1\Sigma$ and $n/\pi\,^1\Pi$ are based on a number of observational facts. Rotational analyses prove that: (1) all of the transitions have a common lower state which, from the experimental conditions, must be metastable to radiative decay to the $X\,^1\Sigma$ state, (2) the transition types are of $\Sigma-\Sigma$ and $\Pi-\Sigma$ type, and (3) the effective molecular constants of the upper states are anomalous in a manner similar to those for $l$-uncoupled states in other molecules.[10,15] General considerations[4,5,7,8] combined with observations on transitions involving the lowest lying excited states and $X\,^1\Sigma$ in the heavier rare gases,[10,13] lead to quite firm assignments of the lower state of these transitions to the metastable $a\,^3\Sigma$ state. In this regard, it should be noted that the $a\,^3\Sigma$ state effective rotational constant reported here ($B = 0.5626 \pm 0.0006$ cm⁻¹) is within 1% of the value given in Ref. 3 ($0.564 \pm 0.004$ cm⁻¹).

Also, dipole selection rules allow transitions $\Pi-\Sigma$, and $\Sigma-\Sigma$, with singlet–triplet transitions allowed only

by strong spin–orbit coupling. States of $\Pi_g$ and $\Sigma_g^+$ type are produced by the addition of $nl\lambda$ orbitals with odd $l$ values to the $X\,^2\Sigma_u^+$ state of Ne$_2^+$, which means that transitions from $a\,^3\Sigma_u^+$ are allowed only to states associated with $np\lambda$, $nf\lambda$, and high $nl\lambda$ orbitals with $l$ odd.

The $a\,^3\Sigma_u^+$ state is associated with a $\sigma$ type Rydberg orbital which often is designated as the lowest member of the $ns\sigma$ manifold. Thus, with weak or no spin–orbit effects, one expects transitions from $a\,^3\Sigma_u^+$ to $np\lambda$($^3\Sigma_g^+$,$^3\Pi_g$) to be strong with the next most intense (but much weaker) transition being to $nf\lambda$($^3\Sigma_g^+$,$^3\Pi_g$). As spin–orbit effects increase, singlet–triplet transitions become weakly allowed with transitions to $np\lambda$($^1\Sigma_g^+$,$^1\Pi_g$) being much more intense than those to $nf\lambda$($^1\Sigma_g^+$,$^1\Pi_g$). The relative intensities of close lying $np\pi$($^1\Pi_g$,$^3\Pi_g$)$-a$ and $nf-a$ transitions, such as seen in Fig. 6, have led us to assign the upper states of the $nf-a$ transitions to triplets rather than singlets.

As noted above, all of the spectra give clear evidence of strong multichannel coupling while the upper states have small quantum defects ($\delta = n^* - n = \sim 0.04$). Both of these features are expected behavior for states associated with nonpenetrating orbitals without ancestors[4] in their core. This, and the observations above, leave little doubt that the transitions reported in the Tables and illustrations of Figs. 7–10 involve the lowest three members of the $nf$($^3\Sigma_g^+$,$^3\Pi_g$) series. Figure 11 depicts the $\Lambda$ doubling (mentioned earlier) that is present within the $^3\Pi_g$ component of the $4f\pi$ complex. Note the rapid rise in the $^3\Pi_g^- - {}^3\Pi_g^+$ splitting with increasing N as $l$ uncoupling becomes prominent.

Attempts were made to find transitions to the remaining ($\Delta_g$,$\Phi_g$) portions of the $nf$ complexes. To a first approximation, the origins of the components of an $f$ complex are expected to obey the $A\Lambda^2$ rule,[4,25] where $A$ is a constant and $\Lambda$ is the $\Lambda$ value of the component $^{2S+1}\Lambda$ state. For a variety

of reasons, this rule should be used with caution but it is expected to be reasonably applicable to the $nf$ complexes of the lighter rare gas dimers. For example, the origins of the $4f$ complex in He$_2$ are known experimentally[12] to be 27 398.3 cm$^{-1}$, 27 407.0 cm$^{-1}$, 27 432.7 cm$^{-1}$, and 27 473.5 cm$^{-1}$ for the $\Lambda = 0$, 1, 2, and 3 components, respectively. These values can be reproduced if $A = 8.4$ cm$^{-1}$ and $E_\Lambda = E_0 + A\Lambda^2$. We have used this rule with $A$ values near the energy separations of $nf\sigma\,^3\Sigma_g$ $-a$ from $nf\pi\,^3\Pi_g$ $-a$ to predict the regions for the (0–0) bands of the $nf\delta\,^3\Delta_g - a\,^3\Sigma_u$ and $nf\phi\,^3\Phi_g - a\,^3\Sigma_u$ segments, but found too few spectral features in these regions to make confirmable spectral assignments. This is not unexpected since such $\Delta-\Sigma$ and $\Phi-\Sigma$ transitions are much more highly forbidden than the observed $\Sigma-\Sigma$ and $\Pi-\Sigma$ transitions. Without data on the $\Delta$ and $\Phi$ components, it is not possible to determine empirical multichannel parameters for these complexes. We will continue efforts to obtain data which will permit experimental characterizations of complete $nf$ complexes in Ne$_2$ and hope to be able to produce such data in the future.

## ACKNOWLEDGMENTS

K. P. Killeen and J. G. Eden, J. Chem. Phys. **84**, 6048 (1986)

R. Sauerbrey, H. Eizenhofer, U. Schaller, and H. Langhoff, J. Phys. B **19**, 2279 (1986)

D. J. Kane, C. J. Zietkiewicz, and J. G. Eden, Phys. Rev. A **39**, 4906 (1989)

R. S. Mulliken, J. Am. Chem. Soc. **91**, 4616 (1969), and references therein

R. S. Mulliken, J. Chem. Phys. **52**, 5170 (1970)

D. J. Kane, Ph.D. thesis, University of Illinois, Urbana-Champaign, 1989

J. S. Cohen and B. Schneider, J. Chem. Phys. **61**, 3230 (1974)

S. Iwata, Chem. Phys. **37**, 251 (1979)

F. Grein and S. D. Peyerimhoff, J. Chem. Phys. **87**, 4684 (1987)

M. L. Ginter, J. Chem. Phys. **45**, 248 (1966)

D. S. Ginter, M. L. Ginter, and C. M. Brown, J. Chem. Phys. **81**, 6013 (1984)

G. Herzberg and Ch. Jungen, J. Chem. Phys. **84**, 1181 (1986)

G. Herzberg and Ch. Jungen, J. Chem. Phys. **77**, 5876 (1982)

E. S. Chang and K. Yoshino, J. Phys. B **16**, 1581 (1983)

P. Arrowsmith, W. J. Jones, and R. P. Tuckett, J. Mol. Spectrosc. **86**, 216 (1981)

M. N. Edgren and J. G. Eden, J. Chem. Phys. **85**, 1757 (1986)

M. L. Ginter, J. Mol. Spectrosc. **18**, 321 (1965)

W. Lichten and T. Wik, J. Chem. Phys. **69**, (1978); W. Lichten, M. V. McCusker, and T. L. Vierima, J. Chem. Phys. **61**, 2200 (1974)

C. M. Brown and M. L. Ginter, J. Mol. Spectrosc. **40**, (1971)

T. N. Colbourn and A. E. Douglas, J. Chem. Phys. **65**, 1741 (1976)

D. E. Freeman and K. Yoshino, J. Chem. Phys. **71**, 1780 (1979), and references therein

P. R. Herman, X. X. Mader, and B. P. Stoicheff, Chem. Phys. Lett. **134**, (1987), and references therein

T. L. Hill and H. Van Vleck, Phys. Rev. **32**, (1928)

# Bound→free emission spectra and photoassociation of $^{114}Cd_2$ and $^{64}Zn_2$

G. Rodriguez and J. G. Eden

*Everitt Laboratory, University of Illinois, Urbana, Illinois 61801*

Structured bound-free emission spectra of $^{64}Zn_2$ and $^{114}Cd_2$ have been observed by photoassociating pairs of ground state atoms ($ns^2\,^1S_0$, $n = 4$ and 5 for Zn and Cd, respectively) at several discrete wavelengths in the 222–277 nm region. The observed fluorescence is attributed to $B\,^1\Sigma_u^+ \to X\,^1\Sigma_g^+$ transitions of the molecules where the bound excited state is correlated with $np\,^1P_1 + ns^2\,^1S_0$ in the separated atom limit. The pressure dependence of the emission intensity demonstrates that the dominant $^1\Sigma_u^+$ production mechanism is photoassociation. Numerical, quantum mechanical simulations of the experimental spectra yield $^1\Sigma_u^+$ spectroscopic constants that are generally $\sim 10\%$ larger than *ab initio* values in the literature.

## I. INTRODUCTION

Since bound–free transitions of diatomic molecules terminate in the vibrational continuum of the lower (dissociative) electronic state, the interference of the free particle (continuum) and bound excited state wave functions gives rise to the familiar Franck–Condon oscillations. Such spectra are often termed *diffuse* and do not as readily yield the detailed molecular structural information that can be extracted from bound–bound band intensity profiles. Nevertheless, as Tellinghuisen[1] has noted in his excellent review of bound–free transitions, "...the [bound–free] spectrum may still display considerable structure, but that structure is entirely Franck–Condon structure...the intensity information is no longer a *redundancy* of the analysis; rather it now represents the primary data and hence is the *only* source of information about the potentials..." Consequently, bound–free emission spectra are an intriguing spectroscopic tool in giving insight into the electronic and vibrational structure of the radiating molecular state but also in providing details regarding the ground state interatomic potential as well.

To date, these oscillatory continua have been observed in a wide range of diatomic molecules including the homonuclear halogens, interhalogens and the alkali, Column IIA and IIB dimers.[1] Particularly extensive observations of bound–free emission have been reported for the Column IIA diatomics $Mg_2$, $Ca_2$, and $Sr_2$ (Refs. 2–6). The $A\,^1\Sigma_u^+$ excited states of each of the three dimers were photopumped at one of several wavelengths with different visible or uv lines from an Ar⁺ or cw dye laser. Since their $X\,^1\Sigma_g^+$ ground states are stable (e.g., $D_e = 1095$ and 1065 cm⁻¹ for $Ca_2$ and $Sr_2$, respectively),[4,6] both discrete and continuum spectra were observed for the Column IIA dimers, the latter of which resulted from transitions to the repulsive portion of the ground state. The presence of discrete line spectra in the $A \to X$ emission permitted Rydberg–Klein–Rees (RKR) potentials to be determined for the $A$ and $X$ states. As pointed out by Gerber *et al.*,[6] this is a distinct advantage when turning to an analysis of the *bound–free* continua by calculating the continuous Franck–Condon factors (FCF), since now

the radiating state structure is well characterized and one is able to concentrate solely on the nature of the dissociative portion of the ground state.

The chemical and optical characteristics of the Column IIB dimers are also interesting since the $(n-1)d$ and $ns$ orbitals of Zn and Cd ($n = 4$ and 5, respectively), for example, are closed. Consequently, aside from a weak van der Waals minimum at large internuclear separation, the dimer ground state interatomic potential is expected to be repulsive. In 1978, Ehrlich and Osgood[7] observed the Franck–Condon modulated fluorescence from vibrationally excited ($v' \sim 57$) $Hg_2(O_u^+)$ excimers produced by pumping Hg ($^1S_0$) ground state collision pairs with an untuned ArF laser (193 nm). Forming this highly excited molecule in the vicinity of the upper state's classical outer turning point results in bound–free emission spectra extending over 30–40 nm which corresponds to a large range (several Bohr) in internuclear separation, $R$. The spectra of Ref. 7 show no sign of discrete structure but rather display the well-modulated interference oscillations described earlier.

Table I of Ref. 1 summarizes those molecules for which bound–free spectra had been observed and characterized prior to 1984. With the notable exceptions of Refs. 2–6, most prior work entailed exciting the molecule at one wavelength and analyzing the resulting spectrum by the semiclassical stationary phase approximation or quantum calculations (Franck–Condon integral).[1,8] Other diatomic molecules for which recent studies have observed interference structure in emission spectra include $Hg_2$ (Ref. 9) and IBr (Ref. 10).

Experimental studies of bound–free emission from $Zn_2$ and $Cd_2$ in the gas phase and numerical analysis of the observed spectra are reported here. For both molecules, a range of vibrational levels of the $^1\Sigma_u^+$ ($O_u^+$) state, derived from $np\,^1P_1 + ns^2\,^1S_0$ ($n = 4$ and 5 for Zn and Cd, respectively), were produced by photoexciting (photoassociating) pairs of ground state atoms with excimer or frequency-quadrupled Nd:YAG laser radiation. Analysis of the modulated bound–free continua by numerical quantum calculations has yielded dissociation energies and vibrational constants for the emitting states. Despite several *ab initio* calculations of Col-

umn IIB interatomic potentials,[11-15] little is known of the higher excited states of $Zn_2$ and $Cd_2$ as previous experimental studies have generally focused on the visible and uv continua emitted by the lowest lying ungerade excited states in transitions to ground.[16]

## II. EXPERIMENTAL DETAILS

Several cylindrical optical cells, 5.5 cm in length and 2.2 cm in diameter (o.d.), were fabricated from Suprasil grade quartz and evacuated to $<10^{-7}$ Torr by a turbomolecular pumping station. After degassing the tube walls with a hydrogen torch, several milligrams of isotopically enriched (98%) $^{64}Zn$ or $^{114}Cd$ were introduced into the cells. Standard distillation techniques were followed to further purify the metal after which each quartz tube was sealed off under vacuum. The cells were placed into a firebrick lined oven and temperature was monitored by chromel-alumel thermocouples located at the cell side arm. Metal atom number densities were determined from the vapor pressure curves. In these studies, the Column IIB operating pressures ranged from 20 to 650 Torr which corresponds to the temperature interval of 789–1013 K for Cd and 905–1173 K for Zn. At 400 Torr, the Zn and Cd number densities are $3.4 \times 10^{18}$ and $3.9 \times 10^{18}$ cm$^{-3}$, respectively.

Photoassociation is an optically assisted collision in which a colliding pair of atoms in the ground state's thermal continuum absorbs a photon, resulting in the production of an electronically excited diatomic molecule. In zinc vapor, for example, $Zn_2$ ($^1\Sigma_u^+$) molecules can be produced by the bound $\leftarrow$ free process

$$Zn(4s \, ^1S_0) + Zn(4s \, ^1S_0) + \hbar\omega \rightarrow Zn_2(^1\Sigma_u^+, v'). \quad (1)$$
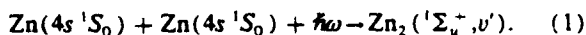
Consequently, as illustrated by the schematic diagram of the experimental apparatus in Fig. 1, excited $Zn_2$ or $Cd_2$ dimers were produced by irradiating pairs of ground state atoms with one of several wavelengths available from a rare gas–halide excimer laser (ArF: 193 nm; KrCl: 222 nm, KrF: 248 nm and XeCl: 308 nm). The Stokes lines of ArF and KrF Raman shifted in $H_2$ and the fourth harmonic of the Nd:YAG laser (266 nm) provided other useful excitation wavelengths as well. Unless stated otherwise, all spectra were acquired for pump laser pulse energies of 20 mJ, although considerably larger energies were available at several wavelengths. For the excimer laser experiments, the pump beam was rectangular in cross section and the quartz cell was irradiated transversely at a pulse repetition frequency of 10 Hz. A cylindrical lens focused the incoming radiation to a line that was coincident with the axis of the optical cell. When the Nd:YAG 266 nm laser wavelength was studied, the beam was propagated along the cell's axis.

Subsequent fluorescence from electronically excited zinc or cadmium molecules was collected through a port at the top of the oven by a large cylindrical collection lens made of Suprasil quartz. An aluminized turning mirror and a final focusing lens (15 cm focal length) directed the emission to the entrance slit of a 1/4 m spectrograph equipped with an optical multichannel diode array (OSMA) which consisted of a 660 element array enhanced for the uv by a phosphor on the multichannel plate. The spectrograph was equipped with 600 and 1200 lines mm$^{-1}$ gratings, giving an overall detection system resolution of $\Delta\bar{\nu} = 3.5$, 7.5, or 15.0 cm$^{-1}$, depending upon the specific grating and spectrometer order in use. All spectra were wavelength calibrated with known lines from low pressure Ar, Ne, Kr, and Hg atomic lamps. In order to suppress scattered pump radiation, one of several
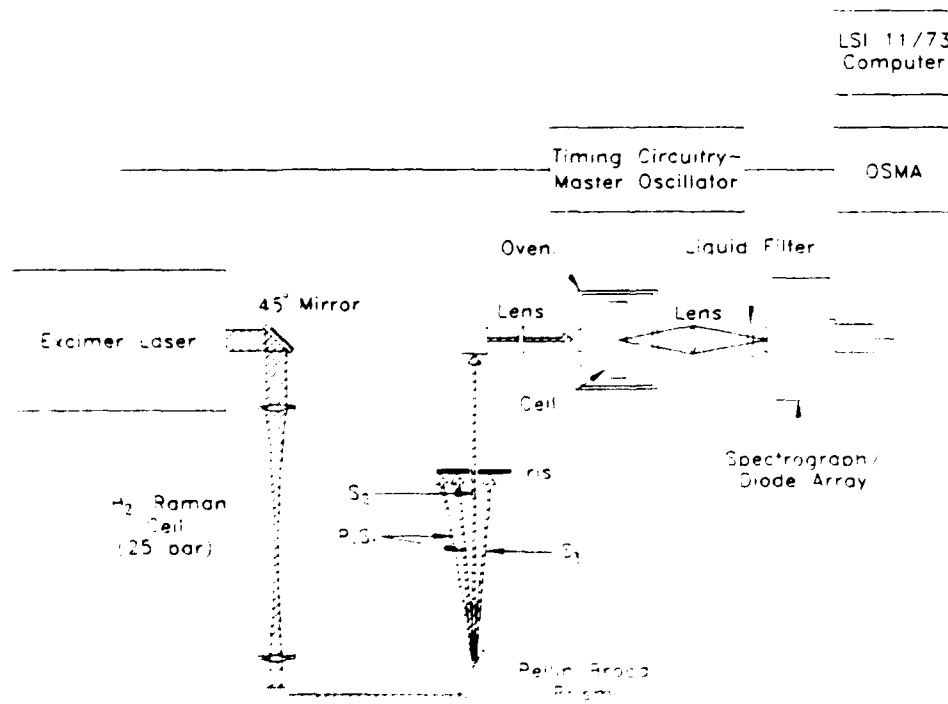


FIG. 1. Partial schematic diagram of the experimental apparatus. For those excitation wavelengths not requiring Raman shifting, the 45° mirror and right angle prism in the excimer laser beam path were removed. The illustration depicts the selection of the second Stokes of ArF Raman shifted in $H_2$ for excitation of Zn vapor.

liquid filters (n-butyl acetate: $\lambda_{CUTOFF} = 254$ nm; chloroform: 245 nm; dichloromethane: 233 nm)[17] was generally placed in the optical path.

Data were acquired and stored by a DEC LSI 11/73 computer. The diode array controller was operated synchronously at 10 Hz in a gated mode. That is, 50 ns after the pump laser was fired, the OSMA was activated (gated "on") and spectra were acquired by integrating the emission signal for 5 $\mu$s. Both background and scattered pump radiation were accounted for in the data reduction procedure.

## III. THEORETICAL CONSIDERATIONS

Both exact quantum calculations and the semiclassical stationary phase approximation[1,8] have been remarkably successful in describing bound–free and free–bound electronic transitions in diatomics. The Einstein $A$ coefficient for spontaneous emission from a bound state $(v',J')$ into the continuum of a (dissociative) lower state is given by the expression[1]

$$A(v',J',\epsilon'') = (64\pi^4/3h)s_{J',J''}(2J'+1)^{-1}$$
$$\times g'v^3|\langle \epsilon''|\mu_e(R)|v',J'\rangle|^2, \qquad (2)$$

where $g'$ is the upper (bound) state degeneracy, $s_{J',J''}$ is the rotational line strength, $\mu_e(R)$ is the electronic dipole moment for the transition, and $v'$ and $\epsilon''$ represent the bound state and free particle (associated with an atomic pair of energy $\epsilon''$) wave functions, respectively. Consequently, the intensity profile of the bound–free emission spectrum can be calculated by evaluating the square of the matrix element. That is:

$$I(\lambda) \propto |\langle \epsilon''|\mu_e(R)|v',J'\rangle|^2, \qquad (3)$$

where $I(\lambda)$ is the experimentally observed emission intensity spectrum. If the dipole moment is assumed to vary slowly over the internuclear separation region of interest, then Eq. (3) can be rewritten as

$$I(\lambda) \propto \mu_e^2|\langle \epsilon''|v',J'\rangle|^2, \qquad (4)$$

where $|\langle \epsilon''|v',J'\rangle|^2$ is the continuous Franck–Condon factor. The almost sinusoidal Franck–Condon oscillations that are frequently characteristic of bound–free transitions arise from the interference between the wave functions for the bound excited state and the free atoms associated with the ground state's dissociation continuum.

Exact quantum calculations of bound–free spectra, therefore, require knowledge of (or an assumed functional form for) the upper and lower state interatomic potentials from which one calculates the continuous FCFs. As will be discussed later, the $Zn_2$ and $Cd_2$ potentials of interest here are not presently well characterized. Consequently, in this study we adopt the approach taken by Bergeman and Liao[5] by assuming *both* molecular potentials to be well described by the Morse function. For convenience, the constant dipole approximation [Eq. (4)], invoked by Scheingraber and Vidal for the $Mg_2$ $A–X$ system,[2] is assumed to be valid for the $Zn_2$ and $Cd_2$ $^1\Sigma_u^+ \rightarrow {}^1\Sigma_g^+$ transitions. The limitations imposed by this assumption will be dealt with later.

As reviewed in detail by Tellinghuisen,[1] the semiclassical stationary phase approximation has also proven to be valuable in describing bound $\rightleftharpoons$ free transitions. For a two state molecular system having a single point of stationary phase,[1,8] the quantum mechanical FCF (overlap integral) accumulates primarily in the region of internuclear separation in the vicinity of this point of stationary phase which, in turn, lies close to the classical outer (or inner) turning point. Considering photoassociative (bound $\leftarrow$ free) transitions, for example, previous work has demonstrated that the stationary phase approximation is a reliable guide in visualizing such situations. One concludes that the photoexcitation of colliding ground state Zn (or Cd) atoms to produce an electronic excited state of $Zn_2$ [i.e., $Zn_2^*(v',J')$] is assumed to occur predominantly in the vicinity of the classical outer turning point for the bound excited state, $v'$.

## IV. EXPERIMENTAL RESULTS AND SPECTRAL ANALYSIS

### A. $^{64}Zn_2$

Irradiating 400 Torr of zinc vapor ($[^{64}Zn] = 3.4 \times 10^{18}$ cm$^{-3}$, $T = 1118$K) with the beam from an untuned XeCl (308 nm) laser yields the unstructured blue continuum illustrated in Fig. 2. The spectral width ($\sim 120$ nm FWHM) and position of the spectrum are in accord with previous gas phase studies of the molecule[16(a)] and the assumption that this visible emission is due to transitions from a low-lying metastable state of the dimer $(^3\Sigma_u^+)$[11,13] to ground $(^1\Sigma_g^+)$. The lowest electronic-excited states of both $Zn_2$ and $Cd_2$ are the $^3\Pi_g$ and $^3\Sigma_u^+$ levels that are derived from $np$ $^3P + ns^2$ $^1S_0$.[11,13] Of course, neither triplet state is strongly connected to ground by dipole transitions and parity considerations preclude emission from the $^3\Pi_g$ state.

The bound–free emission continua that were recorded following the photoexcitation of $^{64}Zn$ vapor at shorter wavelengths—222, 230, and 248 nm—are shown in Figs. 3–5, respectively. For each of the spectra, strongly modulated Franck–Condon oscillations are observed which extend 60–100 nm to the red of the pump wavelength. Continua exhibiting such structure were predicted theoretically by Condon[18] who coined the descriptive term "internal diffraction bands" to portray the interference between the bound and free particle wave functions. Although atomic Zn lines are also frequently present, the bound–free undulations dominate the spectra and the S/N ratio and reproducibility are excellent. The weak, high frequency structure superimposed onto the oscillations of Figs. 3–5 is an artifact of the detection system. It should be noted that the $Zn_2$ spectrum produced with a 248 nm excitation wavelength is distorted at the shorter wavelengths by the n-butyl acetate liquid filter which has a rapidly changing transmission between 240 and 260 nm. Previously published $Zn_2$ emission spectra[16] have shown no evidence of FC interference. Note, however, that the oscillations of Figs. 3–5 do not exhibit complete modulation which are evidence for emission from several bound or quasibound vibrational levels. Because of the depth of the $B$ $^1\Sigma_u^+$ state,
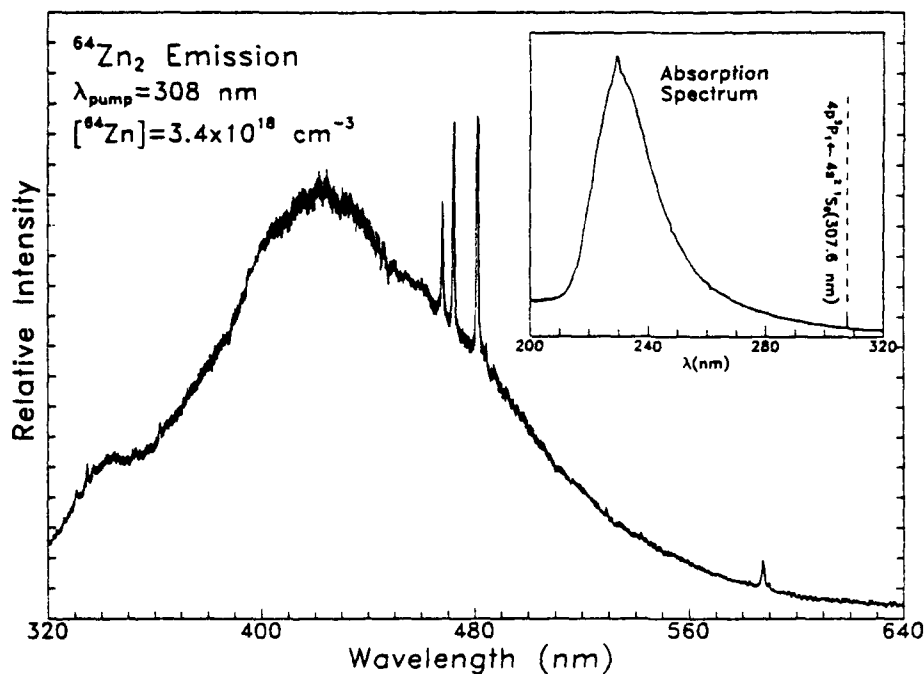
FIG. 2. Unstructured continuum produced by irradiating $^{64}Zn$ vapor at $\lambda = 308$ nm (XeCl laser). The $5s\,^3S_1 \rightarrow 4p\,^3P_J$ triplet in the 468–481 nm region is also present. The inset shows the ultraviolet absorption spectrum of Zn observed under identical experimental conditions (Zn vapor pressure $\approx 400$ Torr). A xenon arc lamp provided the probing continuum for this measurement. Neither spectrum has been corrected for the spectral response of the detection system.

free–free emission is expected to be negligible. However, if one were to form electronically excited $Zn_2$ (or $Cd_2$ ) states indirectly by photoexciting the atomic $^1P_1 \leftarrow {}^1S_0$ transition and relying on three body collisions to produce the excimer, a strong free→free component to the fluorescence spectrum would then be expected and in the vicinity of the resonance transition wavelength, in particular.

No molecular emission was detected in the 200–300 nm region when the vapor was irradiated at 193, 210 (first

Stokes of ArF in $H_2$ ), 266 (fourth harmonic of Nd:YAG), or 277 nm (first Stokes of the KrF laser in $H_2$ ). This result is consistent with the location of the well-known $^1\Sigma_u^+ \leftarrow {}^1\Sigma_g^+$ absorption band of $Zn_2$ that has been observed in the gas phase[19] and in rare gas matrices.[20] As displayed in the inset to Fig. 2, this broad continuum also shows no structure, peaks near 230 nm and has a FWHM of $\sim 22$ nm.

The emission spectra of Figs. 3–5 are, therefore, attributed primarily to bound–free transitions originating from a
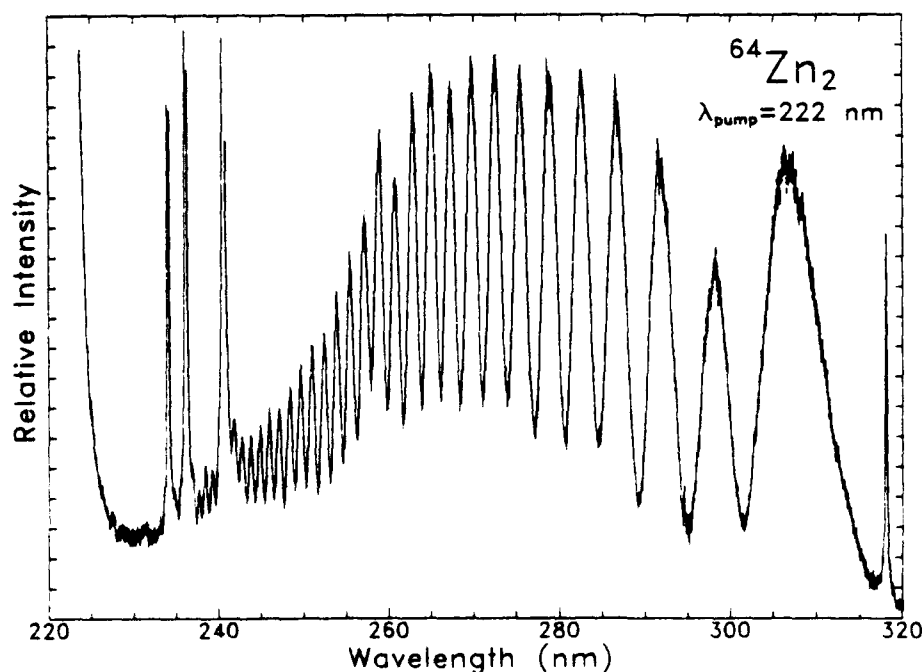


FIG. 3. Emission spectrum observed when 400 Torr of Zn vapor ($[Zn] = 3.4 \times 10^{18}cm^{-3}$) is irradiated at 222 nm (KrCl laser). Although the emission profile has not been corrected for the spectral response of the detection system, the decline in intensity observed at $\lambda \sim 298$ nm is real. No liquid filter was used for these measurements.
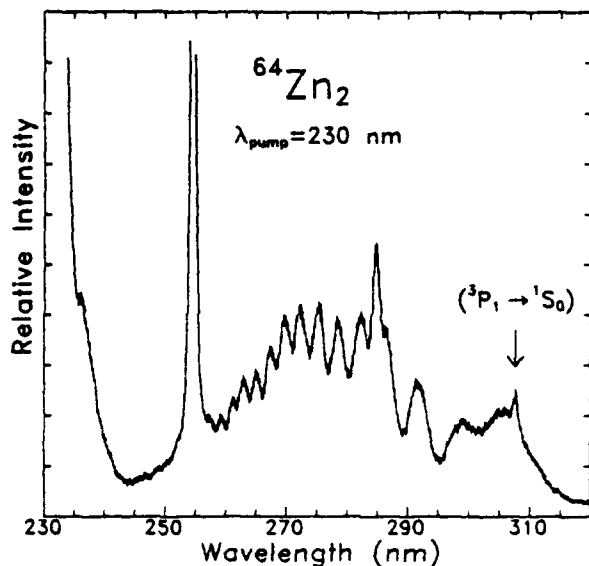
FIG. 4. Spectrum similar to that of Fig. 2 except $\lambda_{PUMP} = 230$ nm ($S_2$ of ArF laser in $H_2$).



FIG. 6. Partial energy level diagram of $Zn_2$ developed by Hay, Dunning, and Raffenetti from ab initio calculations (adapted from Ref. 11). The production of a specific $^1\Sigma_u^+$ vibrational level by the photoassociation (bound–free absorption) of a pair of $Zn$ ($4s^2$ $^1S_0$) atoms is also illustrated. Bound–bound absorption also occurs at larger $R$.

limited number of vibrational levels of the lowest $^1\Sigma_u^+$ state of the dimer. In accord with international convention, we recommend that this electronic state be denoted $B$ $^1\Sigma_u^+$. The nonselective nature of the pumping mechanism utilized here generally precludes exciting a specific $v'$ state. A partial energy level diagram of $Zn_2$, adapted from Ref. 13 and given in Fig. 6, illustrates the fact that this $^1\Sigma_u^+$ state is derived from $4p$ $^1P_1$ and a ground state atom ($3d^{10}$ $4s^2$ $^1S_0$). Hence the molecular fluorescence is correlated with a resonance transition ($^1P_1 \rightarrow {}^1S_0$) of the Zn atom having an upper state lifetime of $\sim 1.6$ ns (Ref. 21). Finally, although the $B$ $^1\Sigma_u^+$ and

($C$) $^1\Pi_u$ states both lie close to one another (and presumably intersect at $R \sim 2.5$ Å),[11] are correlated with the same separated atom limit and are connected to ground by dipole-allowed transitions, the calculated dipole moment for the $B$ $^1\Sigma_u^+ \rightarrow X$ $^1\Sigma_g^+$ transition ($\sim 9$ D at 5.25 Bohr) is considerably larger than that for $C$ $^1\Pi_u \rightarrow X$ $^1\Sigma_g^+$ transitions (1.9 D).[11] One anticipates, therefore, that the observed bound–free emission will primarily arise from the $B$ $^1\Sigma_u^+$ state.

Previous studies[22-24] and the results to be presented later indicate that the ground state of $Zn_2$ is bound by several hundred cm$^{-1}$ and $R_e \sim 4$–$5$ Å. Consequently, as noted in
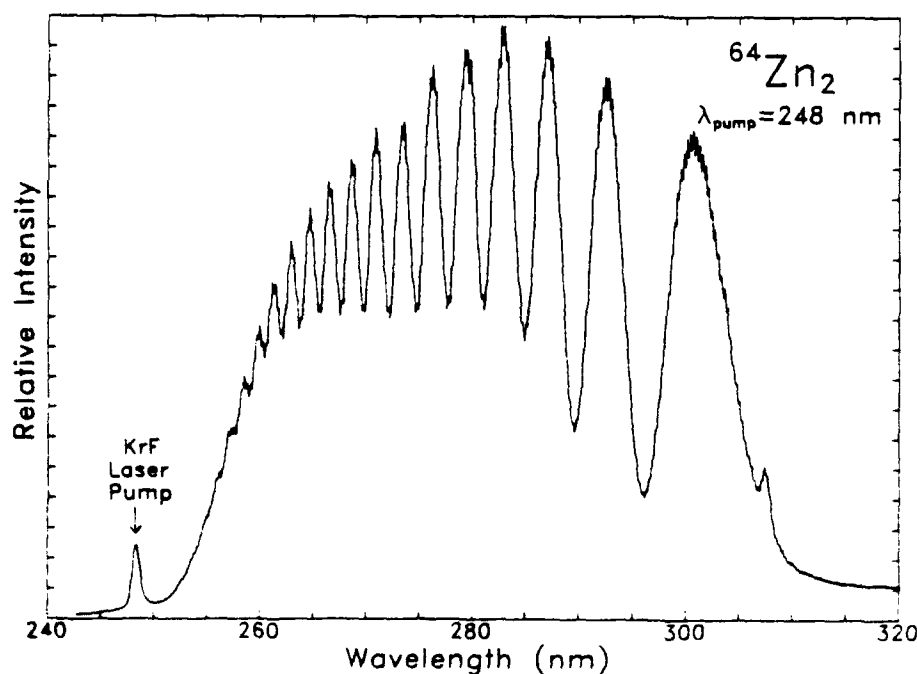


FIG. 5. Bound–free spectrum of $Zn_2$ observed for an excitation wavelength of 248 nm. As in Figs. 2–4, [Zn] $= 3.4 \times 10^{18}$ cm$^{-3}$. The rapid falloff in the emission intensity as one approaches the KrF laser pump wavelength is a consequence of a butyl acetate liquid filter placed in front of the spectrograph.

Sec. II, both bound ← free and bound ← bound processes contribute to the production of particular vibrational levels of the $B\,^1\Sigma_u^+$ state. While photoexcitation of bound $Zn_2$ ground state molecules to specific upper state vibrational levels (i.e., bound–bound transitions) will occur, the $Zn_2$ van der Waals bound ground state is shallow and so the number of atoms in the thermal continuum of the ground state greatly exceeds the number of $Zn_2 X\,^1\Sigma_g^+$ molecules available. Said another way, the equilibrium constant that describes the balance between the ground state atomic and molecular populations favors translational degrees of freedom.

From a semiclassical point of view, the spectra of Figs. 3–5 are textbook examples of reflection emission spectra in which the Franck–Condon "diffraction"[18] of one (or a few) upper state vibrational level ($v'$) onto the dissociative ground state is observed. In terms of their overall structure, then, these spectra indicate that the radiating and ground states are characterized by a single point of stationary phase which lies close to the outer turning point for a given $B\,^1\Sigma_u^+$ vibrational level (Ref. 1). Consequently, the overlap integral describing the absorption process acquires the bulk of its value in the vicinity of the classical outer turning point. It is not surprising, therefore, that excitation wavelengths to the blue side of the Zn $4p\,^1P_1 - 4s\,^1S_0$ resonance line (213.9 nm) or to the red of the $B\,^1\Sigma_u^+ - X\,^1\Sigma_g^+$ molecular absorption band (inset, Fig. 2) will *not* produce $Zn_2$ reflection fluorescence spectra.

As expected, the $Zn_2$ spectra show no evidence of a bound→bound emission component. Since the $B\,^1\Sigma_u^+$ equilibrium internuclear separation $R_e$ is almost 2 Å smaller than that for the $^1\Sigma_g^+$ ground state,[11,13,24] the FC region for

fluorescence dictates that bound → free transitions will dominate the spectrum, and particularly at the longer wavelengths which correspond to transitions occurring at small $R$.

The computational results discussed in Sec. IV C will demonstrate that the oscillatory $Zn_2$ (and $Cd_2$) spectra are well represented by assuming that the emission emanates from three or fewer vibrational levels. This is a plausible result if one can assume that the $B\,^1\Sigma_u^+ \rightarrow X\,^1\Sigma_g^+$ dipole moment is a slowly varying function of $R$. In that case, the $B\,^1\Sigma_u^+$ radiative lifetime (several ns) discourages thorough collisional mixing of the pumped vibrational level with adjacent states, even though the background Zn number densities used in these experiments are as high as $5\times10^{18}$ cm$^{-3}$. However, because of the spectral breadth of the excimer laser's untuned output (typically $\sim 100$ cm$^{-1}$), it is not possible to specify a particular $B\,^1\Sigma_u^+$ vibrational level.

The Zn number density ([Zn]) dependence of the $Zn_2$ bound–free emission spectrum is shown in Fig. 7 which presents data acquired at four different vapor pressures. Note that the overall spectral envelope and the oscillatory structure itself remain unchanged but, for convenience, the lower pressure data have been magnified. The figure also indicates the oven temperature corresponding to a chosen pressure. Although the oven temperature was varied by less than 20% to obtain these spectra, the continuum intensity drops dramatically as [Zn] decreases. Specifically, data plotted in Fig. 8 for three specific wavelengths in the spectra demonstrate that the time-integrated intensity varies quadratically with the zinc pressure. This result is to be expected since the photoassociative process which produces the $Zn_2 B\,^1\Sigma_u^+$ molecules requires two Zn atoms and the third "body" is a pho-
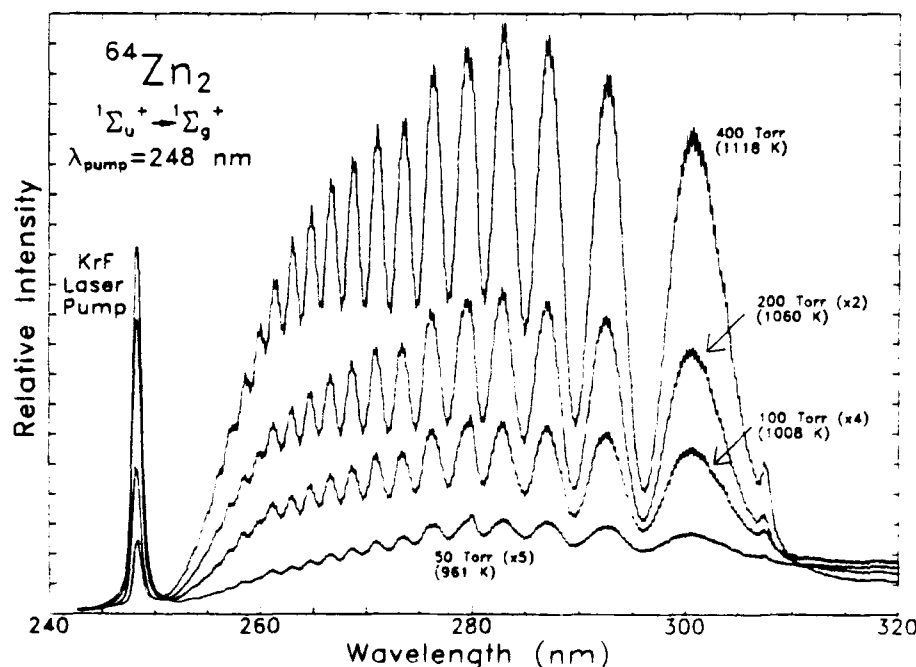


FIG. 7 Dependence of $^{64}Zn_2$ bound–free emission intensity on the metal vapor pressure. For convenience, the lower pressure spectra have been magnified by different factors (shown in parentheses). The pump laser wavelength is 248 nm and the temperature corresponding to each Zn vapor pressure is also indicated.
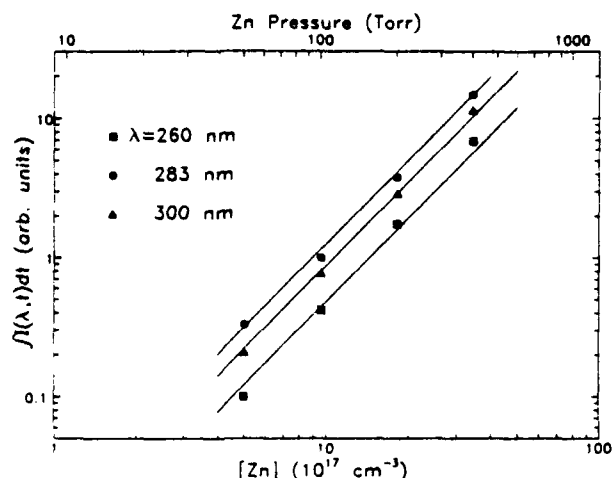
FIG. 8. Data at three wavelengths in the $Zn_2$ bound–free emission spectrum (260, 283, and 300 nm), portraying the quadratic dependence of the time integrated intensity $[\int I(\lambda,t)dt]$ on the zinc number density, [Zn]. The data demonstrate that the $^1\Sigma_u^+$ emitting state is populated by photoassociation (involving the absorption of a photon by a pair of colliding Zn atoms).

ton. Spectra similar to those of Fig. 7 also display a linear dependence of bound–free intensity on the pulse energy of the pump laser (KrF, in this case).

Before leaving this section, one other interesting qualitative feature of these spectra should be noted. Since the anharmonicity of the $Zn_2$ upper state ($^1\Sigma_u^+$) potential becomes more pronounced as the vibrational quantum number increases, $\langle R \rangle$ also gradually rises. Therefore, as shown in Fig. 9, the spacing between adjacent maxima in the bound–free spectra are sensitive to the slope of the ground state.

Specifically, when photoexciting $Zn_2$ at 222 nm, $B\ ^1\Sigma_u^+$ molecules are produced in the $v' \sim 85$ state which, when radiating, is "reflected" onto a portion of the ground state potential that is flatter than is the ground state segment available to lower-lying $^1\Sigma_u^+$ vibrational states. Assuming the $B\ ^1\Sigma_u^+$ potential to be described by the Morse function (discussed in Sec. IV C), then $\langle R \rangle$ for $v' = 25$ and 85, for example, are 3.9 and 5.2 Å, respectively. The $\lambda_{PUMP} = 248$ nm data of Fig. 9 demonstrate that the ground state's slope is changing rapidly in this region of internuclear separation.

## B. ¹¹⁴Cd₂

Figures 10–12 present similar spectra that were obtained for ¹¹⁴Cd₂. For this molecule, oscillatory emission spectra were observed only when the vapor was irradiated at 248 or 266 nm. Pumping at 222 nm did not produce any observable emission which is consistent with the fact that the Cd $5p\ ^1P_1 \leftarrow\ ^1S_0$ transition lies at 228.8 nm. Comments similar to those earlier regarding the electronic states of $Zn_2$ could be made for $Cd_2$. As a result, a comparison of Figs. 5 and 11 shows that, other than the overall intensity envelopes and the smaller vibrational frequency for the heavier $Cd_2$ molecule, the two spectra are quite similar. The longest wavelength maximum in the $Cd_2$ spectra lies only $\sim 5$ nm to the red of the analogous peak in Fig. 5.

The dependence of the emission on the Cd vapor pressure is illustrated in Fig. 13 for a laser wavelength of 248 nm. Once again, the interference structure is more prominent at the higher Cd number densities. It is also expected that, as was the case with $Zn_2$, the emission spectra of Figs. 10–13 result from the non-selective excitation of several $v'$ levels.
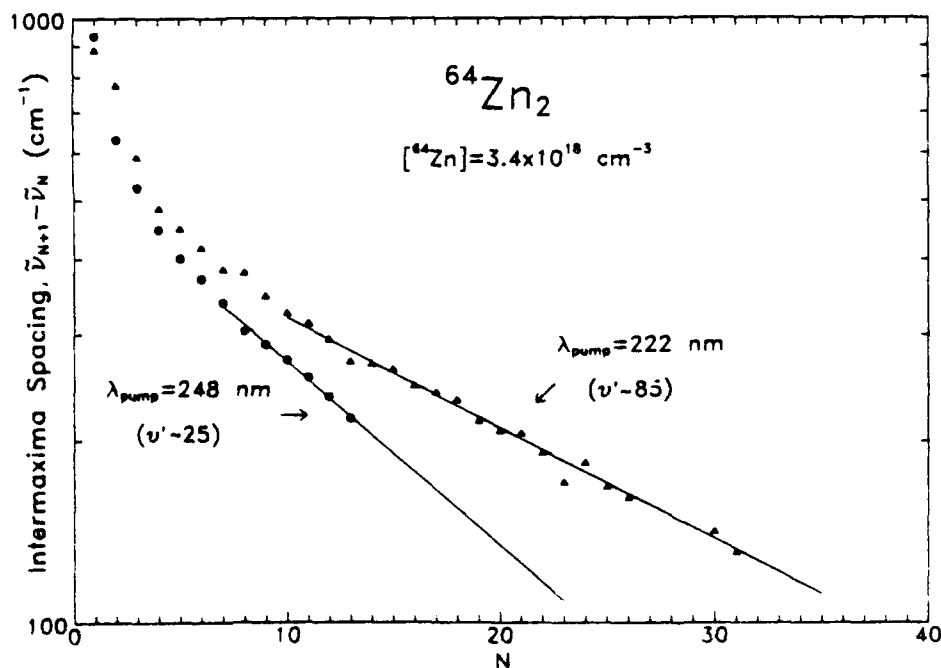


FIG. 9. Spacing between adjacent maxima (denoted by the integer $N$) in the bound–free emission spectra of $Zn_2$. The difference in slope between the 222 nm (triangles) and 248 nm (circles) data is a consequence of the fact that the ground state potential ($^1\Sigma_u^+$) is less steep in the $v' \sim 85$ emission FC corridor than it is for lower-lying vibrational states (since $\langle R \rangle$ increases with $v'$). The approximate vibrational quantum number for the emitting state is also indicated for each set of data and the solid lines represent linear least-squares fits to the highest $N$ data.
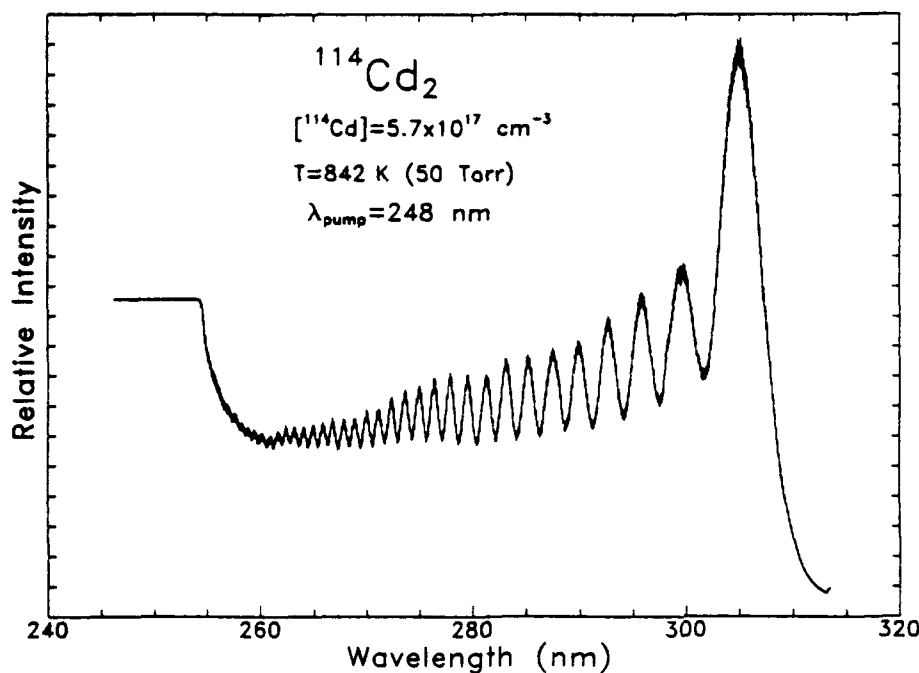
FIG. 10. $Cd_2$ bound–free emission spectrum recorded upon irradiating 50 Torr of Cd vapor with a KrF laser (248 nm). A liquid filter was not used in this case to block scattered pump radiation.

## C. Spectral simulations

Numerical calculations carried out to simulate the experimental bound–free spectra incorporated only the $X\ ^1\Sigma_g^+$ ground and $B\ ^1\Sigma_u^+$ excited states mentioned earlier. The approach entailed integrating Schrödinger's equation to determine the radial wave functions for both potentials. The wave functions were calculated by the Numerov–Cooley procedure which calculates the eigenvalues for a given potential with a finite difference technique using a predictor–corrector formula. Convergence is approached iteratively with a second order variational procedure. For the bound ($^1\Sigma_u^+$) state, the solution was obtained in two segments by integrating inward and outward and the two regions were matched by requiring the wavefunction and its first derivative to be continuous when the two solutions were merged.
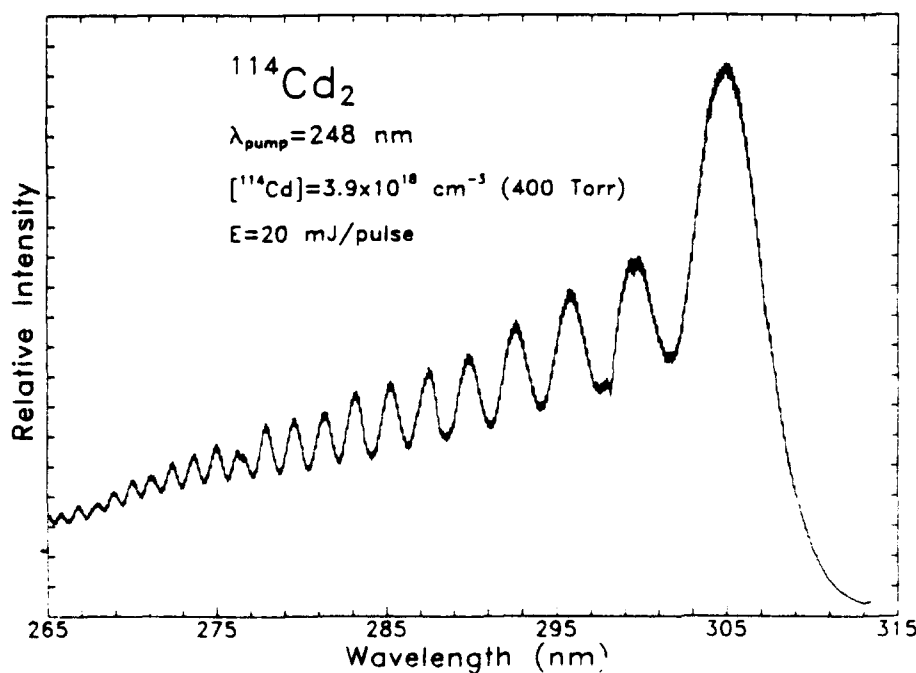


FIG. 11. Expanded view of the KrF laser-produced $Cd_2$ spectrum. For these data, however, the Cd vapor pressure was 400 Torr and the excimer laser pump energy was held constant at 20 mJ/pulse. Also, a butyl acetate liquid was inserted in the optical beam path.
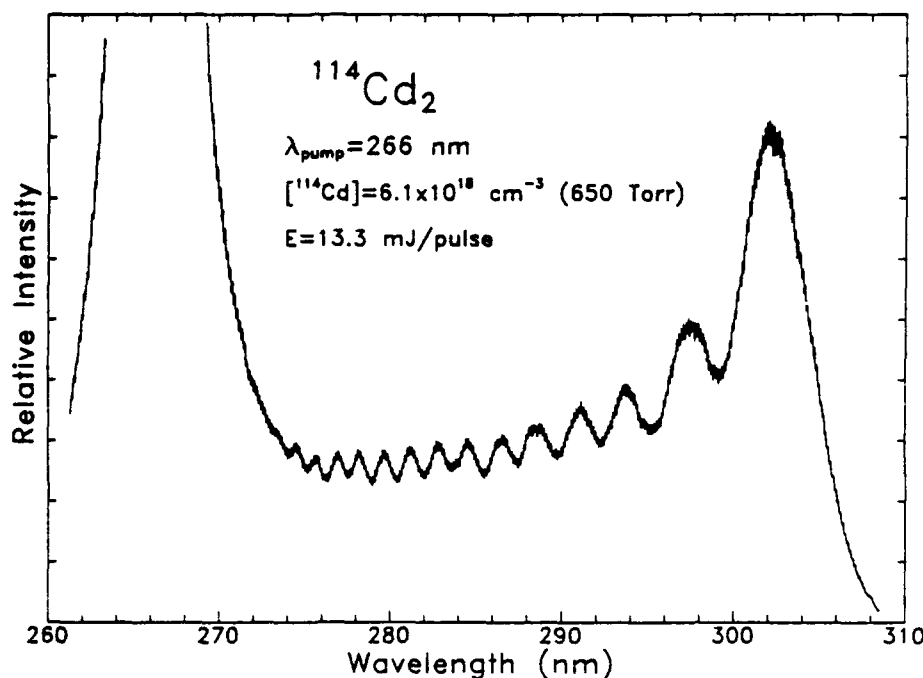
FIG. 12. $Cd_2$ spectrum obtained for $\lambda_{PUMP} = 266$ nm (Nd:YAG fourth harmonic) and $p_{Cd} = 650$ Torr. The single pulse laser energy was fixed at 13.3 mJ.

### 1. $Zn_2$

The wave functions were evaluated over the 2.50 to 7.50 Å internuclear separation region with a radial grid size of $2 \times 10^{-3}$ Å. Also, spatial normalization was accomplished with the trapezoidal integration rule.

After calculating the vibrational wave function for the bound state, the continuous FCFs, $|\langle \epsilon''|v',J'\rangle|^2$, were evaluated for 500 points over the $-274.0$ to $15\,000$ cm$^{-1}$ range in lower state energies (where zero energy represents the ground state separated atom limit). Owing to the spectral breadth of the excimer laser radiation and the thermal distribution of ground state metal atoms, several $v'$ levels are accessible for any one pump laser wavelength. Consequently, the FCF contributions from two or more $B\,^1\Sigma_u^+$ vibrational levels were often summed to produce the final simulation.

The interaction potentials necessary to simulate $Zn_2$ emission or absorption spectra are not well characterized. In fact, until recently, the molecular constants for neither state
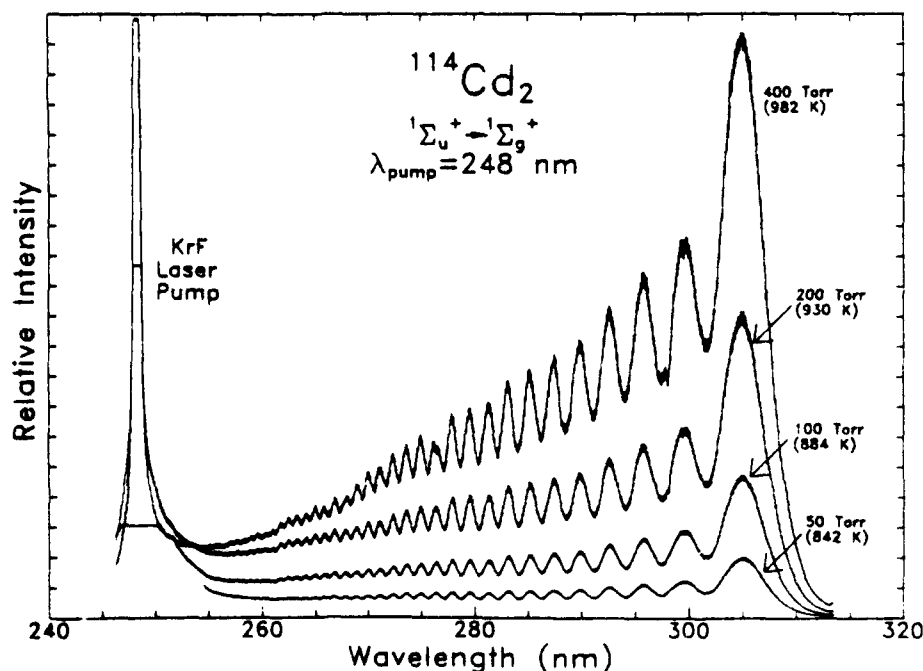


FIG. 13. Vapor pressure dependence of $Cd_2$ bound–free emission. The laser excitation wavelength was 248 nm for all of the data shown.

were known. Fortunately, Czajkowski and co-workers[24] reported in 1990 the *ground state* vibrational constants that were measured in a molecular beam experiment in which the $O_u^+$ ($^3\Pi_u$) van der Waals excited state was examined by laser spectroscopy. Given this starting point and assuming that both states can be adequately represented by Morse potentials, the task of simulating the spectra of Figs. 3–5 was reduced to iterating $D_e$, $R_e$, and $\omega_e$ for the upper ($^1\Sigma_u^+$) state. As initial values for the iterative process, the $B\,^1\Sigma_u^+$ constants determined from the *ab initio* calculations of Ref. 13 were chosen. In an effort to guarantee a unique *and* consistent solution to this process, a final set of constants was not accepted unless it was capable of reproducing all of the $Zn_2$ (or $Cd_2$) experimental spectra, regardless of the particular pump wavelength.

Taking the $X\,^1\Sigma_g^+$ constants to be those of Ref. 24 ($D_e'' = 274\,\mathrm{cm}^{-1}$, $\omega_e'' = 25.7\,\mathrm{cm}^{-1}$, $\omega_e''x_e'' = 0.60\,\mathrm{cm}^{-1}$ and $R_e'' = 4.80$ Å), Figs. 14 and 15 show the best simulations obtained for the 248 and 222 nm pumped spectra, respectively. The process of fitting the data was initiated with the 248 nm spectrum since $v'$ for that pump wavelength is the smallest of those for the three excitation wavelengths investigated and the emission structure is simplest. Examination of the undulations in the experimental spectrum (cf. Figs. 5 and 7) indicate that $v' > 18$ and early simulations showed that $v' \approx 25$. Later work bore this out. In fact, assuming that the $Zn_2$ emission of Fig. 5 emanates from a single vibrational state (Fig. 14) yields a simulated spectrum that is nearly identical to the experimental version except for: (1) the degree of modulation of the FC oscillations, and (2) the overall intensity envelope which degrades too slowly towards short wavelengths. Both shortcomings are, to a large extent, corrected for by allowing for emission from several adjacent vibrational levels and bearing in mind the approximation represented by Eq. (4).

Similar results are obtained when simulating the $\lambda_{PUMP}$ = 222 and 230 nm spectra. As an example, the theoretical and experimental spectra for $\lambda_{PUMP}$ = 222 nm are compared in Fig. 15. As was the case for 248 nm excitation, the positions of the maxima and minima in the spectrum are predicted reasonably well and perhaps 20% of the background continuum intensity can be reproduced by introducing two adjacent vibrational states ($v'$ = 84 and 86) as emitters. The simulated spectrum is, however, unable to reproduce the modulation depth of the intensity variations at the "blue" end of the spectrum. Stated another way, the simulated spectra consistently displayed significant oscillatory structure down to the pump wavelength whereas the experimental spectra did not. Only in a few limited cases can this difficulty be attributed to the spectral resolution of the detection system. Rather, this discrepancy at the shorter wavelengths stems from having, to this point, ignored rotational effects in the simulation. Finally, the obvious differences between the envelopes of the experimental and calculated spectra in Figs. 14 and 15 are directly attributable to the constant dipole approximation [Eq. (4)]. Trial and error iteration of the electronic moment for the $B \rightarrow X$ transition with the goal of reproducing the experimental spectrum's envelope appears to be a feasible approach to estimating the variation of the *relative* value of $\mu_e$ over a limited internuclear separation region.

A summary of the $Zn_2$ $B\,^1\Sigma_u^+$ spectroscopic constants resulting from this work as well as values already in the literature is given in Table I. The uncertainty associated with
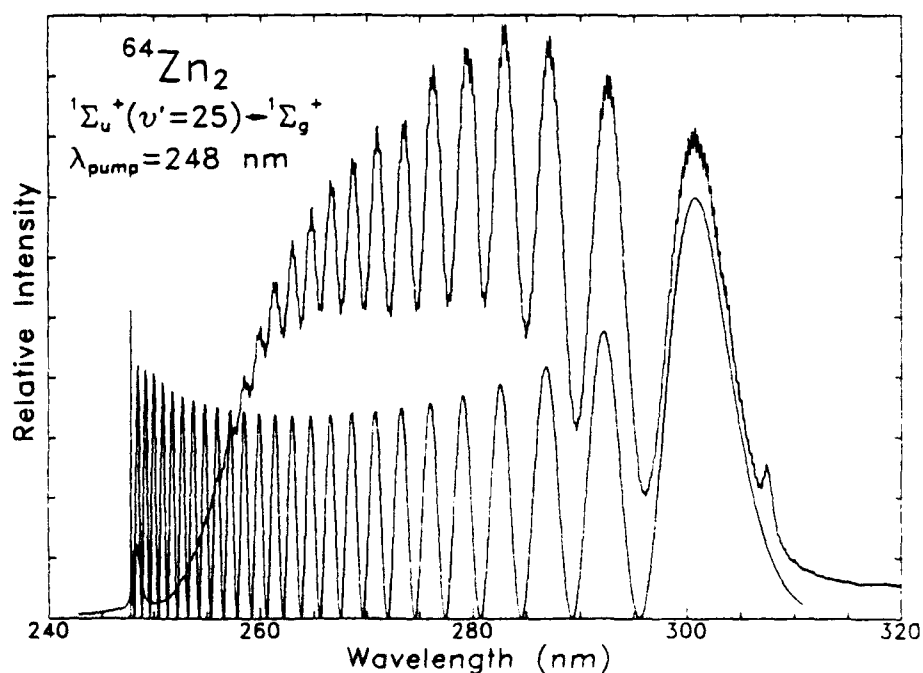


FIG. 14. Comparison of experimental (top) and simulated $Zn_2$ spectra for an excitation wavelength of 248 nm. The calculated spectrum assumes radiation only from $v' = 25$.
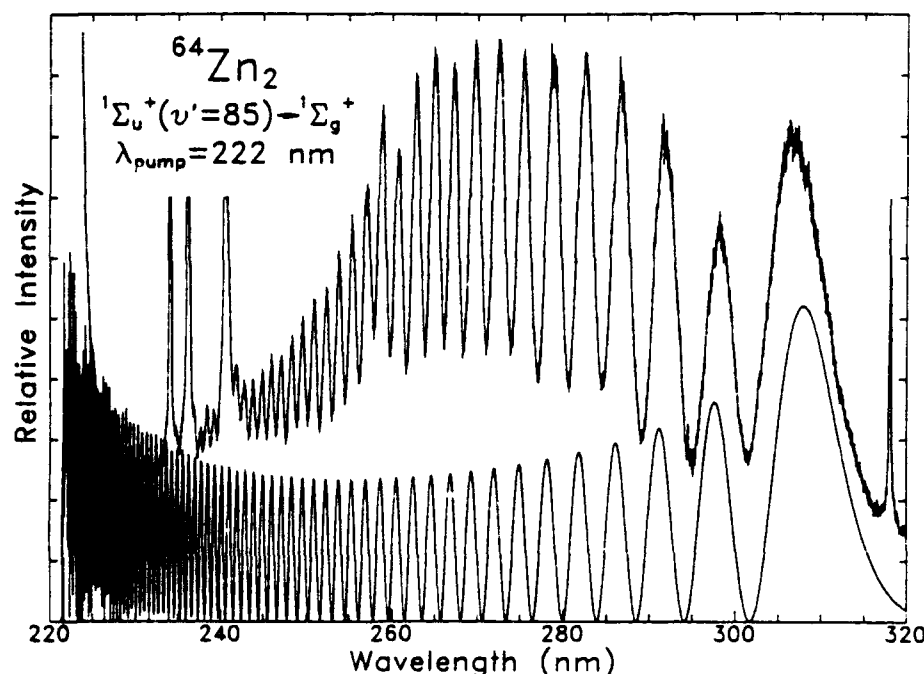
FIG. 15. Spectra similar to those of Fig. 14 except the experimental spectrum (top) was acquired for an excitation wavelength of 222 nm (KrCl laser). The calculated spectrum assumes that only the Zn$_2$ $^1\Sigma_u^+$, $v' = 85$ vibrational level is emitting.

each constant was estimated from the observed sensitivity of simulated spectra to the constant in question.

## 2. $^{114}$Cd$_2$

A similar procedure was followed in simulating the Cd$_2$ emission data. The wavefunctions for the upper and lower state potentials were calculated over the 3.10–6.20 Å internuclear separation interval with a radial grid size of $10^{-3}$ Å. Also, the continuous FCFs were once again evaluated at 500 separate points for lower state energies in the range of $-323$ to 8000 cm$^{-1}$. The potential barrier height in Cd$_2$ is lower than that in the Zn$_2$ case since the difference between the upper and lower state internuclear separations is smaller for Cd$_2$ than for Zn$_2$ [i.e., $\Delta R_e(\text{Zn}_2) > \Delta R_e(\text{Cd}_2)$].

In similar laser spectroscopic experiments to those mentioned earlier for Zn$_2$, Czajkowski, Bobkowski, and Krause[25] measured the vibrational constants for the van der Waals ground state of Cd$_2$. From a Birge–Sponer extrapolation of $O_u^+(^3\Pi_u) \leftarrow XO_g^+(^1\Sigma_g^+)$ vibrational bandheads, the $X^1\Sigma_g^+$ constants were determined to be: $D_e'' = 323.0$ cm$^{-1}$, $\omega_e'' = 23.0$ cm$^{-1}$, $\omega_e'' x_e'' = 0.40$ cm$^{-1}$, and $R_e'' = 5.10$ Å. Again, it is assumed that these constants are valid at shorter internuclear separations as well as in the vicinity of the van der Waals minimum. Therefore, assuming a Morse functional form for both the $X^1\Sigma_g^+$ and $B^1\Sigma_u^+$ interaction potentials and taking the $^1\Sigma_u^+$ ab initio constants of Ref. 13 as the starting values in the iterative process, the solutions that best fit the emission spectra produced by the 248 and 266 nm excitation wavelengths are shown in Figs. 16 and 17, respectively. For Cd$_2$, we present the simulations that result when assuming that emission occurs from an ensemble of vibrational levels and, as stated earlier, they are similar to the results obtained when considering only a single radiating

vibrational state. The significant differences (cf. Fig. 16) are the intensity envelope at the short wavelength extremum of the spectrum and the weak continuous background underlying the FC oscillations in the multivibrational level case that results from broadening of the individual undulations. The fact that the undulations in the experimental spectra are weaker and their spectral widths larger than their counterparts in the simulated spectra testifies to the conclusion that a rigorous simulation will require the inclusion of more radiating vibrational levels. This conclusion is not surprising considering the spectral breadth of the laser excitation pulse, the metal vapor densities ($\sim 10^{18}$ cm$^{-3}$) and the vibrational spacings ($\Delta G$ values) in this energy region. It must be emphasized, however, that adding several vibrational levels has only a minor effect on the spectroscopic constants extracted from the simulation.

The Cd$_2$ $B^1\Sigma_u^+$ structural constants derived from matching the simulations to the experimental spectra are also listed in Table I along with the ab initio values reported in Refs. 11 and 13.

### 3. Rotational effects

The impact of rotational effects on the calculated Zn$_2$ and Cd$_2$ spectra was assessed by incorporating a centrifugal term into the expression for the rotationless potential. Assuming the $B^1\Sigma_u^+(v')$ rotational level manifold to be thermalized, the first iteration took into account only an average value for $J$ ($J_{av} = 142$ for Cd$_2$). A more realistic approximation was subsequently tested by sampling the rotational distribution at seven points (every tenth level in the $J' = 112$–172 interval) and weighting the individual contributions appropriately. Figure 18 illustrates the spectra calculated for emission from the $v' = 22$ level of $^{114}$Cd$_2$ ($B$) assuming no
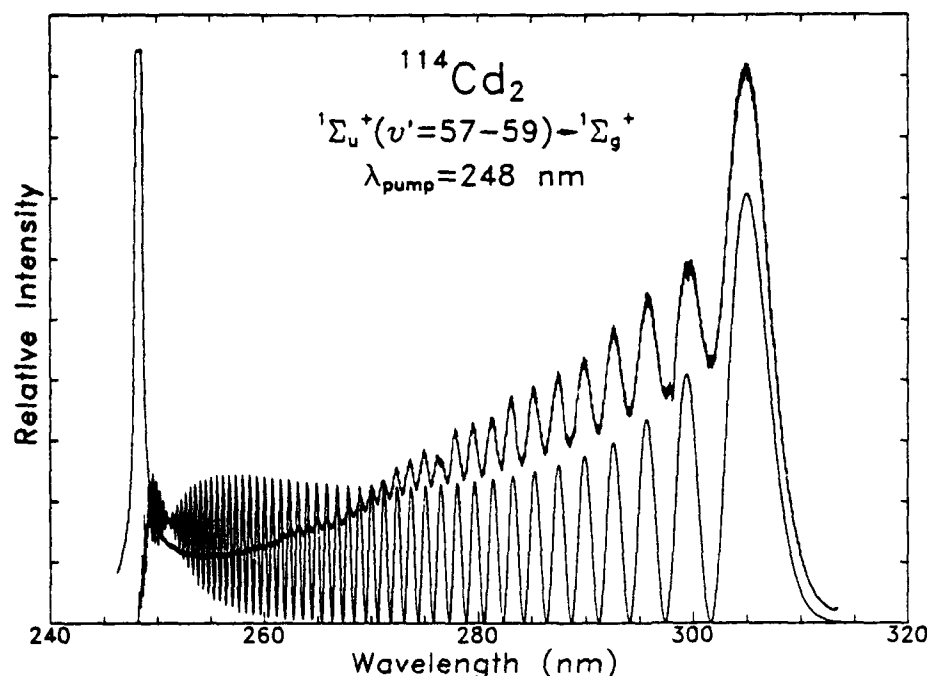
FIG. 16. Experimental ($p_{Cd} = 400$ Torr) and simulated spectra for $Cd_2$ $^1\Sigma_u^+$ assuming that the $v' = 57$–$59$ levels are radiating. The calculated spectrum is almost identical to the $v' = 58$ simulation except for the region below $\sim 260$ nm.
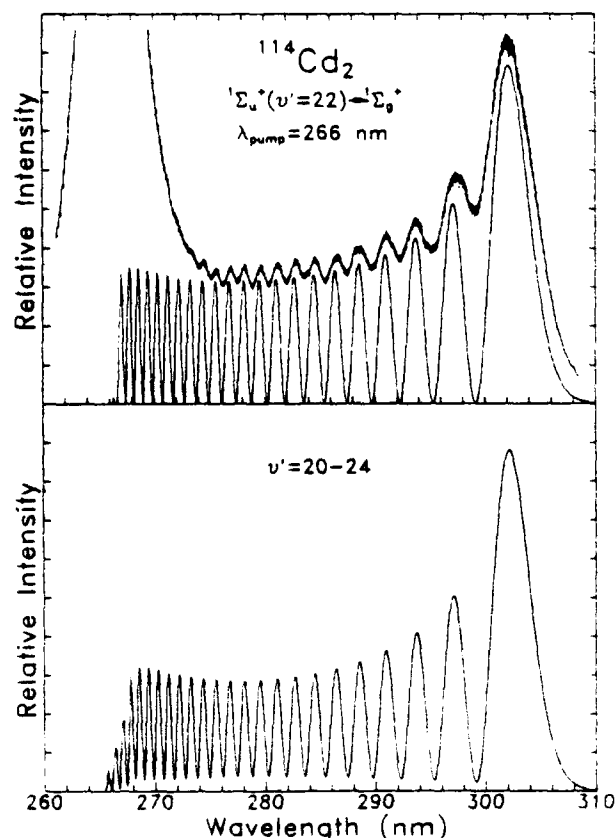


FIG. 17 Comparison of $Cd_2$ $^1\Sigma_u^-$ – $^1\Sigma_g^-$ simulated spectra showing the differences between assuming that one ($v' = 22$, top spectrum) or several ($v' = 20$–$24$, bottom spectrum) vibrational levels are emitting. The excitation wavelength is 266 nm and the experimental spectrum is also given at the top of the figure.

rotational effects (top), an average value for $J$ (middle) and the multilevel approximation (bottom). Although the fit of the simulated spectrum improves somewhat as rotation is added, the impact is slight. Comparison of the $B$ state constants derived from the simulations also revealed only small differences attributable to the rotational distribution. For $v' = 22$, for example, $D'_e$ is determined to be 8350 cm$^{-1}$ if rotational effects are completely ignored and rises to 8400 cm$^{-1}$ if the average $J$ value or the weighted distribution are used. Similarly, $R'_e$ and $\beta'$ remain essentially unchanged and the quoted uncertainties for the constants in Table I more than adequately reflect the error introduced by approximating the rotational distribution.

## V. DISCUSSION AND CONCLUSIONS

Few molecular constants for $Cd_2$ and $Zn_2$ with which our results can be compared exist in the literature. However, the ab initio calculations reported by Hay et al.[11] and Bender and co-workers[13] yield $Zn_2$ constants that are in reasonable agreement with the values determined from our experiments (cf. Table I). Specifically, our constants are $\sim 10\%$ larger than those given in Refs. 11 and 13. However, the constants reported here must be viewed with some caution because of the assumption adopted earlier that Morse potential parameters determined for the $X$ $^1\Sigma_g^+$ state at $R_e$ are valid at much smaller $R$. Consequently, we perceive the differences between the constants resulting from this work and the values of Refs. 11 and 13 to be negligible. Ault and Andrews' experiments[26] with the Column IIB dimers in rare gas matrices, on the other hand, yield estimated values for $D_e$ and $\omega_e$ that are the largest yet reported but are still consistent with both the theoretical and experimental constants of Ta-

TABLE I. Spectroscopic constants for the $B\ ^1\Sigma_u^+$ states of $Zn_2$ and $Cd_2$.

| Molecule | $D_e\,(cm^{-1})$ | $\omega_e\,(cm^{-1})$ | $\omega_e x_e\,(cm^{-1})$ | $\Delta R_e\,(\text{Å})^c$ | Ref(s). | Comments |
|---|---|---|---|---|---|---|
| | 12 065[a] | 132[b] | ... | ... | 20, 26 | Rare gas matrix experiments |
| | 8 145 | 115 | 0.41 | ... | 13 | ab initio calculations |
| $Zn_2$ | 8 065 | 107 | 0.36 | ... | 11 | ab initio |
| | $9\,010 \pm 200$ | $122 \pm 10$ | $0.40 \pm 0.04$ | $1.19 \pm 0.02$ | This work | |
| | 10 650[a] | 104[b] | ... | ... | 20, 26 | Rare gas matrix experiments |
| $Cd_2$ | 7 740 | 78 | 0.2 | ... | 13 | ab initio |
| | $8\,250 \pm 200$ | $92 \pm 10$ | $0.26 \pm 0.04$ | $0.92 \pm 0.02$ | This work | |

[a] Estimated from the value published for $D_0$ (Ref. 26).
[b] The value cited here is not strictly a vibrational constant but is rather the average vibrational spacing measured in experiments in which $Zn_2$ and $Cd_2$ were observed in absorption in argon matrices.
[c] $\Delta R_e = R_{e,u} - R_{e,x}$.

ble I. The spread in values is partially due to the fact that previous studies did not have access to a well-known ground state potential. For example, Ault and Andrews' (Ref. 26) determination of $D_0'$ was based on an expression which assumed a value for $D_0''$ that is now known to be too large [i.e., $D_0''(Zn_2) \simeq 2000\ cm^{-1}$ and $D_0''(Cd_2) \simeq 600\ cm^{-1}$]. Conse-

quently, the resulting value for $D_0'$ is also excessive.[26]

The simulation procedure described in Sec. IV C is extremely sensitive to the value assumed for the difference between the equilibrium internuclear separations for the $X\ ^1\Sigma_g^+$ and $B\ ^1\Sigma_u^+$ states ($\equiv \Delta R_e$). Combining the value for $\Delta R_e$ resulting from the spectral simulations (1.19 Å) with $R_e(^1\Sigma_g^+)$ given in Ref. 24 ($R_e'' = 4.80$ Å) yields $R_e' = 3.61$ Å which was used to calculate the $^1\Sigma_u^+$ vibrational wave functions. Although this excited state equilibrium internuclear separation is $\sim 0.7$ Å larger than those reported in Refs. 11 and 13 (2.9 and 2.97 Å, respectively), our value is only $\sim 10\%$ larger than the $R_e$ determined by Su et al. from gas phase absorption measurements (3.30 Å).[23]

Similar comments can be made regarding a comparison of the $Cd_2$ constants. The values from Ref. 13 for $\omega_e$ and $D_e$ in Table I agree with the constants derived from the present experiments to within $\sim 12\%$ whereas Ault and Andrews' value (10 650 $cm^{-1}$) is 13%–14% larger than the other two.

Our value for $\Delta R_e$ for $Cd_2$ (0.92 Å) yields $R_e'(^1\Sigma_u^+) = 4.18$ Å if the ground state equilibrium internuclear separation is taken to be 5.10 Å (Ref. 25). Once again, this value for $R_e'$ is larger than that predicted by the ab initio calculations (3.24 Å)[13] but agrees quite closely with the value reported by Su et al.[23] ($R_e = 4.10$ Å). Although rotationally resolved laser spectroscopic experiments will be required to accurately determine molecular bond lengths for the $Zn_2$ and $Cd_2$ excited states, it is reasonable to conclude that: (1) the spectroscopic constants derived from comparing the simulated spectra with the experimental spectra are plausible within an uncertainty of 10%–20% and 2) the description of both molecular states with Morse potentials appears to be a valid representation over a limited range in $R$.

Several comments, however, must be made regarding the simplifications made in simulating the emission spectra. Rotational effects affect the positions and widths of undulations in bound-free spectra and, as discussed earlier, are largely responsible for the uncertainties in he constants of Table I. Assessing the impact on the results of assuming a
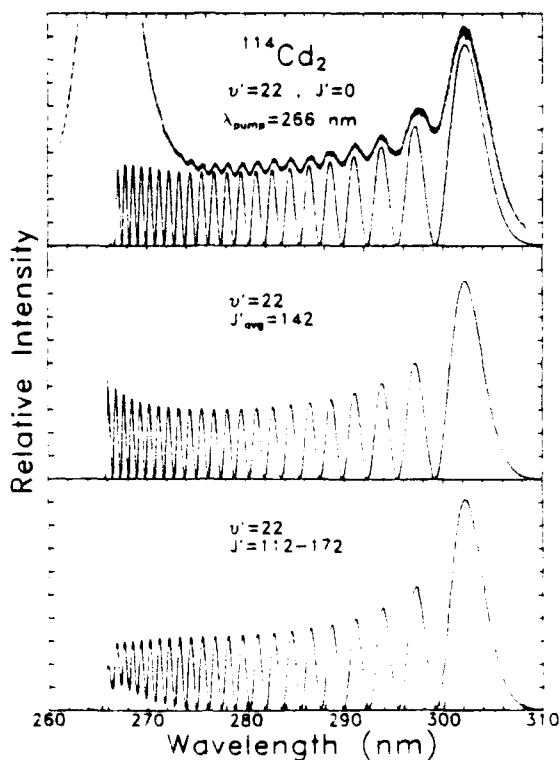


FIG. 18 Effect of various approximations regarding the upper state rotational distribution on the calculated spectra for the $v' = 22$ level of $^{114}Cd_2$ ($B\ ^1\Sigma_u^+$): (top) rotational effects ignored; (middle) an average value for $J$; and (bottom) a multilevel distribution in which the contribution from each of seven rotational states in the 112–172 interval (i.e., 112, 122, 132,..., 172) is weighted appropriately.

dipole moment that is insensitive to $R$ is more difficult because of the competing effect of collisional relaxation of $B\,^1\Sigma_u^+$ vibrational states on the emission spectrum. Evaluation of simulated spectra for a wide range in molecular parameters indicates that the adoption of Eq. (4) affects primarily the spectrum's envelope and the constants $D_e$, $\omega_e$, and $\Delta R_e$ of Table I are, therefore, expected to be valid to within the stated uncertainties. Because of the present experimental conditions *and*, for a fixed laser wavelength, the overlap of partial waves for the photoassociation of Cd–Cd or Zn–Zn pairs to adjacent, excited state vibrational levels, it is not possible to excite a specific $B\,^1\Sigma_u^+$ vibrational level. Indeed, the data and simulations confirm that the spectra reported here are the result of contributions from an ensemble of radiating $v'$ levels.

## VI. SUMMARY

Bound–free emission spectra of $^{64}Zn_2$ and $^{114}Cd_2$ have been observed in the 200–300 nm spectral region by irradiating the respective metal vapors with several discrete wavelengths from an excimer or Nd:YAG laser. The observed fluorescence is attributed to $B\,^1\Sigma_u^+ \rightarrow X\,^1\Sigma_g^+$ transitions of the molecule where the bound upper state is derived from $np\,^1P_1 + ns^2\,^1S_0$ ($n = 4$ and 5 for Zn and Cd, respectively). For the higher metal vapor densities ($\gtrsim 5\times10^{17}$ cm$^{-1}$), the spectra are dominated by Franck–Condon interference oscillations that are broadened by rotational effects and the contributions from adjacent $v'$ levels that are also radiating. Also, the dependence of the bound–free emission intensity on vapor pressure (number density) demonstrates that the $^1\Sigma_u^+$ excited molecules are produced primarily by photoassociative processes involving two free ground state atoms and an ultraviolet photon. Numerical simulations of the experimental spectra yield constants that, in general, are within $\sim 10\%$ of *ab initio* values.

## ACKNOWLEDGMENTS

[1] J. Tellinghuisen, in *Photodissociation and Photoionization*, edited by K. P. Lawley, Advances in Chemical Physics, Vol. LX (Wiley, New York, 1985), pp. 299–369

[2] C. R. Vidal and H. Scheingraber, J. Mol. Spectrosc. **65**, 46 (1977); H. Scheingraber and C. R. Vidal, J. Chem. Phys. **66**, 3694 (1977).

[3] K. Sakurai and H. P. Broida, J. Chem. Phys. **65**, 1138 (1976).

[4] C. R. Vidal, J. Chem. Phys. **72**, 1864 (1980).

[5] T. Bergeman and P. F. Liao, J. Chem. Phys. **72**, 886 (1980).

[6] G. Gerber, R. Möller, and H. Schneider, J. Chem. Phys. **81**, 1538 (1984).

[7] D. J. Ehrlich and R. M. Osgood, Jr., Phys. Rev. Lett. **41**, 547 (1978); Chem. Phys. Lett. **61**, 150 (1979).

[8] S. M. Adler and J. R. Wiesenfeld, J. Mol. Spectrosc. **66**, 357 (1977); Chem. Phys. **43**, 21 (1979).

[9] J. Supronowicz, R. J. Niefer, J. B. Atkinson, and L. Krause, J. Phys. B **19**, L717 (1986).

[10] K. P. Lawley, D. Austin, J. Tellinghuisen, and R. J. Donovan, Mol. Phys. **62**, 1195 (1987).

[11] P. J. Hay, T. H. Dunning, Jr., and R. C. Raffenetti, J. Chem. Phys. **65**, 2679 (1976).

[12] F. H. Mies, W. J. Stevens, and M. Krauss, J. Mol. Spectrosc. **72**, 303 (1978).

[13] C. F. Bender, T. N. Rescigno, H. F. Schaefer III, and A. E. Orel, J. Chem. Phys. **71**, 1122 (1979).

[14] M. Krauss and F. H. Mies, in *Excimer Lasers*, 2nd ed., edited by C. K. Rhodes (Springer, Berlin, 1984), pp. 28–32.

[15] H. Tatewaki, M. Tomonari, and T. Nakumura, J. Chem. Phys. **82**, 5608 (1985).

[16] (a) In the gas phase see, for example, H. Hamada, Philos. Mag. **12**, 50 (1931); J. G. Winans, Phys. Rev. **37**, 902 (1931); R. E. Drullinger and M. Stock, J. Chem. Phys. **68**, 5299 (1978); A. Kowalski, Z. Naturforsch. Teil A **39**, 1134 (1984); (b) The emission spectrum of $Zn_2$ in a rare-gas matrix was reported by W. Schroeder, H. Wiggenhauser, W. Schrittenlacher, and D. M. Kolb, J. Chem. Phys. **86**, 1147 (1987).

[17] The cutoff wavelengths for these filters are those for which the absorbance is 1.0 for a path length of 1.0 cm.

[18] E. U. Condon, Phys. Rev. **32**, 858 (1928).

[19] For a recent review, see M. D. Morse, Chem. Rev. **86**, 1049 (1986).

[20] J. C. Miller and L. Andrews, Appl. Spectrosc. Rev. **16**, 1 (1980).

[21] C. H. Corliss and W. R. Bozman, *Experimental Transition Probabilities for Spectral Lines of Seventy Elements*, NBS Monograph 53 (U.S. Government Printing Office, Washington, DC, 1962), p. 540.

[22] K. D. Carlson and K. R. Kuschnir, J. Phys. Chem. **68**, 1566 (1964).

[23] C.-H. Su, P.-K. Liao, Y. Huang, S.-S. Liou, and R. F. Brebrick, J. Chem. Phys. **81**, 11 (1984).

[24] M. Czajkowski, R. Bobkowski, and L. Krause, Phys. Rev. A **41**, 277 (1990).

[25] M. Czajkowski, R. Bobkowski, and L. Krause, Phys. Rev. A **40**, 4338 (1989).

[26] B. S. Ault and L. Andrews, J. Mol. Spectrosc. **65**, 102 (1977).

# Laser excitation spectroscopy of Ne$_2$ $np\pi$ $\Pi_g$ Rydberg states observed in the afterglow of a corona discharge

D. J. Kane,[a] S. B. Kim, and J. G. Eden

*Everitt Laboratory, University of Illinois, Urbana, Illinois 61801*

M. L. Ginter

*Institute for Physical Science and Technology, University of Maryland, College Park, Maryland 20742*

Several Rydberg series attributable to transitions originating from the $a\ ^3\Sigma_u^+$ metastable state of the neon dimer have been observed by laser excitation spectroscopy in the afterglow of a pulsed corona discharge. The $n = 4$–9 members of an $np\pi$ $\Pi_g \leftarrow a(0$–$0)$ series have been rotationally resolved and the upper states characterized. The probable multiplicity of the $\Pi_g$ states is discussed. An unusual loss of intensity in the $Q$ branches for the higher $n$ member transitions and a weak perturbation between the $v = 1$ vibrational level of the $5f\sigma\ ^3\Sigma_g^+$ state and the $6p\pi$ $\Pi_g$, $v = 0$ level are also reported.

## I. INTRODUCTION

The rare gas dimers are members of a larger class of interesting molecules having dissociative ground states and Rydberg excited states. Herzberg[1] has proposed the term Rydberg molecules to describe these species which represent a subset of the excimer molecules. Such diatomic molecules afford an excellent opportunity to investigate Rydberg–Rydberg interactions without the added complexities introduced by interactions with valence or ion pair states such as are present in N$_2$, NO, the group II B dimers, or the diatomic hydrogen halides.

Several experimental difficulties have, however, hindered study of the heavier rare gas dimers. For most of the excited states of the Ne$_2$, Ar$_2$, Kr$_2$, and Xe$_2$ dimers, predissociation dominates radiative decay. Consequently, the spontaneous emission studies that proved so effective in elucidating in detail the electronic structure of He$_2$ are of less utility for the other members of the rare gas dimer family. Furthermore, the equilibrium internuclear separation for Rydberg levels built on the diatomic ion ground state [Rg$_2^+$ ($X\ ^2\Sigma_u^+$)] and the van der Waals (vdW) minimum of the neutral species' ground state typically differ by more than 1 Å, which complicates investigation of the lower vibrational levels of dimer excited levels by photoabsorption. Thus, past experiments generally have examined the high $v$ portions of selected excited states by either: (1) single photon absorption (or photoionization) experiments involving ungerade Rydberg states excited by incoherent lamp, tunable VUV laser, or synchrotron radiation; or (2) multiphoton laser excitation combined with ion mass or photoelectron energy spectroscopies.

In 1985, Killeen and Eden[2] reported low resolution absorption spectra of electron beam-produced rare gas plasmas which revealed clear Rydberg series believed to originate from the lowest excited states of Kr$_2$ and Ar$_2$. When combined with subsequent[3] work on Ne$_2$ and Xe$_2$, these data

yielded rough values for the first ionization limit of each of the four dimers. Laser pump–probe techniques introduced by Ediger and Eden[4,5] for Kr$_2$ involved: (1) multiphoton and collisional production of the initial (metastable) dimer state; (2) production of higher Rydberg levels by probing the metastable diatomic species with a second laser pulse; and (3) detection of the Rydberg levels by monitoring the atomic photofragment emission resulting from the predissociation of these molecular states. Experimental advantages associated with a pump–probe approach include improved spectral resolution (arising from the narrow probe laser linewidth and operation at reduced gas pressures) and temporal information. However, while multiphoton excitation is an effective technique for preparing the lowest excited states of the Kr and Xe dimers, the ~15–22 eV ionization potentials of the lighter rare gases make the procedure less attractive for producing Ne$_2$ or Ar$_2$ excited states. To circumvent this difficulty, Ne$_2$ metastables were produced in the afterglow of a pulsed discharge (and optically probed as described above) in the studies reported in Ref. 6, with the result that several bands of the neon dimer were resolved and a rotational constant was determined for the lowest $^3\Sigma_u^+$ metastable state which agreed well with theory. More recently, Kim et al.[7] extended the approach with ~1 GHz spectral resolution to studies of the rotationally resolved $^3\Sigma_g^+$ and $^3\Pi_g$ components of the $4f$, $5f$, and $6f$ complexes of Ne$_2$.

In this paper, the results of similar experiments involving $np\pi$ $\Pi_g$ Rydberg states of Ne$_2$ are presented. The (0–0) bands of transitions originating from the lowest $^3\Sigma_u^+$ excited state of Ne$_2$ (denoted here as $a\ ^3\Sigma_u^+$) and terminating at $np\pi$ $\Pi_g$ states ($n = 4$–9) have been rotationally resolved and characterized. Several additional Rydberg series also are discussed briefly and a perturbation between the $6p\pi$ $\Pi_g$ ($v = 0$) and $5f\sigma\ ^3\Sigma_g^+$ ($v = 1$) levels is identified.

## II. Ne$_2$ ORBITAL AND STATE LABELS

The majority of the excited states reported here appear to be associated with the addition of a Rydberg electron to

the $X\,^2\Sigma_u^+$ ground state configuration[8,9] of $Ne_2^+$,

$$1\sigma_g^2 1\sigma_u^2 2\sigma_g^2 2\sigma_u^2 3\sigma_g^2 1\pi_u^4 1\pi_g^4 3\sigma_u, \quad X\,^2\Sigma_u^+, \qquad (1)$$

to produce the Rydberg configurations

$$1\sigma_g^2 1\sigma_u^2 2\sigma_g^2 2\sigma_u^2 3\sigma_g^2 1\pi_u^4 1\pi_g^4 3\sigma_u n l\lambda. \qquad (2)$$

The $X\,^1\Sigma_g^+$ ground state of the neutral dimer can be associated with the configuration

$$1\sigma_g^2 1\sigma_u^2 2\sigma_g^2 2\sigma_u^2 3\sigma_g^2 1\pi_u^4 1\pi_g^4 3\sigma_u^2, \qquad (3a)$$

which, when expressed in terms of the $nl\lambda$ united atom molecular orbital (UAMO) designations, becomes

$$1s\sigma^2 2p\sigma^2 2s\sigma^2 3p\sigma^2 3d\sigma^2 2p\pi^4 3d\pi^4 4p\sigma^2. \qquad (3b)$$

Excitation of a $4p\sigma$ electron to the next available $ns\sigma$ orbital, $3s\sigma$, results in the formation of the $a\,^3\Sigma_u^+$ and $A\,^1\Sigma_u^+$ excited states, the lowest excited singlet and triplet $\Lambda = 0$ states, from the configuration

$$(1s\sigma^2 2p\sigma^2 2s\sigma^2 3p\sigma^2 3d\sigma^2 2p\pi^4 3d\pi^4 4p\sigma)3s\sigma, \quad ^{1,3}\Sigma_u^+, \qquad (4a)$$

which can also be expressed as

$$[Ne_2^+(X\,^2\Sigma_u^+)]3s\sigma, \quad ^{1,3}\Sigma_u^+, \qquad (4b)$$

where $3s\sigma$ denotes the Rydberg orbital and the square bracketed term identifies the ground state configuration of the molecular ion core. The usual practice in labeling Rydberg states is to specify an appropriate Rydberg UAMO and term symbol such as $3s\sigma\,^3\Sigma_u^+$. Addition of a standard alphabetical label yields $3s\sigma\,a\,^3\Sigma_u^+$ which we will usually shorten for convenience to $a\,^3\Sigma_u^+$. From Eqs. (3b) and (4b), it follows that the first $nl\lambda$ UAMOs outside the core with $l = 1$ or 3 are $5p\sigma$, $3p\pi$, $4f\sigma$, $4f\pi$, $4f\delta$, and $4f\phi$. If the $2\pi_u$ orbital were to lie below $1\pi_g$ as it does in $He_2$, then the lowest $np\pi$ orbital would be $4p\pi$. While we will employ a labeling scheme con-

sistent with Eqs. (1)–(4), we note that caution should be employed in interpreting the principal quantum number ($n$) value as anything other than a relative index.

## III. EXPERIMENTAL APPROACH

Details regarding the experimental apparatus and data acquisition procedure have been described previously.[6,7,10] Briefly, production of the $a\,^3\Sigma_u^+$ metastable dimers is accomplished with a corona discharge (having an $E/N \simeq 390$ Td; 1 Td $\equiv 10^{-17}$ V cm²) in research grade $^{20}Ne$ or $^{22}Ne$ gas at room temperature pressures of 120–200 Torr. At an adjustable time delay ($\Delta t$) into the plasma afterglow, the dimer metastables are photoexcited by a pulsed dye laser having a linewidth of either $\sim 0.04$ cm$^{-1}$ ($\sim 1.3$ GHz) or 2 cm$^{-1}$ (for survey spectra). Atomic Ne fluorescence resulting from the predissociation of the photoexcited $Ne_2$ states is collected at 90° to the laser beam path (and the discharge axis) by a lens telescope and is detected by a cooled photomultiplier. Dielectric bandpass filters were used to isolate the particular Ne transition of interest which, for most of the experiments to be described here, was the $3p(1/2)_1 \rightarrow 3s(3/2)_2^0$ transition at 703.2 nm. Because of collisional mixing of the fine structure levels of the $ns$ and $np$ atomic manifolds, few differences are observed between excitation spectra acquired by monitoring different $np \rightarrow ns$ transitions. Throughout each spectral scan, the relative dye laser wavelength was monitored by an etalon [free spectral range (FSR) = 2 cm$^{-1}$], while absolute wavelength calibration was carried out by optogalvanic spectroscopy in a U/He discharge. Also, the dye laser pulse energy was maintained by computer control to within $\pm 2\%$ across the entire scan region for a given dye.

Figure 1 shows the contrast between the temporal histories of the Ne $3s(3/2)_2^0$ atomic and $Ne_2$ $a\,^3\Sigma_u^+$ molecular
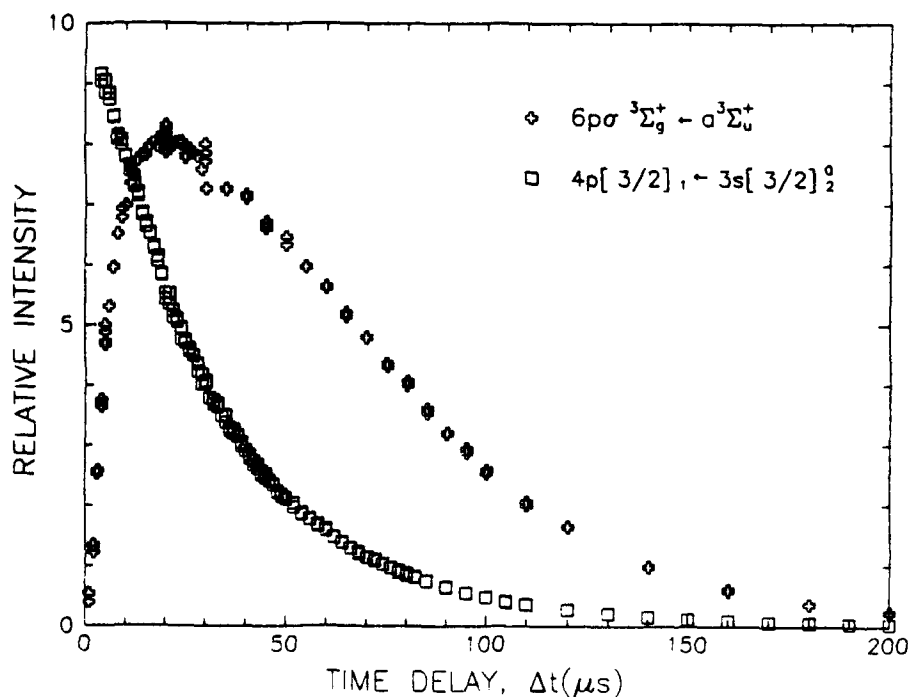


FIG. 1. Temporal variation of the excited atomic (open squares) and diatomic (open crosses) neon populations monitored by laser-induced fluorescence in the afterglow of a pulsed Ne discharge. The Ne pressure was 200 Torr and the relative Ne $3s(3/2)_2$ metastable and $Ne_2$ $a\,^3\Sigma_u^+$ number densities were recorded by exciting the $4p(3/2)_1 \rightarrow 3s(3/2)_2^0$ ($\lambda = 345.08$ nm) and $6p\sigma\,^3\Sigma_g^+ \leftarrow a\,^3\Sigma_u^+$ transitions ($\lambda = 425.25$ nm), respectively, and monitoring the relative intensity of the Ne $3p(1/2)_1 \rightarrow 3s(3/2)_2^0$ transition. Note that the peak atomic signal is off scale.
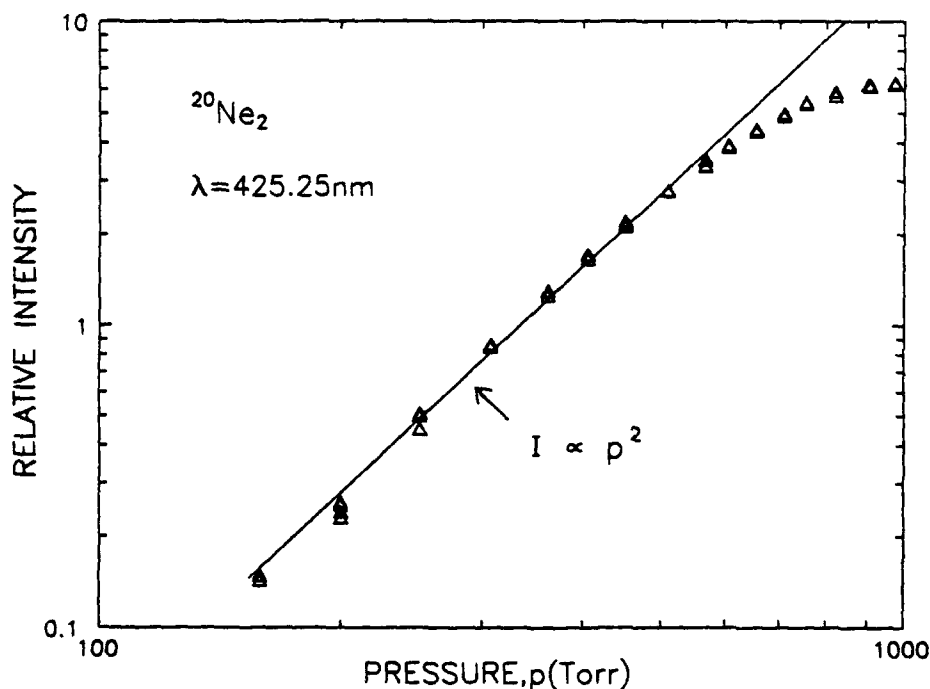
Plot legend:
◇ $6p\sigma\,^3\Sigma_g^+ \leftarrow a\,^3\Sigma_u^+$
□ $4p[3/2]_1 \leftarrow 3s[3/2]_2^0$

Y-axis: RELATIVE INTENSITY (0 to 10)
X-axis: TIME DELAY, $\Delta t(\mu s)$ (0 to 200)

FIG. 2. Pressure dependence of the relative Ne$_2$ $a\,^3\Sigma_u^+$ number density (monitored at 425.25 nm) for $\Delta t = 20\,\mu s$. The solid line drawn through the data represents a quadratic variation of the Ne$_2$ $6p\sigma\leftarrow a$ transition intensity with the neon pressure $p$.

populations following the discharge. The atomic metastable number density [monitored by pumping the $4p(3/2)_1\leftarrow 3s(3/2)_2^0$ transition at 345.08 nm] decays monotonically following the termination of the discharge, whereas the molecular population [observed by atomic laser-induced fluorescence upon pumping the $6p\sigma\leftarrow a(0\text{--}0)$ transition in the blue-425 nm] peaks $\sim 20\,\mu s$ into the afterglow. Experience has shown that the long effective lifetime of the Ne$_2$ $a\,^3\Sigma_u^+$ metastable state results in excellent experimental signal-to-noise ratios for $\Delta t$ as large as 100 $\mu s$. In addition, as illustrated in Fig. 2, the relative Ne$_2$ $a\,^3\Sigma_u^+$ number density varies quadratically with the Ne pressure for $p_{Ne}\lesssim 600$ Torr. One concludes that the temporal and pressure dependencies presented in Figs. 1 and 2 are consistent with those expected for a transient molecular species formed by a three body collision.

Not surprisingly, the atomic fluorescence resulting upon photoexciting a Ne$_2$ inter-Rydberg transition differs markedly from that observed during the active discharge. A comparison of the spectra recorded with a 1/4 m spectrograph (30 Å/mm reciprocal dispersion in first order) equipped with a multichannel array detector (OSMA) is given in Fig. 3. In acquiring these data, the intensified detector array was gated "on" for 60 ns. Final spectra are the result of averaging 2400 shots, obtained at a repetition frequency of 2 Hz, and accounting for both scattered dye laser and ambient radiation. The top spectrum [Fig. 3(a)] was recorded just prior to terminating the corona discharge, while the data of Fig. 3(b) were acquired 20 $\mu s$ into the afterglow by pumping the $6p\sigma\,^3\Sigma_g^+\leftarrow a(0\text{--}0)$ transition at 425 nm. In the absence of a dye laser pulse, no fluorescence was observed in this spectral region for $\Delta t = 20\,\mu s$.

Several reproducible differences between the two spectra of Fig. 3, which are representative of observations made

from a number of experimental trials, are evident. The most obvious of these is the virtual absence of $3p'$ emission in the laser-induced fluorescence spectrum of Fig. 3(b)—note especially the decline of the $3p'(1/2)_0\rightarrow 3s'(1/2)_1^0$ and $3p'(1/2)_1\rightarrow 3s'(1/2)_1^0$ transitions at 585.25 and 659.9 nm, respectively. One is unable to invoke collisional processes to explain the differences in the spectra of Fig. 3 since both were acquired under virtually identical conditions. Rather, the dominance of emission from $3p$ states [and the $3p(3/2)_1\rightarrow 3s(3/2)_1^0$ transition lying at 638.3 nm, in particular] is likely attributable to: (1) the higher energies of the Ne($3p'$) states relative to the $3p$ manifold and (2) the position and slope of the repulsive interaction potentials, correlated with Ne($3p'$) + Ne($^1S_0$) in the vicinity of the photoexcited Ne$_2$ state ($6p\sigma\,^3\Sigma$).

## IV. RESULTS AND DISCUSSION

The energy levels $E(n)$ for relatively unperturbed Rydberg series follow the expression[7,11]

$$E(n) - E(n = \infty) = -\frac{R}{(n^*)^2} = -\frac{R}{(n-\delta)^2}, \quad (5)$$

where $E(n = \infty)$, $R$, $n^*$, $n$, and $\delta$ are the ionization energy for the series, the Rydberg constant, the effective quantum number, the principal quantum number, and the quantum defect, respectively. For $^{20}$Ne$_2$, $R = 109\,735.81$ cm$^{-1}$ while the values of $E(n = \infty)$ and $E(n)$ depend on the reference zero of energy chosen. In the Ne$_2$ data presented below, we have chosen to use the $N = 0$, $v = 0$ rotational–vibrational level of the $a\,^3\Sigma_u^+$ state as the zero of energy, and have employed the level energies reported in Table V of Ref. 7 throughout this work.

As discussed in Ref. 7, triplet splitting has not, to date, been resolved in Ne$_2$ spectra which implies that excited state
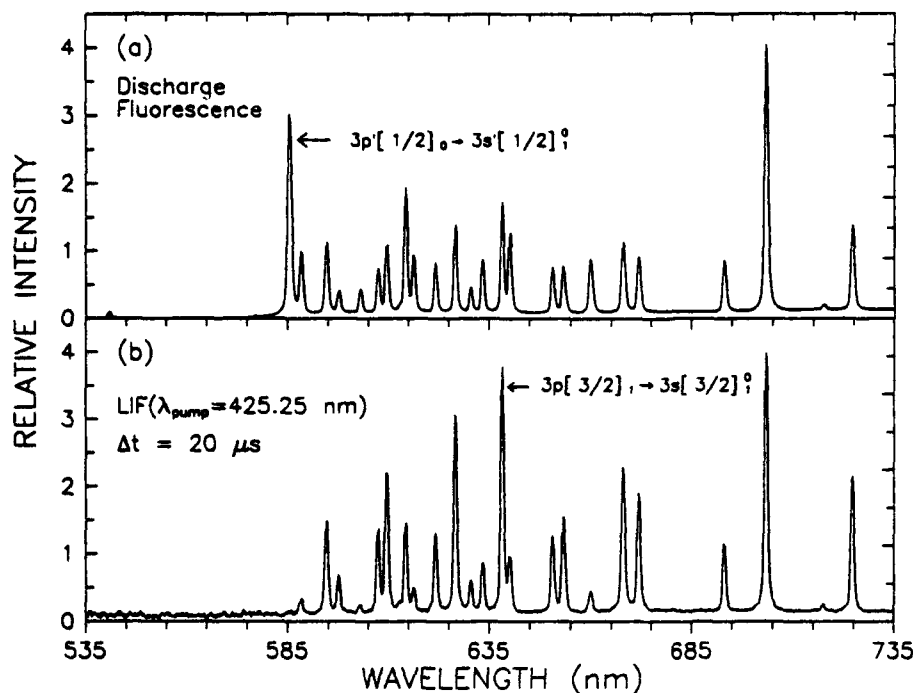
FIG. 3. Comparison of (a) the atomic Ne spontaneous emission spectrum observed from the active discharge (i.e., no probe laser pulse) and (b) the laser-induced atomic fluorescence (LIF) detected in the afterglow for a dye laser wavelength of 425.25 nm (corresponding to the peak of the unresolved $6p\sigma\,^3\Sigma_g^+ - a\,^3\Sigma_u^+$ band) and $\Delta t = 20\,\mu$s. Without a dye laser pulse, no emission was detectable in this spectral region at 20 $\mu$s into the afterglow. Two of the most prominent lines are identified.

structures are described by case $b'$ coupling (singlet or unresolved spin multiplets). This result is analogous to the situation observed for He₂ where such splittings are generally negligible. In addition, because the nuclear spins are zero in $^{20}$Ne₂, only alternate branch lines will appear in $\Sigma_g^+ - \Sigma_u^+$ and $\Pi_g - \Sigma_u^+$ type transitions. Consequently, each band of Ne₂ associated with transitions of $\Sigma_g^+ - \Sigma_u^+$ type will consist

of one $R(N)$ and one $P(N)$ branch having only odd $N$ values, where $N$ is the quantum number for total angular momentum, excluding spin. Case $b'$ transitions of $\Pi_g - \Sigma_u^+$ type will have three branches which can be divided into two groups: one $R(N)$ and one $P(N)$ branch with $N$ odd for $\Pi_g^+ \leftarrow \Sigma_u^+$ transitions and one $Q(N)$ branch with $N$ odd for $\Pi_g^- - \Sigma_u^+$ transitions. The $\Pi_g^+$ and $\Pi_g^-$ states are reflection
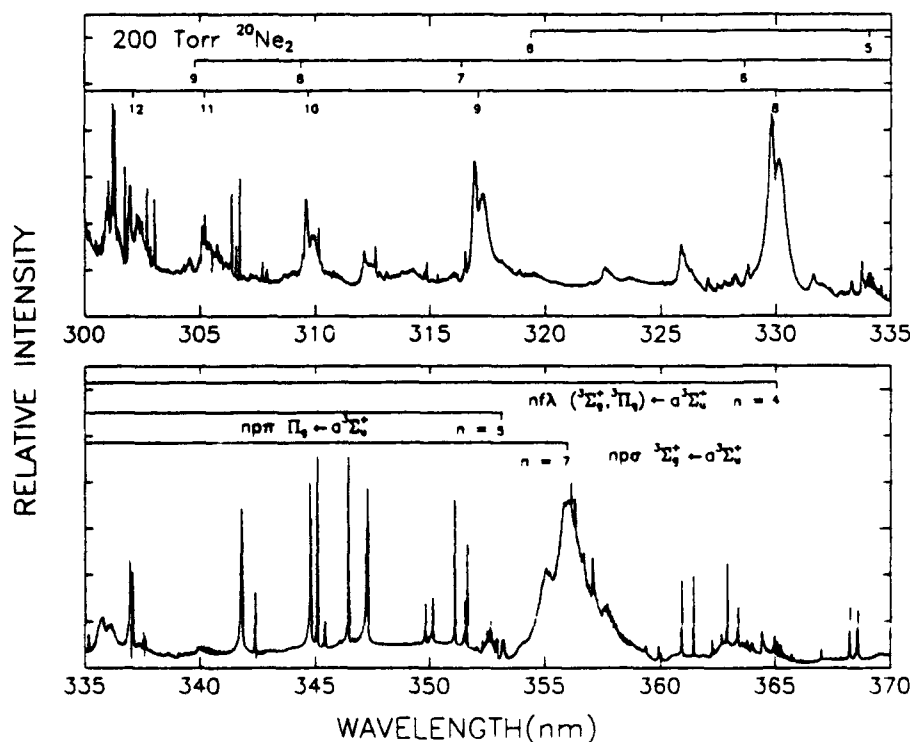


FIG. 4. Excitation spectrum of $^{20}$Ne₂ $(a\,^3\Sigma_u^+)$ in the 300–370 nm region. In addition to the $np\pi\,\Pi_g - a\,^3\Sigma_u^+$ (0–0) series discussed in this paper, the dominant series, attributed to $np\sigma\,^3\Sigma_g^+ - a$(0–0) transitions, and several members of the $nf\pi\,^3\Pi_g - a$(0–0) and $nf\sigma\,^3\Sigma_g^+ - a$(0–0) Rydberg series (Ref. 7) are also indicated. The $n = 4$ member of the $np\pi\,\Pi_g - a$(0–0) series lies at $\lambda \approx 417$ nm and is not included here (see Fig. 5). Also, the $^{20}$Ne pressure was 200 Torr and the dye laser linewidth for this survey was 0.2 cm⁻¹.
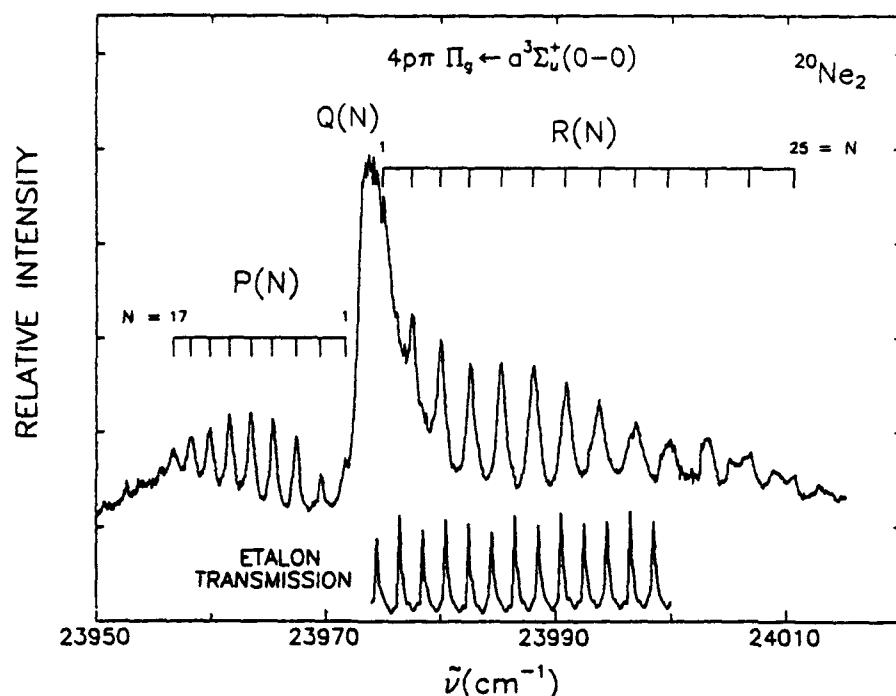
FIG. 5. Laser excitation spectrum of $^{20}$Ne$_2$ in the $23\,950 < \tilde{\nu} \leq 24\,010$ cm$^{-1}$ region showing the resolved $P$ and $R$ branches of the $4p\pi\ \Pi_g - a\ ^3\Sigma_u^+$ (0–0) transition. While the strong $Q$ branch is collapsed and not resolved, the $N = 1$ lines of both the $P$ and $R$ branches are evident. The pressure of the 99.5% enriched $^{20}$Ne was 200 Torr. The lower trace shows the scan of the etalon's relative transmission (FSR = 2 cm$^{-1}$) over a portion of the frequency range.

symmetry eigenstates which are referred to as $\Lambda$ doublets when their energy splittings are small. As $\Lambda$ doubling increases, the effect is known as $l$ uncoupling.

## A. Experimental spectra, effective rotational constants

A panoramic view of the 300–370 nm region of the Ne$_2$ $a\ ^3\Sigma_u^+$ excitation spectrum is displayed in Fig. 4. The most

prominent bandheads in the figure (and another not pictured at 425 nm) constitute a Rydberg series that, for qualitative reasons, was tentatively attributed previously[3,7] to $np\pi\ ^3\Pi_g - a\ ^3\Sigma_u^+$ (0–0) transitions with $n = 5$–10. Further experiments at higher resolution have shown no evidence of a $Q$ branch. Consequently, while the details of rotationally resolved spectra of these features will be discussed else-
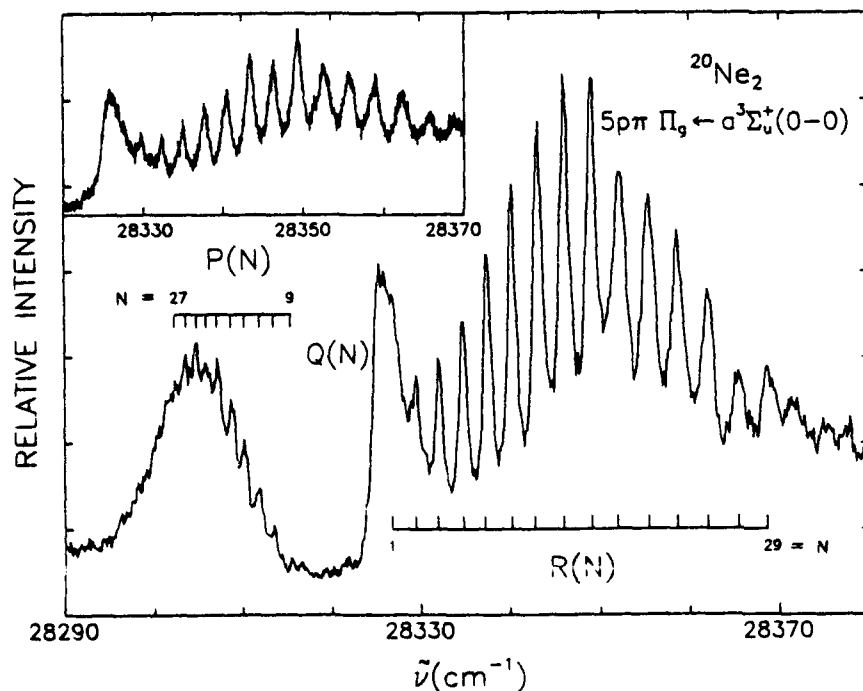


FIG. 6. Laser excitation spectrum of the $5p\pi\ \Pi_g - a$ (0–0) band obtained at a resolution of 0.2 cm$^{-1}$. Note that the $Q$ branch is not resolved. The inset gives a higher resolution ($\Delta\tilde{\nu} \approx 0.04$ cm$^{-1}$) scan of the 28 320–28 370 cm$^{-1}$ region.
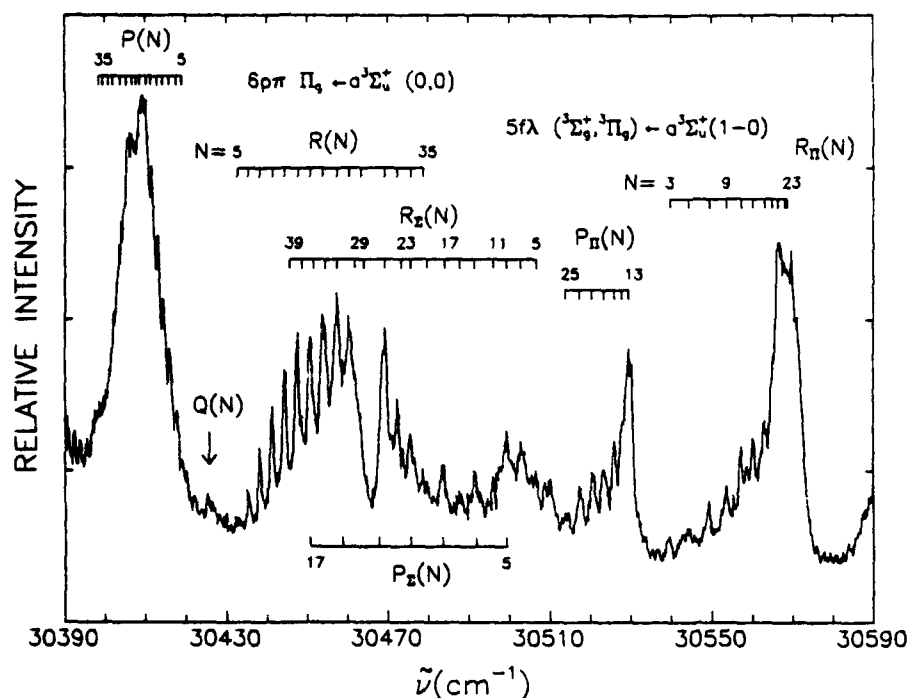
FIG. 7. Overview spectrum of the 30 390–30 590 cm$^{-1}$ region showing $^{20}$Ne$_2$ rotational structure arising from $6p\pi$ $\Pi_g - a(0-0)$ and $5f\lambda(^3\Sigma_g^+, ^3\Pi_g) - a(1-0)$ transitions. Note the perturbation occurring between the $6p\pi$ $\Pi_g$ ($v = 0$) and $5f\sigma$ $^3\Sigma_g^+$ ($v = 1$) states near 30 465 cm$^{-1}$. For convenience, the $P$ and $R$ branches associated with the $^3\Sigma_g^+$ or $^3\Pi_g$ components of the $5f$ complex are denoted by $\Sigma$ or $\Pi$ subscripts.

where,[12] suffice it to say that the strongest bands of Fig. 4 are assigned as $np\sigma$ $^3\Sigma_g^+ - a$ $^3\Sigma_u^+$ (0–0) transitions.

As can be seen in Fig. 4, the increased sensitivity of the laser-induced fluorescence technique, coupled with pulsing the photomultiplier, reveals several Rydberg series which are considerably weaker than the $np\sigma$ $^3\Sigma_g^+ - a(0-0)$ transitions, but still well above the noise floor. Rotational analyses of the strongly $l$-uncoupled $^3\Sigma_g^+$ and $^3\Pi_g$ components of the $4f$, $5f$, and $6f$ complexes of Ne$_2$ were reported recently.[7] The

remainder of this section deals with the analysis of a third Ne$_2$ molecular series displaying rotational structure. One member of this series (near $\lambda \sim 417$ nm), previously labeled[6] as the (0–0) band of the $4p\pi$ $^3\Pi_g - a$ transition, is now identified as the $n = 4$ member of the $np\pi$ $\Pi_g - a$ series. Six bands of this new Rydberg series have been rotationally-resolved and analyzed. Figures 5-10 present representative spectra for the (0–0) bands of the $n = 4$–9 members of the $np\pi$ $\Pi_g - a$ $^3\Sigma_u^+$ (0–0) series that were recorded in 200 Torr
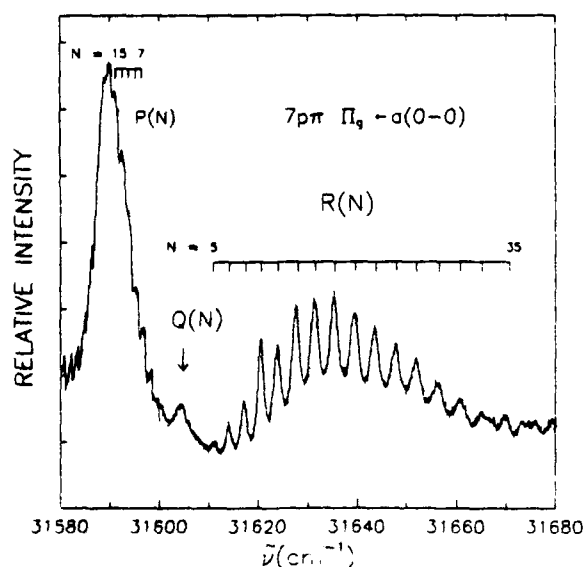


FIG. 8. $7p\pi$ $\Pi_g - a$ $^3\Sigma$(0–0) excitation spectrum of Ne$_2$ in the 31 580–31 680 cm$^{-1}$ region.
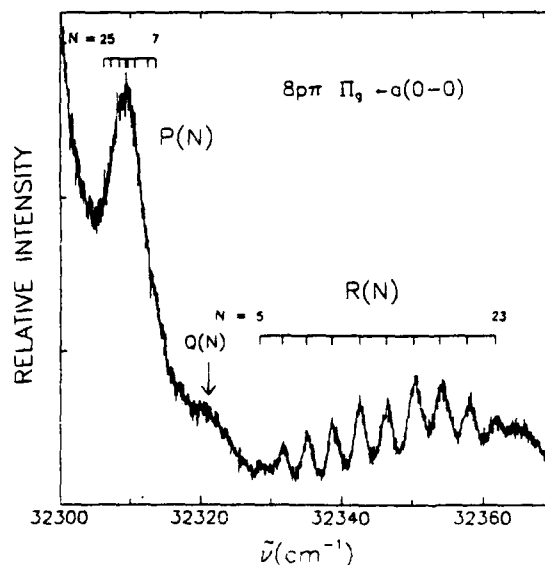


FIG. 9. 32 300–32 370 cm$^{-1}$ region showing the $n = 8$ member of the $np\pi$ $\Pi_g - a$ Rydberg series. Only those members of the $P$ branch that are consistently reproducible are indicated.
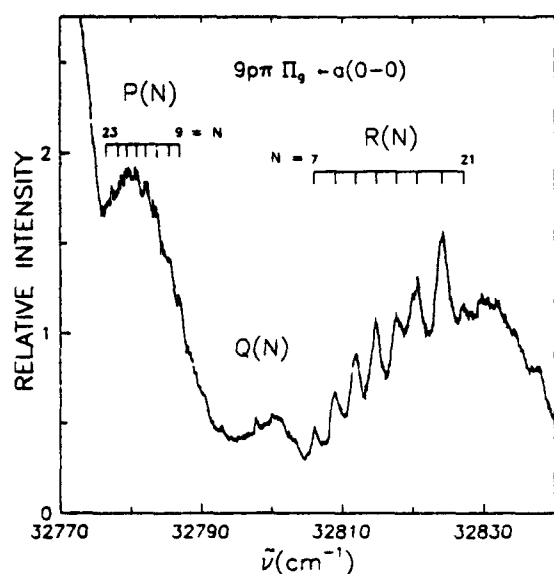
FIG. 10. Ne₂ excitation spectrum in the 32 770–32 840 cm⁻¹ region showing the partially resolved $9p\pi\ \Pi_g - a$ bands.

of ²⁰Ne (99.5% enriched). Similar spectra were also recorded for the stable isotope ²²Ne. Although the $4p\pi\ \Pi_g - a\ ^3\Sigma_u^+$ (0–0) band was published previously, the resolution available at that time (0.2 cm⁻¹) was considerably lower than that for the spectrum of Fig. 5 (~0.04 cm⁻¹). The apparent

$Q$ branch is still not resolved, but the lowest terms of both the $P$ and $R$ branches are now observed. In comparing Figs. 5–10, it is obvious that the $\Pi_g - a$ transitions become weaker and more difficult to resolve as the principal quantum number increases.

Rotational line positions for the $n = 4$–9 members of the ²⁰Ne₂ $np\pi\ \Pi_g - a$(0–0) Rydberg series in Figs. 5–10 are given in Table I. The data of Table I demonstrate that all of the transitions share the same lower state. The $\Delta_2 F''(N) = R(N-1) - P(N+1)$ lower state energy separations determined from the bands of Table I agree, to within experimental uncertainties, with the published[7] energy spacings of the $a\ ^3\Sigma_u^+$ ($v = 0$) state, thus confirming our lower state assignments.[6,7] The upper state assignments given in Table I will be discussed in the next section.

Energies (term values) of the upper state levels were calculated from the data in Table I and the $a\ ^3\Sigma_u^+$ ($v = 0$) rotational level energies reported in Ref. 7. The results are summarized in Table II in which all entries are referenced to $N = 0$, $v = 0$ of the $a\ ^3\Sigma_u^+$ state. The data of Table II are estimated to have an overall uncertainty of ±0.15 cm⁻¹. Band origins and effective rotational constants determined from the data of Tables I and II using the power series relations and least-squares fitting procedure described previously[7] are summarized in Table III.

### B. Q branch intensity anomaly

One intriguing trend noticeable in Figs. 5–10 is the weakening of the apparent $Q$ branch in the $np\pi\ \Pi_g - a\ ^3\Sigma_u^+$

TABLE I. Energies (cm⁻¹) of the rotational lines observed for the $np\pi\ \Pi_g - a\ ^3\Sigma_u^+$ (0–0) transitions of ²⁰Ne₂, $n = 4$–9.[a]

| N | $4p\pi\ \Pi_g - a$(0–0)[b] R(N) | P(N) | $5p\pi\ \Pi_g - a$(0–0)[c] R(N) | P(N) | $6p\pi\ \Pi_g - a$(0–0)[d] R(N) | P(N) | $7p\pi\ \Pi_g - a$(0–0)[f] R(N) | P(N) | $8p\pi\ \Pi_g - a$(0–0)[g] R(N) | P(N) | $9p\pi\ \Pi_g - a$(0–0)[h] R(N) | P(N) |
|---|---|---|---|---|---|---|---|---|---|---|---|---|
| 1 | 23 975.08 | 23 971.68[b] | 28 326.8 | | | | | | | | | |
| 3 | 23 977.49 | 23 969.54 | 28 329.40 | | | | | | | | | |
| 5 | 23 980.02 | 23 967.43 | 28 331.93 | | 30 432.63 | 30 419.1 | 31 610.88 | | 32 328.4 | | | |
| 7 | 23 982.53 | 23 965.35 | 28 334.80 | | 30 435.15 | 3υ 417.79 | 31 614.24 | 31 596.41 | 32 331.64 | 32 313.6 | 32 806.03 | |
| 9 | 23 985.31 | 23 963.48 | 28 337.22 | 28 315.4 | 30 438.07 | 30 416.04 | 31 617.50 | 31 595.15 | 32 335.02 | 32 312.5 | 32 809.02 | 32 786.87 |
| 11 | 32 988.01 | 23 961.61 | 28 340.20 | 28 313.54 | 30 441.27 | 30 414.43 | 31 620.55 | 31 593.79 | 32 338.64 | 32 311.6 | 32 811.85 | 32 785.41 |
| 13 | 23 990.83 | 23 959.92 | 28 342.73 | 28 311.86 | 30 444.19 | 30 413.13 | 31 624.01 | 31 592.53 | 32 342.46 | 32 310.55 | 32 814.76 | 32 783.74 |
| 15 | 23 993.77 | 23 958.22 | 28 345.94 | 28 310.17 | 30 447.56 | 30 411.52 | 31 628.01 | 31 591.17 | 32 346.26 | 32 309.63 | 32 817.67 | 32 782.04 |
| 17 | 23 996.82 | 23 956.72 | 28 348.98 | 28 308.66 | 30 450.63 | 30 410.37 | 31 631.48 | | 32 350.16 | 32 309.29 | 32 820.6 | 32 780.78 |
| 19 | 23 999.74 | | 28 351.86 | 28 307.14 | 30 453.84 | 30 408.75 | 31 635.36 | | 32 353.81 | (32 308.36) | 32 824.1 | 32 779.4 |
| 21 | 24 002.99 | | 28 355.40 | 28 305.94 | 30 457.44 | 30 407.87 | 31 639.57 | | 32 357.8 | (32 308.36) | 32 827.2 | 32 778.2 |
| 23 | 24 006.74 | | 28 358.62 | 28 304.78 | 30 460.37 | 30 406.86 | 31 643.78 | | 32 361.6 | 32 307.2 | | 32 776.5 |
| 25 | 24 010.62 | | 28 362.00 | 28 303.60 | 30 463.40 | 30 405.41 | 31 647.98 | | | | | |
| 27 | | | 28 365.38 | 28 302.3 | * | 30 403.95 | 31 651.98 | | | | | |
| 29 | | | 28 368.60 | | 30 469.19 | 30 402.06* | 31 656.51 | | | | | |
| 31 | | | 28 371.3 | | 30 472.25 | 30 401.03 | 31 660.72 | | | | | |
| 33 | | | 28 374.9 | | 30 475.63 | 30 399.58 | 31 665.14 | | | | | |
| 35 | | | 28 377.9 | | 30 478.69 | 30 398.56 | 31 670.6 | | | | | |

[a] Parentheses denote a blended line.

[b] The intense peak near 23 973 cm⁻¹ is likely an unresolved $Q$ branch (see the text and Fig. 5). If the feature at 23 971.68 cm⁻¹ is $P(1)$ as it appears to be, then the upper state cannot be a ¹Π state.

[c] The moderately intense peak near 28 325 cm⁻¹ is probably an unresolved $Q$ branch (see the text and Fig. 6).

[d] Higher $N$-value levels perturbed by $v = 1$ of the $5f\sigma\ ^3\Sigma_g^+$ state. A very weak peak near 30 425 cm⁻¹ is likely an unresolved $Q$ branch (see the text and Fig. 7).

[e] Perturbed assignment still questionable. The corresponding $R(27)$ line would appear as a poorly defined shoulder near 30 466 cm⁻¹.

[f] Higher $P(N)$ lines unresolved with a peak near 31 589 cm⁻¹. Weak head near 31 604 cm⁻¹ probably is an unresolved $Q$ branch (see the text and Fig. 8).

[g] The very weak feature near 32 320 cm⁻¹ possibly is an unresolved $Q$ branch (see the text and Fig. 9).

[h] Weak features near 32 798 cm⁻¹ are likely an unresolved $Q$ branch (see the text and Fig. 10).

**TABLE II.** Level (term) energies (cm$^{-1}$) of the $np\pi$ $\Pi_g$ states of $^{20}$Ne$_2$ for $n = 4$–9.[a]

| N | $4p\pi$ $\Pi_g$ $(v = 0)$ | $5p\pi$ $\Pi_g$ $(v = 0)$ | $6p\pi$ $\Pi_g$ $(v = 0)$ | $7p\pi$ $\Pi_g$ $(v = 0)$ | $8p\pi$ $\Pi_g$ $(v = 0)$ | $9p\pi$ $\Pi_g$ $(v = 0)$ |
|---|---|---|---|---|---|---|
| 0 | 23 972.80[b] | | | | | |
| 2 | 23 976.24 | 28 327.9 | | | | |
| 4 | 23 984.26 | 28 336.19 | 30 436.0 | | | |
| 6 | 23 996.95 | 28 348.76 | 30 449.1 | 31 627.76 | 32 345.3 | |
| 8 | 24 014.06 | 28 366.25 | 30 466.65 | 31 645.75 | 32 363.13 | 32 837.51 |
| 10 | 24 035.89 | 28 387.82 | 30 488.68 | 31 668.10 | 32 385.70 | 32 859.65 |
| 12 | 24 062.27 | 28 414.38 | 30 515.50 | 31 694.81 | 32 412.90 | 32 886.10 |
| 14 | 24 093.22 | 28 445.14 | 30 546.55 | 31 726.34 | 32 444.74 | 32 917.10 |
| 16 | 24 128.78 | 28 480.86 | 30 582.52 | 31 763.02 | 32 481.25 | 32 952.76 |
| 18 | 24 168.89 | 28 520.95 | 30 622.65 | 31 803.55 | 32 522.23 | 32 993.0 |
| 20 | 24 213.43 | 28 565.62 | 30 667.58 | 31 849.05 | 32 567.50 | 33 037.9 |
| 22 | 24 262.77 | 28 615.16 | 30 717.22 | 31 899.35 | 32 617.6 | 33 087.0 |
| 24 | 24 317.10 | 28 668.97 | 30 770.75 | 31 954.14 | 32 671.9 | |
| 26 | 24 375.98 | 28 727.30 | 30 828.75 | 32 013.34 | | |
| 28 | | 28 790.18 | 30 890.69[c] | 32 076.78 | | |
| 30 | | 28 857.23 | 30 957.85 | 32 145.14 | | |
| 32 | | 28 928.2 | 31 029.09 | 32 217.57 | | |
| 34 | | 29 004.4 | 31 105.12 | 32 294.63 | | |
| 36 | | 29 084.5 | 31 185.25 | 32 377.1 | | |

[a] Based on $N = 0$, $v = 0$ of the $a$ $^3\Sigma_u^+$ state.
[b] See footnote b to Table I.
[c] Value may be questionable (see footnote e to Table I).

transitions as $n$ increases. While the $Q$ branch is reasonably strong for the $n = 4$ member (Fig. 5), the analogous transitions for $n > 5$ are barely discernible. As discussed below, it is the existence of the strong $Q$ branchlike features in the $n = 4$ and 5 members which leads one to label the upper states for this series as $\Pi_g$ type.

One possible explanation for the $Q$ branch intensity behavior outlined above revolves around the relative rates at which different Rydberg states predissociate. In the experiments which produced Figs. 5–10, if a particular state is stable against predissociation, its presence in the excitation spectrum might be insignificant or go undetected altogether. Specifically, it is conceivable that the $\Pi^+$ and $\Pi^-$ states behave entirely differently with respect to dissociation. One approach to investigating this possibility is to compare the excitation and absorption spectra for the same transition. Toward that end, attempts were made to record Ne$_2$ $a$ $^3\Sigma_u^+$ absorption spectra by dye laser probe, multipass techniques with a UV-preionized transverse discharge. Although the experiments were successful in the sense that spectra were

obtained, the $S/N$ ratio was too low to yield the detailed information required here. Subsequently, a two dye laser pump–probe technique was developed which has proven to be quite fruitful in observing weak inter-Rydberg absorption spectra.

With the two laser pump–probe approach, one dye laser scans the spectral region of interest as before. However, small changes in the lower state population (in this case $a$ $^3\Sigma_u^+$) can be monitored indirectly by tuning a second dye laser onto the strong $7p\sigma$ $^3\Sigma_g^+$ ←$a$(0–0) transition at 356 nm[12] which terminates on a predissociating Ne$_2$ state. With this laser locked onto the predissociative transition, one then monitors the atomic $3p \rightarrow 3s$ emission resulting from decay of the dissociation products. If the pulse energy of the second dye laser is kept constant, the peak atomic fluorescence intensity is a convenient measure of the instantaneous $a$ $^3\Sigma_u^+$ $(v = 0)$ population. Consequently, even slight reductions in the $a$ $^3\Sigma_u^+$ state population that result from tuning the first dye laser through various transitions are readily detectable. In other words, this technique effectively converts weak ab-

**TABLE III.** Effective molecular parameters (cm$^{-1}$) for the $v = 0$ levels of the $np\pi$ $\Pi_g^+$ ($n = 4$–9) states of $^{20}$Ne$_2$.

| State | $E(N = 0)$[a] | $n^{*b}$ | $B_v \times 10$ | $D_v \times 10^5$ | $H_v \times 10^8$ |
|---|---|---|---|---|---|
| $4p\pi$ $\Pi$ | 23 972.80 ± 0.08 | 3.2442 | 5.743 ± 0.008 | 0.9 ± 0.5 | 1.2 ± 0.8 |
| $5p\pi$ $\Pi$ | 28 324.5 ± 0.1 | 4.250 | 5.758 ± 0.010 | 0.5 ± 0.4 | 0.1 ± 0.2 |
| $6p\pi$ $\Pi$ | 30 424.6 ± 0.2[c] | 5.255 | 5.82 ± 0.02[c] | 0.9 ± 0.5[c] | 0.5 ± 0.3[c] |
| $7p\pi$ $\Pi$ | 31 603.3 ± 0.2 | 6.265 | 5.89 ± 0.02 | 0.9 ± 0.5 | 0.2 ± 0.2 |
| $8p\pi$ $\Pi$ | 32 320.2 ± 0.2 | 7.266 | 5.98 ± 0.02 | 2.2 ± 0.7 | 1.1 ± 0.5 |
| $9p\pi$ $\Pi$ | 32 796.1 ± 0.2[d] | 8.274 | 5.77 ± 0.02[d] | 5.2 ± 0.7[d] | 0.1 ± 0.2[d] |

[a] Energy of the extrapolated $N = 0$ level above the $N = 0$, $v = 0$ state of $a$ $^3\Sigma_u^+$.
[b] Calculated from Eq. (5) assuming an ionization energy of 34 399 cm$^{-1}$ (Ref. 10).
[c] Weakly perturbed by $v = 1$ of $5f\sigma$ $^3\Sigma_g^+$.
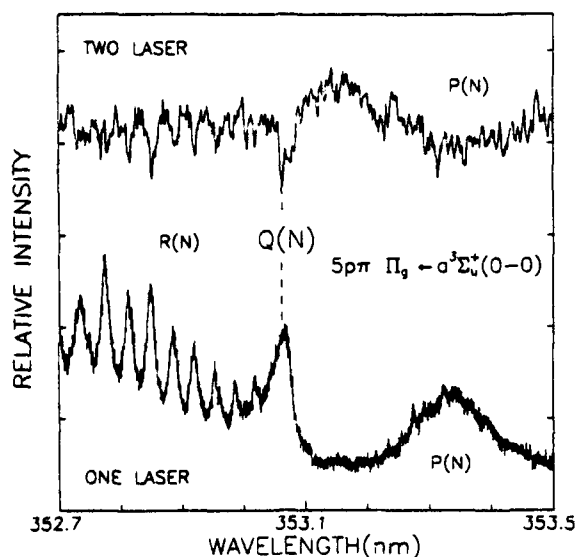[d] Perturbed band.

FIG. 11. Comparison of (bottom) laser excitation spectrum of $5p\pi\ \Pi_g -a$ (0–0) transition in the 352.7–353.5 nm region acquired with one (scanning) dye laser; and (top) two laser spectrum over the same spectral region obtained by scanning one dye laser with the wavelength of the second fixed at 356 nm (see the text). The position of the transition's $Q$ branch is indicated by the dashed vertical line. The spectrum acquired by the two laser technique (where absorption increases downwards) is somewhat noisier than the single laser excitation spectrum due to amplitude jitter in the Nd:YAG laser pumping the fixed wavelength dye laser.

sorption by a molecular transition into a suppression of transient atomic fluorescence. Although further details of the experimental technique will be published elsewhere,[13] several examples of the spectra obtained which are important for our purposes here are presented in Figs. 11 and 12.
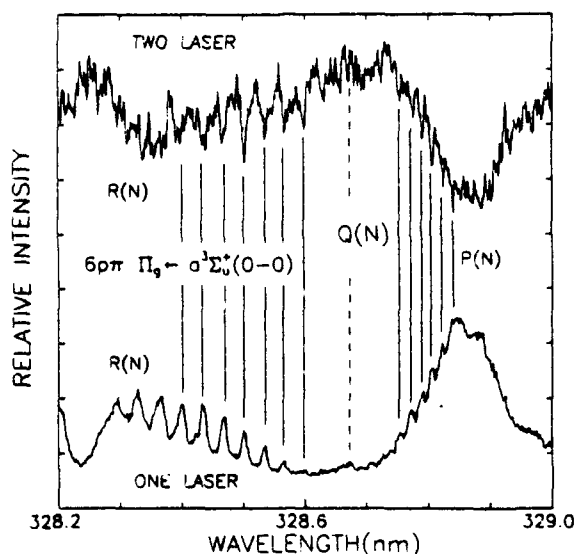


FIG. 12. Spectra similar to those of Fig. 11 for the $6p\pi\ \Pi_g -a$ transition of ²⁰Ne₂. The top spectrum was, again, acquired by the two laser technique and the solid vertical lines show the correlation between prominent lines in both spectra.

The bottom trace in Fig. 11 is a segment of the $5p\pi\ \Pi_g -a$(0–0) excitation spectrum illustrated in Fig. 6, obtained with a single scanning pulsed dye laser by monitoring $3p(1/2)_1 \rightarrow 3s(3/2)_2^0$ fluorescence at 703 nm. The upper spectrum in Fig. 11 was acquired by driving the 356 nm transition of Ne₂ with a fixed wavelength dye laser, while the tunable laser was scanned over the 352.7–353.5 nm region. The fixed wavelength laser was delayed in time with respect to the scanning laser pulse by 100 ns. Consequently, if the Ne $3p \rightarrow 3s$ fluorescence is monitored, two pulses are detected and the peak intensity of the second pulse is proportional to the relative $a\ ^3\Sigma_u^+$ ($v = 0$) population at the moment the second pulse arrives. When the wavelength of the first laser pulse is resonant with an Ne₂ inter-Rydberg transition, the $a$ state population is momentarily depleted which is reflected in a temporary suppression of the Ne ($3p$) population produced by the second laser pulse and, hence, the $3p \rightarrow 3s$ spontaneous emission intensity falls. The upper spectrum of Fig. 11, therefore, is a recording of the suppression of the $3p \rightarrow 3s$ fluorescence that directly results from a reduction in the $a\ ^3\Sigma$ population induced by the first laser pulse. As a result, in the two laser spectrum, absorption increases downward. The two laser spectrum is noisier than the one laser excitation spectrum because of shot-to-shot amplitude jitter in the second Nd:YAG laser which is driving the fixed wavelength dye laser. Finally, one attractive aspect of this technique is that both the one and two laser spectra can be acquired simultaneously using two boxcar integrators.

Figure 12 shows experimental results analogous to those of Fig. 11 for transitions involving the $6p\pi\ \Pi_g$ state. From Figs. 11 and 12, it is obvious that all of the prominent features in the excitation spectrum (lower trace) are reproduced in the two laser experiments. Most important, however, is the fact that the $Q$ branch (denoted by dashed vertical lines in both figures) is anomalously weak for transitions to $np\pi\ \Pi_g$ states with $n \gtrsim 5$ in both experiments. This demonstrates that differences in the stability of the $\Pi^+$ and $\Pi^-$ states against predissociation are not the cause of the weakening of the $Q$ branchlike features in our $np\pi\ \Pi_g - a\ ^3\Sigma_u^+$ spectra that is observed with increasing $n$.

This interpretation of the experimental data of Figs. 11 and 12 would be invalid *if* the photopumped states do not predissociate effectively, but rather reradiate to the $a$ state with a spontaneous lifetime that is short compared to the delay time of 100 ns. If such were true, however, the dye laser pumping process would produce strong molecular emission which has not been observed by us nor reported in the literature.

As mentioned earlier, it is the existence of $Q$ branch features in the transitions of Figs. 5–10 that leads us to believe that the upper states have $\Pi$ character. These $Q$ features are exactly where predicted if one assumes the molecular constants for the $\Pi^+$ (Table III) and $\Pi^-$ sublevels to be similar (i.e., small $\Lambda$ doubling). In addition, the relative intensities of the branches in Fig. 5 are what one would predict for a $\Pi-\Sigma$ type transition between reasonably isolated case $b'$ states, while the relative intensities *within* the band in Fig. 6 are also close to the values predicted on the basis of the same model. The higher members of the series more closely resem-

TABLE IV. Line positions (cm⁻¹) of the $5f\lambda(^1\Sigma_g^-, ^1\Pi_g) - a\ ^3\Sigma_u^-$ (1-0) transitions in ²⁰Ne₂.[a]

| | $5f\sigma\ ^3\Sigma_g^- - a(1\text{-}0)$[b] | | $5f\pi\ ^1\Pi_g - a(1\text{-}0)$ | |
|---|---|---|---|---|
| $N$ | $R(N)$ | $P(N)$ | $R(N)$ | $P(N)$ |
| 1 | | | | |
| 3 | | | 30 539.55 | |
| 5 | 30 506.53 | 30 498.17 | 30 544.11 | (31 529.41) |
| 7 | 30 502.71 | (30 491.43) | 30 549.25 | (31 529.41) |
| 9 | 30 499.34 | (30 483.96) | 30 553.52 | (31 529.41) |
| 11 | 30 495.97 | (30 475.62) | 30 557.05 | (31 529.41) |
| 13 | (30 491.43) | 30 467.50* | 30 559.99 | (31 529.41) |
| 15 | 30 487.77 | 30 458.91 | 30 562.93 | 31 527.60* |
| 17 | (30 483.96) | (30 450.77) | 30 564.92 | 31 525.89 |
| 19 | 30 479.72 | | 30 566.45 | 31 523.25 |
| 21 | (30 475.62) | | 30 567.79 | 31 520.31 |
| 23 | (30 473.25) | | 30 568.52 | 31 517.24 |
| 25 | (30 469.19) | | | 31 513.71 |
| 27 | 30 464.85 | | | |
| 29 | 30 461.83 | | | |
| 31 | (30 457.44) | | | |
| 33 | 30 454.43 | | | |
| 35 | 30 451.51 | | | |
| 37 | 30 448.58 | | | |
| 39 | 30 445.57 | | | |

[a] Parentheses and an asterisk denote a blended line and a shoulder feature, respectively. Note that although two decimal places are quoted for these line positions, in most cases the uncertainties in the last quoted digit are ± 5–10.

[b] All of the $P(N)$ lines for $N > 17$ are obscured by much stronger transitions.

ble $\Delta\Lambda = 0$, $\Lambda > 0$ transitions, but such an observation is of little help in explaining our observations because the one state whose character does not change throughout the observed series of transitions is the lower state $a\ ^3\Sigma_u^+$ for which $\Lambda = 0$.

TABLE V. Level (term) energies (cm⁻¹) of the $v = 1$, $5f\sigma\ ^3\Sigma_g^-$ and $5f\pi\ ^3\Pi_g$ states of ²⁰Ne₂.[a]

| $N$ | $5f\sigma\ ^3\Sigma_g^-$ | $5f\pi\ ^3\Pi_g^+$ |
|---|---|---|
| 4 | 30 515.0 | 30 546.29 |
| 6 | 30 523.4 | 30 556.96 |
| 8 | 30 534.2 | 30 580.74 |
| 10 | 30 550.0 | 30 604.15 |
| 12 | 30 569.7 | 30 631.28 |
| 14 | 30 593.8 | 30 662.37 |
| 16 | 30 622.9 | 30 697.95 |
| 18 | 30 656.0 | 30 736.97 |
| 20 | 30 693.4 | 30 780.12 |
| 22 | 30 735.4 | 30 827.60 |
| 24 | 30 783.6 | 30 888.96 |
| 26 | 30 834.6 | |
| 28 | 30 889.6 | |
| 30 | 30 950.5 | |
| 32 | 31 014.3 | |
| 34 | 31 083.9 | |
| 36 | 31 158.1 | |

[a] Based on $N = 0$, $v = 0$ of the $a\ ^3\Sigma_u^-$ state.

While we are reasonably confident that the upper states for this Rydberg series are of $np\pi\ \Pi_g$ character, it is difficult to be as certain about the states' multiplicity. Two factors have prompted us to, at present, refrain from making a more definitive assignment. (1) a fourth, and much weaker series lies in the same energy region as the $np\pi$ series, but as yet has not yielded any rotational structure and, therefore, remains unassigned; and (2) there *appears* to be a $P(1)$ line in the $4p\pi\ \Pi_g - a$ transition (see Fig. 5) which cannot exist in a $^1\Pi_g - ^3\Sigma_u^+$ transition. Studies of transitions associated with higher $n$ terms of $np\pi$ series and careful examination of the weak, unidentified series should remove this remaining ambiguity in the near future.

### C. $7p\pi\ \Pi_g - 5f\sigma\ ^3\Sigma_g^+$ perturbation

A careful examination of the 30 390–30 590 cm⁻¹ region (shown in Fig. 7) reveals a weak perturbation occurring between the $6p\pi\ \Pi_g$ ($v = 0$) and $5f\sigma\ ^3\Sigma_g^+$ ($v = 1$) states near 30 465 cm⁻¹. This perturbation is first evident in the sudden drop in intensity of the $6p\pi\ \Pi_g - a(0\text{-}0)$ $R$ branch at higher $N$. The observed spectral line positions for the $5f\sigma\ ^3\Sigma_g^+$, $5f\pi\ ^3\Pi_g - a(1\text{-}0)$ transitions and the $5f\sigma\ ^1\Sigma_g^+$, $5f\pi\ ^3\Pi_g$ ($v = 1$) level energies levels appear in Tables IV and V, respectively. Plots of the rotational level energies $E(N)$ for both the $5f\sigma\ ^3\Sigma_g^+$ ($v = 1$) and $6p\pi\ \Pi_g$ ($v = 0$) levels in Fig. 13 show the convergence of the $E(N)$ values for both states and the crossing of the two series near $N = 26$. The inset gives the same data, but the ordinate represents the difference between the level energies of the two interacting states as a function of $N$. Examination of the data shows that the interaction results in the $N = 26$ levels being displaced from their unperturbed positions by ~ 1 cm⁻¹ with much smaller shifts for the $N = 28$ levels. Thus, the perturbation involves both transition intensities and energy although the effects are relatively weak.

### V. SUMMARY AND CONCLUSIONS

Several Rydberg series of the neon dimer have been studied at a resolution of ~ 1 GHz by laser excitation spectroscopy in the afterglow of a pulsed discharge. By photoexciting the metastable $a\ ^3\Sigma_u^+$ species with a time-delayed dye laser pulse, Rydberg states of the ²⁰Ne₂ and ²²Ne₂ molecules were examined in detail. Six members of the $np\pi\ \Pi_g - a(0\text{-}0)$ series ($4 \leq n \leq 9$) were rotationally resolved and characterized. An anomalous decrease in the intensity of the $Q$ branches for the higher $n$ members of the series has been discussed and a weak perturbation between the $6p\pi\ \Pi_g$ ($v = 0$) and $5f\sigma\ ^3\Sigma_g^+$ ($v = 1$) states has been identified. In passing, it should be noted that it is the $5p\pi\ \Pi_g - a$ photoabsorption band of Ne₂ that interferes with the extraction of energy from the XeF laser at 353 nm. Apparently, it was this band that motivated Chang and Champagne[14] to search for the origin of absorption they had observed in electron beam-pumped Ne/Xe/NF₃ gas mixtures.

While at present we are unable to unambiguously assign the multiplicity of the $np\pi\ \Pi_g$ Rydberg states presented here, it is expected that subsequent investigation of the complex region lying between the $9p\pi\ \Pi_g - a(0\text{-}0)$ band and
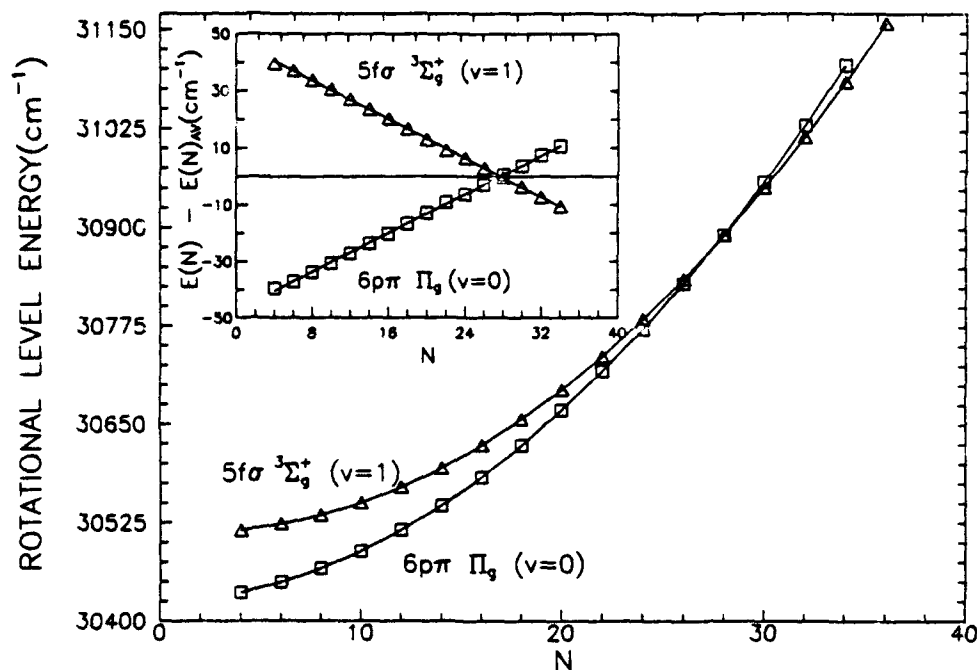
FIG. 13. Rotational level energies for both the $6p\pi\ \Pi_g$ $(v=0)$ and $5f\sigma\ ^3\Sigma_g^+$ $(v=1)$ states as a function of $N$. The larger graph shows the absolute values for the term energies, whereas the ordinate for the inset gives the deviations of the energies for the two states from their average value $E(N)_{AV}$.

the first ionization limit will resolve the outstanding questions that remain. Since the spectral region beyond $\sim 700$ nm contains transitions from $a\ ^3\Sigma_u^+$ to the first member of all of the $nl\lambda$ Rydberg series with $l < 4$, we also plan to investigate transitions in the near infrared.

## ACKNOWLEDGMENTS

[1] G. Herzberg, Annu. Rev. Phys. Chem. 38, 27 (1987).
[2] K. P. Killeen and J. G. Eden, J. Chem. Phys. 83, 6209 (1985).
[3] K. P. Killeen and J. G. Eden, J. Chem. Phys. 84, 6048 (1986).
[4] M. N. Ediger and J. G. Eden, Chem. Phys. Lett. 126, 158 (1986).
[5] M. N. Ediger and J. G. Eden, J. Chem. Phys. 85, 1757 (1986).
[6] D. J. Kane, C. J. Zietkiewicz, and J. G. Eden, Phys. Rev. A 39, 4906 (1989).
[7] S. B. Kim, D. J. Kane, J. G. Eden, and M. L. Ginter, J. Chem. Phys. 94, 145 (1991).
[8] Elsewhere in the literature, the lowest energy bound state of Ne$_2^+$ is occasionally denoted $A\ ^2\Sigma_{1/2u}^+$. We adopt $X$ as its designation for consistency with international conventions for labeling the ground state of a molecule.
[9] S. Iwata, Chem. Phys. 37, 251 (1979).
[10] D. J. Kane, Ph.D. thesis, University of Illinois, Urbana, 1989.
[11] See, e.g., B. Edlén, in Handbuch Der Physik, edited by S. Flügge (Springer, Berlin, 1964), Vol. 27, pp. 80–220.
[12] S. B. Kim, J. G. Eden, and M. L. Ginter (unpublished).
[13] S. B. Kim, D. J. Kane, and J. G. Eden (unpublished).
[14] R. S. F. Chang and L. F. Champagne, Appl. Phys. Lett. 36, 879 (1980).

# Detection of Trace Concentrations of Column III and V Hydrides by Laser-Induced Breakdown Spectroscopy

E. A. P. CHENG,* R. D. FRASER, and J. G. EDEN†
*Everitt Laboratory, University of Illinois, Urbana, Illinois 61801*

The measurement of trace concentrations (1-400 ppm) of polyatomic molecular impurities in helium was investigated by laser-induced breakdown spectroscopy (LIBS). For the Column III and V hydrides such as $B_2H_6$, $PH_3$, and $AsH_3$, the detectability limits with the present apparatus were determined to be 1, 3, and ~1 ppm, respectively. It is expected that resorting to synchronous detection techniques will improve the sensitivity of LIBS for this application by as much as an order of magnitude.

Index Headings: Fluorescence; Lasers, Nd:YAG; UV-visible spectroscopy; Laser-induced breakdown spectroscopy.

## INTRODUCTION

The application of laser excitation and ionization processes to the detection of impurities in gases and solids is well developed. In flames, for example, Grant et al.[1] have observed 25 parts per million (ppm) of NO by multiphoton ionization (MPI) with a tunable dye laser. Also, trace concentrations of a variety of elements in both solids and liquids ($2 \cdot 10^{-8}$ at. % Na and $5 \cdot 10^{-7}$ at. % Al, for example, in Ge crystals and seawater, respectively) have been detected by Bekov and Letokhov,[2] again utilizing multi-step, resonantly enhanced laser photoionization. Akilov et al.[3] have invoked similar techniques to observe aluminum concentrations as low as $2 \cdot 10^{-7}$ at. % in ostensibly "pure" germanium.

An alternative, and simpler, approach to impurity detection is laser-induced breakdown spectroscopy (LIBS),[4-8] which involves optical breakdown in a gaseous sample or at a surface that is induced by a laser pulse having a peak intensity typically in the range of $10^7$–$10^{10}$ W cm$^{-2}$. Such high optical fields result in the dissociation of molecular species present into their atomic constituents. Consequently, LIB spectra are largely free of molecular structure, and the small volume sampled by the technique makes it attractive for the micro- (and remote, if necessary) analysis of toxic or corrosive substances. Furthermore, as noted by Cremers and Radziemski,[9] LIBS avoids the need for electrodes, which are common to spark spectrometry.

Two further advantages of this technique that have been pointed out previously[4-8] are that LIBS is noninvasive and does not require that the laser be tuned to a resonance of the species under study. The latter is reflected in the fact that LIB spectra are relatively insensitive to the wavelength of the excitation laser, thus allowing one to simultaneously examine the relative concentrations of several impurities that may be present in the sample. Cremers[8] has clearly demonstrated the utility of this feature of LIBS in recent experiments in which minor constituents in steel were observed.

Loree, Radziemski, and co-workers[4-6] have demonstrated the ability of LIBS to measure small concentrations of impurities in a hostile environment such as the corrosive effluent from a coal gasifier plant. Early experiments involved the detection of 1–3% Na or K in the product stream. In subsequent time-resolved studies, 690 ppm of phosphorus (from diisopropylmethyl phosphonate, DIMP), 8 ppm of chlorine, and 38 ppm of fluorine were observed in air.[9]

In this paper, the preliminary results of several experiments are described in which the detection of sub-100-ppm concentrations of several Column III and V hydride polyatomic molecules in the gas phase by LIBS was explored. These studies were motivated by the growing demands being placed on the purity of gases of industrial importance and the concomitant requirement for (preferably) noninvasive and rapid diagnostic techniques for measuring trace concentrations of contaminants in such gases. As discussed earlier, the inherent characteristics of the method allow LIBS to lend itself well to such an application.

The goal of these experiments was the identification of one or more *atomic* emission lines associated with a given *molecular* impurity that are reliable indicators ("fingerprints")[4] of the contaminant's relative concentration, particularly at the ppm level. Our initial efforts have centered on monitoring the concentrations of $PH_3$, $AsH_3$, and $B_2H_6$ diluted in He. Although the use of these three gases in the semiconductor industry is widespread, the toxicity of each has impeded the development of diagnostic procedures. Nevertheless, the impact of source gas purity on electronic device quality, for example, is illustrated by the observation[10,11] of the presence of Ge as a donor in GaAs epitaxial films grown by metal organic

chemical vapor deposition (MOCVD). It now appears that the Ge impurity is introduced to the reactor in the form of germane ($GeH_4$) as a contaminant in $AsH_3$.

## EXPERIMENTAL

The experimental apparatus, shown schematically in Fig. 1, is described in detail elsewhere[12] and will be briefly reviewed here. Optical field intensities up to $\sim10^{11}$ W $cm^{-2}$ were produced in a vacuum chamber by focusing the second harmonic beam ($\lambda = 532$ nm) from a pulsed Nd:YAG laser [10 Hz, 8 ns full width at half-maximum (FWHM) pulses] with a 10-cm-focal-length (FL) lens. The chamber was evacuated by a turbomolecular pump to a base pressure of $5 \cdot 10^{-8}$ Torr, and the entire gas handling/vacuum chamber system was constructed of stainless steel. Visible and ultraviolet radiation from the laser-induced spark was collected at 90° to the pump laser beam and dispersed by a simple lens telescope/spectrometer combination. A 3.1-cm-diameter, 7-cm-FL lens collimated the radiation from the plasma, and a second lens (2.5-cm diameter, 10-cm FL) focused the beam into a 0.25-m spectrograph having an $f$ number of 3.8.

Spectra were acquired by mounting one of two intensified diode arrays at the exit plane of the spectrograph. The first, composed of 512 diodes, had a sensitivity of $\sim100$ photons/count and a useful spectral range of $\sim350$–830 nm. Equipped with this optical multichannel analyzer (OSMA) detector, 25-$\mu$m entrance slits, and a 300-lines/mm diffraction grating, the entire detection system had a first-order spectral resolution of $\sim0.28$ nm/diode. When necessary, the resolution could be improved by a factor of two by interchanging gratings or operating the spectrograph in second order. For the arsine and diborane experiments, it was desirable to monitor atomic lines lying below 300 nm, which required a second intensified array having adequate response over the 200–300 nm region. Unless stated otherwise, all wavelengths dis-

cussed here are measured in air. All spectral data were stored and processed by a DEC LSI 11/73 computer.

Although the gas handling system was equipped for either flowing or static fill experiments, no detectable differences were observed between the LIB spectra for the two cases. Consequently, all of the measurements with these toxic gases were made under static fill conditions and, after each experiment, the gas was exhausted through a $KMnO_4$ bubbler.

Known levels of the impurity gas under study were prepared by diluting calibrated samples (provided by the Liquid Air Corp.) with high-purity He (UHP; $>99.999\%$). In this manner, it was straightforward to reliably mix samples containing $<1$ ppm of the desired "contaminant." Fresh gas mixtures were prepared for each data run, which simply consisted of firing a fixed number of laser shots (typically 700–800) while monitoring a $\sim150$-nm-wide spectral region. Preparation for the next run consisted of evacuating the cell, backfilling with He, and evacuating one final time before admitting a fresh gas mixture.

## RESULTS AND DISCUSSION

**Phosphine.** Experiments were carried out with mixtures of 3, 10, 50, and 180 ppm of $PH_3$ in He that were prepared by diluting a calibrated 361 ppm in He mixture. Scans of the 300–900 nm region revealed several phosphorus and hydrogen lines, but most (such as the 391.4-nm and 434.0-nm transitions of P and H, respectively) vanished for $PH_3$ concentrations below $\sim90$ ppm.

In the 600–660 nm spectral region, five lines—four arising from the phosphorus singly charged ion and one from hydrogen ($P^+$: 602.4, 603.4, 604.3, and 605.5 nm; H: 656.3 nm)—were readily detected. A low-resolution view of the 600–610 nm interval is given in Fig. 2 for both 361 ppm $PH_3$/He and He-only static fills. The four lines mentioned earlier, of which the 604.3-nm transition is the strongest, are clearly noticeable. Figures 3 and 4 show the dependence of the $P^+$ 604.3-nm and H 656.3-nm transition peak intensities, respectively, on the $PH_3$ concen-
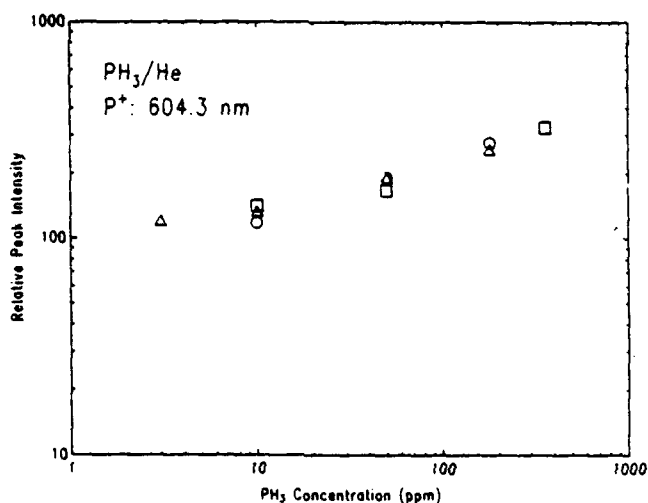


FIG. 2. Low-resolution view of the 600–610 nm spectral region for a mixture of 361 ppm of $PH_3$ in He (top) and He only (bottom). The upper and lower traces have been intentionally offset for clarity.

FIG. 3. Dependence of the P⁺ 604.3-nm line intensity on the PH₃ concentration for impurity levels ranging from ~3 to ~400 ppm.


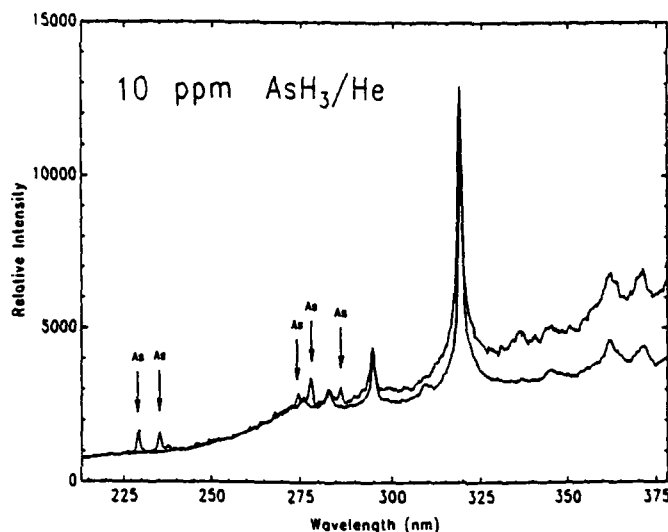
FIG. 5. Ultraviolet LIB emission spectrum of 10-ppm arsine in He. The strong As lines lying between 225 and ~300 nm are indicated. The lower spectral trace is that for pure He.

tration. Note that, for PH₃ concentrations above 20–30 ppm, the variation of the time-integrated 604.3-nm transition intensity (cf. Fig. 3) is logarithmic in PH₃ number density. Below 10 ppm, the signal falls less slowly, but the underlying blackbody continuum complicated measurements at lower PH₃ concentrations. Consequently, with the present apparatus, the minimum PH₃ level detectable by monitoring the phosphorus orange line was limited to ~3 ppm. However, we estimate that, by utilizing synchronous detection techniques, one could improve the PH₃ detectability limit to below 500 ppb. Finally, data from three separate experimental trials, given in Fig. 3, illustrate the reproducibility of the measurements.

**Arsine.** A known mixture of 100 ppm AsH₃ in helium was used to prepare all diluted samples. Scans of the visible and ultraviolet revealed the most reliable atomic transitions to be those of arsenic lying between 220 and

290 nm. Figure 5 displays the spectra that were recorded between ~212 and 378 nm for both 10 ppm AsH₃ in He and He itself. Five lines of neutral As (228.8, 235.0, 278.0, and 286.0 nm) are quite clear and, as shown in Fig. 6 for the 228.8-nm transition, monitoring the intensity of any of the five limited one to detecting AsH₃ concentrations of roughly 1 ppm or higher. Again, it is expected that the incorporation of synchronous detection techniques or the use of a fiber-optics bundle introduced into the vacuum chamber to improve the fluorescence collection efficiency would lower the detectability limit by as much as an order of magnitude.

**Diborane.** Results similar to those obtained with AsH₃ and PH₃ were also realized with B₂H₆. Two lines of atomic boron, 434.5 and 336.0 nm, were readily observed, and the latter was reproducibly detected down to B₂H₆ concentrations as low as ~1 ppm (cf. Fig. 7).



FIG. 4. Data similar to those of Fig. 3 except that the H line at 656.3 nm is being monitored.



FIG. 6. Variation of the peak intensity of the 228.8-nm line of arsenic with the arsine concentration.

$B_2H_6/He$

$B$: 336.0 nm

Relative Peak Intensity

$B_2H_6$ Concentration (ppm)

Fig. 7. Data similar to those of Figs. 3, 4, and 6 for the 336.0-nm line of boron. The B 434.5-nm transition intensity was found to have a dependence on $[B_2H_6]$ that was nearly identical to that shown here.

## SUMMARY AND CONCLUSIONS

The capability of detecting small concentrations of selected polyatomic molecules in He by LIBS has been demonstrated. In accord with previous studies, the sensitivity of the technique is system dependent, but our studies yielded a ~1-ppm concentration "floor" for $AsH_3$, $PH_3$, and $B_2H_6$. Consequently, the detectability limits reported here are comparable to those determined previously for atomic species such as Cl and F. As noted earlier, it is estimated that the implementation of synchronous detection techniques would reduce these limits by as much as an order of magnitude. Of course, the homogeneity of neat samples available in an industrial environment might adversely affect the limits reported

here. Nevertheless, these preliminary results demonstrate that LIBS is an attractive technique for making remote measurements of sub-100-ppm concentrations of gases which are of critical importance to the semiconductor industry. In general, the rapid acquisition and analysis of spectral data that are characteristic of LIBS make it amenable to the computerized, *in situ* analysis of small volumes of toxic and/or corrosive gases.

1. E. R. Grant, B. H. Rockney, and T. A. Cool, Chem. Phys. Lett. 87, 141 (1982).
2. G. I. Bekov and V. S. Letokhov, Appl. Phys. B 30, 161 (1983).
3. R. Akilov, G. I. Bekov, V. S. Letokhov, G. I. Maksimov, V. I. Mishin, V. N. Radaev, and V. N. Shishov, Kvan. Elektron. (Moscow) 9, 1859 (1982) [Sov. J. Quant. Electron. 12, 1201 (1982)].
4. T. R. Loree and L. J. Radziemski, Plasma Chem. and Plasma Proc. 1, 271 (1981).
5. L. J. Radziemski and T. R. Loree, Plasma Chem. and Plasma Proc. 1, 281 (1981).
6. L. J. Radziemski, T. R. Loree, D. A. Cremers, and N. M. Hoffman, Anal. Chem. 55, 1246 (1983).
7. D. A. Cremers and L. J. Radziemski, in Laser Spectroscopy and Its Applications, L. J. Radziemski, R. W. Solarz, and J. A. Paisner, Eds. (Marcel Dekker, New York, 1987), pp. 351–415.
8. D. A. Cremers, Appl. Spectrosc. 41, 572 (1987).
9. D. A. Cremers and L. J. Radziemski, Anal Chem. 55, 1252 (1983).
10. G. E. Stillman, C. M. Wolfe, and J. O. Dimmock, in Semiconductors and Semimetals, R. K. Willardson and A. C. Beer, Eds. (Academic Press, New York, 1977), Vol. 12, pp. 169–290.
11. S. S. Bose, B. Lee, M. H. Kim, and G. E. Stillman, Appl. Phys. Lett. 51, 937 (1987).
12. E. A. P. Cheng, M.S. thesis, University of Illinois, Urbana (1987).

# Detection of Trace Concentrations of Column III and V Hydrides by Laser-Induced Breakdown Spectroscopy

E. A. P. CHENG,* R. D. FRASER, and J. G. EDEN†

*Everitt Laboratory, University of Illinois, Urbana, Illinois 61801*

The measurement of trace concentrations (1–400 ppm) of polyatomic molecular impurities in helium was investigated by laser-induced breakdown spectroscopy (LIBS). For the Column III and V hydrides such as $B_2H_6$, $PH_3$, and $AsH_3$, the detectability limits with the present apparatus were determined to be 1, 3, and ~1 ppm, respectively. It is expected that resorting to synchronous detection techniques will improve the sensitivity of LIBS for this application by as much as an order of magnitude.

Index Headings: Fluorescence; Lasers, Nd:YAG; UV-visible spectroscopy; Laser-induced breakdown spectroscopy.

## INTRODUCTION

The application of laser excitation and ionization processes to the detection of impurities in gases and solids is well developed. In flames, for example, Grant et al.[1] have observed 25 parts per million (ppm) of NO by multiphoton ionization (MPI) with a tunable dye laser. Also, trace concentrations of a variety of elements in both solids and liquids ($2 \cdot 10^{-8}$ at. % Na and $5 \cdot 10^{-7}$ at. % Al, for example, in Ge crystals and seawater, respectively) have been detected by Bekov and Letokhov,[2] again utilizing multi-step, resonantly enhanced laser photoionization. Akilov et al.[3] have invoked similar techniques to observe aluminum concentrations as low as $2 \cdot 10^{-7}$ at. % in ostensibly "pure" germanium.

An alternative, and simpler, approach to impurity detection is laser-induced breakdown spectroscopy (LIBS),[4–8] which involves optical breakdown in a gaseous sample or at a surface that is induced by a laser pulse having a peak intensity typically in the range of $10^7$–$10^{10}$ W cm$^{-2}$. Such high optical fields result in the dissociation of molecular species present into their atomic constituents. Consequently, LIB spectra are largely free of molecular structure, and the small volume sampled by the technique makes it attractive for the micro- (and remote, if necessary) analysis of toxic or corrosive substances. Furthermore, as noted by Cremers and Radziemski,[9] LIBS avoids the need for electrodes, which are common to spark spectrometry.

Two further advantages of this technique that have been pointed out previously[4–8] are that LIBS is noninvasive and does not require that the laser be tuned to a resonance of the species under study. The latter is reflected in the fact that LIB spectra are relatively insensitive to the wavelength of the excitation laser, thus allowing one to simultaneously examine the relative concentrations of several impurities that may be present in the sample. Cremers[8] has clearly demonstrated the utility of this feature of LIBS in recent experiments in which minor constituents in steel were observed.

Loree, Radziemski, and co-workers[4–6] have demonstrated the ability of LIBS to measure small concentrations of impurities in a hostile environment such as the corrosive effluent from a coal gasifier plant. Early experiments involved the detection of 1–3% Na or K in the product stream. In subsequent time-resolved studies, 690 ppm of phosphorus (from diisopropylmethyl phosphonate, DIMP), 8 ppm of chlorine, and 38 ppm of fluorine were observed in air.[9]

In this paper, the preliminary results of several experiments are described in which the detection of sub-100-ppm concentrations of several Column III and V hydride polyatomic molecules in the gas phase by LIBS was explored. These studies were motivated by the growing demands being placed on the purity of gases of industrial importance and the concomitant requirement for (preferably) noninvasive and rapid diagnostic techniques for measuring trace concentrations of contaminants in such gases. As discussed earlier, the inherent characteristics of the method allow LIBS to lend itself well to such an application.

The goal of these experiments was the identification of one or more *atomic* emission lines associated with a given *molecular* impurity that are reliable indicators ("fingerprints")[4] of the contaminant's relative concentration, particularly at the ppm level. Our initial efforts have centered on monitoring the concentrations of $PH_3$, $AsH_3$, and $B_2H_6$ diluted in He. Although the use of these three gases in the semiconductor industry is widespread, the toxicity of each has impeded the development of diagnostic procedures. Nevertheless, the impact of source gas purity on electronic device quality, for example, is illustrated by the observation[10,11] of the presence of Ge as a donor in GaAs epitaxial films grown by metal organic

FIG. 1. Schematic diagram of the experimental arrangement.



FIG. 2. Low-resolution view of the 600–610 nm spectral region for a mixture of 361 ppm of PH₃ in He (top) and He only (bottom). The upper and lower traces have been intentionally offset for clarity.
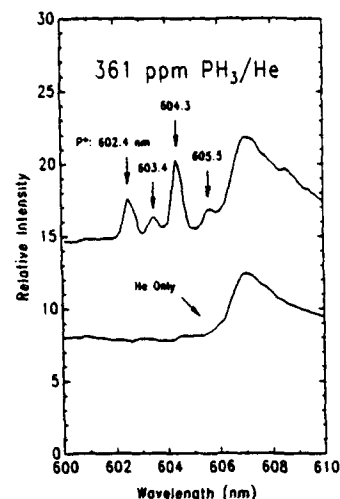
chemical vapor deposition (MOCVD). It now appears that the Ge impurity is introduced to the reactor in the form of germane ($GeH_4$) as a contaminant in $AsH_3$.

## EXPERIMENTAL

The experimental apparatus, shown schematically in Fig. 1, is described in detail elsewhere[12] and will be briefly reviewed here. Optical field intensities up to ~$10^{11}$ W cm$^{-2}$ were produced in a vacuum chamber by focusing the second harmonic beam ($\lambda$ = 532 nm) from a pulsed Nd:YAG laser [10 Hz, 8 ns full width at half-maximum (FWHM) pulses] with a 10-cm-focal-length (FL) lens. The chamber was evacuated by a turbomolecular pump to a base pressure of $5 \cdot 10^{-8}$ Torr, and the entire gas handling/vacuum chamber system was constructed of stainless steel. Visible and ultraviolet radiation from the laser-induced spark was collected at 90° to the pump laser beam and dispersed by a simple lens telescope/spectrometer combination. A 3.1-cm-diameter, 7-cm-FL lens collimated the radiation from the plasma, and a second lens (2.5-cm diameter, 10-cm FL) focused the beam into a 0.25-m spectrograph having an $f$ number of 3.8.

Spectra were acquired by mounting one of two intensified diode arrays at the exit plane of the spectrograph. The first, composed of 512 diodes, had a sensitivity of ~100 photons/count and a useful spectral range of ~350–830 nm. Equipped with this optical multichannel analyzer (OSMA) detector, 25-$\mu$m entrance slits, and a 300-lines/mm diffraction grating, the entire detection system had a first-order spectral resolution of ~0.28 nm/diode. When necessary, the resolution could be improved by a factor of two by interchanging gratings or operating the spectrograph in second order. For the arsine and diborane experiments, it was desirable to monitor atomic lines lying below 300 nm, which required a second intensified array having adequate response over the 200–300 nm region. Unless stated otherwise, all wavelengths dis-

cussed here are measured in air. All spectral data were stored and processed by a DEC LSI 11/73 computer.

Although the gas handling system was equipped for either flowing or static fill experiments, no detectable differences were observed between the LIB spectra for the two cases. Consequently, all of the measurements with these toxic gases were made under static fill conditions and, after each experiment, the gas was exhausted through a $KMnO_4$ bubbler.

Known levels of the impurity gas under study were prepared by diluting calibrated samples (provided by the Liquid Air Corp.) with high-purity He (UHP; >99.999%). In this manner, it was straightforward to reliably mix samples containing <1 ppm of the desired "contaminant." Fresh gas mixtures were prepared for each data run, which simply consisted of firing a fixed number of laser shots (typically 700–800) while monitoring a ~150-nm-wide spectral region. Preparation for the next run consisted of evacuating the cell, backfilling with He, and evacuating one final time before admitting a fresh gas mixture.

## RESULTS AND DISCUSSION

Phosphine. Experiments were carried out with mixtures of 3, 10, 50, and 180 ppm of $PH_3$ in He that were prepared by diluting a calibrated 361 ppm in He mixture. Scans of the 300–900 nm region revealed several phosphorus and hydrogen lines, but most (such as the 391.4-nm and 434.0-nm transitions of P and H, respectively) vanished for $PH_3$ concentrations below ~90 ppm.

In the 600–660 nm spectral region, five lines—four arising from the phosphorus singly charged ion and one from hydrogen (P⁺: 602.4, 603.4, 604.3, and 605.5 nm; H: 656.3 nm)—were readily detected. A low-resolution view of the 600–610 nm interval is given in Fig. 2 for both 361 ppm $PH_3$/He and He-only static fills. The four lines mentioned earlier, of which the 604.3-nm transition is the strongest, are clearly noticeable. Figures 3 and 4 show the dependence of the P⁺ 604.3-nm and H 656.3-nm transition peak intensities, respectively, on the $PH_3$ concen-
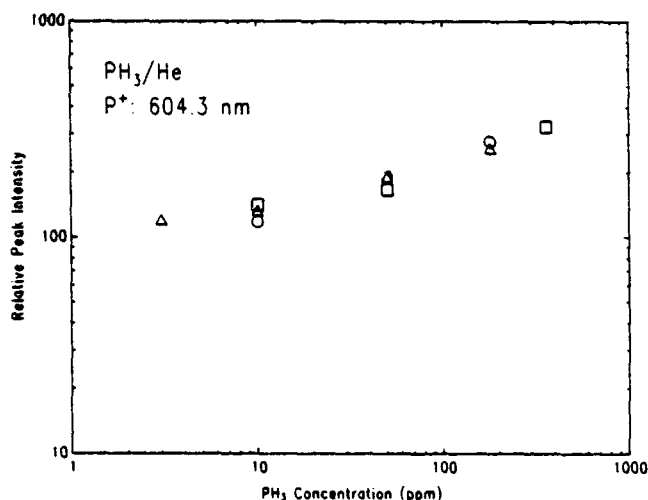
FIG. 3. Dependence of the $P^+$ 604.3-nm line intensity on the $PH_3$ concentration for impurity levels ranging from ~3 to ~400 ppm.
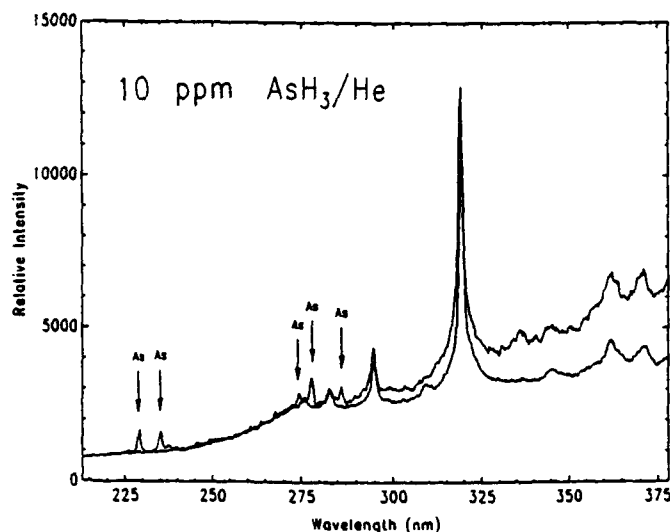


FIG. 5. Ultraviolet LIB emission spectrum of 10-ppm arsine in He. The strong As lines lying between 225 and ~300 nm are indicated. The lower spectral trace is that for pure He.

tration. Note that, for $PH_3$ concentrations above 20–30 ppm, the variation of the time-integrated 604.3-nm transition intensity (cf. Fig. 3) is logarithmic in $PH_3$ number density. Below 10 ppm, the signal falls less slowly, but the underlying blackbody continuum complicated measurements at lower $PH_3$ concentrations. Consequently, with the present apparatus, the minimum $PH_3$ level detectable by monitoring the phosphorus orange line was limited to ~3 ppm. However, we estimate that, by utilizing synchronous detection techniques, one could improve the $PH_3$ detectability limit to below 500 ppb. Finally, data from three separate experimental trials, given in Fig. 3, illustrate the reproducibility of the measurements.

**Arsine.** A known mixture of 100 ppm $AsH_3$ in helium was used to prepare all diluted samples. Scans of the visible and ultraviolet revealed the most reliable atomic transitions to be those of arsenic lying between 220 and

290 nm. Figure 5 displays the spectra that were recorded between ~212 and 378 nm for both 10 ppm $AsH_3$ in He and He itself. Five lines of neutral As (228.8, 235.0, 278.0, and 286.0 nm) are quite clear and, as shown in Fig. 6 for the 228.8-nm transition, monitoring the intensity of any of the five limited one to detecting $AsH_3$ concentrations of roughly 1 ppm or higher. Again, it is expected that the incorporation of synchronous detection techniques or the use of a fiber-optics bundle introduced into the vacuum chamber to improve the fluorescence collection efficiency would lower the detectability limit by as much as an order of magnitude.

**Diborane.** Results similar to those obtained with $AsH_3$ and $PH_3$ were also realized with $B_2H_6$. Two lines of atomic boron, 434.5 and 336.0 nm, were readily observed, and the latter was reproducibly detected down to $B_2H_6$ concentrations as low as ~1 ppm (cf. Fig. 7).



FIG. 4. Data similar to those of Fig. 3 except that the H line at 656.3 nm is being monitored.



FIG. 6. Variation of the peak intensity of the 228.8-nm line of arsenic with the arsine concentration.
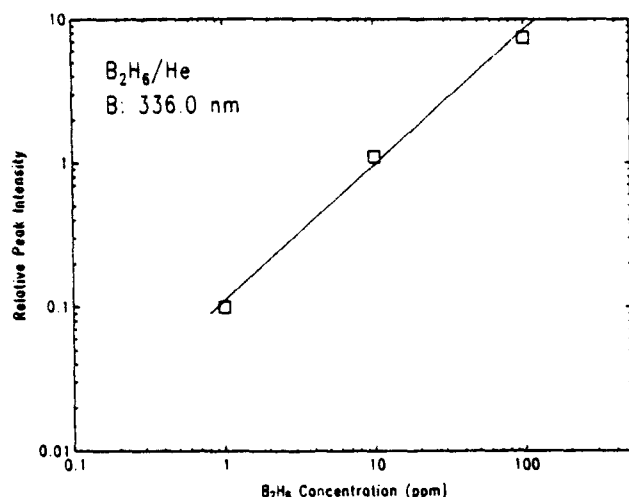
FIG. 7. Data similar to those of Figs. 3, 4, and 6 for the 336.0-nm line of boron. The B 434.5-nm transition intensity was found to have a dependence on [$B_2H_6$] that was nearly identical to that shown here.

## SUMMARY AND CONCLUSIONS

The capability of detecting small concentrations of selected polyatomic molecules in He by LIBS has been demonstrated. In accord with previous studies, the sensitivity of the technique is system dependent, but our studies yielded a ~1-ppm concentration "floor" for $AsH_3$, $PH_3$, and $B_2H_6$. Consequently, the detectability limits reported here are comparable to those determined previously for atomic species such as Cl and F. As noted earlier, it is estimated that the implementation of synchronous detection techniques would reduce these limits by as much as an order of magnitude. Of course, the homogeneity of neat samples available in an industrial environment might adversely affect the limits reported

here. Nevertheless, these preliminary results demonstrate that LIBS is an attractive technique for making remote measurements of sub-100-ppm concentrations of gases which are of critical importance to the semiconductor industry. In general, the rapid acquisition and analysis of spectral data that are characteristic of LIBS make it amenable to the computerized, *in situ* analysis of small volumes of toxic and/or corrosive gases.

1. E. R. Grant, B. H. Rockney, and T. A. Cool, Chem. Phys. Lett. 87, 141 (1982).
2. G. I. Bekov and V. S. Letokhov, Appl. Phys. B 30, 161 (1983).
3. R. Akilov, G. I. Bekov, V. S. Letokhov, G. I. Maksimov, V. I. Mishin, V. N. Radaev, and V. N. Shishov, Kvan. Elektron. (Moscow) 9, 1859 (1982) [Sov. J. Quant. Electron. 12, 1201 (1982)].
4. T. R. Loree and L. J. Radziemski, Plasma Chem. and Plasma Proc. 1, 271 (1981).
5. L. J. Radziemski and T. R. Loree, Plasma Chem. and Plasma Proc. 1, 281 (1981).
6. L. J. Radziemski, T. R. Loree, D. A. Cremers, and N. M. Hoffman, Anal. Chem. 55, 1246 (1983).
7. D. A. Cremers and L. J. Radziemski, in *Laser Spectroscopy and Its Applications*, L. J. Radziemski, R. W. Solarz, and J. A. Paisner, Eds. (Marcel Dekker, New York, 1987), pp. 351–415.
8. D. A. Cremers, Appl. Spectrosc. 41, 572 (1987).
9. D. A. Cremers and L. J. Radziemski, Anal Chem. 55, 1252 (1983).
10. G. E. Stillman, C. M. Wolfe, and J. O. Dimmock, in *Semiconductors and Semimetals*, R. K. Willardson and A. C. Beer, Eds. (Academic Press, New York, 1977), Vol. 12, pp. 169–290.
11. S. S. Bose, B. Lee, M. H. Kim, and G. E. Stillman, Appl. Phys. Lett. 51, 937 (1987).
12. E. A. P. Cheng, M.S. thesis, University of Illinois, Urbana (1987).

# Ultraviolet laser-assisted metalorganic chemical vapor deposition of GaAs

P. K. York, J. G. Eden, J. J. Coleman, G. E. Fernández, and K. J. Beernink
*Materials Research Laboratory and Everitt Laboratory, University of Illinois, 1406 West Green Street, Urbana, Illinois 61801*

The growth of GaAs irradiated with ultraviolet laser light in a metalorganic chemical vapor deposition reactor has been investigated. Growth rate enhancements of up to 15% were observed at 450 °C by illuminating the substrate with no more than 13 mJ/cm$^2$ of KrF laser (248 nm) radiation. For 5-eV photons, arsine is virtually transparent, while the trimethylgallium (TMG) photoabsorption cross section is approximately $10^{-19}$ cm$^2$. Data acquired with and without the optical beam impinging on the substrate are well described by the Langmuir–Hinshelwood model, and the results point to photodissociation of adsorbed TMG as the origin of the growth rate enhancement. Nearly identical experiments carried out at 351 nm (XeF) corroborate this conclusion since no measurable increase in growth rate was observed at this wavelength, where both arsine and TMG photoabsorption is negligible. Conversely, significant improvement in surface morphology for samples grown below 700 °C is observed with ultraviolet laser irradiation of the substrate at *each* of the wavelengths investigated (193, 248, and 351 nm). Smooth and specular surfaces are obtained with substrate temperatures as low as 550 °C and at fluences well below those which induce a significant rise in the surface temperature.

## I. INTRODUCTION

Laser photochemical vapor deposition (LPVD) draws on laser photochemistry to produce, independently of substrate temperature, atoms, molecular radicals, or excited species which are not normally present in significant concentrations in conventional metalorganic chemical vapor deposition (MOCVD) or molecular-beam epitaxy. The large photon energies available from existing ultraviolet lasers (and the excimer lasers, in particular) are generally more than ample to rupture metal-ligand bonds in a precursor molecule by the absorption of a single photon. Hence the reactor chemistry can be altered in a controllable, although unconventional manner. Examples of the potential utility of this technique include the growth of Si$_3$N$_4$ by photodissociating mixtures of SiH$_4$ and NH$_3$ with an excimer laser beam (ArF: 193 nm)[1,2] or the recently demonstrated growth of epitaxial Ge on GaAs with the assistance of laser produced hydrogen atoms.[3]

Over the past 4 years, several groups[4-7] have demonstrated the growth of III-V films by irradiating the substrate with focused or collimated excimer laser beams. In each case, however, transient heating of the substrate and growing film was a significant or controlling factor in the growth process owing to the high laser fluences employed (> 50 mJ/cm$^2$).

Recently, we reported[8] a photoenhancement in the growth of epitaxial GaAs films on GaAs substrates at a temperature of 450 °C by illuminating the substrate in an MOCVD reactor with no more than 13 mJ/cm$^2$ of KrF radiation (248 nm). The absence of any enhancement at 351 nm (XeF laser) demonstrated the photochemical (as opposed to thermal) nature of this effect. Isolating the observed photoenhancement mechanism is a difficult task if the operating regimes for the reactor are not known. Therefore, a series of

experiments to clearly identify and model the epitaxial crystal growth regimes with and without ultraviolet (UV) laser irradiation have been carried out and are reported here. The KrF laser was used in the bulk of these studies to simplify analysis since arsine is virtually transparent at this wavelength,[9] while TMG has a gas phase photoabsorption cross section[10] of ~ $10^{-19}$ cm$^2$. On the basis of the results, the mechanism responsible for the enhancement in the film growth rate of GaAs for $\lambda = 248$ nm is attributed to photolysis of trimethylgallium (TMG) in the adlayer.

Furthermore, the influence of UV radiation on the epitaxial layer morphology has been investigated in the 500–650 °C temperature range where the surface morphology has deteriorated from the smooth and specular appearance typically observed at higher growth temperatures. Noticeable improvements in layer morphology are observed with UV illumination for each temperature studied, and under appropriate growth conditions, specular surfaces are obtained for temperatures as low as 550 °C. In contrast to the film growth rate, this improvement is independent of wavelength in the $193 < \lambda < 351$ nm range.

## II. EXPERIMENTAL DESCRIPTION

A schematic diagram of the MOCVD reaction chamber and UV laser optical system is illustrated in Fig. 1. Experiments were carried out in a 2.5-cm-square horizontal quartz chamber at atmospheric pressure with hydrogen as the carrier gas and source vapors of TMG ( − 10 °C) and arsine (10% in hydrogen). The untilted graphite susceptor is 2.5 cm in length with its leading edge 10 cm from the gas inlet. Quartz plates are placed between the inlet and the susceptor to eliminate any discontinuity in the gas flow to the substrate. Heat is provided by rf induction, and the temperature is monitored by a thermocouple at the center of the susceptor
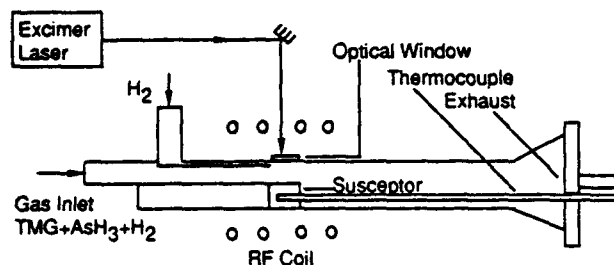
FIG. 1. Schematic diagram of the horizontal MOCVD reaction chamber with optical window purge configuration and perpendicular substrate irradiation geometry.

directly below the substrate. Although most experiments were performed between 450 and 650 °C, growth temperatures ranged from 425 to 800 °C.

The substrate was irradiated at normal incidence by a collimated excimer laser beam (ArF, KrF, or XeF) which was spatially filtered to a cross-sectional area of 1.4 cm², and entered the chamber directly above the substrate through an optical window equipped with a hydrogen purge, as depicted in Fig. 1. Pure hydrogen flowing through this purge path prevents reactants in the main gas stream from reaching and thus depositing on the optical window and thereby attenuating the laser beam. The hydrogen flows through the purge window and the chamber are balanced for equal gas velocities (60 cm/s) with a total flow rate of ~ 10 slpm.

Prior to each growth, the (100) GaAs:Si substrates were cleaned with organic solvents and hot 1:1 HCl:H$_2$O. After the substrate was heated to 700 °C in an arsine-hydrogen ambient for 10 min to remove any residual oxide, a 0.25-$\mu$m GaAs buffer layer and a 150-Å AlAs spacer layer were grown. The purpose of the AlAs layer is to serve as a marker to aid in delineation of the top GaAs layer. For the samples grown below 700 °C, the temperature was lowered after the growth of the AlAs layer and stabilized for 5 min. Finally, 0.1–0.2 $\mu$m of GaAs was grown with the desired growth and optical excitation parameters. For each sample, a total growth time of 30 min was the maximum length of time over which the excimer laser power output was stable relative to the initial output power at the start of the growth run.

Several experiments were performed to characterize reactor growth temperature regimes and film growth rates with and without laser irradiation. First, the temperature variation of the GaAs growth rates was ascertained by keeping the TMG and arsine mass flow rates fixed at 3 and 500 sccm, respectively, while varying the temperature in increments from 425 to 750 °C. Next, to verify diffusion limited growth at 700 °C, the TMG flow rate was varied between 2 and 10 sccm for a constant arsine flow rate of 100 sccm. Finally, the growth rates at 450 °C were measured for arsine flow rates between 30 and 500 sccm (0.23–3.7 Torr) with the TMG flow rate held constant at 3 sccm (0.23 Torr). In this last set of experiments, half of the substrate was masked from the optical beam and the remaining half was irradiated ($\lambda$ = 248 or 351 nm) with 7–13 mJ/cm² at a pulse repetition frequency (PRF) of 30 Hz. In order to minimize beam diffraction effects at the substrate, the laser beam mask was

placed immediately on top of the chamber.

Growth rates were determined by measuring layer thicknesses with a high-resolution scanning electron microscope (SEM). Samples were cleaved and stained using the aluminum selective etch 1 HF: 5 CrO$_3$: 30 H$_2$O. The effects of the GaAs buffer and AlAs spacer layer on crystallinity were investigated by growing a series of samples with and without buffer and spacer layers. When no GaAs buffer layer was grown, the AlAs spacer was omitted, and growth was initiated directly onto the substrate. The buffer and spacer layers were both grown at 700 °C. The crystalline quality of these epitaxial layers was determined[11] from transmission electron microscopy (TEM) electron diffraction patterns. TEM specimens were prepared with standard thinning and mounting techniques, and examined with a Phillips EM 430 microscope operating at 300 kV.[12]

Surface morphological studies were carried out at growth temperatures ranging from 500 to 650 °C in 50 °C increments with a TMG flow rate of 2.5 or 10 sccm, an arsine flow rate of 100–500 sccm, a total hydrogen flow rate of 5100 sccm, and subsequent epitaxial layer thicknesses of 0.1–0.75 $\mu$m. For these studies, the 700 °C preheat and the GaAs buffer/AlAs spacer layers were eliminated. Illuminated and nonilluminated samples were grown separately to spatially characterize morphology features. The substrate was illuminated by the UV laser beam at 193, 248, or 351 nm with fluences up to 19 mJ/cm² for KrF and 8 mJ/cm² for ArF and XeF and pulse repetition frequencies between 4 and 30 Hz. Morphologies of epitaxial layers were examined with a Nomarsky interference phase contrast microscope at magnifications of up to 1000×.

## III. RESULTS

### A. Reactor characterization

An Arrhenius plot for the growth rate of GaAs is shown in Fig. 2, where two of the three regimes[13,14] in conventional
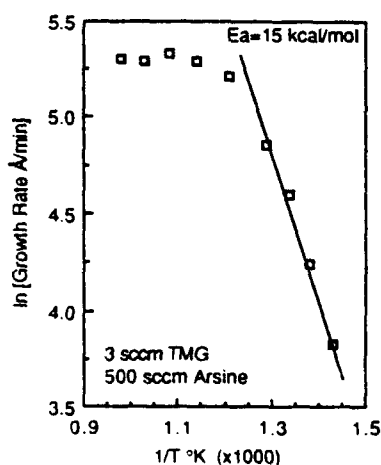


FIG. 2. Arrhenius plot of the growth rate for GaAs with fixed TMG (3 sccm) and arsine mass flow rates (500 sccm) to illustrate two of the three growth regimes dictated by temperature in the MOCVD growth of GaAs. The apparent activation energy $E$, in the kinetically controlled growth regime is 15 kcal/mol.

atmospheric pressure MOCVD are readily identified. These three regimes are (i) low-temperature surface kinetics limited growth, (ii) midtemperature diffusion limited growth, and (iii) high-temperature desorption and diffusion limited growth. In the kinetic regime (typically below 525–575 °C), the surface reaction rates are slow compared to the diffusion of the source molecules to the surface, and the growth rate is controlled by the adsorption of both arsine and TMG molecules onto the surface.[15] For this regime, the apparent activation energy $E_a$ was found to be 15 kcal/mol. Between ~600 and 800 °C, diffusion of the source molecules to the surface becomes slow compared to the surface reaction rates, and the film growth rate is then source diffusion limited. Arsine adsorption is strong in this temperature range, and the growth rate is independent of arsine partial pressure as long as the concentration of arsenic-containing species is larger than the concentration of the gallium precursor.[15] Under these conditions, the growth rate varies linearly with the TMG mass flow rate. At temperatures above ~800 °C, the growth rate continues to be TMG diffusion limited, but decreases in magnitude, most probably caused by depletion of reactants from gas-phase prenucleation and increased desorption of adsorbed molecules.[14] For the reactor configuration of these experiments, the growth rate appears, from Fig. 2, to be diffusion limited above ~550 °C. The dependence of the GaAs growth rate on the TMG mass flow rate for a constant arsine flow rate of 100 sccm that is observed at 700 °C is shown in Fig. 3. The linear variation of the growth rate confirms TMG diffusion limited growth at this temperature, which is in a region which will not be of further interest in this paper.

All samples grown with a GaAs buffer layer were single crystal, even at 425 °C, and for those grown without the AlAs spacer, the interface between the low-temperature layer and the buffer layer could not be discerned in cross-sectional specimens. Those grown at 500 °C without the higher temperature buffer layer were polycrystalline, and there was no measurable growth below 500 °C without the buffer layer. The presence of the AlAs marker layers resulted in no observable change in the crystallinity of the samples.
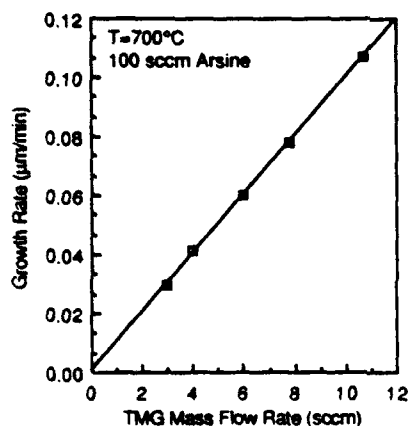


FIG. 3. Dependence of the GaAs growth rate on TMG mass flow rate for the substrate temperature and arsine mass flow rate held constant at 700 °C and 100 sccm, respectively. The linear variation demonstrates diffusion limited growth at this temperature.
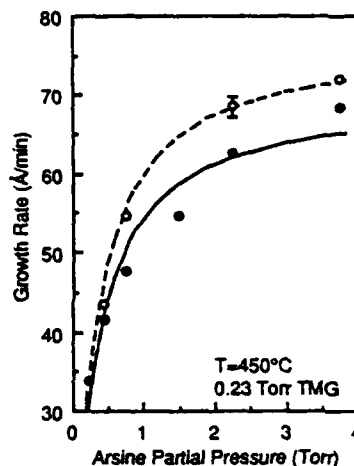


FIG. 4. Data obtained for the growth rate variation with arsine partial pressure for both masked substrates (solid circles) and substrates illuminated with ~11 mJ/cm² of 248-nm radiation (open circles) for fixed TMG partial pressure (0.23 Torr) and temperature (450 °C). The solid curve represents the best fit of the Langmuir–Hinshelwood model to the nonilluminated data, while the dashed curve corresponds to the best fit for data measured in the presence of UV radiation.

## B. Effect of UV laser radiation at the substrate

Data acquired for the GaAs growth rate variation with arsine partial pressure for both the nonilluminated (solid circles) and illuminated substrates (open circles) are plotted in Fig. 4 for $\lambda = 248$ nm, ~10 mJ/cm² (30 Hz), $T = 450$ °C, and the TMG partial pressure fixed at 0.23 Torr. The estimated relative error between illuminated and masked samples, arising primarily from variations in the growth rate with position on the wafer, is 2.5% and is represented by the error bar in Fig. 2. To account for small fluctuations in the laser intensity and to obtain a realistic comparison between data points, the as-measured growth rates for the irradiated samples were normalized to an average fluence over the entire run as well as to an average initial fluence.[8] Note the increase in growth rate for the illuminated regions for each arsine flow investigated, giving an enhancement over the masked regions of between 5% and 15%. A sublinear dependence on arsine partial pressure is observed for both masked and irradiated regions of the substrate, and the growth rates eventually saturate with increasing concentrations of arsine. An increase in the pusle repetition frequency of the laser would be expected to increase the enhancement in the growth rate in a linear fashion, provided laser-induced temperature effects do not become important.

Surface-kinetics-controlled growth in MOCVD can be described by the Langmuir–Hinshelwood model,[14–16] which, indeed, predicts a sublinear variation with both TMG and arsine partial pressure. The growth rate $R$ for this model is given by

$$R = k\theta_G\theta_A = k\left(\frac{p_G\beta_G}{1 + p_G\beta_G}\right)\left(\frac{p_A\beta_A}{1 + p_A\beta_A}\right), \tag{1}$$

where $k$ is a rate constant, $\beta$ is the adsorption rate constant divided by the desorption rate constant for TMG ($G$) or arsine ($A$), $p$ is the partial pressure, and $\theta$ is the molecular

surface coverage. This sublinear dependence is caused by a saturation in surface coverage for large partial pressures of the source molecules.

Identifying the cause of the increase in growth rate with laser irradiation requires an examination of the low-temperature growth mechanisms. The Langmuir–Hinshelwood model assumes noncompetitive adsorption of TMG and arsine followed by surface reaction,[14] as opposed to gas-phase reaction. Furthermore, the growth rate is not hindered by the desorption of reaction by-products such as methane.[15] It has been suggested[15] that arsine adsorption occurs prior to decomposition, with rapid loss of the first hydrogen atom after surface adsorption, probably followed by the first bimolecular methane elimination. At higher temperatures where the growth is TMG diffusion limited, arsine adsorption is very strong (indicating unity surface coverage), while desorption of TMG remains important[14] so that $p_A \beta_A \gg 1$ and $p_G \beta_G \ll 1$. Under these conditions, Eq. (1) predicts that the growth is proportional to the TMG and independent of arsine partial pressure, as expected for diffusion limited growth.

A least-squares fit of the Langmuir–Hinshelwood model [Eq. (1)] to our experimental data is represented by the solid (no laser) and dashed (laser) curves in Fig. 4. The adjustable parameters in obtaining the fit are $\beta_A$ and the product $k\theta_G$. Without further empirical data on TMG surface adsorption and the measurement of the surface reaction rate constant $k$, in particular, $\beta_G$ and $k$ cannot be determined separately. From the analysis, $\beta_A$ is found to decline by $\sim 15\%$ from 3.4 for masked samples to 2.9 when the surface was illuminated. However, the product $k\theta_G$ increased by $\sim 13\%$ from 70 to 79 Å/min with laser irradiation. Figure 5(a) depicts the sensitivity of the fit of Eq. (1) to the data for a change of $\pm 15\%$ in $k\theta_G$. Here the best fit is represented by the solid line, and clearly, the agreement with the data deteriorates rapidly with small changes in $k\theta_G$. Conversely, the insensitivity of the curve fit to $\beta_A$ is demonstrated in Fig. 5(b) where a $\pm 15\%$ change in $\beta_A$ produces a much smaller perturbation in the fit to the data, indicating that arsine surface adsorption is virtually unaffected by optical irradiation at this wavelength. These results are consistent with the fact that arsine is nearly transparent, while TMG has a gas-phase photoabsorption cross section of $\sim 10^{-19}$ cm$^2$ at 248 nm. We conclude, therefore, that the GaAs growth rates measured in these experiments at 450 °C are governed by the Langmuir–Hinshelwood model and confirm the premise that the UV optical beam interacts primarily with adsorbed TMG at this wavelength. As an aside, it should be noted that Tanaka, Deguchi, and Hirose[17] have interpreted their recent experiments involving the laser photochemical vapor deposition of Si with an ArF laser in an analogous manner.

## C. Surface morphological studies

In the course of these experiments, it was discovered that epitaxial layers grown at and below 500 °C had smooth and specular morphology if a GaAs buffer layer was first grown at 700 °C. Additionally, no measurable growth was initiated below 500 °C unless a buffer layer was present, inde-
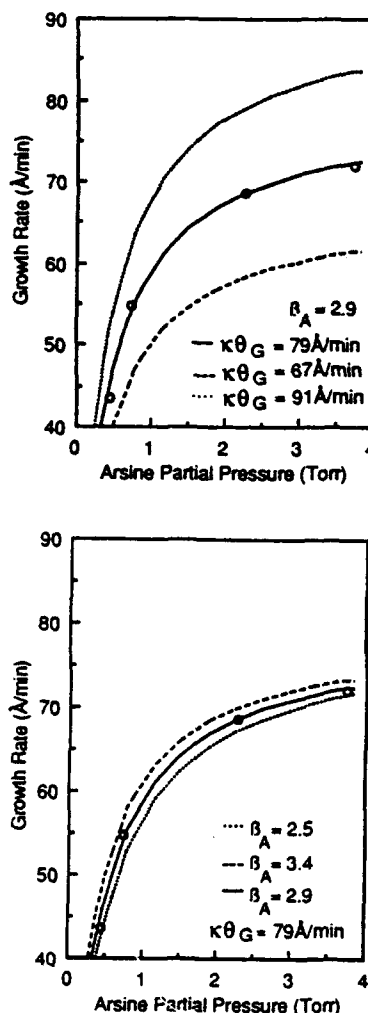


FIG. 5. Curve fits of the Langmuir–Hinshelwood model to the data obtained for the GaAs growth rate in the presence of UV radiation (11 mJ/cm$^2$, 248 nm) for different values of the parameters used in the analysis to ascertain the sensitivity of the curve fit to these parameters. The solid curves represent the best fit using the values $\beta_A = 2.9$ and $k\theta_G = 79$ Å/min; the dashed and dotted curves are computed for (a) $k\theta_G$ values of 67 and 91 Å/min, and (b) $\beta_A$ values of 3.4 and 2.6, respectively.

pendent of laser radiation, and there were few or no distinguishable morphological characteristics caused by optical irradiation between these samples. For these reasons, we focused our attention on samples grown without buffers in the temperature range 500–650 °C. Undoubtedly, incomplete removal of the native oxide from the GaAs surface prior to growth degrades the quality of the epitaxial layer,[18] particularly at temperatures near or below the desorption temperature of the oxide ($\sim 580$ °C[19]). For this reason, the 700 °C preheat and GaAs buffer layer were eliminated from the set of experiments carried out between 500 and 650 °C to ascertain the effects of residual oxide, since, as a practical matter, it is desirable to do away with pregrowth thermal treatments.

The epitaxial layer morphology of nonilluminated samples grown within this temperature range (500–650 °C) with

5004    J. Appl. Phys., Vol. 66, No. 10, 15 November 1989

York et al.    5004

a TMG flow rate of 10 sccm and arsine mass flow rates > 100 sccm were rough with irregular features. Reducing the growth rate by lowering the TMG flow rate to 2.5 sccm (0.23 Torr) significantly reduced the density of the irregular features, but did not produce specular surfaces at any of these temperatures. Increasing the arsine flow rate from 100 to 500 sccm while keeping the TMG mass flow rate constant had no observable effect on morphology. Growth at 700 °C was determined to be the lowest temperature for which featureless surfaces could be obtained for each of these TMG flow rates.

Optical irradiation at all wavelengths (193, 248, and 351 nm), fluences (5–19 mJ/cm$^2$), and PRF (4–30 Hz) investigated promoted smooth surface morphology for the chosen temperature range 500–650 °C, most notably for



(a)

|———————————|
40 μm



(b)

|———————————|
40 μm

FIG. 6 Surface morphological features observed with a Nomarsky-interference phase-contrast microscope at 625 × (a) without laser irradiation and (b) with laser irradiation (KrF, 19mJ/cm$^2$) of the substrate during growth at a temperature of 550 °C, and TMG and arsine mass flow rates of 2.5 and 100 sccm, respectively. The elongated region of rough morphology in (b) corresponds to an imperfection in the quartz window where the laser beam has been attenuated.

samples grown at a TMG flow rate of 2.5 sccm. For fluences below 8 mJ/cm$^2$, the resulting morphologies for the three different wavelengths were very similar—mostly specular and smooth between small clusters of irregular features. By raising the fluence to 19 mJ/cm$^2$ at 248 nm, it was possible to obtain featureless surfaces at a TMG mass flow rate of 2.5 sccm even for temperatures as low as 550 °C. Micrographs of morphological features taken in a Nomarsky-interference phase-contrast microscope at 625 × are shown for a sample grown at 550 °C both (b) with (KrF, 19 mJ/cm$^2$) and (a) without illumination of the substrate in Fig. 6. The elongated region of poor morphology in Fig. 6(b) corresponds to an imperfection in the quartz window where the beam was attenuated. ArF and XeF laser fluences above 8 mJ/cm$^2$ were not available with our laser, and consequently, completely featureless morphologies have not been observed for these wavelengths. In general, increasing the PRF causes the clusters of irregular growth to spread out, leading to a smoothening in the surface morphology. Featureless surfaces were achieved at each temperature only for the combined highest PRF (30 Hz) and fluence (19 mJ/cm$^2$) available.

## IV. ANALYSIS

### A. Growth rates

The conclusion that the growth rate enhancement of Figs. 5 and 6 stems from the interaction of 5-eV photons with adsorbed (as opposed to gas phase) TMG molecules is based on a comparison between the optical properties of metal-alkyl molecules in an adlayer or in the gas phase. Rytz-Froidevaux, Salathé, and Gilgen,[20] Haigh,[21] and, more recently, Itoh et al.[22] have shown that 248 nm lies in the red wing of the gas-phase photoabsorption spectrum of TMG. At that wavelength, the single-photon (Beers law) absorption cross section is $\sigma \sim 1 \times 10^{-19}$ cm$^2$ which, when combined with the low peak powers used in these experiments ($7 < \Phi < 13$ mJ/cm$^2$, $0.35 < I < 0.65$ MW/cm$^2$), yields low gas-phase photodissociation rates for the metal-alkyl. That is, since $\sigma I \Delta t (h\omega)^{-1} \sim 1.5 \times 10^{-3}$ (where $\Delta t$ is the KrF laser pulse width of 20 ns FWHM), the optical transition is far from saturation and, for a TMG partial pressure at 300 K of 0.23 Torr, the volumetric rate at which $(CH_3)_2Ga$-$(CH_3)$ bonds are ruptured,[22,23] is $\sim 2.4 \times 10^{14}$ cm$^{-3}$ s$^{-1}$ (assuming the scission of one bond for every absorbed photon). This result is consistent with the observation that $\leqslant 1\%$ of the beam energy is absorbed by TMG in the gas phase for a window-to-substrate distance of $\sim 1.2$ cm. It appears, therefore, that the 248-nm laser radiation produces predominantly dimethylgallium radicals in the gas phase, and multiphoton effects are negligible.

While it is likely that partially photodecomposed TMG molecules [such as $(CH_3)_2Ga$] in the gas phase have an increased surface chemisorption probability owing to the removal of one or more methyl ligands, photodissociation products lying outside the boundary layer will have little impact on film growth. This constraint alone makes it impossible to attribute the growth rate enhancement of Fig. 4 to the gas phase photodissociation of TMG.

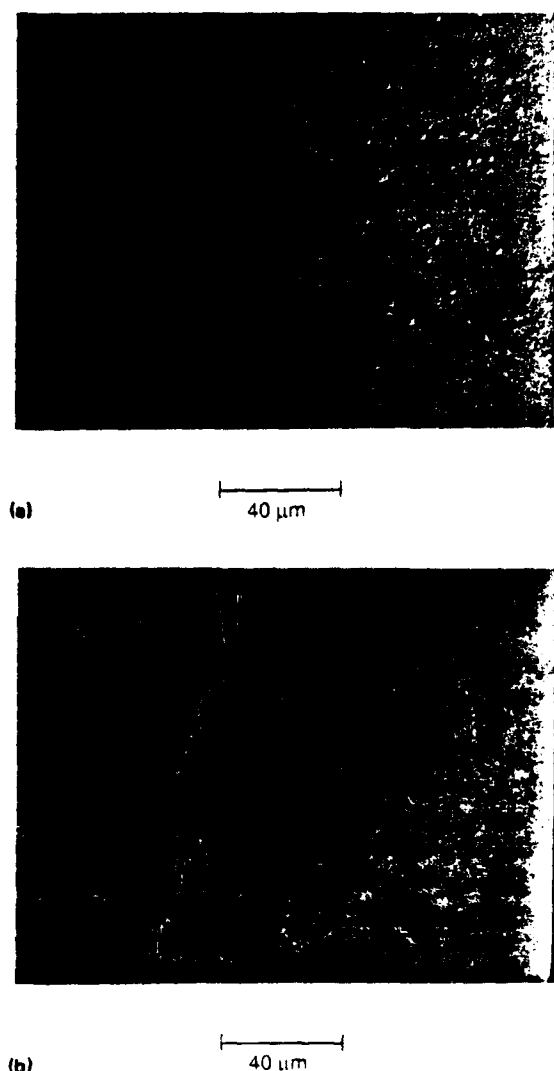Several groups[22,24–30] have clearly demonstrated the importance of the adlayer in determining the growth rate of

5005    J. Appl. Phys., Vol. 66, No 10, 15 November 1989

York et al.    5005

metal films by photodissociating column IIB or IIIA or noble metal-alkyl molecular precursors. With regard to the present experiments, in particular, the TMG adlayer has several characteristics which indicates that it is the dominant factor in film growth. Foremost is the fact that, as noted previously,[30] the number density of reactive species at the surface that is produced by adlayer photolysis will typically be orders of magnitude larger than that available from gas-phase photodissociation since ( 1 ) the TMG number density in the adlayer is generally six to eight orders of magnitude larger than it is in the gas phase; and (2) as noted by Braichotte and van den Bergh,[30] the limited diffusion rates of molecules in the adlayer are conducive to film growth if the removal of more than one ligand of the alkyl is necessary to initiate growth. That is, more than one photon can be readily absorbed by an adsorbed TMG molecule since its mobility is low. At least two experimental studies[25,31] have provided strong evidence that the photoabsorption spectrum for an adsorbed metal-alkyl species is elongated to the red as compared to the same spectrum for its gas-phase counterpart. This has been most convincingly demonstrated by the recent, detailed experiments of Zhang and Stuke[31] for several alkyls of aluminum. Furthermore, the exposure of column IIB metal-alkyl adlayers to UV radiation has been shown to convert physisorbed molecules into chemisorbed species,[27] a process which manifests itself in further broadening of the adlayer's absorption spectrum.

The relevance of these factors to our experiments is obvious. The ratio of TMG densities in the adlayer to that in the gas phase under typical experimental conditions is estimated to be $10^6$. Also, as noted earlier, 248 nm does lie in the red wing of the TMG *gas phase* absorption spectrum.[20–22] Hence it is plausible to expect the absorption spectra for the physisorbed and chemisorbed species to shift progressively towards the red with the result that, as noted by Chen and Osgood[27] for $(CH_3)_2Cd$, the absorption strength at 248 nm of a chemisorbed TMG layer can be expected to be considerably larger "...than for an equivalent quantity of molecules in the gas phase." Rough calculations relating the observed increase in film growth rate to the photon flux available at the substrate demonstrate the plausibility of the last point, namely, that the effective cross section for TMG adsorbed onto GaAs is one to two orders of magnitude larger than that for the gas phase species.[25]

The most conclusive support for the claim of a photochemically induced enhancement in growth rate at 248 nm was provided by measuring samples which were grown under otherwise identical reactor conditions, but irradiating the substrate with a XeF laser beam (351 nm). For laser fluences and PRF similar to those used at 248 nm, no change in growth rate in the illuminated portion of the substrate as compared to the masked portion of the substrate was observed. These findings are consistent with the fact that gas phase TMG and arsine are optically transparent at 351 nm, despite broadening of the alkyl absorption spectrum towards the red in the adlayer.

Furthermore, calculations of the instantaneous and average temperature rise of the substrate surface due to laser transient heating were carried out by solving the one dimensional, time-dependent heat-flow equation[32]

$$T(t) = \left(\frac{2I_0(1 - R)}{K\sqrt{\pi}}\right)\sqrt{Dt},\qquad(2)$$

where $I_0$ is the peak laser intensity, $D$ is the thermal diffusivity, $K$ is the thermal conductivity, and $R$ is the reflectivity of the substrate. Although this relation assumes that the parameters defined above are temperature independent, $K$ is actually a strong function of temperature[33]; therefore, an average value in the temperature range of interest was used. For the values[33] $K = 0.2$ W/cm K at 450 °C, $C_p = 0.327$ J/g K, $\rho = 5.315$ g/cm$^3$, $D(\equiv K/\rho C_p) = 0.11$ cm$^2$/s, $R = 0.6$ at 248 nm, and a peak laser intensity of 0.55 MW/cm$^2$ (which corresponds to a fluence of ~11 mJ/cm$^2$), the peak instantaneous temperature rise after one pulse is ~55 °C. At a repetition rate of 30 Hz, there is ~33 ms between pulses so that the average temperature rise is negligible, as expected.

From Fig. 2, the growth rate at 500 °C (substrate temperature of 450 °C plus laser transient heating of ~50 °C) is nearly twice that at 450 °C, which is substantially larger than the growth rate enhancement of 5%–15% observed here. However, the duty cycle of the laser (allowing for heating and cooling transients comparable to the laser pulse width) is still $10^{-6}$. Extrapolation of the gas phase thermal cracking rates[34] of TMG between 450 and 500 °C yield dissociation times on the order of milliseconds. Consequently, the instantaneous temperature rise of ~55 °C in a time frame on the order of tens of nanoseconds is unlikely to be responsible for the observed film growth rate enhancement.

## B. Surface morphology

Lowering the substrate temperature in conventional MOCVD correspondingly brings about a degradation of the surface morphology, which is caused primarily by a reduction in surface mobility of the source species on the growing surface.[35] More specifically, the consequence of reduced mobility is that molecular or atomic species are not always able to migrate to the energetically most favorable lattice sites, resulting in a roughening of the growth surface. This will be of particular importance at low growth temperatures ( $\ll 500$ °C) where an independent source of energy must be supplied to break up source molecules as well as provide ample surface mobility to obtain homoepitaxial layers.

In the present experiments, it became increasingly difficult to affect improvements in the surface morphology as the temperature was dropped. Presumably, this was due to the dramatic decline in surface mobility of the source species and perhaps because of the decrease in decomposition efficiency of the source molecules, particularly arsine. Additionally, the native oxide on GaAs desorbs at ~580 °C, and may, in part, account for the rough surface observed at 500 °C even at the highest available fluences, and the fact that no growth was initiated without a buffer at temperatures below 500 °C. In fact, preliminary studies indicate that preheating the substrate above the oxide desorption temperature without growing a buffer layer improves the subsequent epitaxial morphology. Source decomposition efficiency and residual oxide, however, are not likely to be

limiting factors in the quality of the morphology in the 600–650 °C range. Hence the attainment of featureless surfaces at these higher temperatures by illumination with optical fluences sufficiently low that the rise in the substrate temperature during growth is negligible indicates that an enhancement is occurring in the surface mobility of molecular or atomic species at the growth interface.

These results are similar to those obtained in previous studies,[36,37] where it was demonstrated that UV irradiation of the substrate during growth at temperatures lower than optimal improves the morphology of the epilayer. In the later study, Kukimoto et al.[37] observed the same trends as those reported here except that they were unable to generate featureless surface morphology below 700 °C, even at a higher fluence of 30 mJ/cm$^2$ (1.5 W/cm$^2$, 50 Hz). We believe, however, that this is due to the high growth rates (1000 Å/min) characteristic of their studies as opposed to those ($\leqslant$300 Å/min) that we found necessary to obtain specular morphologies in our experiments. Although completely specular surfaces were achieved in the present investigation only when using KrF (248 nm) at the highest fluence of 19 mJ/cm$^2$, it is believed that similar results would be observed with ArF (193 nm) and perhaps even XeF (351 nm) if sufficiently high fluences were available. The important point to be made here is that the improvement in surface morphology must be attributed to a photochemical mechanism since the lowest temperature at which mirrorlike surfaces can be obtained without UV irradiation of the substrate is ~700 °C. The apparent lack of dependence of the effect on laser wavelength in the UV suggests that the photogeneration of free carriers by the optical source may be the dominant process. Experiments conducted at still longer wavelengths (i.e., $\lambda > 350$ nm) will be required to verify this possibility in GaAs. Similar observations have been reported[38] for the photochemical growth of ZnSe and ZnS, where the growth rate exhibited a threshold for photoinduced enhancement at a wavelength corresponding to the band gap of the material.

## V. SUMMARY

Significant and reproducible enhancements in the growth rate of GaAs have been observed in an MOCVD reactor by illuminating the substrate with 7–13 mJ/cm$^2$ of 248-nm radiation. Several factors demonstrate that this effect is photochemical in nature. Data acquired with and without laser radiation are well described by the Langmuir–Hinshelwood model for which the curve fit to the raw data is virtually insensitive to $\beta_1$, regardless of whether the substrate is irradiated or not. Therefore, photothermal effects (i.e., laser-induced substrate heating) may be discounted since significant heating of the substrate rapidly accelerates arsine adsorption,[14] which would, in turn, create a significant dependence on $\beta_1$. Calculation of the average temperature rise of the substrate surface supports this conclusion. In contrast, $k\theta_2$ increases from 70 Å/min without laser irradiation to 79 Å/min in the presence of 5-eV photons, which is also consistent with the known gas-phase absorption spectrum for TMG and the expected broadening of that spectrum toward the red for the adsorbed species. An increase in the absorption cross section at 248 nm is expected to become

particularly strong (as compared to that for the gas-phase species) for chemisorbed TMG.

Finally, experiments carried out with 351-nm (XeF) irradiation of the substrate revealed no measurable enhancement of the film growth rate, which clearly demonstrates that the effect observed at 248 nm is photochemical in origin. All of the available evidence suggests that the role played by the laser is to photodissociate physisorbed or chemisorbed (rather than gas phase)[36] TMG. Since Zhang and Stuke[31] have demonstrated that the photolysis of adsorbed trimethylaluminum at 248 nm generates considerably more AlCH$_3$ than does the corresponding reaction in the gas phase; it is likely that a similar conclusion holds true for TMG, as well, and that, as suggested in Ref. 31, a logical course for the future of laser-assisted MOCVD experiments would be to explore halogen containing precursors such as dimethylgallium chloride.

Contrary to the wavelength dependence observed for the growth rate enhancement, significant improvement in surface morphology is observed at temperatures as low as 500 °C with UV laser irradiation at each of the three wavelengths investigated (193, 248, and 351 nm). Mirrorlike surfaces are obtained for temperatures $\geqslant$550 °C with KrF at fluences well below those which will generate a significant average substrate temperature rise. Residual surface oxide contributes deleteriously to the resulting layer morphology at growth temperatures below that at which the native oxide desorbs, and at the lowest growth temperature (500 °C), laser irradiation does not render completely smooth morphology. Between 425 and 500 °C, oxide or an otherwise imperfect substrate surface may be the limiting factor in initiating growth. Other groups[7,18] have reported success with in situ pregrowth cleaning by illuminating the substrate with fluences of ~100 mJ/cm$^2$ (ArF), owing probably to the nonnegligible transient temperature rise expected at this fluence. Clearly, it is desirable to remove all unnecessary thermal treatments from the growth process, and we intend to investigate photochemical means of in situ pregrowth preparation of the substrate surface.

## ACKNOWLEDGMENTS

[1] P. K. Boyer, G. A. Roche, W. H. Ritchie, and G. J. Collins, Appl. Phys. Lett. 40, 716 (1982); R. Solanki, W. H. Ritchie, and G. J. Collins, Appl. Phys. Lett. 43, 454 (1983); P. K. Boyer, K. A. Emery, H. Zarnani, and K. J. Collins, Appl. Phys. Lett. 45, 979 (1984).
[2] T. F. Deutsch, D. J. Silversmith, and R. W. Mountain, Mater. Res. Soc. Symp. Proc. 17, 129 (1983).
[3] C. J. Kiely, V. Tavitian, C. Jones, J. J. G. Eden, Appl. Phys. Lett. 55, 65 (1989).
[4] V. M. Donnelly, D. Brasen, A. Appelbaum, and M. Geva, J. Appl. Phys. 58, 2022 (1985).

[5]C. W. Tu, V. M. Donnelly, J. C. Beggy, F. A. Baiocchi, V. R. McCrary, T. D. Harris, and M. G. Lamont, Appl. Phys. Lett. **52**, 966 (1988).

[6]V. M. Donnelly, C. W. Tu, J. C. Beggy, V. R. McCrary, M. G. Lamont, T. D. Harris, F. A. Baiocchi, and R. C. Farrow, Appl. Phys. Lett. **52**, 1065 (1988).

[7]S. S. Chu, T. L. Chu, C. L. Chang, and H. Firouzi, Appl. Phys. Lett. **52**, 1243 (1988).

[8]P. K. York, J. G. Eden, J. J. Coleman, G. E. Fernández, and K. J. Beernink, Appl. Phys. Lett. **54**, 1866 (1989).

[9]See, for example, J. Nishizawa and T. Kurabayashi, Mater. Res. Symp. Proc. **101**, 275 (1988); C. M. Humphries, A. D. Walsh, and P. A. Warsop, Discuss. Farady Soc. **35**, 148 (1963); J. H. Clark and R. G. Anderson, Appl. Phys. Lett. **32**, 46 (1978); B. Koplitz, Z. Xu, and C. Wittig, Appl. Phys. Lett. **52**, 860 (1988); H. Okabe, *Photochemistry of Small Molecules* (Wiley, New York, 1978), p. 269.

[10]Y. Rytz-Froidevaux, R. P. Salathé, and H. H. Gilgen, Mater. Res. Soc. Symp. Proc. **17**, 29 (1983).

[11]C. J. Kiely, P. K. York, J. G. Eden, J. J. Coleman, G. E. Fernández, and K. J. Beernink (unpublished data).

[12]S. J. Jeng, C. M. Wayman, G. Costrini, and J. J. Coleman, Mater. Lett. **2**, 359 (1984).

[13]D. Shaw in *Crystal Growth Theory and Techniques*, edited by C. Goodman (Plenum, New York, 1974), Vol. 1, p. 1.

[14]D. H. Reep and S. K. Ghandi, J. Electrochem. Soc. **130**, 675 (1983).

[15]D. J. Schlyer and M. A. Ring, J. Electrochem. Soc. **114**, 9 (1976).

[16]S. Thomson and G. Webb, *Heterogeneous Catalysis* (Wiley, New York, 1968), p. 87.

[17]T. Tanaka, K. Deguchi, and M. Hirose, Jpn. J. Appl. Phys. **26**, 2057 (1987).

[18]V. M. Donnelly, V. R. McCrary, A. Appelbaum, D. Brasen, and W. P. Lowe, J. Appl. Phys. **61**, 1410 (1987).

[19]A. J. SpringThorpe, S. J. Ingrey, B. Emmerstorfer, and P. Mandeville, Appl. Phys. Lett. **50**, 77 (1987).

[20]Y. Rytz-Froidevaux, R. P. Salathé, and J. H. Gilgen, Mater. Res. Soc. Symp. Proc. **17**, 29 (1983).

[21]J. Haigh, J. Mater. Sci. **18**, 1072 (1983).

[22]H. Itoh, M. Watanabe, S. Mukai, and H. Yajima, J. Cryst. Growth **93**, 165 (1988).

[23]S. Oikawa, M. Tsuda, M. Morishita, M. Mashita, and Y. Kuniya, J. Cryst. Growth **91**, 471 (1988).

[24]D. J. Ehrlich, R. M. Osgood, Jr., and T. F. Deutsch, Appl. Phys. Lett. **38**, 946 (1981).

[25]D. J. Ehrlich and R. M. Osgood, Jr., Chem. Phys. Lett. **79**, 381 (1981).

[26]Y. Rytz-Froidevaux, R. P. Salathé, H. H. Gilgen, and H. P. Weber, Appl. Phys. A **27**, 133 (1982).

[27]C. J. Chen and R. M. Osgood, Jr., Mater. Res. Soc. Symp. Proc. **17**, 169 (1983).

[28]J. Y. Tsao and D. J. Ehrlich, J. Chem. Phys. **81**, 4620 (1984).

[29]G. S. Higashi and L. J. Rothberg, Appl. Phys. Lett. **47**, 1288 (1985); G. S. Higashi, and C. G. Fleming, Appl. Phys. Lett. **48**, 1051 (1986).

[30]D. Braichotte and H. van den Bergh, Appl. Phys. Lett. A **45**, 337 (1988).

[31]Y. Zhang and M. Stuke, J. Cryst. Growth **93**, 143 (1988).

[32]P. Baeri and S. Campisano, in *Laser Annealing of Semiconductors*, edited by J. Poate and J. Mayer (Academic, New York, 1982), pp. 75–109.

[33]J. S. Blakemore, J. Appl. Phys. **53**, R123 (1982).

[34]M. Suzuki and M. Sato, J. Electrochem. Soc. **132**, 1684 (1988).

[35]Surface morphology.

[36]N. Pütz, H. Heinecke, E. Veuhoff, G. Arens, M. Heyen, H. Lüth, and P. Balk, J. Cryst. Growth **68**, 194 (1984).

[37]H. Kukimoto, Y. Ban, H. Komatsu, M. Takechi, and M. Ishizaki, J. Cryst. Growth **77**, 223 (1986).

[38]S. Fujita, A. Tanabe, T. Sakamoto, M. Isemura, and S. Fujita, J. Cryst. Growth **93**, 259 (1988).

# Low-temperature laser photochemical vapor deposition of GaAs

P. K. York, J. G. Eden, J. J. Coleman, G. E. Fernández, and K. J. Beernink
*Materials Research Laboratory and Everitt Laboratory, University of Illinois, 1406 West Green Street, Urbana, Illinois 61801*

The growth of epitaxial GaAs at temperatures below 500 °C by ultraviolet laser-assisted metalorganic chemical vapor deposition has been investigated. Experiments were conducted at 248 nm (KrF excimer laser) and 351 nm (XeF) in normal incidence with laser fluences maintained below 13 mJ/cm$^2$. While the growth rate was enhanced by 5–15% at 450 °C upon irradiating the substrate with 248 nm photons, no measurable effect was observed at 351 nm. This strong wavelength dependence at low fluence demonstrates that the film growth enhancement mechanism is photochemical in nature.

Laser-assisted chemical vapor deposition is often broadly subdivided into laser photochemical vapor deposition (LPVD) or laser-induced chemical vapor deposition (LCVD), depending on whether the role played by the laser in the growth process is primarily a photochemical or thermal one. Both spatially delineated (selective area) and broad-area epitaxy have been demonstrated with focused visible[1,2] or ultraviolet[3-5] (typically, frequency-doubled Ar$^+$) lasers and collimated excimer laser beams,[6-9] respectively. Although several studies have been reported in which III-V films were grown in metalorganic chemical vapor deposition[3-6,8,9] (MOCVD) or molecular beam epitaxy[7] systems accompanied by illumination of the substrate with ultraviolet (UV) radiation, the energy fluences and wavelengths used have made it difficult to resolve the relative contributions of thermal and photochemical processes to the overall growth rate. Furthermore, prior studies have typically involved laser energy fluences at the substrate of 50 to >100 mJ/cm$^2$. Under such conditions, thermal effects dominate[7] since, for example, instantaneous surface temperatures exceeding 1200 K are attained for an incident energy fluence of 100 mJ/cm$^2$ and 10–20 ns pulses. In short, whether UV laser-assisted film growth is driven photochemically or photothermally critically depends on the laser fluence and wavelength.

The photochemically enhanced growth of epitaxial GaAs by UV radiation in a MOCVD reactor is reported here. Experiments were conducted at 248 and 351 nm in normal incidence with the laser fluence maintained below 13 mJ/cm$^2$ at all times in order to prevent transient heating of the substrate and adlayer. At 248 nm, arsine is transparent[6,10] while the absorption cross section[11] for trimethylgallium (TMG) in the gas phase is $\sim 10^{-19}$ cm$^2$. Neither arsine nor TMG absorbs significantly at 351 nm[6,11] which provides a convenient experimental means for differentiating between photothermal and photochemical enhancement mechanisms.

A schematic diagram of the reaction chamber and laser apparatus is shown in Fig. 1. Experiments were carried out in a square (2.5×2.5 cm$^2$) horizontal quartz chamber at atmospheric pressure using hydrogen carrier gas and source vapors of TMG ( − 10 °C) and 10% arsine in hydrogen. The rectangular beam from an excimer laser operating at

248 nm (KrF) and at 351 nm (XeF) irradiated the substrate at normal incidence. Prior to each growth, the (100) GaAs:Si substrates were cleaned with organic solvents and hot 1:1 HCl:H$_2$O. The substrate was then heated to 700 °C in an arsine-hydrogen ambient for 10 min to remove any residual oxide, after which a 0.25 μm GaAs buffer layer was grown. The temperature was then lowered and the final GaAs layer grown with the desired growth and optical excitation parameters. Laser irradiation was present only during the growth of the final GaAs layer.

Extensive experiments were performed to characterize the reactor growth regimes[12] and growth rates with and without laser irradiation. Specifically, the growth rates at 450 °C were measured for arsine mass flow rates between 30 and 500 sccm (0.23–3.7 Torr) with the TMG mass flow rate fixed at 3 sccm (0.23 Torr). Half of the substrate was masked from the UV beam while the remainder was irradiated ($\Phi$<13 mJ/cm$^2$) at a repetition rate of 30 Hz. Measurements of the average power were taken immediately before and after each growth run to monitor power fluctuations for a given excimer laser gas mixture during any given run as well as changes between different runs. Growth rates were determined by measuring layer thicknesses of cleaved and stained cross sections with a high-resolution scanning electron microscope (SEM). The crystalline quality of these epitaxial layers was determined from transmission electron microscopy electron diffraction patterns.[13,14]

Figure 2 illustrates the sublinear dependence of the growth rate on arsine partial pressure that was measured
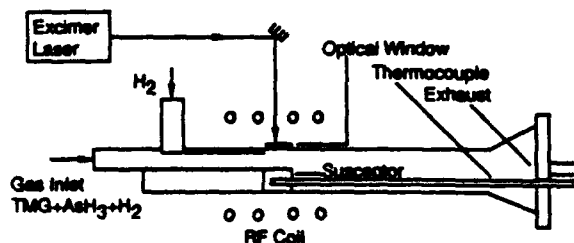


FIG. 1. Schematic diagram of the horizontal MOCVD reaction chamber with optical window purge configuration and perpendicular substrate irradiation geometry.
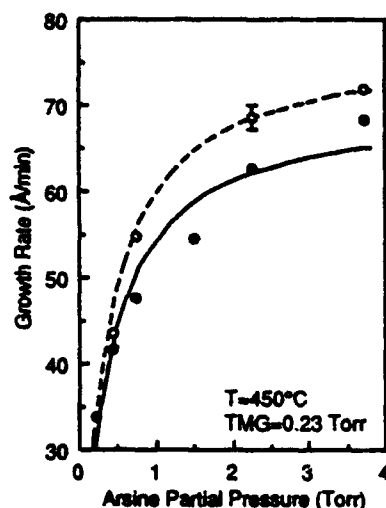
FIG. 2. Data illustrating the enhancement of the GaAs growth rate as a function of arsine partial pressure that is observed upon illuminating the substrate with ~10.7 mJ/cm² of 248 nm radiation with fixed TMG partial pressure (0.23 Torr) and temperature (450 °C). The solid circles represent the results obtained in the absence of UV irradiation and the solid curve indicates the best fit of the Langmuir–Hinshelwood model to these data, while the open circles and the dashed curve correspond to growth rates and the best fit for data measured in the presence of UV irradiation, respectively.

with a fixed TMG partial pressure for the substrates blocked from the laser beam. An absolute uncertainty of approximately 10% in the ordinate of the graph was introduced in the measurement by procedures such as sample staining and SEM micrograph measurement. At 450 °C, the growth rate $R$ is surface kinetically controlled and governed by the Langmuir–Hinshelwood model[15–17] which, indeed, predicts a sublinear growth rate dependence on both TMG and arsine partial pressure:

$$R = k\theta_G\theta_A = k\left(\frac{p_G\beta_G}{1+p_G\beta_G}\right)\left(\frac{p_A\beta_A}{1+p_A\beta_A}\right), \qquad (1)$$

where $k$ is a rate constant, $\beta$ is the adsorption rate constant divided by the desorption rate constant for TMG ($G$) or arsine ($A$), $p$ is the partial pressure, and $\theta$ is the molecular surface coverage. This sublinear dependence is caused by a saturation in surface coverage for large partial pressures of the source molecules. The best fit of Eq. (1) to this data, which is represented by the solid curve in the figure, yields $k\theta_G = 70$ Å/min and $\beta_A = 3.4$. The details of this model and the sensitivity of the fit to assumed values for the constants $k$, $p$, and $\beta$ will be discussed elsewhere.[12]

The dependence of the normalized growth rate on arsine partial pressure for substrates irradiated at a fluence of ~10.7 mJ/cm² ($\lambda = 248$ nm) and otherwise identical growth conditions is shown by the open circles in Fig. 2. The estimated relative error between illuminated and masked samples was 2.5% arising primarily from variations in the growth rate with position on the wafer and is represented by the error bar in Fig. 2. As was observed for the masked samples, the growth rate dependence is sublinear but the magnitude of the growth rate is reproducibly increased by approximately 5 to 15%, depending on arsine partial pressure. The as-measured growth rates and laser fluences are shown in

Table I, where it can be seen that the fluence was not constant over the course of an entire run and between runs. To account for this small linear variation in laser intensity and to obtain a realistic comparison between data points, the as-measured growth rate was normalized to an average fluence over the entire run as well as to an average initial fluence. These values are given in the last column of Table I. The Langmuir–Hinshelwood fit to the normalized data points obtained with UV irradiation is represented by the dashed curve in Fig. 2 for which $k\theta_G = 77$ Å/min and $\beta_A = 3.4$. Clearly, both masked and illuminated data are well described by the Langmuir–Hinshelwood model under the specified growth conditions.

Although the film growth enhancements obtained in these experiments were no greater than 15%, these data are representative of a larger set of data generated under different growth conditions, which consistently demonstrate enhancement with UV illumination of the substrate at 248 nm. However, experiments carried out at 351 nm with similar fluences, repetition rates, and otherwise identical growth conditions show no measurable change in growth rate. This wavelength-dependent growth rate is consistent with the absorption cross sections for TMG and arsine at each wavelength and demonstrates that the growth enhancement observed at 248 nm is photochemical in origin.

This result is also in agreement with estimates of the peak (instantaneous) and average temperature rise at the substrate surface which are induced by the incident laser beam. Integration of the time-dependent, one-dimensional heat flow equation[18]

$$T(t) = [2I_0(1 - R)/K\sqrt{\pi}]\sqrt{Dt}, \qquad (2)$$

where $I_0$ is the peak laser pulse intensity ($\sim 7 \times 10^5$ W/cm²), $D$ is the thermal diffusivity, $K$ is the thermal conductivity, and $R$ is the reflectivity of the substrate, yields a negligible average temperature rise.

Previous investigations[19–26] of the photochemistry of UV-irradiated column IIIA, IIB, or noble metal-alkyl adlayers have clearly demonstrated the enhanced efficiency of photodissociating alkyl molecules in the adlayer as opposed to the gas phase. As discussed in detail by Wood et al.[4] and Braichotte and van den Bergh,[23] the total number of alkyl molecules which are able to contribute to film growth is considerably higher in the adlayer than in the gas phase. This is a consequence of the large ratio of adlayer to gas phase number densities and the fact that only those gas phase molecules that are photodissociated near the substrate actually contribute to film growth. Not surprisingly, then, simple calcu-

TABLE I. As-measured GaAs growth rates for illuminated samples (248 nm) normalized to changes in fluence during and between growth runs.

| $p_A$ (Torr) | Growth rate (Å/min) | Initial fluence (mJ/cm²) | Final fluence (mJ/cm²) | Average fluence (mJ/cm²) | Normalized growth rate (Å/min) |
|---|---|---|---|---|---|
| 0.44 | 49.3 | 10.8 | 13.2 | 12.0 | 43.7 |
| 0.73 | 50.7 | 10.6 | 9.1 | 9.9 | 54.7 |
| 2.26 | 69.3 | 10.6 | 11.1 | 10.7 | 68.7 |
| 3.74 | 71.8 | 10.7 | 10.5 | 10.6 | 72.0 |

lations show that the 5–15% enhancement in the growth rate cannot be accounted for by photodissociation of TMG in the gas phase. Physisorbed TMG molecules, on the other hand, are prone to chemisorption once the scission of one or more Ga—CH$_3$ bonds by photodissociation occurs. Furthermore, Rytz-Froidevaux et al.[25] and Zhang and Stuke[26] have investigated in detail the visible and UV photochemistry of cadmium and aluminum alkyl adlayers, respectively, and, in the latter study, the fragments resulting from the photodissociation of both the gas phase and adsorbed species were compared at 193, 248, and 351 nm. These results,[26] in particular, demonstrate that the highly nonequilibrium distribution of products emanating from the adlayer is determined by photochemical considerations and photothermal effects can be ignored. We conclude therefore, that photolysis of adsorbed TMG at 248 nm is the dominant mechanism responsible for the photochemical growth enhancement reported here.

In summary, an enhancement in the growth rate of GaAs has been observed by irradiating the substrate in a MOCVD reactor at 248 nm in normal incidence. No measurable increase in growth rate is observed for similar experiments conducted at 351 nm. This strong wavelength dependence demonstrates that the enhancement mechanism at 248 nm is photochemical in nature and is attributed to the photolysis of TMG in the surface adlayer.

[1]Y. Aoyagi, M. Kanazawa, A. Doi, S. Iwai, and S. Namba, J. Appl. Phys. 60, 3131 (1986).

[2]S. M. Bedair, J. K. Whisnant, N. H. Karam, D. Griffis, N. A. El-Masry, and H. H. Stadelmaier, J. Cryst. Growth 77, 229 (1986).

[3]D. J. Ehrlich, R. M. Osgood, Jr., and T. F. Deutsch, J. Vac. Sci. Technol. 21, 23 (1982).

[4]T. H. Wood, J. C. White, and B. A. Thacker, Appl. Phys. Lett. 42, 408 (1983).

[5]G. S. Higashi and C. G. Fleming, Appl. Phys. Lett. 48, 1051 (1986).

[6]J. Nishizawa and T. Kurabayashi, Mater. Res. Symp. Proc. 101, 275 (1988).

[7]V. M. Donnelly, C. W. Tu, J. C. Beggy, V. R. McCrary, M. G. LaMont, T. D. Harris, F. A. Baiocchi, and R. Farrow, Appl. Phys. Lett. 52, 1065 (1988).

[8]S. S. Chu, T. L. Chu, C. L. Chang, and H. Firouzi, Appl. Phys. Lett. 52, 1243 (1988).

[9]H. Kukimoto, Y. Ban, H. Komatsu, M. Takechi, and M. Ishizaki, J. Cryst. Growth 77, 223 (1986).

[10]See, for example, C. M. Humphries, A. D. Walsh, and P. A. Warsop, Discuss. Faraday Soc. 35, 148 (1963); J. H. Clark and R. G. Anderson, Appl. Phys. Lett. 32, 46 (1978); B. Koplitz, Z. Xu, and C. Wittig, Appl. Phys. Lett. 52, 860 (1988); H. Okabe, Photochemistry of Small Molecules (Wiley, New York, 1978), p. 269.

[11]Y. Rytz-Froidevaux, R. P. Salathé, and H. H. Gilgen, Mater. Res. Soc. Symp. Proc. 17, 29 (1983).

[12]P. K. York, J. G. Eden, J. J. Coleman, G. E. Fernández, and K. J. Beernink (unpublished data).

[13]C. J. Kiely, P. K. York, J. G. Eden, J. J. Coleman, G. E. Fernández, and K. J. Beernink (unpublished data).

[14]S. J. Jeng, C. M. Wayman, G. Costrini, and J. J. Coleman, Mater. Lett. 2, 359 (1984).

[15]D. H. Reep and S. K. Ghandi, J. Electrochem. Soc. 130, 675 (1983).

[16]D. J. Schlyer and M. A. Ring, J. Electrochem. Soc. 114, 9 (1976).

[17]S. Thomson and G. Webb, Heterogeneous Catalysis (Wiley, New York, 1968), p. 87.

[18]P. Baeri and S. Campisano, in Laser Annealing of Semiconductors, edited by J. Poate and J. Mayer (Academic, New York, 1982), pp. 75–109.

[19]D. J. Ehrlich and R. M. Osgood Jr., Chem. Phys. Lett. 79, 381 (1981).

[20]C. J. Chen and R. M. Osgood, Jr., Mater. Res. Soc. Symp. Proc. 17, 169 (1983).

[21]J. Y. Tsao and D. J. Ehrlich, J. Chem. Phys. 81, 4620 (1984).

[22]G. S. Higashi and L. J. Rothberg, Appl. Phys. Lett. 47, 1288 (1985).

[23]D. Braichotte and H. van den Bergh, Appl. Phys. A 45, 337 (1988).

[24]C. D. Stinespring and A. Freeman, Appl. Phys. Lett. 52, 1959 (1988).

[25]Y. Rytz-Froidevaux, R. P. Salathé, H. H. Gilgen, and H. P. Weber, Appl. Phys. A 27, 133 (1982).

[26]Y. Zhang and M. Stuke, J. Cryst. Growth 93, 143 (1988).

# Laser photochemical deposition of germanium-silicon alloy thin films

Hubert H. Burke and Irving P. Herman
*Department of Applied Physics, Columbia University, New York, New York 10027*

Viken Tavitian and J. Gary Eden
*Everitt Laboratory, University of Illinois, Urbana, Illinois 61801*

Thin films of Ge-Si alloys were deposited by 193 nm photolysis of $GeH_4/Si_2H_6$ gas mixtures using an ArF laser. For substrate temperatures below 350 °C, deposition occurred only with the laser present, while for temperatures above 400 °C, film growth was little influenced by laser photolysis and resembled conventional chemical vapor deposition (CVD). The Si/Ge ratio in the films was about three times the $P_{Si_2H_6}/P_{GeH_4}$ ratio of reactant partial pressures for deposition in either the laser photolysis or the CVD regime. This result indicates that there is strong cross chemistry between silicon and germanium-bearing species in the gas phase. Film stoichiometry was measured by Auger analysis and Raman spectroscopy, with both methods leading to the same film composition.

The intriguing structural, electrical, and optical properties of germanium-silicon alloys can be tuned by varying the relative Ge/Si composition.[1] This fact, along with the compatibility of these compounds with existing silicon-based technology, has led to the growing number of applications of thin-film Ge-Si alloys in band-gap engineering of silicon-based microelectronic devices, solar cells, infrared detectors, and optical fiber communications.[1] Although several different techniques of depositing Ge-Si alloy films have been investigated, including pyrolytic chemical vapor deposition (CVD), and laser and plasma-assisted CVD,[2] no studies of laser photochemical vapor deposition (LPVD) of these compounds have been performed to date. The advantages of LPVD include high deposition rates at substrate temperatures lower than those characteristic of conventional CVD, decreased atomic diffusion due to low-temperature operation, and monolayer control. These latter two points are particularly important for multilayer fabrication. Investigations of excimer laser assisted LPVD of Ge-Si alloy thin films are reported here for the first time.[3,4]

Details concerning the experimental apparatus for the deposition experiments can be found elsewhere[5,6] and will only be briefly reviewed here. An ArF laser beam (193 nm, 40 Hz, 15 mJ/cm$^2$), filtered by a rectangular slit (0.5 × 2.0 cm$^2$), entered the quartz reactor through one wall and propagated parallel to and 2.2 mm above quartz and Si substrates. Both substrates were resistively heated ($T_s = 250$–500 °C) by an inconel heater containing a 1-mm-diam hole, which permitted the passage of a He-Ne laser beam through the quartz substrate, enabling *in situ* monitoring of the film growth by transmission. An infrared pyrometer measured the quartz surface temperature at the point where the He-Ne laser passed through the substrate.

During deposition, a disilane/germane gas mixture (diluted in a helium buffer-5% reactant gases/95% He) flowed over the substrate at a mass flow rate of 100 sccm, and a total reactor pressure of 10 Torr. The mole fraction of disilane in the gas, defined by $x_g = P_{Si_2H_6}/(P_{Si_2H_6} + P_{GeH_4})$, where $P_{Si_2H_6}$ and $P_{GeH_4}$ are the partial pressures of disilane and germane, respectively, is taken to be a measure of the relative concentration of reactive gases. Furthermore, the total reactant pressure was fixed: $P_{Si_2H_6} + P_{GeH_4} = 0.5$ Torr. This disilane fraction $x_g$ was varied in different experiments to grow films over the full compositional range $0 < x_f < 1$, where $x_f = [Si]/([Si] + [Ge])$ is the atomic fraction of Si in the film.

The thickness of Ge-Si films on quartz was determined by etching a trench down the center of film, and subsequently measuring the step height by profilometry. Film stoichiometry (silicon substrates) was measured by Auger electron spectroscopy (AES). Depth profiles were obtained by probing the 1147 eV Ge and 1619 eV Si peaks using 3 keV electrons directed to the center of the region that was sputtered by argon ions. Quantitative analysis was accomplished by comparing the amplitude (peak-to-peak height) of the Auger signal from the component in the alloy to the corresponding amplitude from a pure elemental standard analyzed under identical experimental conditions. Si-rich films and films grown on quartz were analyzed by x-ray photoelectron spectroscopy (XPS) using the Al $K_\alpha$ line.

Several AES studies of alloys have shown that backscattering of primary electrons and the escape depth of Auger electrons depend on alloy composition,[7] and that, during sputtering, the surface can be enriched by the alloy component with the lower relative sputtering yield.[8] Since these effects can influence the Auger determination of $x_f$, their importance in Ge-Si alloys was tested by determining the film composition of thick ~1-$\mu$m-thick CVD-grown films by both electron beam induced x-ray energy-dispersive analysis (EDAX) and AES. EDAX gave the same film composition as did the AES analysis, to within ± 0.02.

The stoichiometry of these thicker films was also determined by Raman scattering, using the shift of the Si-Si like peak near 500 cm$^{-1}$. Of the three peaks in the Ge-Si alloy Raman spectrum, the variation of the frequency of this peak with $x_f$ is the least sensitive to the method of preparation.[2,9,10] Measurements were performed with a microprobe system (described previously),[11] and using the 5145 Å line of an Ar$^+$ laser operated at low power ($\lesssim 2$ mW, 0.6 $\mu$m spot size) to minimize substrate heating. After initial laser probing of the sample, the laser power was increased to about 40 mW for approximately 5–10 min, and then the sample was

reexamined at low power to check for the effect of annealing.

For $T_s > 400$ °C, the ArF laser was found to have only a minor impact on film growth, which occurred primarily by conventional CVD. However, below 350 °C, no film growth was observed in the absence of UV laser radiation, indicating complete laser control of growth in this experimental regime of high flow velocity (20 cm/s) and low reactant gas partial pressure (0.5 Torr). Probe transmission, monitored during the growth of photolytic films, showed that incubation times immediately preceding film growth were negligible for $x_g \gtrsim 0.005$ ($<1$ min), but were significant for $x_g = 0$ (pure GeH$_4$, $\gtrsim 8$ min). Deposition rates ranged from 150 to 300 Å/min for both 250 and 350 °C substrate temperatures, and were insensitive to the disilane and germane mole fraction, with the disilane fraction $x_g > 0.1$ and with constant total reactant gas partial pressure.

Depth profiles of the photolytic films and several CVD films grown on silicon showed the composition to be independent of depth, and revealed the presence of an oxide layer at the film-substrate interface for the photolytic films despite *in situ* cleaning of the substrate with a 5% HCl/95% He gas

mixture for several minutes prior to initiating growth of the alloy.

The film composition ($x_f$) determined by Auger and XPS was in reasonable agreement with the Raman measurements. The Raman spectrum given in Fig. 1(a) depicts the three-peak spectrum for CVD films grown on c-Si at 500 °C with gas composition $x_g = 0.10$, and film composition $x_f = 0.45$, and indicates that the film is polycrystalline. Figure 1(b) shows the Raman profile of a film deposited under similar conditions except that $x_g = 0.90$ and $x_f = 0.91$. The broad peak shows that the as-deposited film is amorphous; the narrow peak is the result of Raman analysis after the film was converted to polycrystalline material by laser annealing. Under these conditions, the CVD films were shown to be amorphous for $x_f > 0.78$ and polycrystalline for $x_f < 0.45$ (and were not examined for intermediate $x_f$).

If the dissociation (and film incorporation) probability of Si$_2$H$_6$ were $\beta$ times that of GeH$_4$, then it can be shown that the silicon fraction in the film ($x_f$) and the disilane fraction in the reactant mixture ($x_g$) are related by the expression

$$x_f^{\text{model}}(\beta) = \frac{\beta x_g}{(\beta - 1)x_g + 1}. \qquad (1)$$

In Fig. 2, the measured silicon fraction in the film ($x_f$) is plotted versus the right-hand side of Eq. (1) for $\beta = 3$, showing very good agreement for the photolytically grown films and relatively good agreement for the CVD films, for which $\beta \sim 5 \pm 2$. This means that the [Si]/[Ge] ratio in the photolytically grown film is enriched by a factor of 3 relative to $P_{\text{Si}_2\text{H}_6}/P_{\text{GeH}_4}$ (the gas phase partial pressure ratio) and a factor of 1.5 relative to the atomic [Si]/[Ge] ratio in the reactant mixture.

At 193 nm, germane is weakly absorbing with an absorption cross section of approximately $3 \times 10^{-20}$ cm$^2$,[12] while Si$_2$H$_6$ is strongly absorbing with an absorption cross section $\sim$two orders of magnitude larger, $\sim 2 \times 10^{-18}$ cm$^2$.[13] If, after laser photolysis of the reactants, there were no "cross chemistry" between Ge and Si-containing species, then $\beta$ would expected to be roughly 70 or 140 based on the
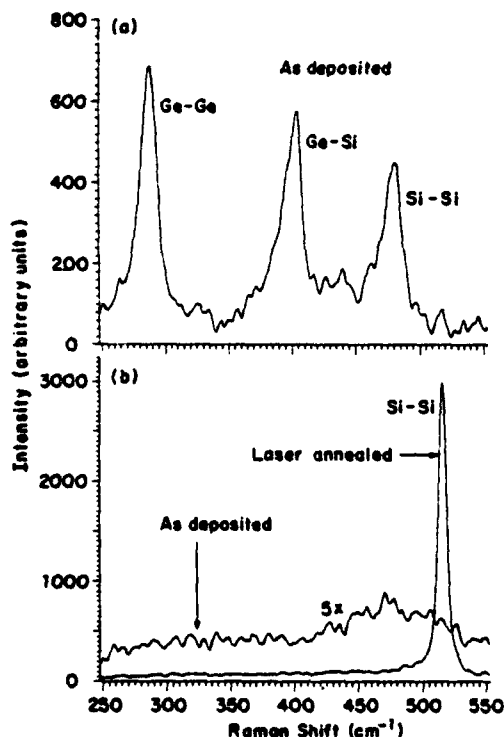


FIG. 1. Raman microprobe analysis of Ge-Si alloy thin films grown by CVD on c-Si with $T_s = 500$ °C and 1 mW of 5145 Å Ar$^+$ laser power. The Si fraction in the film ($x_f$) is determined by the frequency shift of the Si-Si peak. (a) Spectrum acquired for a disilane fraction in the gas mixture of $x_g = 0.10$ during deposition. Auger and EDAX measurements give $x_f = 0.45$ and 0.46, respectively, while Raman analysis gives 0.34 (using Ref. 9 for calibration) or 0.42 (using Ref. 10), depending upon the calibration curve, and shows that the as-deposited film is polycrystalline. (b) Analogous spectrum acquired for $x_g = 0.90$, with $x_f$ determined to be 0.91 by XPS. The as-deposited film is amorphous, while the laser-annealed film (40 mW, 5 min) is polycrystalline, giving $x_f = 0.92$. For $x_g = 0.50$, $x_f$ was measured to be 0.78 from AES, 0.80 from EDAX, and 0.76 from the Raman spectrum of the laser-annealed film (spectrum not shown). Each of the Si-Si Raman shift vs silicon fraction calibrations in Refs. 2, 9, and 10 gave the same $x_f$ for the $x_g = 0.90$ experiment. This was also true for the $x_g = 0.50$ run.
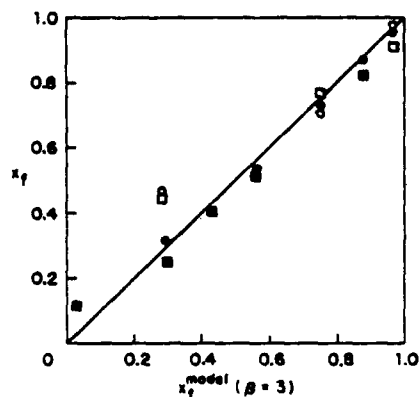


FIG. 2. Measured Si fraction of the film ($x_f$) as a function of $x_f^{\text{model}}$ ($\beta = 3$) for various $x_g$ under different experimental conditions. The solid symbols depict films grown by 193 nm photolysis at lower substrate temperatures where the laser is necessary for deposition: (circles) $T_s = 250$ °C; (squares) $T_s = 350$ °C. The open symbols depict films grown by conventional CVD at higher temperatures: (circles) $T_s = 400$ °C; (squares) $T_s = 500$ °C.

relative absorption cross sections, depending on whether only one or both of the disilane Si atoms contribute to film growth. Since the value of $\beta$ for LPVD is considerably smaller, collisions between $GeH_4$ and Si-bearing radicals or H atoms from disilane photolysis, which form Ge-bearing radicals, undoubtedly play a pivotal role in deposition. Similar cross chemistry between Ge and Si-containing species is also likely in conventional CVD since $\beta \sim 3$ also describes the CVD-grown films fairly well. One further argument in support of the impact of cross chemistry in forming the laser-deposited films stems from the measured rate of deposition of Ge atoms, which exceeds the calculated rate at which germane molecules are photolyzed when disilane is present in the reactant mixture (specifically, for $x_g > 0.01$). For example, the Ge atom deposition rate is $8.5 \times 10^{14}/cm^2$ s during photolytic growth of Ge-Si alloy films when the disilane fraction $x_g = 0.1$ and $T_s = 350\,°C$, while the rate of photolyzing $GeH_4$ molecules is only $\sim 1.4 \times 10^{14}/cm^2$ s.

It appears, therefore, that deposition of the alloy is initiated by laser photodissociation of disilane, and photolysis of $GeH_4$ is negligible except when $x_g < 0.01$. Recent studies suggest that in the laser fluence range of these experiments, $Si_2H_6$ absorbs only one 193 nm photon,[14] and that the primary dissociation quantum yield is $\sim 0.7$.[15] At least 20 exit channels are energetically accessible in the photolysis of disilane at 193 nm.[15,16] Many of these channels may well be important, producing H, $H_2$, $SiH_2$, $SiH_3$, and other Si-bearing species.[15] Once formed, the silylene radical ($SiH_2$), for example, reacts with $GeH_4$ via the process $SiH_2 + GeH_4 + M \rightarrow GeSiH_6 + M$ (where $M$ is any third body) which is analogous to the insertion reaction $SiH_2 + SiH_4 + M \rightarrow Si_2H_6 + M$ that is known to be critical to the pyrolysis of silane.[17] In addition, H atoms produced from the photodissociation of $Si_2H_6$ will form $GeH_3$ and $H_2$ by hydrogen abstraction from $GeH_4$. Since a given species formed by the laser within the photolysis zone suffers roughly 5000 collisions with background reactant molecules before reaching the surface, the nascent products of disilane photolysis are collisionally transformed by reactive collisions into the final deposition precursors, perhaps $Ge_n Si_m H_{2(n+m)}$, while en route to the surface.

In summary, low-temperature growth of Ge-Si alloy films has been demonstrated by laser LPVD. Cross reactions between Ge and Si species have been found to be important during film deposition and Raman spectroscopy has been shown to be a useful diagnostic of Ge-Si alloy film composition.

[1]For example, see J. C. Bean, Science 230, 127 (1985); G. Abstreiter, H. Brugger, T. Wolf, H. Jorke, and H. J. Herzog, Phys. Rev. Lett. 54, 2441 (1985).

[2]I. P. Herman and F. Magnotta, J. Appl. Phys. 61, 5118 (1987), and references cited therein.

[3]These results were first discussed by H. H. Burke, I. P. Herman, S. A. Piette, V. Tavitian, and J. G. Eden at the Conference on Lasers and Electro-Optics (CLEO'88), April 25-29, 1988, Anaheim, CA, paper WR2, Technical Digest p. 264.

[4]After the completion of this work, the authors became aware of an experimental study entailing the photochemical vapor deposition of $Ge_{1-x}Si_x$ alloys, in which the optical source was a Hg lamp: A. Yamada, Y. Jia, M. Konagai, and K. Takahashi, Jpn. J. Appl. Phys. 27, L2164 (1988).

[5]V. Tavitian, C. J. Kiely, D. B. Geohegan, and J. G. Eden, Appl. Phys. Lett. 52, 1710 (1988).

[6]C. J. Kiely, V. Tavitian, and J. G. Eden, J. Appl. Phys. 65, 3883 (1989).

[7]L. C. Feldman and J. W. Mayer, Fundamentals of Surface and Thin Film Analysis, 1st ed. (North-Holland, New York, 1986).

[8]H. J. Mathieu and D. Landolt, Surf. Sci. 53, 228 (1975).

[9]T. Ishidate, S. Katagiri, K. Inoue, M. Shibuya, K. Tsuji, and S. Minomura, J. Phys. Soc. Jpn. 53, 2584 (1984).

[10]M. A. Renucci, J. B. Renucci, and M. Cardona, in Proceedings of the Conference on Light Scattering in Solids, edited by M. Balkanski (Flammarion, Paris, 1971), p. 326.

[11]G. D. Pazionis, H. Tang, and I. P. Herman, IEEE J. Quantum Electron. 25, 976 (1989).

[12]M. J. Mitchell, X. Wang, C. T. Chin, M. Suto, and L. C. Lee, J. Phys. B 20, 5451 (1987).

[13]U. Itoh, Y. Toyoshima, H. Onuki, N. Washida, and T. Ibuki, J. Chem. Phys. 85, 4867 (1986).

[14]E. Boch, C. Fuchs, E. Fogarassy, and P. Siffert, Mater. Res. Soc. Symp. Proc. 129 (in press).

[15]J. O. Chu, M. H. Begemann, J. S. McKillop, and J. M. Jasinski, Chem. Phys. Lett. 155, 576 (1989); J. M. Jasinski, J. O. Chu, and M. H. Begemann, Mater. Res. Soc. Symp. Proc. 131, 487 (1989).

[16]H. Stafast, Appl. Phys. A 45, 93 (1988).

[17]For example, see B. A. Scott, W. L. Olbricht, B. A. Meyerson, J. A. Reimer, and D. J. Wolford, J. Vac. Sci. Technol. A 2, 450 (1984).

## Microstructural studies of epitaxial Ge films grown on [100] GaAs by laser photochemical vapor deposition

C. J. Kiely,   V. Tavitian, and J. G. Eden
*University of Illinois. Urbana. Illinois 61801*

# Microstructural studies of epitaxial Ge films grown on [100] GaAs by laser photochemical vapor deposition

C. J. Kiely,[a] V. Tavitian, and J. G. Eden
*University of Illinois, Urbana, Illinois 61801*

Ge films grown on [100] GaAs by laser photochemical vapor deposition (LPVD) in parallel geometry at temperatures ($T_s$) ranging from ~240 to 415 °C have been examined by transmission electron microscopy. For $285 < T_s \lesssim 330$ °C, a thin (250–700 Å) epitaxial film is grown initially but a switch to amorphous material is subsequently observed. At higher substrate temperatures ($T_s \gtrsim 400$ °C), thicker ($\gtrsim 800$ Å) epitaxial Ge films are grown before the transition to polycrystalline material takes place. In the absence of external 193-nm laser radiation (i.e., growing by conventional low-pressure chemical vapor deposition), the Ge films are completely amorphous ($285 < T_s < 330$ °C) or heavily defected polycrystalline ($T_s \sim 400$ °C). The $> 100$ °C temperature reduction for the growth of epi Ge films made possible by LPVD is attributed to the direct production of a species ($GeH_3$) by the laser which is collisionally converted to $Ge_2H_6$ *en route* to the substrate. Upon reaching the [100] GaAs surface, the digermane is pyrolyzed. Experiments with [100] substrates tilted 3° toward [110] yielded thinner (~120 Å), but smooth, epitaxial films which is attributed to the higher density of available nucleation sites. Films grown at 280–330 °C on [111] oriented GaAs were completely amorphous which appears to arise from reduced adatom mobilities on [111] surfaces. These results clearly demonstrate the feasibility of photochemically generating a species which migrates to the surface and alters the chemistry at a substrate (which is itself not illuminated by the optical source) so as to permit the growth of epitaxial semiconductor films.

## I. INTRODUCTION

The field of laser photochemical vapor deposition (LPVD) was born in the late 1970s amid considerable optimism regarding its potential for growing films at temperatures lower than those accessible to conventional growth techniques. Since that time, most of the effort in this area has focused on the deposition of metals by photodissociating a precursor polyatomic molecule.[1] Much less is known of the feasibility of growing device quality, epitaxial semiconductor films.[2]

Early work with the optically assisted growth of elemental semiconductors involved polycrystalline Ge (and to a lesser extent, Si) films that were grown on [100] NaCl, SiO₂, and [1102] sapphire[3,4] at substrate temperatures ($T_s$) as low as ~25 °C (room temperature) by photodissociating GeH₄ (or SiH₄) with an excimer (ArF or KrF) laser. Although mercury photosensitization has been known (for two decades)[5] to be capable of depositing amorphous Si films,[6,7] Nishida *et al.*[8,9] have recently grown polycrystalline Si:H layers and epitaxial Si films at 200 °C by irradiating mixtures of $Si_2H_6$, $SiH_2F_2$, $H_2$, and Hg vapor with a low-pressure Hg lamp ($\lambda = 185$ 254 nm; fluence $\Phi \sim 30$ mW cm⁻²). Resorting to the higher silanes allows one to avoid the sensitizer entirely and several groups[10–15] have reported the deposition of *a*-Si films at temperatures below 300 °C by directly photodissociating $Si_2H_6$ or $Si_3H_8$ with a lamp [Hg (Refs. 10–12) or D₂ (Ref. 13)] or a vacuum ul-

traviolet (VUV) laser [ArF (Refs. 14 and 15) or F₂ (Ref. 15)]. At much higher temperatures ($730 \lesssim T_s \lesssim 925$ °C), Ishitani and co-workers[16–18] have reported volatilization of impurities and enhanced film growth rates when illuminating Si substrates with 1–3 W cm⁻² (average power) of ultraviolet (UV) radiation (from a Hg/Xe lamp or KrF or ArF excimer lasers) during the pyrolysis of $SiH_2Cl_2/H_2$ mixtures.

Among the compound semiconductors, crystalline InP and polycrystalline GaAs have been grown by photodissociating mixtures of columns III and V alkyls with excimer laser radiation.[19–22] In the past several months, the results of coupling an excimer laser to MOCVD (metalorganic chemical vapor deposition),[23] MBE (molecular beam epitaxy),[24] or CBE (chemical beam epitaxy)[25] reactors have also been reported. Upon irradiating the substrate with 193-nm (ArF laser) energy fluences of ~40–300 mJ cm⁻², epitaxial GaAs or AlGaAs films were obtained. For such high peak powers (5–20 MW in ~15 ns pulses), however, film crystallinity and enhancements in the growth rate are primarily attributable[25] to substrate heating (i.e., pyrolysis) rather than a photochemical effect.

Irvine and co-workers[26–29] were the first to grow high-quality II-VI epitaxial films (HgTe, HgCdTe) by Hg photosensitization. Similar results have been obtained recently by Ahlgren and co-workers.[30] Morris[31] and, more recently, Zinck *et al.*[32] demonstrated the epitaxial growth of HgCdTe on CdTe and CdTe on GaAs, respectively, by photodissociating the associated column II and VI alkyls with an ArF or KrF (248 nm) laser.

Ultraviolet and visible laser (or lamp) radiation has also

[a] Visiting Postdoctoral Associate: 1986–88.

been shown to be effective in improving the quality of III-V and II-VI films grown by conventional techniques. Nishizawa and co-workers[33] reported photochemically induced changes in film growth rates for GaAs grown by vapor phase epitaxy (chloride transport) for $480 < T_s < 700$ °C. Similar results (improved growth rates and film morphology) were obtained by Pütz et al.[34] for GaAs films and Fujita and co-workers[35] for ZnSe films grown by MOCVD while irradiating the substrate with a low pressure Hg or Xe lamp. Significant experimental activity[36–42] has also been devoted to modifying the structural and electrical characteristics of MBE or MOCVD grown films with $Ar^+$ ion (visible) laser illumination of the substrate.

Virtually all of these previous experiments involved illuminating the surface with UV (or visible) radiation and, in most cases, transient (or cw) heating of the substrate and growing film played a significant or dominant role in the formation of crystalline material. Aside from the early studies of Collins and co-workers,[43–45] and Deutsch et al.,[46] in depositing compound insulators ($Al_2O_3$, $SiO_2$, $Si_3N_4$), few LPVD experiments have been carried out in *parallel* geometry (i.e., substrate is not irradiated). Notable exceptions are the recent II-VI experiments (mentioned earlier) of Morris[31] and Zinck and co-workers[32] and the Si:H work of Taguchi et al.,[47] the latter of which yielded amorphous material.

In summary, despite successful demonstrations of the growth of both elemental and compound semiconductor films by optically assisted processes, few experiments have appeared in the literature reporting the LPVD growth of epitaxial materials. Those instances in which crystalline films were reported have generally involved laser (or lamp) heating of the substrate or a sensitizer to couple the optical source to the gaseous precursor molecule. Also, as Houle[2] has stressed in a 1986 review paper, systematic studies correlating reactor conditions and laser parameters with film quality (microstructural characteristics) have been few.

Recently, we reported[48–50] the LPVD growth of thin epitaxial Ge films on [100] GaAs for substrate temperatures as low as 285 °C. By photodissociating $GeH_4$ at 193 nm in *parallel* geometry, single-crystal Ge films 250–800 Å thick were grown at rates of typically 0.6–5 nm/min ($\sim 1$ Å s$^{-1}$ max). One attractive aspect of these experiments is that transient heating of the substrate and adlayer photolysis are not involved in the growth process, thus making it possible to isolate the gas phase photochemical processes. Normally, resolving the contributions of bulk and adlayer heating, adsorbate photochemistry and gas phase processes is problematic. However, separating adlayer chemistry and other surface reactions from laser-induced gas phase reactions is important for determining those conditions ($T_s$, pressure, flow) under which epitaxial material can be grown by LPVD or of the potential impact of gas phase photochemical processing on conventional growth technologies. Although this approach does not involve a gaseous sensitizer and the experiments are carried out in parallel geometry, epitaxial material is consistently obtained for $T_s$ in the range 285–410 °C and for low laser fluences ($\lesssim 15$ mJ cm$^{-2}$). The most significant aspect of these results is that, in the absence of external laser radiation, this reactor produces *only* amorphous or polycrystalline films. Therefore, it is apparent that the laser directly produces a species which migrates $> 10$–60 mean free paths (MFPs) to reach the surface or is collisionally transformed *en route* into a more stable species. Upon arriving at the substrate (which is itself not illuminated), this species dramatically alters the surface kinetics so as to make the growth of *epitaxial* films possible. Specifically, it is concluded that the key role played by the laser is to produce $GeH_3$ radicals which subsequently form $Ge_2H_6$ by three body collisions.

This paper describes in detail the microstructural characteristics of these Ge films as examined by transmission electron microscopy (TEM) and energy dispersive x-ray (EDX) analysis. The next section discusses the experimental apparatus and data-acquisition procedure. Section III presents the experimental results and the key conclusions of this study are summarized in Sec. IV.

## II. EXPERIMENTAL APPARATUS, DATA ACQUISITION, AND ANALYSIS

### A. Apparatus: Reactor design and film thickness measurements

A partial schematic diagram of the experimental arrangement is given in Fig. 1. The reactor is constructed of commercial quartz tubing having a square cross section ($2.5 \times 2.5$ cm$^2$) and a length of $\sim 30$ cm. Each end of the reactor is gradually tapered down to a final diameter of 8 mm. Gas flow and pressure are both monitored and controlled upstream and downstream of the reactor by mass flow controllers, transducers, and a capacitance manometer. The entire gas handling and flow system (except the reactor itself) is constructed from welded stainless-steel tubing and VCR fittings.[51]

The unfocused beam from an ArF excimer laser (193 nm) was spatially filtered by a $0.5 \times 2.0$ cm$^2$ rectangular slit, entered the reactor (transverse to gas flow) through one quartz wall and, as illustrated in Fig. 1, passed $\sim 2.2$ mm above and parallel to the substrate. For the gas pressures of these experiments, 2.2 mm is the equivalent of 10–60 mean free paths (MFPs) for a collision with a background $GeH_4$ molecule. Statements made throughout the paper relative to the height of the laser beam above the substrate are referenced to the bottom of the beam since care was taken to ensure that the ArF radiation did not illuminate the substrate. Also, the transmittance of each wall of the reactor was measured to be 62% $\pm$ 3% at 193 nm.

Although focusing of the UV laser beam was not necessary, the 193 nm intensity in the reactor could readily be varied from $\sim 0.1$ to 1.3 MW cm$^{-2}$ by diluting the gas mixture in the laser with He or by inserting quartz flats into the beam path. Unless stated otherwise, all of the films in these experiments were grown at an initial (i.e., at the beginning of the growth run) laser fluence of 15 mJ cm$^{-2}$ [$\sim 25$ ns pulse width (full width at half maximum—FWHM)] at a pulse repetition frequency of typically 40 Hz. It must be emphasized that this fluence is considerably smaller (by more than an order of magnitude) than those typical of parallel geometry LPVD growth experiments to date.[43–45,52]
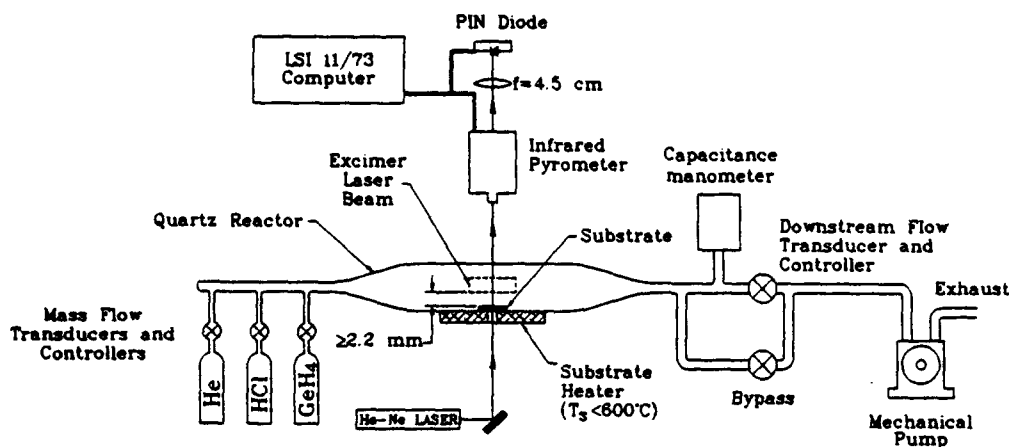
FIG. 1. Partial schematic diagram of the experimental apparatus (not drawn to scale). Although only the quartz substrate is shown, quartz and GaAs substrates were placed in the reactor for each growth run. The in situ measurement of the film thickness for the quartz substrate was generally (as shown) a He–Ne laser transmission measurement while, for higher film growth rates, the interference produced by $\lambda \sim 5\ \mu$m radiation propagating through the growing Ge film was recorded by the pyrometer. The outline of the excimer beam, propagating parallel to the substrate and coming out of the page, and its position above the substrate are also shown.

After exiting the reactor, the UV beam was deflected by a prism onto a pyroelectric detector (Gen-Tec) or absorbing calorimeter (Scientech) for measurements of the beam's pulse energy or average power. For a given growth run, two substrates—one $\sim 0.5 \times 0.5$ cm$^2$ SiO$_2$ (quartz) and the other $0.5 \times \sim 2.0$ cm$^2$ Cr or Si-doped [100] GaAs—were placed in the reactor and could be resistively heated (by an inconel heater held in a Macor glass ceramic block) to temperatures as high as 870 K. Both substrates were situated at the bottom of the reactor with the GaAs substrate placed further from the laser entrance wall so as to minimize the possibility of particles produced by laser ablation of the wall (expected to be minimal) from reaching the semiconductor surface. A $\sim 1$-mm-diam hole drilled in the heater allowed for a He-Ne laser beam to pass through the quartz substrate (and subsequently detected by a p-i-n photodiode), thus allowing in situ measurements of film growth rates to be carried out in transmission. An infrared (IR) pyrometer (IRCON) monitored the substrate temperature by viewing either the quartz or GaAs surfaces through a sapphire window sealed to the top of the reactor. When viewing the SiO$_2$ substrate surface, the IR pyrometer was optically aligned by the He-Ne laser beam in order to ensure that the pyrometer monitored the same region of the substrate that was sampled by the red laser probe. The thickness of the Ge film on the SiO$_2$ substrate was also measured in real time in a second way; namely, by recording the interference fringes produced by blackbody radiation from the GaAs substrate propagating through the growing Ge film. A pyrometer output trace that is typical of those observed throughout these experiments is given in Fig. 2 for the CVD growth of Ge at $T_s = 410$ °C. All data—He-Ne transmission, substrate temperatures, gas flow rate and pressure, and ArF laser intensity—were stored by a DEC LSI 11/73 computer. It should also be mentioned that the in situ film thickness measurements were subsequently verified by TEM observations.

Over the pressure range investigated in these experiments (5% GeH$_4$ in He; $p_{TOTAL} \equiv p_{GeH_4} + p_{He} \approx 5$ to 30 Torr), the Ge film growth rate ($R_0$) was found to vary linearly with pressure. At $T_s \approx 300$ °C, for example, $R_0$ is observed to increase from $\sim 0.6$ nm min$^{-1}$ for $p_{TOTAL} = 5.6$ Torr to almost 5 nm/min$^{-1}$ at 30 Torr.
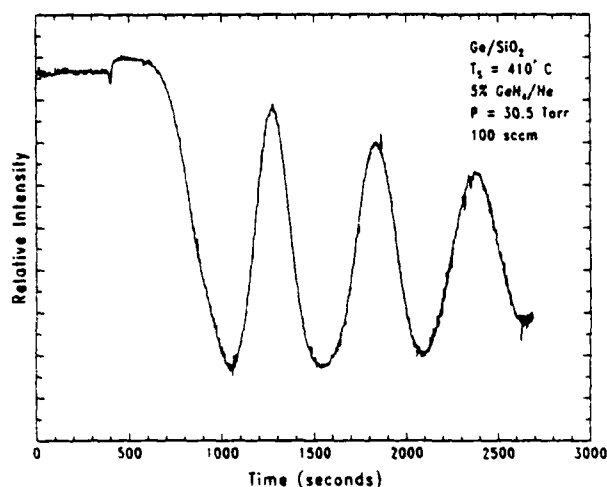


FIG. 2. Interference signal recorded by the IR pyrometer from a Ge film grown by conventional pyrolysis at $T_s = 410$ °C. Each cycle in the pattern corresponds to the growth of an additional 0.625 $\mu$m in film thickness. In acquiring these data, the IRCON pyrometer monitored blackbody radiation from the film/SiO$_2$ substrate in the $\lambda \sim 5\ \mu$m wavelength region. Similar traces were observed for the epitaxial Ge films grown by LPVD at lower temperatures ($T_s > 285$ °C) but because of the much smaller film growth rates, the He–Ne transmission technique was more frequently used.
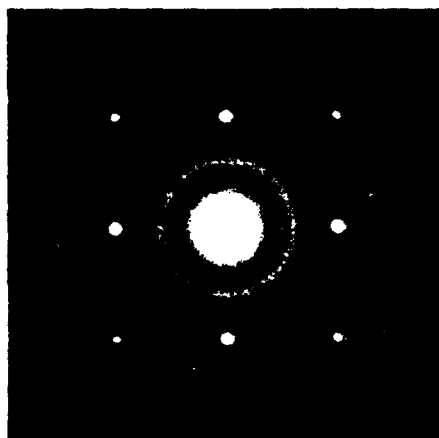
FIG. 3. Selected area electron diffraction pattern (SADP) of an LPVD Ge film grown on [100] GaAs at 305 °C and a GeH₄ partial pressure of 1.5 Torr ($P_{TOTAL} \approx 30$ Torr). The pattern is characteristic of Ge [100] single crystal. (Note the absence of $g = \{200\}$ reflections.) The diffuse rings arise from the presence of an amorphous Ge overlayer.

throughout the growth period which typically lasted 40–50 min. Film growth rates varied from ∼6 to 50 Å/min, depending upon $T_s$ and (as mentioned earlier) gas pressure. The gas pressure limits (5.6 and 30.4 Torr) correspond, respectively, to flow velocities of 40 and ∼6 cm s⁻¹.

## C. Sample preparation

Plan view samples of the LPVD grown Ge/GaAs interfaces were prepared for TEM studies by the method previously described by Rackham.[54] This involved chemically backthinning the sample (from the substrate side) with a 0.5-mm-diam jet of chlorine in methanol until perforation occurred. Large areas of electron transparent material could then be found around the periphery of the hole. Cross-sectional samples were prepared by the procedure outlined by Bravman and Sinclair.[55] The LPVD wafers were cut into strips which were then glued together (with epoxy resin) into blocks of four in such a way that the Ge face was arranged to lie closest to the center of the block. Subsequently, the blocks were cut perpendicular to the interfaces with a diamond saw and the resulting strips were mechanically polished down to a thickness of ∼40 μm. After being mounted onto Ni slot grids, the strips were ion milled to perforation by a 6 keV Ar⁺ ion beam at a 16° angle of incidence. All samples were examined in a Phillips EM 430 transmission electron microscope operating between 150 and 300 kV.

## B. Substrate cleaning procedure, gas flow cycle

Immediately prior to being placed in the reactor, the GaAs substrates were chemically cleaned by the procedure described by Anderson, Christou, and Davey.[53] The quartz substrates were rinsed in spectrophotometric grade acetone and methanol and blown dry with $N_2$ prior to being introduced into the reactor. In order to obtain epitaxial films, it was found to be necessary to dry etch the substrates at the growth temperature ($240 \lesssim T_s \lesssim 415$ °C) by flowing a 5% HCl/He mixture (total pressure = 3.5 Torr, ∼50 sccm flow rate) for 5 min. Subsequently, a 5% GeH₄ in He mixture at a total pressure of 5.6–30.4 Torr and 100 sccm mass flow rate purged the reactor for ∼270 s. The UV laser was then turned on and pulsed at 40 Hz (peak intensity ∼0.75 MW cm⁻²)

## III. RESULTS AND DISCUSSION

More than 20 LPVD Ge/[100] GaAs samples, grown at temperatures ranging from room temperature to ∼415 °C, have been examined to date by TEM. Moreover, several films have been grown by conventional low-pressure chemical vapor deposition (LPCVD) or by LPVD but on GaAs substrates of orientations other than [100]. Several specific growth regimes have been identified and this section presents and discusses the results of TEM (and EDX) observations from samples in each category. Although micro-
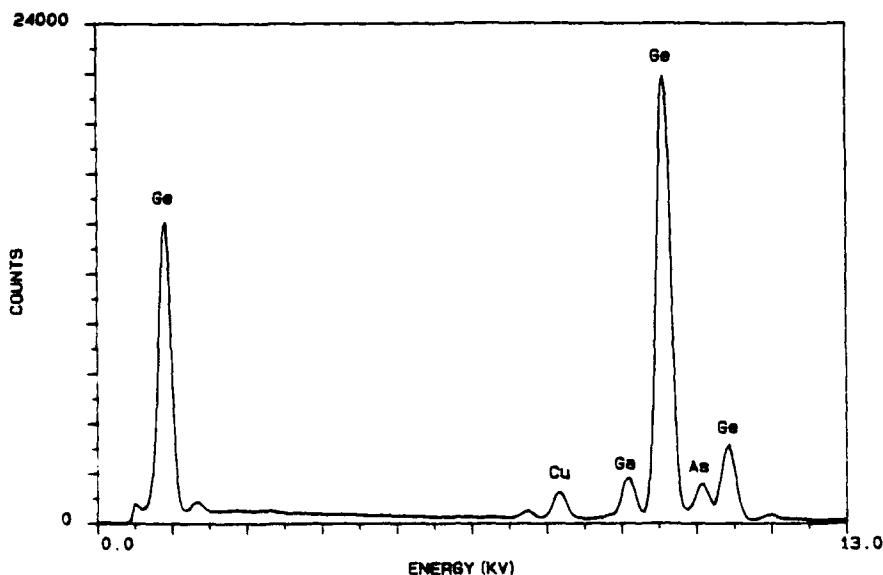


FIG. 4. Energy dispersive x-ray (EDX) spectra of the Ge film (grown at $T_s$ = 305 °C) of Fig. 3.
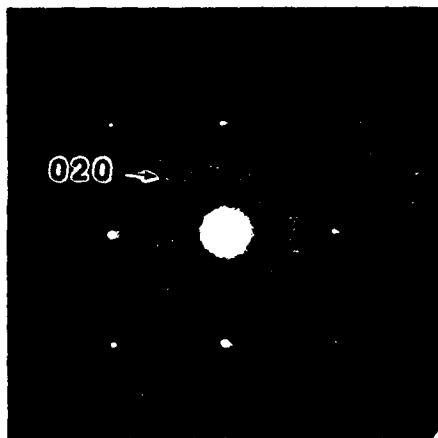
FIG. 5. [100] SADP of the Ge/GaAs bicrystal for the sample of Fig. 3. Note that the **g** = {200} reflections characteristic of GaAs are now present.

graphs and diffraction patterns for a single film in a particular category will generally be shown, the comments and data summarize observations made over a number of samples.

## A. LPVD Ge films (285 < $T_s$ < 330 °C)

### 1. Microstructure of films

Figure 3 shows a selected area diffraction pattern (SADP), acquired along the substrate normal direction, of a Ge overlayer that is representative of those observed for all the LPVD films grown in the 285–330 °C temperature range. The film of Fig. 3 was grown at 305 °C ($p_{GeH_4/He}$ = 30.2 Torr) and the SADP pattern is that for Ge [100] single crystal. Since germanium has the diamond structure (*FD* 3*m* space group), the structure factor for **g** = {200} is zero and

hence the reflection is kinematically forbidden. Consequently, {200} reflections are absent from the pattern. Several diffuse rings centered around the undiffracted beam indicate the existence of an amorphous layer in addition to the crystalline film. As illustrated in Fig. 4, EDX analysis of the Ge overlayer region reveals characteristic Ge peaks with only a weak Ga and As background and, therefore, one suspects that the diffuse ring in the SADP in Fig. 3 also arises from Ge and not an impurity.

An SADP of the Ge/GaAs bicrystal, presented in Fig. 5, is a superposition of a Ge [100] diffraction pattern (identical to that of Fig. 3), a GaAs [100] pattern (with **g** = {200} reflections now present) and the weak diffuse scattered rings from the amorphous Ge layer. The patterns of Figs. 3 and 5 demonstrate clearly that crystalline [100] Ge has been grown on GaAs.

Cross-sectional TEM images of the Ge/GaAs interfaces verify the assumption that the Ge film is initially crystalline but subsequently switches to amorphous material. Figure 6 is a cross-sectional micrograph of a ~600-Å-thick amorphous layer atop a crystalline film whose thickness varies from ~250 to 350 Å. It is also obvious that the GaAs substrate surface is somewhat wavy ( ~20-Å undulations) but there is no evidence for a gallium oxide layer at the interface. Therefore, although the *in situ* HCl dry etch is apparently effective in removing oxides from the substrate, it by no means leaves the surface atomically smooth. Several inclined growth defects in the Ge layer, which appear to propagate from the Ge/GaAs interface, are also evident in Fig. 6.

Convergent beam electron diffraction patterns of the crystalline Ge layer and the GaAs substrate (near the interface) are shown in Figs. 7 and 8, respectively. Both diffraction patterns were acquired by viewing the crystalline regions along the [011] GaAs direction with a 150-Å-diam electron beam probe. As expected, the **g** = {200} disks are



FIG. 6. Cross-sectional micrograph of the Ge/GaAs interface (from the same growth run as the sample of Figs. 3–5) showing the 250–350-Å-thick crystalline film and a 600-Å amorphous layer. The rough topography of the crystalline film is partially attributed to a switch from crystalline to amorphous material following the coalescence of epitaxial Ge islands. A few inclined growth defects (denoted *d*) are apparent in the Ge film as is an occasional void (denoted *v*) but the interface is essentially free of gallium oxide.
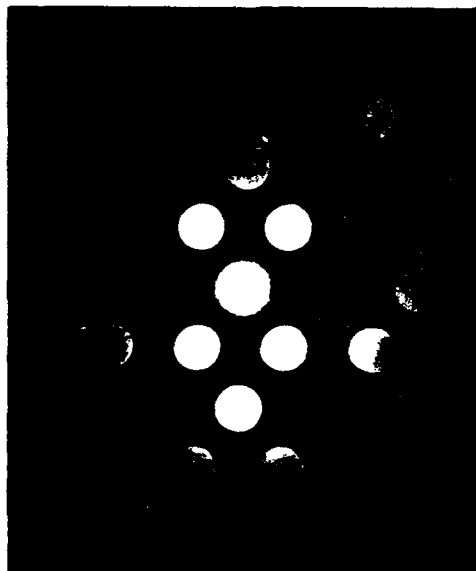
FIG. 7. [011] Convergent beam electron diffraction pattern of a Ge film grown by LPVD at 305 °C. Acquired with a 150-Å-diam electron beam by viewing the crystalline layer along the [011] GaAs direction, this diffraction pattern is virtually identical with those for other photochemically grown films in the 285–330 °C range. Note the absence of $g = \{200\}$ disks.

absent for Ge (cf. Fig. 7) and the fact that no symmetry information is visible within the disks is a consequence of the sample being only a few hundred Å thick. These patterns (as well as those taken on plan view specimens) demonstrate that the thin Ge films are not only crystalline but have the following epitaxial relationship with the substrate:

Ge[100]//GaAs[100]; Ge[010]//GaAs[010].

Further evidence for the epitaxial nature of the LPVD films
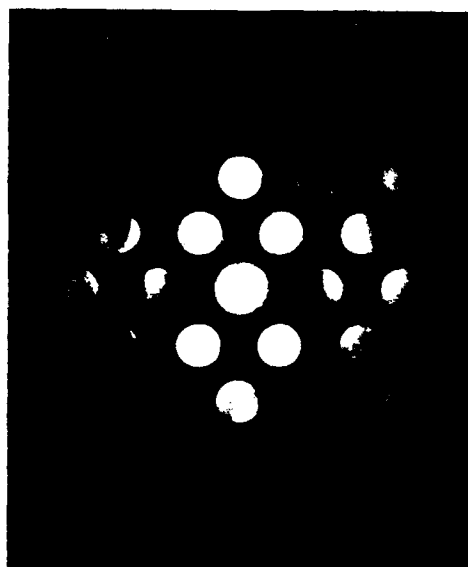
is afforded by lattice images of the crystalline Ge/GaAs interface. Also taken along [011] GaAs at 300 kV, the image of Fig. 9, for example, displays two sets of $\{111\}$ lattice fringes (with a characteristic spacing of 3.26 Å) which are inclined at 54.7° with respect to the interfacial plane. These fringes run *continuously* across the interface from the GaAs substrate into the Ge layer, thus illustrating the epitaxy between the two crystalline materials.

All of the Ge films grown on [100] GaAs and examined to date by cross-sectional TEM exhibit the rough morphology evident in Fig. 6 which suggests that the Ge initially nucleates on the substrate as epitaxial islands which grow in size and eventually coalesce to form a film. Soon after coalescence, however, the material switches from crystalline to amorphous. As a result, the thickness of the epitaxial films has thus far been limited to ~250–800 Å. Consequently, the LPVD growth of Ge films in this temperature range is characteristic of the Volmer–Weber process rather than the Frank–van de Merwe or Stranski–Krastanov mechanisms.[56] Not only does the cluster (island) nucleation process account for the observed rough morphology of the films (owing to the differing growth histories of the individual islands) but may also explain the small amorphous zones that are occasionally seen between Ge islands at the Ge/GaAs interface (one such zone or void, denoted $v$, is indicated in Fig. 6). A high magnification plan view micrograph of the Ge layer ($T_s = 305$ °C), taken under strongly diffracting conditions, is shown in Fig. 10. The mottled appearance of the film arises primarily from the variations in crystalline Ge overlayer film thickness that are apparent in Fig. 6.

Figures 3–9 are quite representative of the characteristics of all of the LPVD films studied to date by TEM. Epitaxial Ge films can be reproducibly grown on GaAs [100] for $T_s$ in the range of 285–330 °C. Upon increasing $T_s$ from ~300 to 330 °C, the thickness of the epi Ge layer increases slightly (~20%). Also, no obvious improvement in the film morphology or structure was observed if the film was slowly etched *during* the growth run (by adding HCl to the $GeH_4$/He flow). Rather, the morphology remained unchanged and



FIG. 8. [011] convergent beam electron diffraction pattern of the GaAs region near the Ge/GaAs interface for the sample of Fig. 7.



FIG. 9. Lattice image of the Ge/GaAs interface (sample of Figs. 3–8) taken along [011] GaAs. The continuity of the two sets of $\{111\}$ lattice fringes across the interface demonstrates the epitaxy between the two crystals.
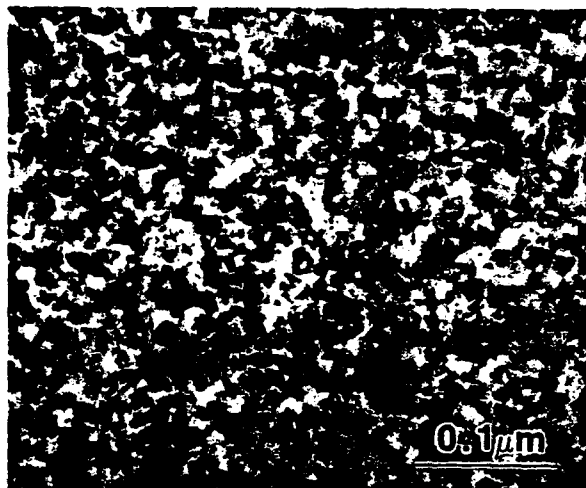
FIG. 10. Plan view micrograph of a Ge surface grown at $T_s = 305$ °C. The mottled appearance of the film arises primarily from the variations in Ge film thickness that are also apparent in Fig. 6.

the major difference was that the thickness of the crystalline layer was considerably thinner ($< 200$ Å), owing to the competition of growth and etching processes. Furthermore, the quality of the epitaxial Ge film actually deteriorates somewhat if HCl is continuously flowed through the reactor with the GeH$_4$/He mixture. This conclusion is based on the observation of misoriented domains of Ge that are apparent in samples grown under these conditions. However, dry chemical etching of the substrate (*in situ*) prior to film growth was found to be essential for obtaining epitaxial layers. Failure to do this consistently yielded amorphous films.

## 2. Reactor kinetics

It is not likely that the crystalline-to-amorphous switch in the film structure arises from the decrease in excimer laser beam intensity that occurs as the growth run proceeds owing to the formation of a thin Ge film on the quartz wall where the beam enters the reactor. After 600 s of growth time, the laser fluence entering the reactor was measured to have fallen only 12% $\pm$ 1% from its initial value. Rather, it appears that the transition from epitaxial to amorphous material can be attributed to one of three explanations which immediately present themselves. Each argument implicitly assumes that the species produced (indirectly) by the UV laser is digermane.

The peak laser intensities in these experiments have intentionally been maintained below 1 MW cm$^{-2}$ in order to minimize the impact of two photon absorption processes on the gas phase photochemistry occurring in the reactor. Hence, extensive photofragmentation of GeH$_4$ (beyond GeH$_3$ or, perhaps, GeH$_2$) is considered to be unlikely. Single photon dissociation of GeH$_4$ at 193 nm is expected to predominantly yield a germyl radical (GeH$_3$) which rapidly forms Ge$_2$H$_6$ by the reaction:

$$\text{GeH}_3 + \text{GeH}_3 + M \rightarrow \text{Ge}_2\text{H}_6 + M , \qquad (1)$$
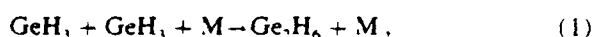
where M is any background species (such as He).[57] Regardless of whether GeH$_3$ or the germylene radical GeH$_2$ are produced initially, several arguments point to Ge$_2$H$_6$ as the species most likely responsible for film growth.[58] Although laser spectroscopic experiments will be necessary to fully resolve this issue, it is interesting to note that Taguchi and co-workers[47] have inferred the photochemical production of Si$_2$H$_6$ from SiH$_4$ (by an ArF laser) and its role in accelerating the growth rate of hydrogenated amorphous Si films.

Recent studies of the CVD of GeH$_4$/Ge$_2$H$_6$ mixtures by Gow et al.[59] demonstrated that the introduction of even trace amounts of digermane (0.2% Ge$_2$H$_6$/4.8% GeH$_4$ in buffer) into the reactor dramatically reduces the temperature at which pyrolysis can occur. Experiments with pure Ge$_2$H$_6$ revealed that pyrolysis occurred on oxidized Si substrates at temperatures $< 200$ °C which is well below the lowest tempeature (285 °C) at which we have grown epitaxial Ge films by LPVD. The pyrolytic temperature for monogermane, on the other hand, is $\sim 280$ °C (Ref. 60).

Further support for the pivotal role of Ge$_2$H$_6$ in the LPVD film growth process is suggested by the recent work of Gates[61] who investigated the chemisorption of the (analogous) silanes on Si(111)-(7×7) by temperature programmed desorption. The results showed a large enhancement in the adsorption rate for Si$_2$H$_6$ as opposed to that for monosilane.[62] Although this enhancement was attributed to the presence of the Si—Si bond in disilane, a second Si—Si bond (for Si$_3$H$_8$) leads to a much less dramatic improvement in the adsorption rate. It was concluded that the monosilane "...is relatively unreactive due to its short residence time and because adsorption requires Si—H bond scission."[61] Moreover, Perrin and Allain[63] have also recently demonstrated that, in the presence of UV radiation, GeH$_3$ radicals will form Ge$_2$H$_6$ at the surface.

All of the available evidence, therefore, points to Ge$_2$H$_6$ as the critical species in these LPVD experiments. Although not directly produced by the excimer laser, the molecule is apparently formed in the gas phase (or, for low GeH$_4$ partial pressures, at the surface) by the recombination of germylene radicals. The photochemical production of digermane not only accelerates the film growth rate (owing to a presumed higher adsorption rate for Ge$_2$H$_6$ as opposed to that for GeH$_4$) but also allows for the growth of epitaxial films at lower $T_s$ since digermane pyrolyzes at lower temperatures than does monogermane.

Let us now turn our attention to the Ge film growth process itself and, in particular, to the epitaxial-to-amorphous transition that is observed. The first plausible view is that, if the GaAs [100] surface is more catalytically active (in pyrolyzing Ge$_2$H$_6$) than is Ge, then once the substrate is covered by the coalescing islands, epitaxial film growth will stop. The second possibility revolves around the limited mobility of Ge adatoms that is an inherent characteristic of the low surface temperatures of these experiments. If these adatoms have a higher mobility on GaAs [100] or Ge [100] than they do on other surface orientations [such as GaAs (111), for example], film thickness may be limited by the fact that the growth of individual crystalline islands hinges on the migration of Ge adatoms over [111] surfaces.
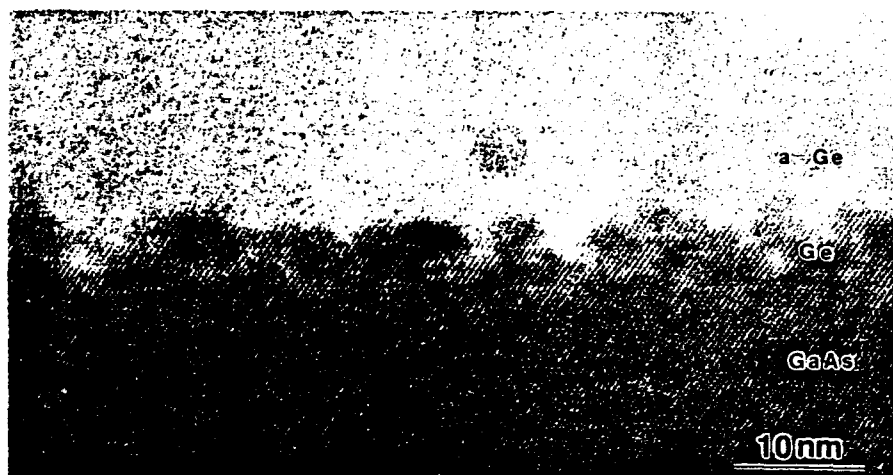
FIG. 11. TEM lattice image of a thin epitaxial Ge film grown on a tilted GaAs [100] substrate (offcut 3° toward [110]) at $T_s = 320$ °C. Note the relatively smooth morphology of the epilayer as compared to the film of Fig. 6.

In order to explore these possibilities further, several Ge layers were grown by LPVD at $280 < T_s < 320$ °C on substrates of various orientations. Films grown at 320 °C on [100] substrates which were offcut 3° towards [110] once again were initially epitaxial but the crystalline-to-amorphous transition occurred sooner (at $t \approx 120$ Å). Also, as is apparent in the cross-sectional TEM micrograph (lattice image) of Fig. 11, the epilayers were considerably smoother than those discussed earlier (on untilted [100] substrates). Both of these results are a consequence of the higher density of surface steps that are available with the tilted surface orientation. Since each of these steps is a potential nucleation site, more islands are presumably formed initially and coalescence occurs sooner due to the reduced lateral growth required of an island.

Several LPVD Ge layers were grown on [111] oriented substrates and all were completely amorphous. Under no conditions (varying $T_s$ up to 350 °C, etc.) was a crystalline film observed. One tentatively concludes that adatom mobility is, indeed, a crucial factor in determining the thickness of the LPVD grown Ge films. The development of nonthermal approaches to increasing Ge atom surface mobilities will likely remove the thickness limit encountered and allow for continuous epitaxial Ge films to be grown on GaAs at even lower temperatures.

Recent analysis of these films by SIMS suggests that an additional (and perhaps critical) factor in the transition to amorphous material is the gradual buildup of carbon in the epitaxial film as time proceeds. It is quite possible that, since the solubility of C in c-Ge is low, the carbon concentration at the Ge/gas phase growth front will rise as the front moves out from the substrate surface. Eventually, the C number density will exceed a critical level beyond which only a-Ge will grow. Studies to explore this possibility further with an improved vacuum system are continuing.

## B. LPVD grown films: $T_s \gtrsim 400$ °C

All of the Ge films grown on GaAs [100] in the ~240–280 °C range by LPVD are amorphous in character. At higher temperatures ($T_s \gtrsim 400$ °C), on the other hand, epilayers ~800 Å thick are grown. Subsequently, a transition to poly-

crystalline (rather than amorphous) material is observed.

The microstructure of a Ge/GaAs [100] sample grown at 400 °C can be seen in the cross-sectional micrograph of the interface (Fig. 12). Immediately adjacent to the interface is a layer of epitaxial Ge having a thickness of ~800 Å. On top of this is a region, ~0.9 $\mu$m thick, consisting of heavily microtwinned, columnar-type polycrystals with typical grain diameters of 0.25 $\mu$m and lengths of ~0.5 $\mu$m.

Figures 13 and 14 are [0$\bar{1}$1] convergent beam patterns of the GaAs substrate and the single-crystal Ge layer (sam-



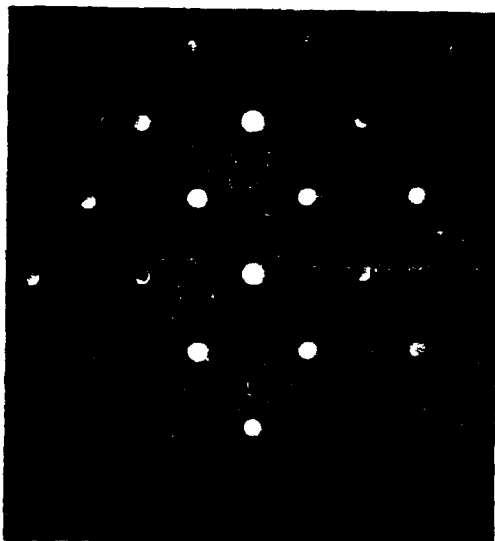FIG. 12. Cross-sectional TEM micrograph of a LPVD Ge/GaAs [100] interface grown at 400 °C.

FIG. 13. [0$\bar{1}$1] convergent beam diffraction pattern of the GaAs substrate for the sample of Fig. 12 ($T_s$ = 400 °C).
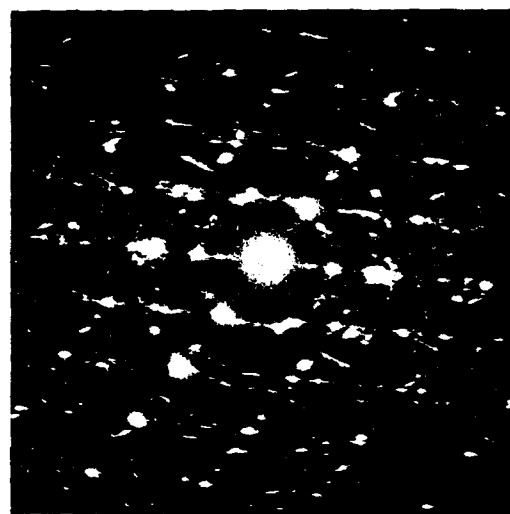


FIG. 15. Plan view SADP of the polycrystalline layer in the LPVD grown sample of Figs. 12–14.

ple of Fig. 12), respectively, and illustrate the epitaxy between the two crystals. As expected, the Ge pattern again reveals no {200}-type reflections. An SADP of the polycrystalline layer, given in Fig. 15, is characteristic of a textured polycrystalline morphology and the obvious streaking of the diffraction pattern is caused by the microtwinning within individual columnar grains.

A g = {111} dark field image of the Ge/GaAs interface for the sample of Figs. 12–15, is shown in Fig. 16. The entire

crystalline layer is strongly in contrast in this imaging condition which provides further confirmation of the epitaxial nature of the thin interfacial Ge film. It is worth noting, however, that the top surface of the epitaxial layer again has a fairly rough topography and inclined defects are frequently observed within the film.

Before leaving this section, it should be mentioned that Baert et al.[64] have recently observed thin ( ~ 200 Å) epitaxial Si films at the interface between [100] Si substrates and hydrogenated amorphous silicon. In their experiments, films were grown at 250 °C by dissociating $SiH_4$ in a radio frequency discharge. Although the transition from epitaxial to amorphous films was not discussed, the presence of the crystalline layer was attributed to cleaning of the substrate (chemically with HF and *in situ* by species produced in the discharge).

### C. Ge films grown by LPCVD (285< $T_s$ <410 °C)

In the absence of the external UV radiation (i.e., conventional low-pressure CVD), the Ge films grown in the 285–330 °C range are completely amorphous while those grown at higher temperatures ( ~ 410 °C) are heavily defected polycrystalline.

Figure 17 is a plan view micrograph of an amorphous Ge overlayer grown on [100] GaAs by LPCVD at $T_s$ = 305 °C. Recall that, at the edge of the hole in the TEM specimen, the Ge film overhangs the GaAs substrate. Note that in this region no band contours can be seen which is an earmark of amorphous material. Such contours are clearly evident in the GaAs substrate but end abruptly at the a-Ge/GaAs interface. A SADP of this layer, displayed in Fig. 18, exhibits only the diffuse rings expected for amorphous material. A cross-sectional view of this sample is shown in Fig. 19. Although this film is ~ 1000 Å thick, in contrast to the epi-



FIG. 14. [0$\bar{1}$1] convergent beam electron diffraction pattern of the ~ 800-Å-thick epitaxial Ge film for the sample of Figs. 12 and 13.

FIG. 16. Dark field image $(g = \{111\})$ of the Ge/GaAs interface ($T_s = 400$ °C).

taxial films discussed earlier, it has a smooth surface and exhibits no diffraction contrast.

Ge films grown pyrolytically on GaAs in the same reactor but at higher temperatures ($T_s \gtrsim 400$ °C) are polycrystalline. A plan view micrograph of a Ge layer grown at $T_s = 415$ °C is given in Fig. 20. The grains are typically 0.4 $\mu$m in diameter along this projection and exhibit no obvious texturing (nor do the boundaries between individual grains exhibit well-defined facetting). Furthermore, as illustrated in Fig. 21, most of the microcrystallites are heavily defected. This micrograph shows several Ge grains from the same sample imaged in Fig. 20 that are viewed along Ge [011]. The two equivalent types of twin planes that are observed are

$\{111\}$ type and are being viewed edge-on. The lamellae thickness of the microtwins are, in some cases, as small as a few Ge unit cells (i.e., down to ~ 17 Å). Dislocation structure is also frequently observed within individual Ge grains as well as at the grain boundaries. A SADP of a plan view specimen ($T_s$ again = 415 °C) is shown in Fig. 22. Acquired with a 20-$\mu$m selected area aperture, this pattern verifies that the film is indeed polycrystalline and the diffraction rings can be indexed (working out from the center) as corresponding to $\{111\},\{220\}$, $\{311\}$, $\{400\}$, $\{331\}$, $\{442\}$, ..., plane spacings, respectively. The obvious streaking of some reflections is attributable to the high density of microtwins discussed earlier.

A cross-sectional view of this textured polycrystalline sample, taken along GaAs [0$\bar{1}$1], is given in Fig. 23. The total thickness of the Ge layer is ~ 1.9 $\mu$m and the film is seen
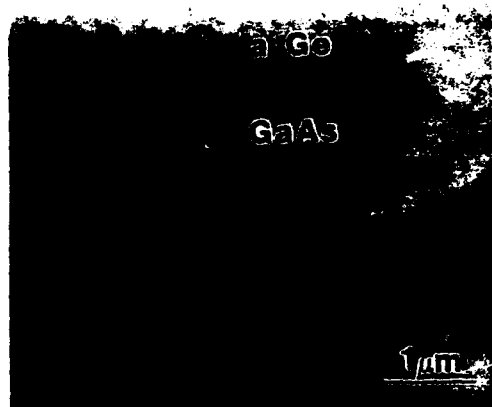


FIG. 17. Plan view micrograph of an amorphous Ge film grown at ~ 305 °C by conventional low pressure chemical vapor deposition (i.e., in the absence of parallel UV radiation).
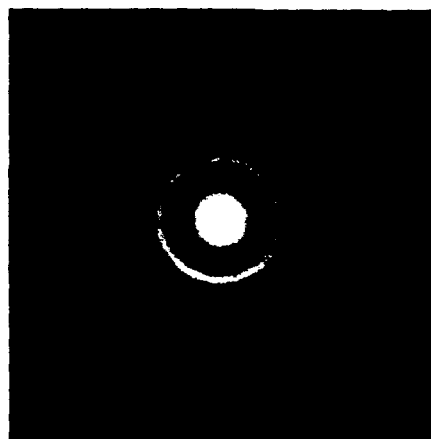


FIG. 18. SADP of the Ge overlayer of Fig. 17 ($T_s = 305$ °C, $I_{laser} = 0$).

FIG. 19. Cross-sectional view of the ~1000-Å-thick amorphous Ge film of Figs. 17 and 18 ($T_s$ = 305 °C).



FIG. 20. Plan view micrograph of a polycrystalline Ge layer grown on [100] GaAs at $T_s$ = 415 °C in the absence of (parallel) excimer laser radiation.

to be composed of three distinct and separate regions. Adjacent to the substrate is a layer, ~950 Å in thickness, which consists of fine-grained, randomly oriented polycrystals of Ge. The intermediate region is ~0.7 μm in thickness and is composed of columnar-shaped Ge grains. The outer layer consists of large columnar grains, typically 0.4 μm in diameter and ~1.1 μm in length, that are heavily microtwinned.

## D. General comments

As mentioned previously, epitaxial Ge films have been *reproducibly* grown on [100] GaAs for substrate temperatures as low as 285 °C. More than a half-dozen films have been grown in the 285–320 °C region and examined by TEM and all exhibit the same characteristics as those for the film of Figs. 3–11. That is, the Ge film initially grows epitaxially and, after reaching a thickness of 250–700 Å, converts to amorphous material. These results represent a decrease of more than 100 °C over the lowest temperature in the literature at which epitaxial Ge films have been grown on GaAs. Kräutle and co-workers[65] have reported the epitaxial growth of Ge on GaAs by CVD at temperatures as low as 400 °C (in contrast to our polycrystalline results) but, even at this temperature, the Ge film is heavily auto-doped. Therefore, the present experiments demonstrate that the nonequilibrium chemical environment produced by the ultraviolet laser permits the growth of epitaxial Ge films at temperatures at least 100 °C lower than those required for conventional CVD. The lower growth temperatures should considerably reduce interdiffusion at the Ge/GaAs interface.

## IV. SUMMARY AND CONCLUSIONS

Ge films grown on [100] GaAs by LPVD have been examined in detail by transmission electron microscopy. The LPVD growth process consisted of photodissociating GeH$_4$ at 193 nm (ArF laser, $\Phi$ ~ 15 mJ cm$^{-2}$) in parallel geome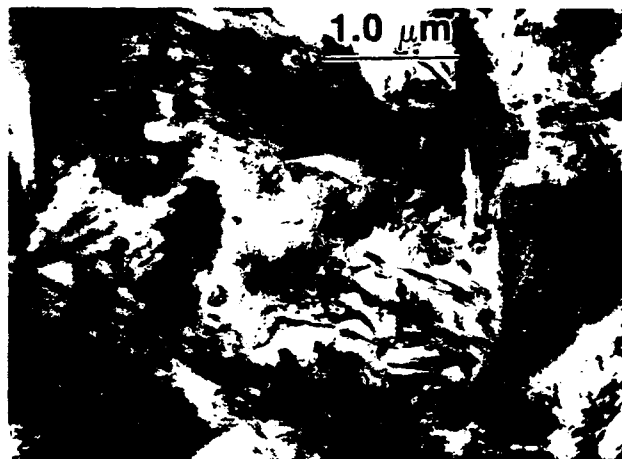try for $T_s$ ranging from room temperature to 415 °C. Resorting to parallel geometry prevents transient heating of the substrate and adlayer photolytic processes.

For 285 < $T_s$ ≲ 330 °C, the Ge film initially grows epitaxially but, after reaching a thickness of 250–700 Å (depending on gas pressure and flow, $T_s$, and the etching procedure), switches to *amorphous* material. At higher substrate temperatures ($T_s$ ≳ 400 °C), the epitaxial Ge film grows thicker (≳ 800 Å) before a transition to a *polycrystalline* layer takes place.

One of the most interesting aspects of these experiments is that, over the temperature range investigated, film growth *does* occur in the absence of UV laser radiation. Since the pyrolytic temperature for GeH$_4$ is ~280 °C, Ge films grown by LPCVD (i.e., with the laser blocked) are amorphous for 285 < $T_s$ ≲ 330 °C but, at the higher temperatures ($T_s$ ≳ 400 °C), heavily defected polycrystalline material is obtained.

The reduction in the epitaxial growth temperature made possible by the UV laser is attributed to the photochemical production of digermane (Ge$_2$H$_6$) in the reactor. Specifically, GeH$_3$ radicals produced from monogermane rapidly form Ge$_2$H$_6$ (by three body collisions) once outside the beam or at the substrate. Digermane has previously been identified[58] as one of the few (collisionally) stable photochemical products of the excimer laser photodissociation of GeH$_4$ and is known to pyrolyze at temperatures below 200 °C (Refs. 57 and 59).

It is apparent, then, that the laser directly produces a species (radical) which is collisionally transformed *en route* to the substrate into a more stable species. Upon reaching the GaAs [100] surface, this species (Ge$_2$H$_6$) is pyrolyzed, resulting in the growth of a Ge epilayer. The ability to grow epitaxial Ge layers at such low temperatures is critically de-

FIG. 21. Ge grains grown on GaAs [100] at $T_s = 415$ °C and viewed along [011], showing distinct microtwinning.

pendent upon both the surface orientation and cleaning procedure. For the present apparatus, *in situ* etching of the GaAs and the use of [100] (or slightly offcut [100]) substrates are essential for obtaining crystalline films. The data obtained to date indicate that the mobility of Ge adatoms on GaAs[111] is smaller than that for [100] surfaces. From the results reported in Ref. 57, one would expect that, if adatom mobility were not a problem, higher ArF laser fluences (and, perhaps, lower pressures) would allow for epi Ge films to be grown at temperatures below 200 °C. That is, at the higher 193-nm intensities, the peak Ge number density (produced directly from $GeH_4$ by multiphoton absorption) rises to sufficiently high levels to allow monolayer $s^{-1}$ growth rates without the need to pyrolyze polyatomics (higher germanes) such as $Ge_2H_6$.

The results presented are interesting in that we are aware of no other example in which photons have altered the gas phase (and subsequently, the surface) chemistry of a reactor which, in the absence of external radiation, produces amorphous or polycrystalline material. The laser initiated chemistry, however, culminates in the growth of epitaxial films.
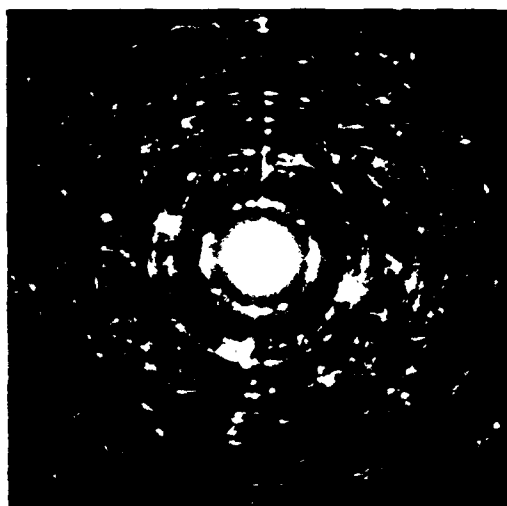




FIG. 22. Plan view SADP of a polycrystalline Ge film ($T_s = 415$ °C). The streaking of the diffraction pattern is attributable to the high microtwin density in the sample.

FIG. 23. Cross-sectional micrograph, taken along GaAs [011], of the polycrystalline sample of Figs. 20–22. The total thickness of the Ge layer is ~1.9 $\mu$m.

[1]For a review of early work in the field, see R. M. Osgood, Jr., Ann. Rev. Phys. Chem. **34**, 77 (1983).

[2]F. A. Houle, Appl. Phys. A **41**, 315 (1986).

[3]R. W. Andreatta, C. C. Abele, J. F. Osmundsen, J. G. Eden, D. Lubben, and J. E. Greene, Appl. Phys. Lett. **40**, 183 (1982).

[4]J. G. Eden, J. E. Greene, J. F. Osmundsen, D. Lubben, C. C. Abele, S. Gorbatkin, and H. D. Desai, Mater. Res. Soc. Symp. Proc. **17**, 185 (1983).

[5]H. Niki and G. J. Mains, J. Phys. Chem. **68**, 304 (1964).

[6]T. Saitoh, S. Muramatsu, T. Shimada, and M. Migitaka, Appl. Phys. Lett. **42**, 678 (1983).

[7]T. Inoue, M. Konagai, and K. Takahashi, Appl. Phys. Lett. **43**, 774 (1983).

[8]S. Nishida, H. Tasaki, M. Konagai, and K. Takahashi, J. Appl. Phys. **58**, 1427 (1985).

[9]S. Nishida, T. Shiimoto, A. Yamada, S. Karasawa, M. Konagai, and K. Takahashi, Appl. Phys. Lett. **49**, 79 (1986).

[10]Y. Mishima, M. Hirose, Y. Osaka, K. Nagamine, Y. Ashida, N. Kitagawa, and K. Isogaya, Jpn. J. Appl. Phys. **22**, L46 (1983).

[11]Y. Mishima, Y. Ashida, and M. Hirose, J. Non-Cryst. Solids **59&60**, 70 (1983).

[12]K. Kumata, U. Itoh, Y. Toyoshima, N. Tanaka, H. Anzai, and A. Matsuda, Appl. Phys. Lett. **48**, 1380 (1986).

[13]N. Gonohe, S. Shimizu, K. Tamagawa, T. Hayashi, and H. Yamakawa, Jpn. J. Appl. Phys. **26**, L1189 (1987).

[14]A. Yoshikawa and S. Yamaga, Jpn. J. Appl. Phys. **23**, L473 (1984).

[15]Y. Toyoshima, K. Kumata, U. Itoh, and A. Matsuda, Appl. Phys. Lett. **51**, 1925 (1987).

[16]A. Ishitani, M. Kanamori, and H. Tsuya, J. Appl. Phys. **57**, 2956 (1985).

[17]A. Ishitani and S. Itoh, Paper D 3.6, Materials Research Society Fall Meeting, Boston, MA (1985).

[18]A. Ishitani, Y. Ohshita, K. Tanigaki, K. Takada, and S. Itoh, J. Appl. Phys. **61**, 2224 (1987).

[19]V. M. Donnelly, M. Geva, J. Long, and R. F. Karlicek, Appl. Phys. Lett. **44**, 951 (1984).

[20]V. M. Donnelly, D. Brasen, A. Appelbaum, and M. Geva, J. Appl. Phys. **58**, 2022 (1985).

[21]V. M. Donnelly, V. R. McCrary, A. Appelbaum, D. Brasen, and W. P. Lowe, J. Appl. Phys. **61**, 1410 (1987).

[22]V. R. McCrary, V. M. Donnelly, D. Brasen, A. Appelbaum, and R. C. Farrow, Mater. Res. Soc. Symp. Proc. **75**, 223 (1987).

[23]S. S. Chu, T. L. Chu, C. L. Chang, and H. Firouzi, Appl. Phys. Lett. **52**, 1243 (1988).

[24]C. W. Tu, V. M. Donnelly, J. C. Beggy, F. A. Baiocchi, V. R. McCrary, T. D. Harris, and M. G. Lamont, Appl. Phys. Lett. **52**, 966 (1988).

[25]V. M. Donnelly, C. W. Tu, J. C. Beggy, V. R. McCrary, M. G. Lamont, T. D. Harris, F. A. Baiocchi, and R. C. Farrow, Appl. Phys. Lett. **52**, 1065 (1988).

[26]S. J. C. Irvine, J. B. Mullin and J. Tunnicliffe, J. Cryst. Growth **68**, 188 (1984).

[27]S. J. C. Irvine, J. Giess, J. B. Mullin, G. W. Blackmore, and O. D. Dosser, J. Vac. Sci. Technol. B **3**, 1450 (1985).

[28]S. J. C. Irvine and J. B. Mullin, J. Vac. Sci. Technol. A **5**, 2100 (1987).

[29]S. J. C. Irvine, J. B. Mullin, H. Hill, G. T. Brown, and S. J. Barnett, J. Cryst. Growth **86**, 188 (1988).

[30]W. L. Ahlgren, E. J. Smith, J. B. James, T. W. James, R. P. Ruth, E. A. Patten, R. D. Knox, and J.-L. Staudenmann, J. Cryst. Growth **86**, 198 (1988).

[31]B. J. Morris, Appl. Phys. Lett. **48**, 867 (1986).

[32]J. J. Zinck, P. D. Brewer, J. E. Jensen, G. L. Olson, and L. W. Tutt, Appl. Phys. Lett. **52**, 1434 (1988); Mater. Res. Soc. Symp. Proc. **101**, 319 (1988).

[33]J. Nishizawa, Y. Kokubun, H. Shimawaki, and M. Koike, J. Electrochem. Soc. **132**, 1939 (1985).

[34]N. Pütz, H. Heinecke, E. Veuhoff, G. Arens, M. Heyen, H. Lüth, and P. Balk, J. Cryst. Growth **68**, 194 (1984).

[35]S. Fujita, A. Tanabe, T. Sakamoto, M. Isemura, and S. Fujita, Jpn. J. Appl. Phys. **26**, L2000 (1987).

[36]A. Doi, Y. Aoyagi, and S. Namba, Mater. Res. Soc. Symp. Proc. **75**, 217 (1987); Appl. Phys. Lett. **49**, 785 (1986).

[37]N. H. Karam, N. A. El-Masry, and S. M. Bedair, Appl. Phys. Lett. **49**, 880 (1986); S. M. Bedair, J. K. Whisnant, N. H. Karam, D. Griffis, N. A. El-Masry, and H. H. Stadelmaier, J. Cryst. Growth **77**, 229 (1986).

[38]Y. Aoyagi, M. Kanazawa, A. Doi, S. Iwai, and S. Namba, J. Appl. Phys. **60**, 3131 (1986).

[39]H. Kukimoto, Y. Ban, H. Komatsu, M. Takechi, and M. Ishizaki, J. Cryst. Growth, 223 (1986).

[40]Y. Ban, M. Takechi, M. Ishizaki, H. Murata, and H. Kukimoto, Jpn. J. Appl. Phys. **25**, L967 (1986).

[41]R. N. Bicknell, N. C. Giles, and J. F. Schetzina, Appl. Phys. Lett. **49**, 1735 (1986).

[42]R. Solanki, U. Sudarsan, and J. C. Johnson, Appl. Phys. Lett. **52**, 919 (1988).

[43]P. K. Boyer, G. A. Roche, W. H. Ritchie, and G. J. Collins, Appl. Phys. Lett. **40**, 716 (1982); R. Solanki, W. H. Ritchie, and G. J. Collins, Appl. Phys. Lett. **43**, 454 (1983).

[44]P. K. Boyer, C. A. Moore, R. Solanki, W. K. Ritchie, G. A. Roche, and G. J. Collins, Mater. Res. Soc. Symp. Proc. **17**, 119 (1983).

[45]P. K. Boyer, K. A. Emery, H. Zarnani, and G. J. Collins, Appl. Phys. Lett. **45**, 979 (1984).

[46]T. F. Deutsch, D. J. Silversmith, and R. W. Mountain, Mater. Res. Soc. Symp. Proc. **17**, 129 (1983).

[47]T. Taguchi, M. Morikawa, Y. Hiratsuka, and K. Toyoda, Appl. Phys. Lett. **49**, 971 (1986).

[48]V. Tavitian, C. J. Kiely, and J. G. Eden, Mater. Res. Soc. Symp. Proc. **101**, 349 (1988).

[49]J. G. Eden, V. Tavitian, and C. J. Kiely, Proc. SPIE **894**, 26 (1988).

[50]V. Tavitian, C. J. Kiely, D. B. Geohegan, and J. G. Eden, Appl. Phys. Lett. **52**, 1710 (1988).

[51]VCR is a trademark of the Cajon Company, 9760 Shepard Road, Macedonia, OH 44056.

[52]J. J. Zinck, P. D. Brewer, J. E. Jensen, G. L. Olson, and L. W. Tutt, Mater. Res. Soc. Symp. Proc. **75**, 233 (1987).

[53]W. T. Anderson, Jr., A. Christou, and J. E. Davey, J. Appl. Phys. **49**, 2998 (1978).

[54]G. M. Rackham, Ph.D. thesis, University of Bristol (1976).

[55]J. C. Bravman and R. Sinclair, J. Electron Microsc. Tech. **1**, 53 (1984).

[56]See, for example, I. W. Boyd, Laser Processing of Thin Films and Microstructures (Springer, Berlin, 1987), pp. 85–88 and references cited therein.

[57]K. K. King, V. Tavitian, D. B. Geohegan, E. A. P. Cheng, S. A. Piette, F. J. Scheltens, and J. G. Eden, Mater. Res. Soc. Symp. Proc. **75**, 189 (1987).

[58]J. F. Osmundsen, C. C. Abele, and J. G. Eden, J. Appl. Phys. **57**, 2921 (1985).

[59]T. R. Gow, D. G. Coronell, and R. I. Masel, J. Mater. Res. (to be published).

[60]L. H. Hall, J. Electrochem. Soc. **119**, 1593 (1972).

[61]S. M. Gates, Surf. Sci. (in press).

[62]The $Si_2H_6$ adsorption rate was measured to be roughly an order of magnitude larger than that for $SiH_4$ at an exposure of $\sim 10^{16}$ molecules cm$^{-2}$. The difference appears to be even greater for smaller surface exposures.

[63]J. Perrin and B. Allain, J. Non-Cryst. Solids **97&98**, 261 (1987).

[64]K. Baert, J. Symons, W. Vandervorst, J. Vanhellemont, M. Caymax, J. Poortmans, J. Nijs, and R. Mertens, Appl. Phys. Lett. **51**, 1922 (1987).

[65]H. Kräutle, P. Roentgen, and H. Beneking, J. Cryst. Growth **65**, 439 (1983).